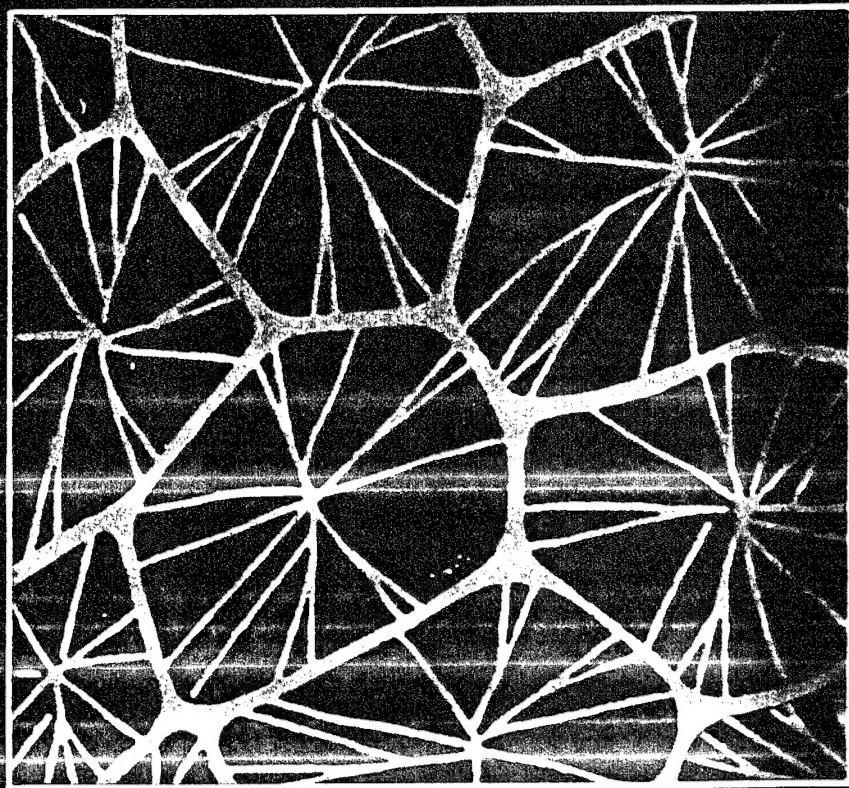
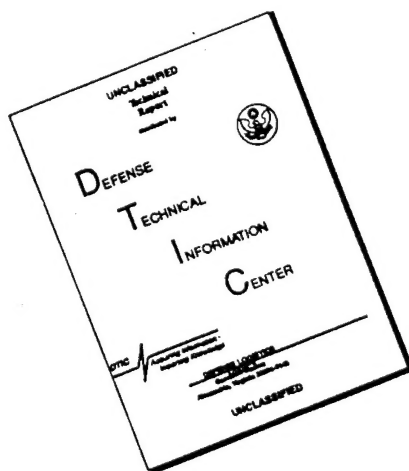


Nondestructive Characterization of Materials VI



Edited by
Robert E. Green, Jr.,
Krzysztof J. Kozaczek,
and Clayton O. Ruud

DISCLAIMER NOTICE



THIS DOCUMENT IS BEST
QUALITY AVAILABLE. THE COPY
FURNISHED TO DTIC CONTAINED
A SIGNIFICANT NUMBER OF
PAGES WHICH DO NOT
REPRODUCE LEGIBLY.

Nondestructive Characterization of Materials VI



Accession For	
NTIS CRA&I	<input checked="" type="checkbox"/>
DTIC TAB	<input type="checkbox"/>
Unannounced	<input type="checkbox"/>
Justification	
By	
Distribution /	
Availability Codes	
Dist	Avail and/or Special
A-1	

1995 0130 116

DISTRIBUTION STATEMENT A
Approved for public release;
Distribution Unlimited

Nondestructive Characterization of Materials VI

Edited by

Robert E. Green, Jr.

The Johns Hopkins University
Baltimore, Maryland

Krzysztof J. Kozaczek

Oak Ridge National Laboratory
Oak Ridge, Tennessee

and

Clayton O. Ruud

The Pennsylvania State University
University Park, Pennsylvania

PLENUM PRESS • NEW YORK AND LONDON

Library of Congress Cataloging-in-Publication Data

On file

Proceedings of the Sixth International Conference on Nondestructive Characterization of Materials,
held June 7-11, 1993, in Oahu, Hawaii

ISBN 0-306-44816-5

© 1994 Plenum Press, New York
A Division of Plenum Publishing Corporation
233 Spring Street, New York, N. Y. 10013

All rights reserved

No part of this book may be reproduced, stored in a retrieval system, or transmitted in any form or by
any means, electronic, mechanical, photocopying, microfilming, recording, or otherwise, without
written permission from the Publisher

Printed in the United States of America

The papers published in these proceedings represent some of the latest developments in nondestructive characterization of materials and were presented at the Sixth International Symposium on Nondestructive Characterization of Materials held June 7-11, 1993, at the Turtle Bay Hilton Hotel on the north shore of Oahu, Hawaii.

SYMPOSIUM CO-CHAIRMEN

Robert E. Green, Jr.
Center for NDE
The Johns Hopkins University
3400 N. Charles Street
Baltimore, MD 21218

Murli H. Manghnani
Hawaii Institute of Geophysics
University of Hawaii at Manoa
2525 Correa Road
Honolulu, Hawaii 96822

Teruo Kishi
The University of Tokyo
4-6-1 Komaba, Merguro-Ku
Tokyo 153, Japan

Clayton O. Ruud
The Pennsylvania State University
159 Materials Research Lab.
University Park, PA 26802

ORGANIZING COMMITTEE

Alfred Broz, Federal Aviation Administration, U.S.A.
Jean P. Bussiere, National Research Council, Canada
Joseph S. Heyman, NASA/Langley Research Center, U.S.A.
Katsuhiro Kawashima, Nippon Steel Corporation, Japan
Michael Kroning, IzfP, Fraunhofer-Institut, Germany
Soung-Nan Liu, Electric Power Research Institute, U.S.A.
Charles H. McGogney, Federal Highway Administration, U.S.A.
Yapa Rajapakse, Office of Naval Research, U.S.A.
Tetsuya Saito, National Research Institute for Metals, Japan
Donald O. Thompson, Iowa State University, U.S.A.
James W. Wagner, Johns Hopkins University, U.S.A.
F. Alan Wedgwood, NNDTC, Harwell Laboratory, England
H. Thomas Yolken, NIST, U.S.A.

FINANCIAL SUPPORTERS

Army Research Office
American Society for Nondestructive Testing
Federal Aviation Administration
Federal Highway Administration
National Aeronautics and Space Administration
National Institute of Standards and Technology
National Science Foundation
Office of Naval Research

PREFACE

Traditionally the vast majority of materials characterization techniques have been destructive, e.g., chemical compositional analysis, metallographic determination of microstructure, tensile test measurement of mechanical properties, etc. Also, traditionally, nondestructive techniques have been used almost exclusively for the detection of macroscopic defects, mostly cracks, in structures and devices which have already been constructed and have already been in service for an extended period of time. Following these conventional nondestructive tests, it has been common practice to use somewhat arbitrary accept-reject criteria to decide whether or not the structure or device should be removed from service. The present unfavorable status of a large segment of industry, coupled with the desire to keep structures in service well past their original design life, dramatically show that our traditional approaches must be drastically modified if we are to be able to meet future needs.

The role of nondestructive characterization of materials is changing and will continue to change dramatically. It has become increasingly evident that it is both practical and cost effective to expand the role of nondestructive evaluation to include all aspects of materials' production and application and to introduce it much earlier in the manufacturing cycle. In fact, the recovery of a large portion of industry from severe economic problems is dependent, in part, on the successful implementation of this expanded role. Currently, efforts are directed at developing and perfecting techniques which are capable of monitoring and controlling the materials production process; materials stability during transport, storage, and fabrication; and the amount and rate of degradation during the materials in-service life. To be more precise, the role of nondestructive testing has expanded far beyond its historical mission of detecting macroscopic defects in structures and devices which had already been constructed and most often had been in service for an extended period of time. Today, and ever increasingly in the future, using advanced sensors and modern measurement technology, along with signal/data processing techniques, information on the processing conditions and the properties and characteristics of the materials being processed can be continuously generated. Real-time process monitoring for more effective and efficient real-time process control and improved product quality and reliability will now become a practical reality.

The optimization of the processing and properties of polymers, ceramics and composites, the development of synthetically structured materials, the characterization of surfaces and interfaces, the measurement and character-characterization of amorphous metals and semiconductors, the growth of perfect electronic and optical crystals and thin films, and in all cases, the structures, devices and systems made from these materials

demand the innovative application of modern nondestructive materials characterization techniques to monitor and control as many stages of the production process as possible. Simply put, intelligent manufacturing is impossible without integrating modern nondestructive evaluation into the production system.

Robert E. Green, Jr.
Center for Nondestructive Evaluation
The Johns Hopkins University

ACKNOWLEDGEMENTS

A special thanks is due Academician Leonid M. Lyamshev from the Acoustical Institute of the Russian Academy of Sciences, Moscow, for presentation of a special invited lecture on Radiation Acoustics and Nondestructive Evaluation. Although the complete manuscript of the presentation by Academician Lyanshev is not available for printing in the proceedings, a publication is available elsewhere which contain details of his subject matter, namely: L.M. Lyamshev, Radiation Acoustics, Sov. Phys. Usp. 162, 43-94 (1992) [in English].

The conference organizers are indebted to a number of individuals for their assistance in making the symposium a success. Thanks to: the authors for their excellent contributions and cooperation in providing manuscripts; to the session chairpersons for keeping the sessions on time and stimulating lively discussions; to the University of Hawaii for assistance with the poster sessions; to Moshe Rosen, Jim Spicer, Jim Wagner, and John Winter, all of the Center for Nondestructive Evaluation of The Johns Hopkins University, for manuscript reviews.

The symposium and the ensuing proceedings would have not been possible without the enthusiasm and extremely hard work of Debbie Harris, The Johns Hopkins University Center for Nondestructive Evaluation Center Coordinator, and her assistant, Debby Manley. All of us who enjoyed the symposium venue, the technical sessions, and the social events owe both of these women our most sincere vote of thanks.

CONTENTS

PROCESS CONTROL

Monitoring of Resin-Transfer Molding Using Laser-Based Ultrasound.....	1
A.D.W. McKie, R.C. Addison, Jr., T.-L.T. Liao, and H.-S. Ryang	
Embedded Acoustic Sensors for Process Control and Health Monitoring of Composite Materials.....	7
M.J. Ehrlich, C.V. O'Keefe, B.B. Djordjevic, and B.N. Ranganathan	
Surface Controlled Materials Evaluation for Al-Implanted Ni Alloys.....	13
T. Aizawa, J. Mitsuo, and J. Kihara	
Development and Evaluation of a Workpiece Analyzer for Industrial Furnaces.....	21
P. Kotidis, J. Woodroffe, J. Shah, and T. Schultz	
Sensor System for Intelligent Processing of Hot-Rolled Steel.....	29
A.V. Clark, M.G. Lozev, B.J. Filla, and L.J. Bond	
On-Line Ultrasonic Characterization of Polymer Flows.....	37
L. Piché, D. Lévesque, R. Gendron, and J. Tatibouët	
An Ultrasonic Testing Technique for Monitoring the Cure and Mechanical Properties of Polymeric Materials.....	45
E.C. Johnson, J.D. Pollchik, and S.L. Zacharius	
Elasticity of Single-Crystal Al_2O_3 (Saphikon) Fiber to 1000°C by Brillouin Spectroscopy.....	53
M.H. Manghnani, V. Askarpour, and J.A. DiCarlo	
Characterization of Sheet Steels in the Development of On-Line Sensors for Quality Control Monitoring of Mechanical Properties.....	59
L.J. Swartzendruber, Y. Rosenthal, and G.E. Hicho	

ACOUSTIC TECHNIQUES I

Quantitative Ultrasonic Characterization of Interfacial Adhesion in Metal-Polymer- Metal Multilayer Composites.....	71
L. Piché, D. Lévesque, P. Deprez, A. Michel, and J. Tatibouët	

Surface Roughness and Ultrasonic Materials Characterization.....	79
P.B. Nagy, G. Blaho, and J.H. Rose	
Microscopic Determination of Surface Wave Velocities in Heat Treated Steels by Ultrasonic Reflectivity Measurement.....	87
I. Ihara, T. Aizawa, and J. Kihara	
Ultrasonic Backscattering as a Fingerprint Technique for Identity and Integrity Verification of Components.....	95
H.H. Willems and E. Wogatzki	
Air-Coupled Ultrasonic System for Detecting Delaminations and Cracks in Paintings on Wooden Panels.....	103
A. Murray, E.S. Boltz, M.C. Renken, C.M. Fortunko, M.F. Mecklenburg, and R.E. Green, Jr.	
Model-Based Calibration of Ultrasonic System Responses for Quantitative Measurements.....	111
L.W. Schmerr, Jr., S-J. Song, and H. Zhang	

MATERIALS CHARACTERIZATION I

Ultrasonic Characterization of Texture in Pure and Alloyed Zirconium.....	119
A. Moreau, P.J. Kielczynski, J.F. Bussière, and J.H. Root	
Microtomography Using Conventional X-Ray Sources.....	129
Y. Yamauchi, N. Kishimoto, and T. Ikuta	
X-Ray Measurement of Fatigue Damage by Using Imaging Plate.....	137
S. Yusa, K. Yoshida, and Y. Yoshioka	
Nondestructive Characterization of Metals Subjected to High-Power Ultrasound.....	147
K.A. Green and R.E. Green, Jr.	
A Study of Substructures in Welded Beta Titanium Alloy by Microbeam X-Ray Diffraction Analysis.....	157
Y. Shirasuna, A. Nozue, T. Okubo, K. Kuribayashi, S. Ishimoto, H. Sato, and Y. Yoshioka	
Study of Effect of Methane Concentration in Argon Plasma on Tantalum Compound Sputtering Deposition Process.....	165
S.L. Lee and C.S. Lee	
Quantitative Nondestructive Evaluation of Density of Green State Compressed Products.....	175
J. Muller, L. Ackermann, D. Babot, G. Peix, and P. Zhu	

ACOUSTIC TECHNIQUES II

A Neural Network for Predicting Ultimate Strengths of Aluminum-Lithium Welds from Acoustic Emission Amplitude Data.....	183
E.v. K. Hill and G.L. Knotts	
Acoustic Emission Monitoring of Thick Composite Laminates under Compressive Loads.....	191
C. Byrne and R.E. Green, Jr.	
Ultrasonic Evaluation of Composite Fatigue Damage.....	199
A.J. Gavens and R.E. Green, Jr.	
A Study on the Acoustic Emission Characteristics of the Carbon Fiber Reinforced Plastics.....	207
Y.K. Ji and J.W. Ong	
Tool Wear Monitoring at Turning and Drilling.....	215
E. Waschkies, C. Sklarczyk, and E. Schneider	
Nondestructive Evaluation of Micromechanism of Deformation Process during Fatigue Testing on Polymer by ETFuM (Elastic-wave Transfer Function Method).....	223
Y. Higo, H. Kawabe, Y. Natsume, and S. Nunomura	
Application of Ultrasonic Imaging to Wrap Analysis through Flow Pattern Observation of Injection Molded FRTP Product.....	231
T. Abe, I. Hanada, T. Kuriyama, and I. Narisawa	
Conversion of NDE Inspection Signals into Aural Signals for Enhanced Material Characterization.....	239
G.M. Light, A.E. Holt, K.D. Polk, and W.T. Clayton	

CERAMICS

Development of Real Time Monitoring of Damage by Acousto-Ultrasonic NDE Technique to Study Failure Mechanisms in SiC/CAS Ceramic Composites.....	247
A. Tiwari and E.G. Henneke, II	
Quantitative Nondestructive Evaluation of Ceramic Fibers.....	255
R.M. Kent	
Evaluation of Microfracture Due to Stress Corrosion of Particulate Glass Composite by Acoustic Emission.....	263
K. Kageyama, M. Enoki, and T. Kishi	
AE Studies on the Microfracture Process in Structural Ceramics.....	271
S. Wakayama and M. Kawahara	

Elastic Properties of Thin Film Silicon Nitride by Brillouin Spectroscopy.....	279
V. Askarpour, M.H. Manghnani, M. Mendik, and P. Wachter	
Measurement of Residual Stresses on Ceramic Materials with High Spatial Resolution.....	285
K.J. Kozaczek, C.O. Ruud, and J.D. Fitting	
Characterization of Ceramic/Ceramic Matrix Composite Materials from Elastic Wave Scan Images.....	291
W. Sachse, M. Shiwa, T. Kishi, and M.O. Thompson	
Nondestructive Characterization of Adhesive Bond Strength in Laminated Safety Glass.....	299
H. Reis	

OPTICAL TECHNIQUES

Surface Acoustic Waves Generation by Phase Velocity Scanning of Laser Interference Fringes and Its Application to Nondestructive Materials Evaluation.....	307
H. Nishino, Y. Tsukahara, Y. Nagata, T. Koda, and K. Yamanaka	
Material Characterization by Contactless Measurement of Ultrasonic Absorption Using Laser Ultrasound.....	317
B. Haberer, M. Paul, H. Willems, and W. Arnold	
Microscopic Ultrasonic Imaging Using Non-Contact Ultrasonic Detection by Optical Heterodyne Interferometry.....	325
H. Yamawaki and T. Saito	
A Practical System for Pulsed Laser Array Generation of Ultrasound.....	333
T.W. Murray, J.S. Steckenrider, J.W. Wagner, and J.B. Deaton, Jr.	
Optical Detection of Stress Waves in Glass Fiber Reinforced Plastic Composite Material.....	341
R.D. Huber and J.W. Wagner	
Time-Resolved Holography for the Microscopic Study of Crack-Tip Motion in Dynamic Fracture.....	349
J.S. Steckenrider and J.W. Wagner	
Embedded and Attached Sapphire Optical Fiber Sensors for the Nondestructive Characterization of Materials at High Temperature.....	357
R.O. Claus, K.A. Murphy, A. Wang, R.G. May, and M. de Vries	
Multi-Parameter Fiber Optic Sensing for Composite Material Monitoring.....	363
C.V. O'Keefe, B.B. Djordjevic, and B.N. Ranganathan	
Quantitative Measurement of Strain in Reinforced Concrete Structures Using Calibrated Optical Fiber Sensors.....	369
R.O. Claus, S.F. Masri, M. de Vries, M. Nasta, and K.A. Murphy	

RESIDUAL STRESS

Ultrasonic Measurement of the Kearns Texture Parameter in Zircaloy.....	375
A.J. Anderson and R.B. Thompson	
Ultrasonic Characterization of Stress States in Rims of Railroad Wheels.....	383
E. Schneider, R. Herzer, D. Bruche, and H. Frotscher	
Electromagnetic Acoustic Resonance Method for Measuring Stresses in Metal Plates...	391
M. Hirao, H. Ogi, T. Yamasaki, and H. Fukuoka	
Nondestructive Evaluation of Welding Residual Stress and Mechanical Stress- Relieving by Acoustoelasticity.....	397
I. Oda	
Nondestructive Stress Measurement Using Frequency Dependence of Magnetoacoustic Interaction.....	405
T. Yamasaki, K. Ebata, and H. Fukuoka	
Residual Stresses Induced by Slitting Copper Alloy Strip.....	413
C.O. Ruud and M.E. Jacobs	
Comparison of Residual Stress and Hardness in a Symmetric and an Eccentric Swage Autofrettaged Cylinder.....	425
S.L. Lee, L. Britt, and G. Capsimalis	
Non-Destructive Characterization of Materials with Neutron Experiments at the Pulsed Reactor IBR-2.....	435
F. Häußler, H. Baumbach, and M. Kröning	

ELECTRONIC MATERIALS AND COMPONENTS

In Situ Detection of Flaws in Multilayer Ceramic Capacitors Using Electronic Speckle Pattern Interferometry.....	445
Y.C. Chan, F. Yeung, G.C. Jin, N.K. Bao, and P.S. Chung	
Growth Rates and Interface Shapes in Semiconductor Materials Using Real Time Radiographic Imaging.....	453
R.T. Simchick, S. Sorakach, A.L. Fripp, W.J. Debnam, R.F. Berry, D.J. Jobson, and P.G. Barber	
Environmental Scanning Electron Microscopic Investigation of Interfacial Defects in Electronic Packages.....	461
J. Li and M. Pecht	
Detection of Cracks in Ceramics Used in Electronic Devices Using Light Scattering.....	469
S. Hull	
Electrical Characterization of Precision Piezoelectric Quartz Crystal Resonators.....	479
J.J. Suter, J.R. Norton, and R. Besson	

Interply Pressure Measurements in Rapidly Heated Carbon-Phenolic Composites.....	487
G.F. Hawkins and E.C. Johnson	

Non-Destructive Characterization of Thin Diamond-like Carbon, Semiconducting and High Temperature Superconducting Films.....	493
H.D. Bist, P.S. Dobal, S. Bhargava, R.N. Soni, and P.K. Khulbe	

AIRCRAFT/AEROSPACE

Elastic Wave Propagation in Aluminum/Aramid-Epoxy Plates.....	501
P.J. Shull, D.E. Chimenti, S.K. Datta, and J.H. Ju	

A Multi-Parameter Ultrasonic Inspection Technique.....	509
B.W. Sermon and W.J. Murri	

Nondestructive Characterization of Heat Damage in Graphite/Epoxy Composites.....	517
G.A. Matzkanin	

Intrinsic Amplitude Distributions and the Ultrasonic Inspection of Fiber-Metal Laminates.....	525
M.P. Jones	

An Acousto-Ultrasonic Platform for the Quality Assessment of Thick Radial Ply Composite Structures.....	531
T.J. Gill, Jr. and A.L. Bartos	

MATERIALS CHARACTERIZATION II

Use of Fourier Spectra for Ultrasonic Nondestructive Evaluation of Thin Coatings.....	539
V.K. Kinra and C. Zhu	

Nondestructive Evaluation of Biologically Degraded Wood.....	545
R.J. Ross, R.C. DeGroot, and W.J. Nelson	

Measurement of Ultrasonic Attenuation and Grain Size of Thin Metal Sheets Using Resonance Mode EMAT.....	551
T. Hyoguchi, T. Akagi, O.B. Wright, and K. Kawashima	

Quantitative Analysis of the Elastic Properties of AL-LI-CU Alloys.....	559
B.C. Lee, J.K. Park, and S.S. Lee	

Measurement of Anisotropic Elastic Moduli and Comparison with Equivalent Media Theories.....	567
J.A. Hood, R.B. Mignogna, N.K. Batra, K.E. Simmonds, and H.H. Chaskelis	

Nondestructive Evaluation of Co Agglomeration and WC Growth in WC/Co Superhard Alloy.....	575
T. Aizawa and J. Kihara	

Application of Fractal Analysis for Surface Flaw Inspection of Steel Sheet.....	585
S. Horiata, H. Kashida, H. Kitagawa, M. Satoh, H. Aizawa, and T. Tamiya	
An Integrated Ultrasonic and Eddy Current Imaging System.....	593
E.J. Chern	
Microwave Speckle Contrast for Surface Roughness Measurements.....	599
D.A. Oursler and J.W. Wagner	

BIOMIMETIC and BIOTIC MATERIALS

Biological Processes in Materials Synthesis.....	607
E.R. Valdes	
Enzyme-Catalyzed Polymerization in Microstructured Fluid Media: The Synthesis and Characterization of Novel Biomolecular Materials.....	613
C.F. Karayigitoglu, X. Xu, P. Webb, M. Tata, N.S. Kommareddi, V.T. John, R.D. Gonzalez, G.L. McPherson, M. Ayyagari, J.A. Akkara, and D.L. Kaplan	
Mechanically Sensitive Ion Channels: Biological Models for Nanoscale Stress Sensors.....	621
F. Sachs	
Conversion of Available Energy Forms into Desired Forms by a Biologically Accessible Mechanism.....	629
D.W. Urry	

POSTERS

Microstructure Study of Molybdenum Liners by Neutron Diffraction.....	637
C.S. Choi, E.L. Baker, and J. Orosz	
Ultrasonic NDE of Layered Media Using Time-Domain Information.....	645
V.K. Kinra and C. Zhu	
Imaging of Small Defect and Fracture Process Zone by Using Scientific Visual Analysis in Ultrasonic Inspection.....	651
S. Mikami, T. Oshima, N. Sugawara, T. Yamazaki, and S. Sugiura	
Nondestructive Determination of the Hardening Depth in Inductive Hardened Steels....	659
I. Altpeter and M. Kröning	
Classification of Defects in Thick Section Graphite Epoxy Test Blocks.....	669
L.M. Brown and C.A. Lebowitz	
The Mythology of X-Ray Induced Radiation Damage.....	677
H.W. Bennett, Jr.	

Applications of X-Ray Radiography to the Study of Porosities in Surface Mount Solder Joints.....	683
Y.C. Chan, D.J. Xie, J.K.L. Lai, F. Yeung, and H. Wong	
New Sizing Technique of an Inclined Fatigue Crack on a Free Surface.....	691
K. Harumi, J. Ooshima, Y. Asakuma, and Y. Ogura	
Ultrasonic Set-Up to Characterize Stress States in Rims of Railroad Wheels.....	699
R. Herzer, H. Frotscher, K. Schillo, D. Bruche, and E. Schneider	
Ultrasonic Analysis of Interfacial Debond in Ceramic Matrix Composites.....	707
R.M. Kent, P. Karpur, T.E. Matikas, and P.D. Jero	
A Laser Speckle Image Correlation Instrument for High Temperature Surface Strain and Deformation Measurements.....	715
A. Sarrafzadeh-Khoei, R.J. Churchill, B.L. Thomas, and S.P. Almeida	
Portable Infrared Spectrophotometer for NDT Chemical Analysis of Weathered, Painted Surfaces.....	723
T. Novinson	

MATERIALS CHARACTERIZATION III

Effects of Second-Phase on the Nonlinear Behavior of Metal Matrix Composites.....	733
P.A. Foltyn, K. Ravi-Chandar, and K. Salama	
Measurement of Composite Fiber Volume Fraction Using Thermal and Ultrasonic Inspection Techniques.....	741
J.N. Zalameda and B.T. Smith	
Characterization of Polymer Structure Using Real-Time X-Ray Scattering.....	749
P.P. Huo, P. Cebe, and M. Capel	
Characterization of Corrosion Protective Films on Steel and Aluminum Alloys.....	757
H.W. White, J.E. Chamberlain, J.L. Wragg, F. Mansfeld, and T. Sugama	
Scanning Tunneling Microscopy Studies of Electromigration on Si(100) Surfaces under External Strain.....	765
Y. Wei, W.E. Packard, J.D. Dow, and I.S.T. Tsong	
Materials Characterization with Cold Neutrons.....	773
H.J. Prask	
Surface Characterization by Medium Energy Particle Scattering.....	781
J.H. Arps and R.A. Weller	
In Situ Optical Diagnostics for Pulsed Laser Deposition.....	791
J.L. Lawless and J.E. Parris	
Magnetic Properties of Armor Steels.....	799
S.A. Johnston, J.M. Winter, Jr., and R.E. Green, Jr.	

Nondestructive Characterization of Textures in Cold-Rolled Steel Products Using the
Magnetic Technique..... 807
I. Altpeter and G. Dobmann

Author Index.....817

Subject Index821

MONITORING OF RESIN-TRANSFER MOLDING USING LASER-BASED ULTRASOUND

A.D.W. McKie, R.C. Addison, Jr., T.-L.T. Liao, and H.-S. Ryang

Rockwell International Science Center
1049 Camino Dos Rios
Thousand Oaks, CA 91360

INTRODUCTION

In both the aerospace and automotive industries, polymer-based composite materials are increasingly being used to replace metallic structures. To reduce the cost of fabricating complexly contoured polymer composite structures, manufacturers are actively developing low-cost alternatives to hand lay-up/autoclave curing and other labor and capital-intensive processes. One technique, that has proven to be an economical method for fabricating polymer composite structures containing complex contours, is resin-transfer molding (RTM). In the RTM process a dry fiber preform is placed between two faces of a mold. Resin is injected into the mold at low pressure and fills the mold cavity permeating the fiber reinforcement. After the part is fully cured it is removed from the mold. The key to efficient and cost-effective resin-transfer molding is to have an automated process in which the infusion of resin is controlled so that the flow front rapidly and evenly permeates the fiber preform. Several problems can occur during the transfer of the resin into the mold such as lack of penetration into all regions of the mold or incomplete infiltration of the fiber preform. Thus, *in situ* sensors are required to monitor the RTM process and ensure that pumping of resin is not stopped prematurely. Laser-based ultrasound (LBU) is well suited for this monitoring application since it can work with heated molds having nonplanar surfaces and can acquire ultrasonic C-scan images in times that are short compared to the total transfer time of the resin. These ultrasonic images can be used to enable rapid assessment of degree-of-completion of resin transfer, and indicate problems associated with the resin transfer or with defects in the mold. In this paper, results are presented which demonstrate the capability of laser-based ultrasound to monitor the resin flow front along the inner surface of the mold during the RTM process.

EXPERIMENTAL APPROACH

To verify correlation between the ultrasonic data acquired with the LBU system and the location of the resin flow front, a specially fabricated aluminum mold was used. A Pyrex

window on one side of the mold allowed the resin front to be visually monitored and recorded on video tape concurrently with ultrasonic imaging from the opposite side of the mold with the LBU system (Figure 1).

Resin was injected into the mold via a port located in the lower corner of the aluminum face, and the mold orientation was such that resin flow occurred in a vertical direction. An outlet port was located at the top of the aluminum face in the corner diagonally opposite the inlet port. The resin pot used could be evacuated to degas the resin, heated if desired to reduce the viscosity of the resin, and could be pressurized up to 100 psi to force the resin into the mold and through the fiber preform.

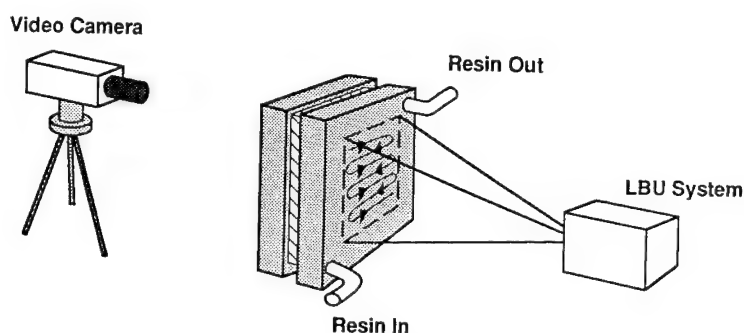


Figure 1. Experimental configuration for simultaneous monitoring of resin-transfer during the RTM process, using a video camera and the laser-based ultrasound system.

The essential features of the LBU system have been described previously^{1,2}. To visualize the resin flow front during the RTM process, the generation (CO_2) and probe (argon-ion) laser beams were scanned over the aluminum mold face. The stand-off distance was ~ 1.5 m and the CO_2 laser pulse repetition rate was 40 Hz. With this configuration the scan time to acquire an ultrasonic C-scan image of a 205 x 335 mm area (42 x 70 pixels) was ~ 120 seconds. Signal averaging was not used although the aluminum surface was painted to provide a surface constraint which enhances the generation of longitudinal waves propagating in the forward direction in the metallic mold³. This is not viewed as a limitation of the usefulness of the technique since coatings are available that can be used at the temperatures required to transfer and cure the typical resins being considered for the RTM process.

The longitudinal pulse generated on the outside surface of the mold wall, by the LBU system, travels through 0.75 inch thick aluminum to the near surface of the mold inner cavity where it is reflected (echo A in Figure 2). If the resin flow has reached the inspection point the longitudinal pulse is partially transmitted into the resin, so that a reduction in pulse amplitude will be measured. If the resin has completely permeated the fiber preform, the longitudinal pulse will propagate through the composite material to the opposite side of the mold cavity where it will be reflected back towards the outside wall of the mold (echo B in Figure 2). Thus, two echoes can be monitored to determine the state of the resin-transfer. The amplitude of the echo from the near side of the mold cavity will sense whether the resin has flowed over the face of the mold, and the amplitude of the echo from the far side of the mold cavity will sense whether the fiber preform has been completely permeated by the resin. However, in the experiments reported here, only the pulse from the near wall of the mold cavity was detected (echo A, Figure 2).

EXPERIMENTAL RESULTS

The RTM process was recorded on video tape and simultaneously monitored with the LBU system for two different resin-fiber configurations. Measurements at room temperature were performed using a vinyl ester (Ashland Q6530) which was transferred through a preform comprised of five plies of high density randomly chopped glass fiber mats. A second experiment was performed in which the flow of a high-temperature epoxy resin (Shell Epon 862) was monitored as it infiltrated a woven graphite preform, at a temperature of 125°C. Since the mold was situated inside an oven for the high-temperature experiment, access was limited to one side and so the process was monitored with the LBU system only.

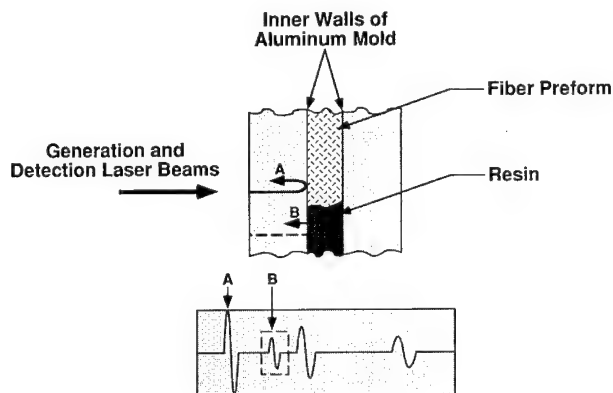


Figure 2. Key reflected ultrasonic pulses for monitoring the resin-transfer molding process.

For the vinyl ester configuration, the resin was injected into the mold under pressure, with a schedule which started at ~ 10 psi for the first 32 mins and was increased to 40 psi until the transfer of resin was completed at $T = 44$ mins. When the pumping of resin was stopped the resin flow front, seen through the Pyrex window, had reached the outlet port and apparently filled the mold. Previously, experiments were reported in which void formation occurred⁴. However, in this experiment the resin flowed uniformly up through the mold cavity forcing entrapped air out of the system so that voids were not present. The images made with the LBU system are based on changes in amplitude of the ultrasonic echo reflected from the near wall of the mold cavity (echo A in Figure 2). A series of ten ultrasonic C-scan images, acquired with the LBU system during the RTM process, clearly shows the resin front advancing uniformly through the mold from the inlet port on the lower right-hand side of the mold to the outlet port on the upper left (Figure 3). These images are in good agreement with the video images acquired of the resin flow up the opposite face of the preform (Figure 4), and suggests that the vertical resin flow is similar on both sides of the preform.

After completion of the resin injection, the charged mold was placed in an oven and cured at 60°C for 30 mins after which the manufactured part was removed from the mold. Even though both the video and LBU visualization of the resin flow front indicated completion of the process, subsequent transmission mode immersion C-scan inspection of the

part after curing (Figure 5) shows that the panel contained a significant void region in the upper corner of the mold near the outlet port. Below this void region, wetting of the fiber reinforcement was nonuniform with large variations in transmissivity. It is evident that even though the vertical resin flow had uniformly covered both sides of the preform, resin flow in the transverse direction had not completely penetrated the preform resulting in incomplete fiber wetting during the resin transfer. This may have resulted from the loose fit of the low

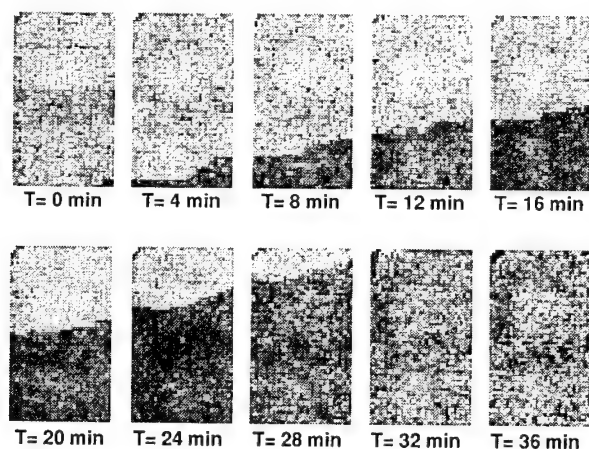


Figure 3. Series of ultrasonic C-scan images acquired using the laser-based ultrasound system to monitor the resin-transfer molding process.

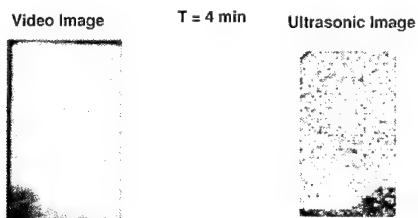


Figure 4. Comparison of the video and laser-based ultrasonic C-scan image acquired simultaneously at $T = 4$ min during the resin-transfer molding process.

fiber volume preform which could conceivably allow the resin to preferentially flow up the faces of the mold. In related experiments, high fiber volume braided graphite preforms which fit in the mold tightly seemed to wet satisfactorily.

For the high-temperature experiment, the mold was placed inside an oven and the LBU system was used to monitor the resin flow. The mold was preheated to 125°C to reduce the viscosity of the injected resin and facilitate easier infusion. A series of five ultrasonic C-scan

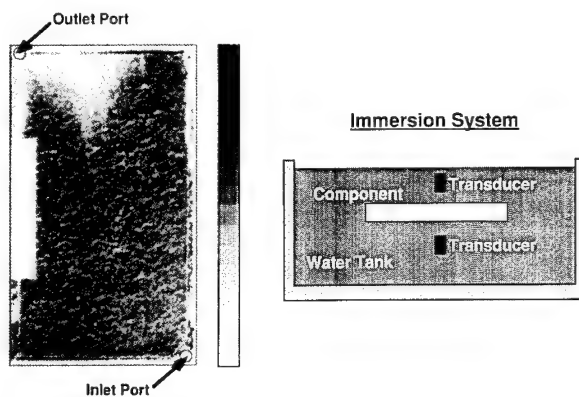


Figure 5. Transmission mode immersion C-scan image showing incomplete wetting of the fiber reinforcement after completion of resin-transfer molding.

images, acquired with the LBU system during the RTM process, again shows the resin front advancing through the mold (Figure 6). However, even with infusion pressures of 40 psi the resin flow was extremely slow and flow front "stall-out" occurred with the mold only partially filled after over 80 mins. The combination of tightly packed preform and deterioration in the chemical properties of the resin is believed to have caused the flow front to stop. Although this experiment was not successful with respect to RTM, it was a success in terms of *in situ* process monitoring at elevated temperature using the LBU system. As far as we are aware, these are the first reported laser-based ultrasonic C-scans performed at elevated temperatures.

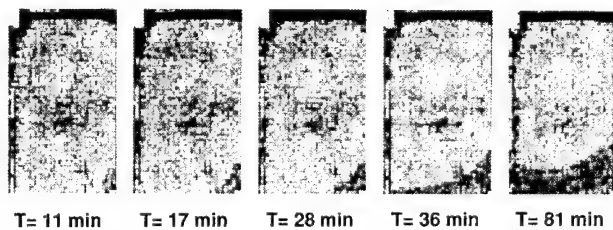


Figure 6. Series of ultrasonic C-scan images acquired using the laser-based ultrasound system to monitor the resin-transfer molding process at elevated temperature.

CONCLUSIONS

Experiments were performed in which the laser-based ultrasound system was used to noninvasively monitor the resin flow front during the resin-transfer molding process of several fiber composite panels. Video images of the resin flow front as it progressed vertically through the mold were in excellent agreement with ultrasonic C-scan images obtained by simultaneous monitoring using the LBU system. In addition, the noncontacting nature of LBU allowed the

RTM process to be monitored at elevated temperature. It was found that flow of resin through the thickness of the preform can significantly lag the vertical resin flow front occurring along the mold wall/preform interface, resulting in incomplete consolidation of the manufactured composite parts. This, however, illustrates the utility of using ultrasonic methods to monitor the RTM process

These preliminary experiments have demonstrated the applicability of the laser-based ultrasound system as an *in situ* process monitoring sensor. To realize the full potential of the LBU technique as a robust sensor for closed loop control of the RTM process, the signal-to-noise ratio of the LBU system must be improved to detect the ultrasonic echo that has traveled through the resin wetted fiber preform and been reflected back to the outer surface of the mold. Efforts are in progress to attain this improvement.

ACKNOWLEDGMENTS

This work has been supported by Rockwell Automotive Plastic Products Division and by Rockwell Independent Research and Development funds.

REFERENCES

1. A. D. W. McKie and R. C. Addison, Jr., Rapid inspection of composites using laser-based ultrasound, *in*: "Review of Progress in Quantitative NDE," D.O. Thompson and D.E. Chimenti, eds., Plenum Press, New York (1993).
2. A. D. W. McKie and R. C. Addison, Jr., Inspection of components having complex geometries using laser-based ultrasound, *in*: "Review of Progress in Quantitative NDE," D.O. Thompson and D.E. Chimenti, eds., Plenum Press, New York (1992).
3. C. B. Scruby and L. E. Drain, "Laser Ultrasonics – Techniques and Applications" Adam Hilger, New York (1990).
4. R. C. Addison, Jr., A. D. W. McKie T. -L. T. Liao and H. -S. Ryang, *In situ* process monitoring using laser-based ultrasound, *in*: "IEEE 1992 Ultrasonic Symposium Proceedings," B. R. McAvoy, ed., IEEE, New York (1992).

EMBEDDED ACOUSTIC SENSORS FOR PROCESS CONTROL AND HEALTH MONITORING OF COMPOSITE MATERIALS

Michael J. Ehrlich, Christian V. O'Keefe,
B. Boro Djordjevic, and B.N. Ranganathan

Martin Marietta Laboratories
1450 South Rolling Road
Baltimore, Maryland 21227

INTRODUCTION

The past few years have seen a marked increase in the use of composite materials for structural applications, many of which put such high demands on the components that they operate just within their performance limits. To ensure that these composite components possess the high reliability and uniformity necessary for critical applications, it is desirable to carefully control the production environment. Although there are numerous facets to composite production, this paper focuses on in-situ monitoring of the cure process.

A number of techniques have been successfully demonstrated for composite cure monitoring, including ultrasonic, dielectric, and optical methods. Of these, only the ultrasonic techniques truly measure the mechanical properties of the composite, and thus may offer the most valuable information regarding the integrity of the part. Unfortunately, many ultrasonic techniques have proven difficult to implement under the harsh conditions of an industrial environment. In particular, contact ultrasonic transducers are poorly suited to operate at high temperatures, and rarely is it possible to mechanically couple the transducer to the part during processing. In an effort to provide large area, real-time cure monitoring capabilities, embedded acoustic "waveguides" have been investigated as a means to effectively couple ultrasound into and out of composite parts in the processing environment [Harrold & Sanjana 1986, Winfree & Parker 1985, Winfree & Sun 1989]. The original technique, developed by R. Harrold [Harrold 1986], used a metal or polymer filament, typically ranging from 0.005 to 0.020 inches in diameter, to guide ultrasonic energy through a composite part in which the filament was embedded. Historically, the amplitude of the received ultrasonic signal was monitored as a function of cure time, and this amplitude related to the cure state of the composite. During the course of the acoustic waveguide experiments reported here (hereafter referred to as an embedded acoustic sensor), it was determined that the reproducibility of the amplitude measurement technique was not high enough to merit its continued investigation. Rather, the cure monitoring work reported here has focused on time-of-flight measurements, which have produced far more reliable results and from which ultrasonic velocities and ultimately elastic moduli may be derived.

EXPERIMENT

To assess the applicability of using embedded acoustic sensors for cure monitoring, a number of experiments were performed aimed at correlating the sensor response with the degree of composite cure. For these experiments, the material used as the acoustic sensor was 0.020 inch Nichrome wire. The wire sensors were embedded in the mid plane of 16-ply graphite/epoxy panels during the prepreg lay-up process. "Acoustic horns" were used to couple ultrasonic tone bursts into the sensor and as a means to conveniently couple energy back out to the receiving transducer, as illustrated in Figure 1. The horns were designed to minimize ultrasonic back-reflection noise and maximize the useful energy transfer between the transducers and the wire. The prepreg panels with the embedded sensors were then cured using a hot-press. Full cure cycles (350°F) and partial cure cycles (250°F) were performed, so a comparison of the results could be made.

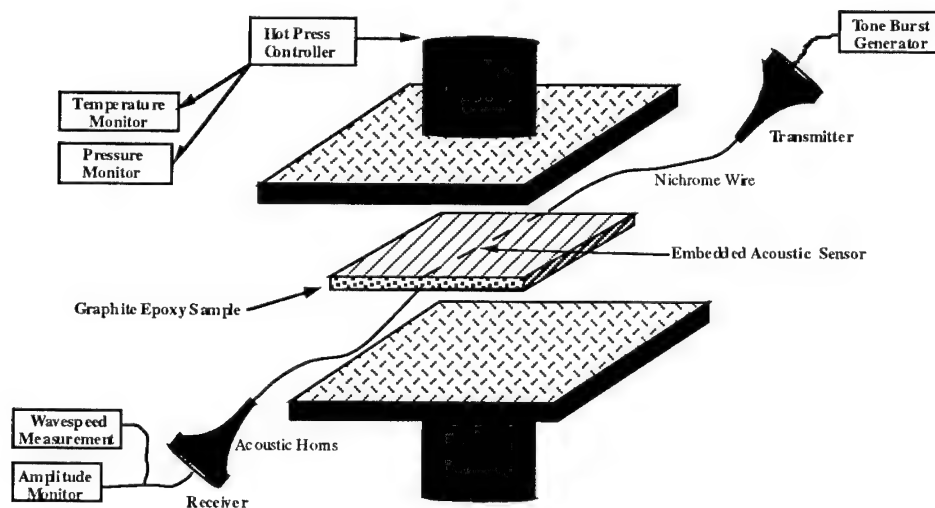


Figure 1. Schematic of the experimental setup used for composite cure monitoring. Specially designed "acoustic horns" were used to couple ultrasound into and out of the Nichrome wire sensor.

Throughout each experiment, the temperature, pressure, ultrasonic amplitude and ultrasonic time-of-flight were recorded. To perform the time-of-flight and amplitude measurements during the cure-cycle, ultrasonic tone bursts (nominally 50kHz) were transmitted into the embedded sensor and received at the other end. Every minute during the cure cycle, a received ultrasonic tone-burst was digitized and used to determine the signal amplitude and time-of-flight through the 12"x12" composite panels. At the same time, hot press temperature and pressure were monitored through a programming interface and recorded.

As stated previously, it was determined from these experiments that ultrasonic amplitude measurements did not exhibit the reproducibility required to perform as a cure-monitoring parameter. The ingress/egress locations where the wire entered and exited the composite panel were likely suspects for introducing variability into the system, as was the actual attachment of the wire to the acoustic horns. For these reasons, most attention was focused on time-of-flight measurements.

The time-of-flight for a 50kHz tone-burst propagating through the composite panel was determined by digitizing the received signal and comparing it to the original drive

signal. Since the original prepreg lay up procedure influenced the time-of-flight (i.e. slight ply misorientation, varying hand pressure, etc.), it was necessary to normalize the data for a given experiment with respect to other experiments. A point ninety minutes into the cure cycle was chosen as the data normalization point, since all sample histories up to the ninety minute mark were identical. Figure 2 shows changes incurred in the time-of-flight during the full cure and partial cure cycles, as well as the cure cycle temperature and pressure profiles. For the 12 inch square by 0.1 inch thick samples, the time-of-flight excursions shown in Figure 2 correspond to velocities ranging from 3400m/s to 4000m/s. (Note: A decrease in time-of-flight corresponds to an increase in velocity).

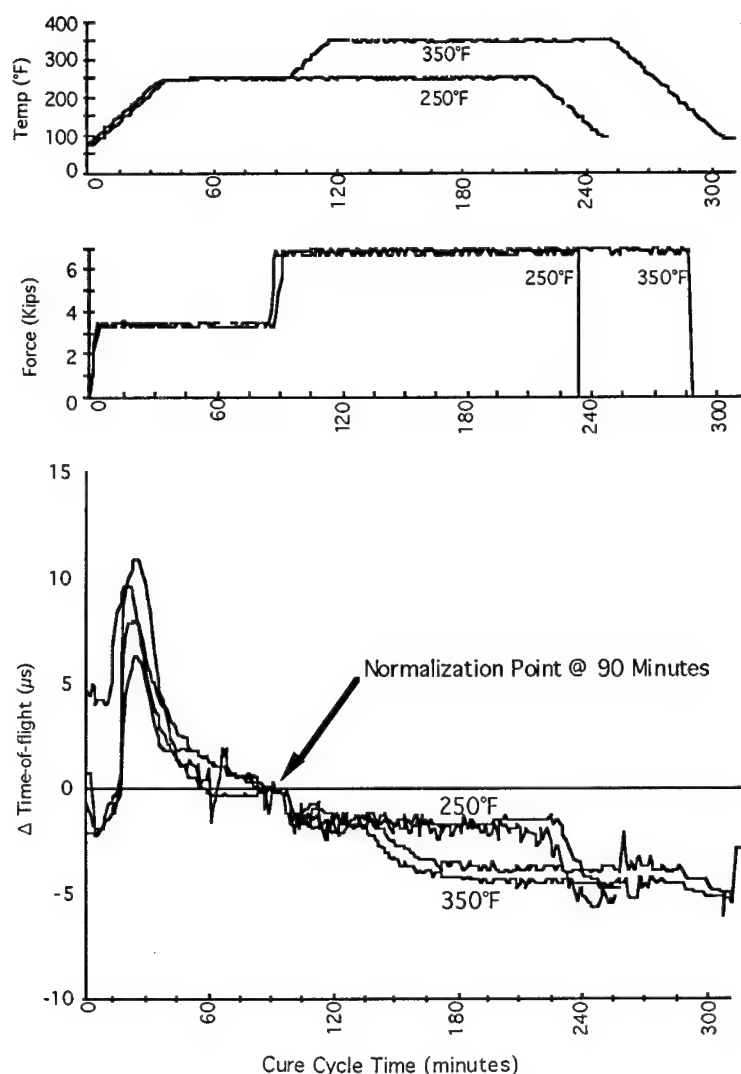


Figure 2. Results for the cure monitoring experiments are shown, detailing the change in ultrasonic signal time-of-flight as a function of cure cycle time. Also shown are the temperature and force profiles for both the 350°F full cure and the 250°F partial cure cycles.

The time-of-flight profiles follow the viscosity/stiffness of the composite panel during cure. Initially, the time-of-flight increases (velocity decreases) as the panel heats up and reaches its gelation point, the point of minimum viscosity. This occurs approximately 25 minutes into the cure-cycle. Following gelation, the time-of-flight decreases (velocity increases) as the epoxy begins to cure. Approximately ninety minutes into the cure cycle, the pressure is increased. An immediate decrease in time-of-flight (increase in velocity) is observed. Thus, at this point in the cure cycle, the sensor does respond to pressure. At the same time, the temperature for the full cure cycles is ramped to 350°F, while the partial cure cycle temperature remains at 250°F. As cure progresses, the difference in response between the 250°F cure and the 350°F cure panels becomes evident (see Figure 2). The 350°F cured panels exhibit higher ultrasonic velocities (shorter times-of-flight) indicative of their stiffer, more completely cured state relative to the 250° samples. In addition, there was no noticeable temperature effect on the fully cured panels once the process was complete, whereas the ultrasonic velocity in the under-cured panels did exhibit a temperature dependency during the cool-down procedure. It is unclear as to why the large temperature dependency exists, although some possible explanations include viscosity effects or relaxation phenomena.

WAVEGUIDE OR NOT?

Some interesting observations were made regarding wave propagation in the embedded acoustic sensor during the cure cycle experiments described above. Most notable was the extent to which the received ultrasonic tone-burst signal was affected when an aluminum plate was positioned on the prepreg panel. The aluminum plate was coated with a release agent and placed on the composite panel so that, once cured, it would not adhere to the steel hot press. Interestingly, as the aluminum plate came in contact with the uncured prepreg composite panel, the received ultrasonic signal transmitted along the embedded sensor dropped in amplitude by as much as one order of magnitude. The amplitude reduction was attributed to ultrasonic energy coupling out of the composite panel and into the aluminum plate. Such a large deviation in amplitude however, would suggest that a large percentage of the ultrasonic energy was in fact not contained or guided by the embedded wire sensor, but rather was carried via plate modes in the host material itself. This would account for the tremendous amplitude reduction observed when the aluminum plate made physical contact with the composite specimen.

To test this theory, an experiment was performed where the Nichrome wire was terminated one inch into each side of the composite prepreg panel, so that only the composite itself could transmit the ultrasonic energy between transmitter and receiver. This is illustrated in Figure 3, and the results for a 350°F cure cycle using this configuration is shown in Figure 4. Results for a 350°F cure cycle using a continuous embedded wire are also shown for comparison. While small differences are noticeable between the continuous versus terminated wire experiments, it is clear that the overall response is quite similar. As such, the term "acoustic waveguide" often used for wires embedded in composite materials is a misnomer. The wire itself does not act as an ultrasonic waveguide, at least not over the frequency range from 50kHz to 200kHz. However, the wire does serve a useful purpose - it provides a convenient way to couple ultrasonic energy into and out of the composite panels.

FUTURE WORK

As described above, it would appear that the only function which the embedded wire serves is to couple energy into and out of the composite, but does not guide the energy within the composite. Since the embedded wire sensor is susceptible to ingress/egress variabilities and coupling effects at the acoustic horns, it would be prudent to eliminate the wire altogether, and replace it with a more robust means of coupling the energy into and out of the composite panels. It is anticipated that most future effort will be directed toward development of embedded acoustic sensors which do not suffer from the problems associated with the ingress/egress areas and which may also provide a controlled sensing

area. Toward this end, a fiber-optic approach will be taken, using a laser to generate ultrasound within the sample, and a fiber-optic detector as the ultrasonic receiver. An all optical system would have the advantages of providing a localized sensing region, possible sensor multiplexing, interrogation of inaccessible areas, and would eliminate the signal variability arising from ingress/egress variabilities and mechanical coupling difficulties.

Lastly, sensors embedded during material manufacture for process control applications also offer a means by which the material health may be monitored throughout its useful lifetime. Changes in acoustic velocity may indicate degradation of the material's elastic properties or a change in the material stress state. Similarly, a reduction in the transmitted acoustic amplitude may result from internal micro-cracking or delaminations. While these effects have yet to be investigated, it would seem a logical extension to in-situ process control monitoring, and would provide true "cradle-to-grave" material monitoring capabilities.

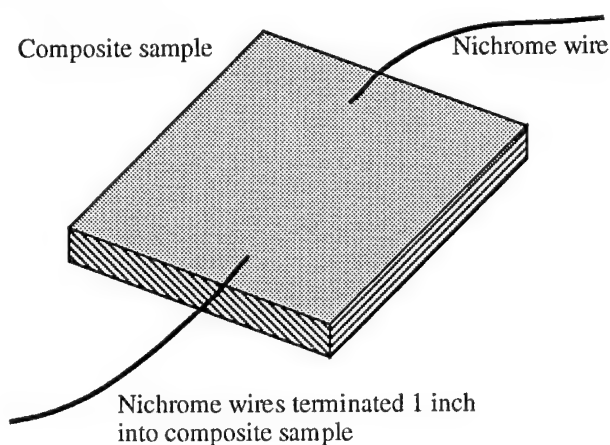


Figure 3. Schematic detailing the configuration used for the terminated "waveguide" experiment. Each piece of Nichrome wire was inserted only 1 inch into the test panels, and were not connected in any manner other than by the host Gr/Ep material.

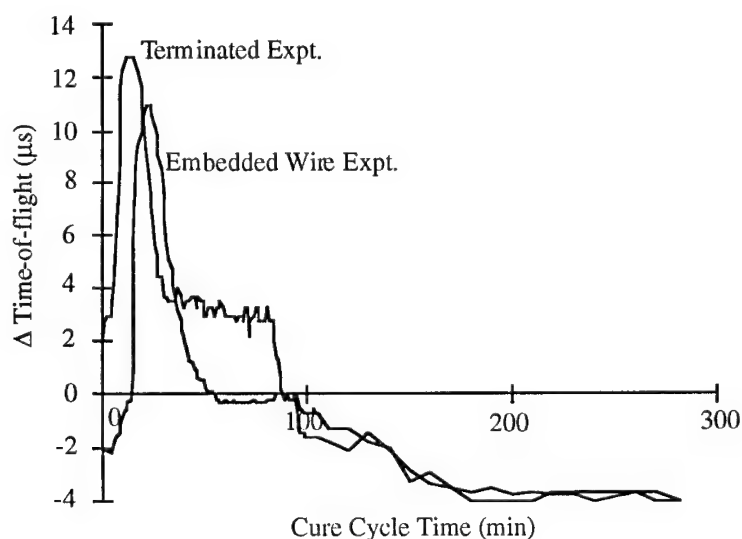


Figure 4. Results for the terminated "waveguide" experiment compared with those obtained from a continuous "waveguide". While there are slight discrepancies, the overall results are quite similar.

REFERENCES

- R.T. Harrold. U.S. Patent No. 4,590,803, Acoustic Waveguide Monitoring, May 27, 1986.
- R.T. Harrold and Z.N. Sanjana, Acoustic waveguide monitoring of the cure and structural integrity of composite materials, *Polymer Eng. & Sci.*, v 26 no 5, 367-372 (1986).
- W.P. Winfree and F.R. Parker, Ultrasonic characterization of changes in viscoelastic properties of epoxy during cure, *Proc. QNDE*, vol 4B, 1203-1208 (1985).
- W.P. Winfree and K.J. Sun, Modelling guided acoustic waves for monitoring epoxy curing, *Proc IEEE Ultrasonics Sym.*, 1227-1230 (1989).

SURFACE CONTROLLED MATERIALS EVALUATION FOR AI-IMPLANTED Ni ALLOYS

T. Aizawa¹, J. Mitsuo² and J. Kihara¹

¹ Department of Metallurgy, University of Tokyo
7-3-1 Hongo, Bunkyo-ku, Tokyo 113

² Tokyo Metropolitan Institute of Technology
Nishigaoka, Kita-ku, Tokyo

INTRODUCTION

In the design of structural materials, we often encounter various kinds of needs for improvement of surface material characteristics like hardness, oxidation toughness or wear resistance [1]. PVD/CVD ceramic coatings are the first approach to make surface control of mechanical properties [2]. These methods are widely used in fabrication of tool and die materials. Typical applications can be seen in TiN, TiC or Ti(CN) coated WC/Co and SKD materials. In parallel with this coating procedure, an ion implantation should become one of the most promising key technologies in the surface control engineering [1,3]. Active control of ion source, power and density of beam in use and its fluence enables us to change patterns of surface modification, to make different types of alloyment and to restructure the surface materials. In order to make full use of the above potential capabilities, however, it should be essentially indispensable to make mechanical and metallurgical evaluations on the synthesized or modified surface material. Such conventional methods as micro indentation and wear testing are difficult to obtain mechanical properties of surface materials with the thickness of submicrons.

Authors [4,5,6] have been developing the acoustic spectro microscopy (ASM) to make quantitative nondestructive evaluation (QNDE) on the elastic properties of ceramic coated materials with consideration of residual stresses inside coating. For PVD-TiN coatings with the thickness less than 10 μm , ASM has succeeded in elastic characterization of coatings and residual stress analysis. The present ASM provides a variety of QNDE methodologies to deal with elastic, elasto-plastic and toughness characterizations of actual materials system. Table 1 lists our developing family of ASM oriented QNDE method and new acoustic tools. In the present paper, our developed ASM is applied to QNDE of Al-implanted Ni-base alloys to investigate the effect of modified surface materials on the measured acoustic structure and to discuss the possibility of QNDE by ASM of surface-modified materials.

ACOUSTIC DIAGNOSIS FOR ION-IMPLANTED MATERIALS

Among various methodologies in the acoustic diagnosis, the present paper is concerning the dispersion analysis of the leaky surface wave velocity with use of the acoustic spectro microscopy (ASM).

Acoustic Spectro Microscopy

Acoustic spectro-microscopy (ASM) has been developed to make quantitative nondestructive evaluation (QNDE) on the mechanical properties of ceramic coated materials [3,4,5]. Several modes of acoustic diagnosis can be designed and constructed on ASM for each class of QNDE problems: 1) Rotational mapping for measurement of Young's moduli of the anisotropic materials and grain-controlled coating materials [6], 2) Two and three dimensional mapping for determination of elastic constant distribution in so small specified region as seen in microscopy, SEM or TEM with sufficient resolution [7], or 3) Insitu measurement of acoustic responses for deforming coated materials [8]. The original apparatus of ASM, which has been developed, is shown in Fig. 1 together with the fundamental measurement mode of ASM schematically illustrated in Fig. 2.

An ultrasonic pulse is injected from spherical lens into the target materials through coupler (water or Hg) with a controlled skew angle θ against the surface of materials. The whole reflected wave running back through the coupler can be received by the planar lens. Hence, even when the target materials could indicate high attenuation or dumping, the present approach should be free from inaccurate measurement or failure of measurement. In case that linear relation holds on the input/output acoustic signals, the planar lens can be utilized as a transmitter and spherical lens as a receiver.

Through the Fast Fourier Transform (FFT), spectra of both power and phase shift can be obtained from the reflected wave. The capacity of spatial resolution should be strongly dependent on the acoustic lens to be used. The point to be noted in the standard measurement by ASM is a sequential measurement mode by incremental increase or decrease $\Delta\theta$ of the incident angle θ . That is to say, the spherical - planar lens pair is controlled for the specified incident angle range $\theta_L \leq \theta \leq \theta_U$ to move by a constant $\Delta\theta$ in the circumferential direction with focussing point fixed on the surface of target materials. Fig. 3 depicts a typical configuration of received signals in one-shot measurement for PVD TiN coated WC/Co substrate. Through FFT, both the power P and the phase shift ϕ of the reflected waves can be obtained in the functional form of both the frequency and the incident angle: $P(f, \theta)$ and $\phi(f, \theta)$. Figs. 4 and 5 show these functional profiles of $P(f, \theta)$ and $\phi(f, \theta)$, respectively. When θ reaches to a critical angle θ_c where the Rayleigh wave is activated, P indicates a large dip and ϕ changes remarkably by 2π shift for a material with less dumping. Hence, we can distinguish this θ_c by these large dip or large phase shift. The leaky surface wave velocity V_{isaw} is directly calculated from this θ_c by $V_{\text{isaw}} = V_w / \sin(\theta_c)$, where V_w is the acoustic velocity of the coupler. As wellknown, V_w changes with temperature when pure water is employed as a coupler. Our developing system is all housed in the clean booth, and fluctuation of temperature is kept to be less than 0.1 K in measurement. Furthermore, pure lead plate with buffed surface was chosen as a reference material to yield homogeneous acoustic structure for comparison.

Estimate of Acoustic Structure for Al-implanted Ni Substrate

As has been investigated in Refs. (7) and (8), ceramic coated substrate material indicates characteristic dispersion of the leaky surface wave velocity V_{isaw} with the frequency f . For the prescribed thickness of coating layer, this dispersion curve is uniquely determined by the elastic properties of coating and substrate materials and their interface. Furthermore, if the interface joining is perfect, or, both velocities and stresses are continuous across the interface, this dispersion curve is also predicted theoretically by the two dimensional elastodynamic analysis⁽⁹⁾. Hence, the acoustic structure of Al-coated or implanted Ni and Ni alloy can be estimated by this method.

Mechanical properties of pure Al and Ni is listed in Table 2 to be used for model materials in computation. Fig. 6 depicts the dispersion curves for Al-coated Ni substrate with different thickness. In this system of two cubic metals, its leaky Rayleigh wave velocity slightly increases with frequency, but its deviation from that for substrate when $f = 120$ MHz is only 3 to 4 m/s for the coating thickness of 200 nm. This slight dispersion is still within tolerance of the present ASM measurement with accuracy of 0.1 % for the leaky surface wave velocity.

As reported in Refs. (5) and (6), nondimensional dispersion curve should be inherent to the coating material where the leaky Rayleigh wave velocity is nondimensionalized by $(V_{\text{isaw}} - V_{\text{substrate}}) / V_{\text{substrate}}$, and related with the nondimensional thickness d/λ or $d \cdot f$. Direct influences of both mechanical properties of substrate and coating thickness can be eliminated from this curve. Fig. 7 depicts the nondimensional dispersion curve of Al-coated Ni system. The obtained unique curve should reveal that single homogenous material is coated on the substrate with perfect joining.

The above calculation has assumed that no chemical reaction should take place and the

Table 1 Various methodologies of QNDE and acoustic tools based on ASM.

Item	Frame of Evaluation	Functions by Evaluation Tools
Nondestructive Quality Assurance	- Detection of flaws by imaging	- 2D acoustic microscopic imaging
	- Evaluation of interfacial defects between coating and substrate	- Dispersion analysis by ultrasonic spectroscopy
Elastic Characterization	- Evaluation of macroscopic and homogenized elastic properties	- Dispersion analysis by ultrasonic spectroscopy
	- Evaluation of anisotropic elastic distribution	- Multi-Dispersion analysis on θ - φ plane
	- Description of grain growth in polycrystalline coating and substrate materials	- Two dimensional mapping method with dispersion analysis
	- Residual stress analysis of coating materials	- Micromechanics with dispersion analysis
Elastic-Plastic Characterization	- Evaluation of wrought zones and yielding/damage zones in materials	- Wide-Band Spectroscopy with acoustic structure analysis
	- Estimate of affected/alloyed zones on surface by ion implantation	- Acoustic structure analysis
Acoustic Emission	- Toughness, K_{Ic} and cracking mode evaluation	- Ceramic acoustic fiber
	- Analysis of micro cracking mode	- Multi-sensor ultrasonic lens - Cracking mode analysis through wave-let analysis of received signals
On-Process Quality Evaluation	- Insitu monitoring of coating processing	- Metallic acoustic fiber
	- On-line nondestructive materials evaluation	- Arrayed-sensor lens - Three dimensional mapping - QNDE at elevated temperature and high pressure

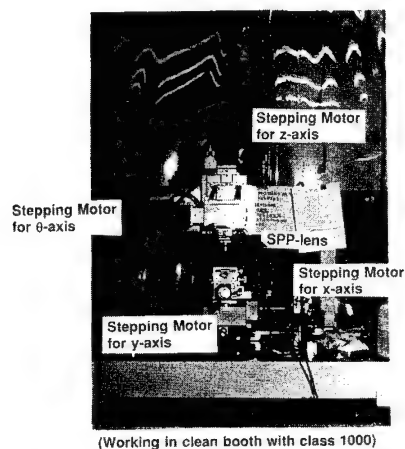


Fig. 1 Acoustic spectro microscopy.

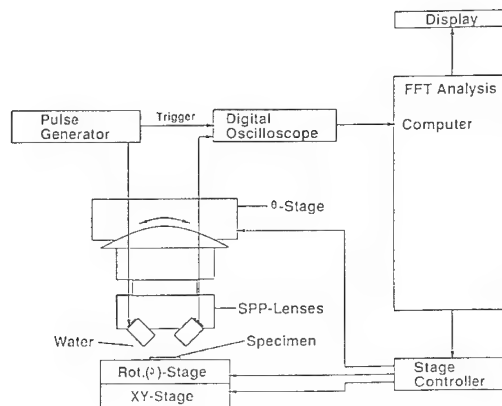


Fig. 2 Schematic view of ASM.

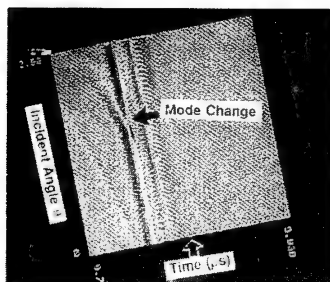


Fig. 3 Profile of received signals.

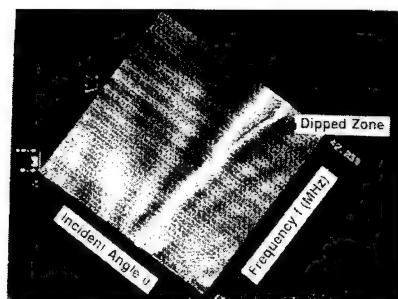


Fig. 4 Profile of power spectrum $P(\theta, f)$.

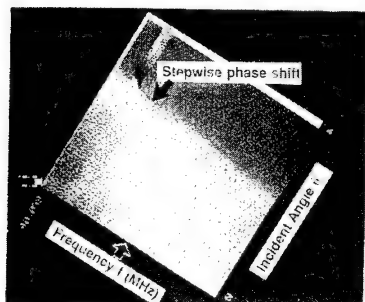


Fig. 5 Profile of phase shift $\phi(\theta, f)$.

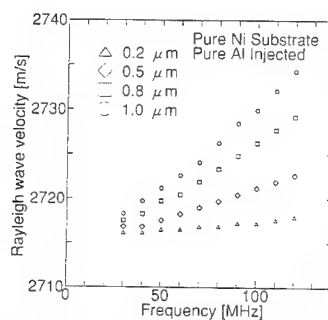


Fig. 6 Dispersion curve of Al-coated Ni.

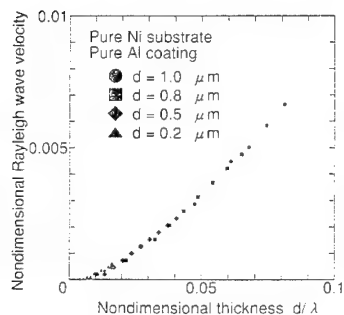


Fig. 7 Nondimensional dispersion curve.

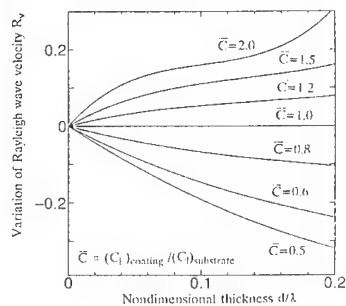


Fig. 8 Effect of surface stiffness on dispersion.

Table 2 Mechanical properties of pure Al and Ni for calculation.

Pure Al: $\rho = 2.70 \text{ g/cm}^3$,

$E = 70.6 \text{ GPa}$, $\nu = 0.345$

$C_1 = 6409 \text{ m/s}$, $C_a = 3118 \text{ m/s}$

Pure Ni (Substrate): $\rho = 8.90 \text{ g/cm}^3$

$E = 199.5 \text{ GPa}$, $\nu = 0.312$

$C_1 = 5591 \text{ m/s}$, $C_a = 2923 \text{ m/s}$

Table 3 Chemical components of Ni-based alloy substrates.

	N i	M n	C r	A l	F e	S i	C u
Inconel 600	Bal.	0.54	15.4	—	7.58	0.27	—
Alumel	Bal.	1.41	—	1.06	—	1.82	—
Chromel	Bal.	—	9.34	—	0.36	0.33	—
Constantan	42.9	0.89	—	—	—	—	56.0

surface structure be composed of pure Al layer and pure Ni substrate. In the actual implanted materials, alloyment takes place between implanted metal element and chemical components of substrate, so that the dispersion curve should change itself by this alloyment. Fig. 8 illustrates typical dispersion curves when mechanical properties of surface material change by alloyment. When the hardened material is synthesized at surface, convex type of curves must be observed. On the other hand, dispersion curve becomes of a concave shape for softened surface structure.

EXPERIMENTAL CONDITION

Four types of Ni-base alloys were employed as test specimens, and their bulk elastic moduli were obtained from the measured longitudinal and shear acoustic wave velocities by the sing-around method.

Testspecimen

The chemical components were listed in Table 3 for the employed four Ni-base alloys: Inconel-600, Alamel, Chromel and Constantan. Their dimensions of specimen are commonly set by 10 x 30 x 4 mm. As a preliminary treatment, the whole specimens are annealed in vacuum and ground by SiC-polishing paper with the mesh of 400. The surface 10 x 30 mm to be implanted is only buffed.

Al Implantation Condition

As wellknown, implantation capacity is controlled by both acceleration energy V_{ion} and radiation density ϕ_{rad} . In the present study, V_{ion} was fixed by $V_{ion} = 50$ KeV as the standard condition, and ϕ_{rad} was varied by 0.5×10^{17} and 1.0×10^{17} dpi/cm². Fig. 9 shows typical distributions of fundamental elements in the direction of depth for Inconel-600 by AES. Although the sputtering time depends on the target materials, Al-implanted penetration depth might be about 200 nm in total for $V_{ion} = 50$ KeV and $\phi_{rad} = 1.0 \times 10^{17}$ dpi/cm².

On the very surface upto 10 nm, concentration of Al is varying by oxidation, but both Al and other constituent elements of substrate have indicated nearly constant distribution beyond 20 - 30 nm.

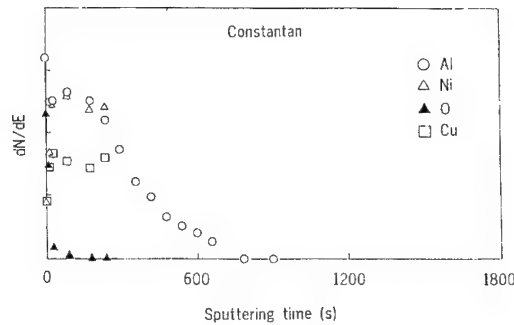


Fig. 9 AES depth profiles of Al implanted alloys.

Bulk Wave Analysis

For investigation of the elastic moduli of Ni-based alloy substrate materials, the sing-around method with 10 MHz was employed to measure both the longitudinal and the shear velocities, or, C_l and C_s . As listed in Table 4, Inconel-600, Alamel and Chromel indicated nearly the same velocities with each other, and their values are slightly shifted from those for the pure Ni substrate. From these measured velocities, both the Rayleigh wave velocities and the Young's moduli can be calculated by the following equations:

$$(1) \quad V_{lsaw} = \kappa \cdot C_s \quad \text{for } \kappa^6 - 8\kappa^4 + (24-16\alpha^2)\kappa^2 + (16\alpha^2-16) = 0, \quad \alpha^2 = (1-2\nu)/(2-2\nu),$$

$$(2) \quad C_l = \{(K+(4/3)G)/\rho\}^{1/2}, \quad C_s = \{G/\rho\}^{1/2}, \quad \text{for } K = E/[3(1-2\nu)], \text{ and } G = E/[2(1+\nu)].$$

The estimated results are listed in Table 5.

Table 4 Measured longitudinal and shear velocities.

No	Substrate	C_l	C_s
A	Inconel-600	5860 m/s	3060 m/s
B	Alumel	6050 m/s	3160 m/s
C	Chromel	5860 m/s	3060 m/s
D	Constantan	5200 m/s	2712 m/s

Table 5 Estimated Rayleigh wave velocity and Young's moduli

No	Substrate	V_R	E
A	Inconel-600	2840 m/s	206 GPa
B	Alumel	2940 m/s	224 GPa
C	Chromel	2840 m/s	212 GPa
D	Constantan	2530 m/s	172 GPa

ACOUSTIC DIAGNOSIS BY DISPERSION ANALYSIS

The acoustic spectro microscopy was applied to make dispersion analysis of Al-implanted Ni alloy substrates and to investigate whether the effective alloyment should take place.

Measurement Condition

The present measurement condition for ASM is listed in Table 6. The incident angle is controlled incrementally by $\Delta\theta = 0.1$ degree. For standardization in measurement, the location in the z-axis is fixed with its deviation less than 100 nm, and x-y stage is kept planar with skew angle less than 2.9×10^{-4} . Since these Ni-based alloys have remarkable acoustic damping, location of critical angle θ_c was determined by both dip in power and large gradient in phase shift.

Table 6 The present measurement condition in ASM.

SPP lens System	Point Focussing
Frequency	$10 \leq f \leq 150$ MHz
Incident Angle	$20 \leq \theta \leq 40$ $\Delta\theta = 0.1^\circ$
Reference Material	Lead

Experimental Results

Among four types of substrate materials, little dispersion was observed for Al-implanted Alumel and constantan. This is partially because 1) Ultrasonic signals are so weak in the present attenuation set-up that dip in power should not be noticeable, and 2) Large attenuation in materials reduces the amount of phase shift. The absence of dispersion assures that little alloyment must take place to make large influence on the mechanical properties of surface materials.

The measured data were depicted in Fig. 10 for unimplanted and Al-implanted Inconel-600 substrate. In case of unimplanted Inconel-600, the leaky surface wave velocity becomes nearly constant by $V_{\text{isaw}} = 2860$ m/s, which is in good agreement with the estimated value in Table 5. In case of Al-implanted substrate with $\phi_{\text{rad}} = 1.0 \times 10^{17}$ dpi/cm², no dispersion was observed in the lower frequency range, but the Rayleigh wave velocity begins to increase with frequency and becomes constant by 2950 m/s, which is larger than V_{isaw} for substrate by 90 m/s. Considering the correlation of sputtering time with thickness in AES, total sputtering time (upto the time when Al-level signal diminished into the background) 1000 s in this case might correspond to at most 250 to 300 nm. If

Al-implanted Inconel-600 could have the same structure as the Al-coated Ni substrate, amount of dispersion to be measured should be 3 to 4 m/s. Actually measured relatively large dispersion reveals that surface material should be hardened by alloyment to indicate large stiffness.

Dispersion curves were shown in Fig. 11 for Al-implanted Chromel. For unimplanted Chromel, nearly constant dispersion was observed, and the measured V_{isaw} becomes 2850 m/s. When $\phi_{\text{rad}} = 0.5 \times 10^{17} \text{ dpi/cm}^2$, no distinct dispersion was measured. However, ϕ_{rad} was increased to be 1.0×10^{17} , the dispersion of concave type was observed: V_{isaw} monotonically decreases with frequency. When $f = 120 \text{ MHz}$, V_{isaw} becomes 2700 m/s, which is smaller than the bulk velocity by 150 m/s. This significant dispersion tells that 1) Implanted aluminum is not only coated on the substrate but alloyed with constituent elements of substrate material only on the surface upto 300 nm, and 2) Synthesized surface alloy indicates softened stiffness than the bulk Chromel.

Discussions

Owing to the ASM measurement and dispersion analysis, both Inconel-600 and Chromel are expected to have alloyed surface layer by Al-implantation among four Ni-base alloys. In general, surface modification has been reported to be effective to improve toughness against oxidation and to reduce wear rate. In the present study, oxidation testings were made for various surface modification procedures including N-implantation, Al-vaporization and their combined methods for comparison. The whole specimens were heated and held constant by $T \approx 970 \text{ K}$ for 50 hours in O_2 atmosphere. The saturated $\text{H}_2\text{O(g)}$ is mixed with O_2 at $T \approx 298 \text{ K}$ and flown together into furnace with the flow rate of 2 l/min. The increase of weight ΔW for each surface treated material was measured and normalized by the increase of weight ΔW_0 for untreated material. The obtained normalized increases of mass are listed in Fig. 12 for four Ni-based alloys. In case of Alumei and Constantan, where no dispersion curves were observed, very little effect of surface modification on improvement of toughness against oxidation can be seen. This reveals that effective alloyment should never be synthesized at the vicinity of surface for these two substrate materials.

On the other hand, distinct difference can be seen between Al-deposited and Al-implanted materials. As before mentioned, the former has no possibility to change surface structure. Since alumina is easy to be synthesized and precipitate at the surface, addition of aluminum layer might lead to reduction of oxidation. In the latter case, essential modification should take place at the surface material so as to make further reduction of oxidation rate. In case of Inconel-600, significant influence of Al-implantation can never be seen. This is partially because 1) Thickness of effective alloyed layer is still too thin to have influence on the resistance against oxidation, and 2) The synthesized alloyment with stiff Young's moduli has little potential to reduce oxidation. On the other hand, oxidation toughness was improved than Al-implantation, since $\Delta W/\Delta W_0$ becomes less than half of that for Al-deposited Chromel. This fact has precise correlation with the surface alloyed layer with softened stiffness, which was mechanically evaluated by ASM.

CONCLUSION

Our developed acoustic spectro microscopy was applied with success to nondestructive evaluation of Al-implanted Ni-base alloys. Acoustic structural analysis tells that little dispersion is expected for Al-coated Ni without surface modification. In case of Alumei and Constantan, although those materials indicate remarkable dumping, no dispersion curves were measured for the leaky Rayleigh wave velocity. This reveals that little surface modification by alloyment is expected for these materials. This prediction has been partially supported by the fact that oxidation toughness should be indifferent to Al-implantation for those two materials. Inconel-600 indicates increasing dispersion of the leaky surface wave velocity with frequency, so that alloyed material should have more stiff Young's modulus than Inconel-600 substrate owing to Al-implantation. The point to be noted is that relatively large decreasing dispersion of the leaky surface wave velocity with frequency for Al-implanted Chromel substrate. It was found that the oxidation toughness should be improved by this type of modification to reduce the elastic stiffness from substrate.

To make large step in progress of surface modification technology, nondestructive mechanical characterization studied in the present research should be indispensable. Authors are interested in Al and N implantation into Ni, Ti and Nb and O-implantation into Al to investigate the synthesized surface material structure from metallurgical aspect of analysis using AES, ESCA and X-diffraction and from mechanical aspect of acoustic analysis by ASM. The related paper will be reported in future.

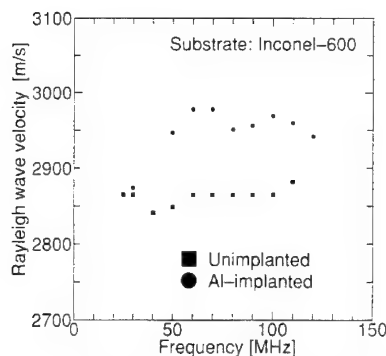


Fig. 10 Dispersion curves for Inconel-600.

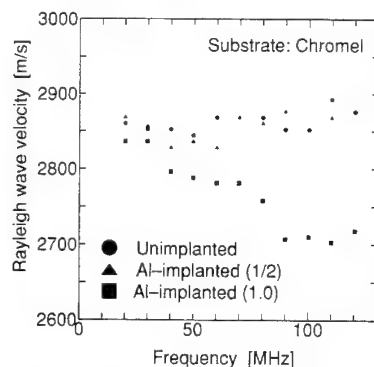


Fig. 11 Dispersion curves for Chromel.

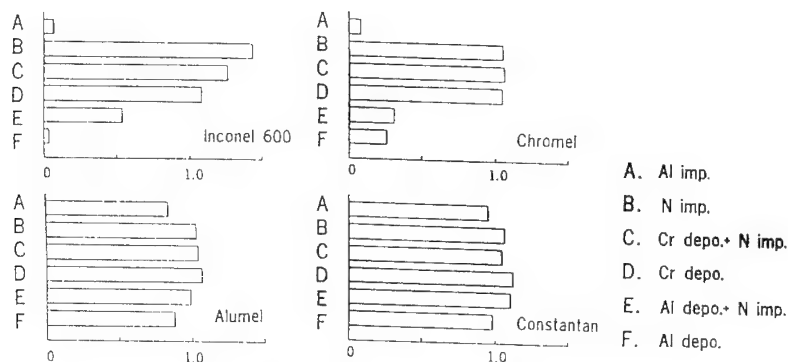


Fig. 12 Nondimensional loss of weight in the oxidation testings.

References

1. Bhushan, M.T.: Handbook of Tribology (1991) McGraw-Hill.
2. Takeda, H.: Ceramic Coating (1988) Nikkan-Kougyo.
3. Sudou, H.: Residual Stress and Distortion (1988) Uchida-Rokakuho.
4. Aizawa, T. and Kihara, J.: Ultrasonic Microscopic Evaluation of PVD/CVD Coated Hard Materials, Proc. Int. Conf. Residual Stress (1991) 346-351.
5. Aizawa, T. et al.: Residual Stress Evaluation of TiN Coated WC/Co Cermets in Hardness and Scratch Testings, Proc. Int. Conf. Residual Stress (1991) 692-697.
6. Aizawa, T. and Kihara, J.: Materials Evaluation of PVD/CVD Coated WC/Co Superhard Alloys by the Ultrasonic Microscopy, Nondestructive Testing Evaluation 9 (1992) 999-1011.
7. Aizawa, T. et al.: Nondestructive Evaluation of PVD/CVD TiN Coated WC/Co by Acoustic Spectro-Microscopy, AMD-140 (1992) 55-70.
8. Aizawa, T. and Kihara, J.: Nondestructive Measurement of Residual Stresses in PVD TiN Coatings (1993) (To be published in J. AmCer).
9. Aizawa, T. et al.: Prediction of Acoustic Structures for Multi-Layered Materials, Proc. COMMP'93 (1993, Sep. Tokyo).

DEVELOPMENT AND EVALUATION OF A WORKPIECE ANALYZER FOR INDUSTRIAL FURNACES

P. Kotidis,¹ J. Woodroffe,¹ J. Shah,² and T. Schultz²

¹Textron Defense Systems
Everett, MA 02149

²Surface Combustion, Inc.
Maumee, OH 43537

INTRODUCTION

The traditional method of determining the temperature of heat-treated workpieces in industrial furnaces is to measure surface temperature with radiation pyrometers or local temperature with contact thermocouples. Contact thermocouples have limited use because they damage the workpiece in a continuous process or require drilling of a hole in the workpiece for batch operation. Radiation pyrometers are used for noncontact surface temperature measurements, but suffer from inherent inaccuracies because of interference by radiation from furnace hot walls and gases in the furnace atmosphere and varying emissivity of the workpiece during thermal processing. Dual-wavelength pyrometers are designed to provide independence from emissivity variations. However, they do not perform on non-gray-bodies, they have difficulty looking through non-gray windows, and they tend to measure background temperature when the background is hotter than the target. Multicolor pyrometers use algorithms to eliminate the variable emissivity problems with limited success and applicability. In addition, traditional nondestructive temperature measuring instruments lack the capability to measure temperature gradients in a workpiece, which are critical for uniform phase transformations. Moreover, the knowledge of the time at which this uniformity is achieved is important for process cycle time optimization. There is a need for an instrument which can measure surface temperature as well as average bulk temperature to provide knowledge of temperature uniformity in the workpiece. An instrument like that could provide substantial cost savings and near-term payback. The Surface Combustion, Inc. and Textron Defense Systems research team, under DoE support, has conceptualized such an instrument to be used as Workpiece Analyzer (WPA).^{1,2} This paper describes results of an analytical study to determine the feasibility of this concept and preliminary experimental data of a bench scale demonstration.

PRINCIPLE OF OPERATION

The fundamental operating principle of the WPA is based on the generation, propagation, and subsequent detection of ultrasonic waves on the surface and through the body of the workpiece (Figure 1). A pulsed laser beam from the Impulse Laser (IL) is

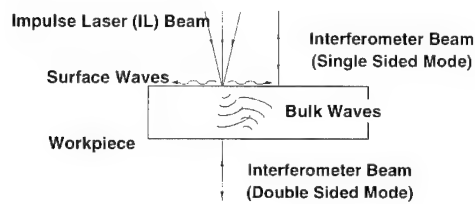


Figure 1. WPA operating principle.

directed to the workpiece to generate the waves. The arrival of the waves at an appropriately selected location (opposite or same side of the target) is monitored using a Polarizing Interferometer (PI). The speed of ultrasound is determined by measuring the time-of-flight of these waves. Since the speed of ultrasound is a function of the temperature of the solid, its bulk and surface temperatures can be measured by using calibration curves. Depending on the location of the PI with respect to the IL (same or opposite side), two WPA configurations can be realized: Single-Sided (SS) and Double-Sided (DS). Under the SS mode, both surface and reflected bulk waves can be simultaneously monitored, providing valuable information about temperature gradients in the workpiece. For thin materials, only surface wave measurements are required because the temperature gradients are negligible. In this case, a low energy impulse laser can be used leading to a much lower cost instrument. Moving workpieces (e.g., continuous strip lines) could also be monitored by the WPA due to its totally noncontact operating principle.

Metallurgical status of a workpiece during heat treatment could also be monitored by the WPA. For example, phase changes from ferrite to austenite in carbon steels have been detected. This is a result of the relationship between ultrasonic speed and crystalline structure of the material. The implication of this WPA feature is that excessive soaking times for workpieces can be eliminated, leading to major energy and cost savings.

BACKGROUND

Laser generation and detection of ultrasound ("Laser Ultrasonics") have been demonstrated and investigated for decades. The interaction of laser radiation with solid targets has been analyzed for years at TDS³⁻⁶ and elsewhere.⁷ The interaction regimes of interest to the WPA are: Thermoelastic (simple surface heating-no surface damage) and Plasma Generation (recoil effect due to confined plasma-possible surface damage). Laser pulses, or any other transient change in the structure of a solid, generate elastic waves (i.e., ultrasound). Four types can in general be generated: Longitudinal, Shear, Surface (Rayleigh), and Lamb.⁸⁻¹⁰ All four types of these waves have been generated by many researchers¹¹⁻¹⁶ with various types of detection schemes, including contact piezoelectric transducers, Electromagnetic Acoustic Transducers (EMAT's), and interferometric or noninterferometric optical techniques. The dissipation of acoustic energy in polycrystalline metals, like steel, is important as far as signal strength is concerned and can in general be attributed to elastic hysteresis, thermoelastic relaxation, and scattering.¹⁷ Strong

dependence of the attenuation on temperature and magnetic properties of steel¹⁸ has been observed, while the attenuation appears to be temperature independent for nonmagnetic steel.¹⁷

The list of references included in this paper is only a representative sample of the enormous body of literature in this field. A more complete list of references can be found in Ref. 1.

SEMI-EMPIRICAL MODEL FOR ULTRASOUND GENERATION AND PROPAGATION

Thermoelastic Regime

Consider a laser pulse of duration t_p with uniform and constant intensity impinging upon the surface of a metal target.

As the area of the laser spot is heated, the metal expands and some strain, ϵ ($\epsilon = \phi \cdot \Delta T$), is generated where ϕ is the linear coefficient of expansion of the material and ΔT is the average temperature rise in the surface layer. Consequently, a displacement, $\Delta \ell_0$ ($\Delta \ell_0 = \epsilon \cdot \delta$), is formed, where $\delta = (2Kt_p)^{1/2}$ is the penetration depth of heat and K the thermal diffusivity. The attenuation of the generated ultrasonic wave is due to spherical (cylindrical for Rayleigh waves) spreading of acoustic energy as well as elastic hysteresis, thermoelastic relaxation, and scattering. This attenuation is frequency dependent and scales with e^{ax} , where a is the attenuation coefficient and x is the distance traveled.¹⁸

Using farfield displacement functions¹³ for both longitudinal and shear waves, the displacements at the detection point are:

$$\Delta \ell^L = \frac{\phi (1-r) \Phi \cdot t_p}{\rho C_v} \frac{d_s}{x} e^{a_L x} \frac{H_0}{\mu}, \quad \Delta \ell^S = \frac{\phi (1-r) \Phi \cdot t_p}{\rho C_v} \frac{d_s}{x} e^{a_s x} \frac{K_0}{\mu} \quad (1)$$

where a_L , a_s are longitudinal and shear attenuation coefficients and $H_0 = H(\theta=0)$, $K_0 = K(\theta=0)$, where $H(\theta)$, $K(\theta)$ are directivity pattern equations. Φ is the laser flux (power per unit area), r is the surface reflection coefficient, d_s is the spot diameter, ρ is the mass density, C_v is the specific heat, and μ the Lamé constant or modulus of rigidity. This solution corresponds to a system where the detection laser is located at the epicenter of the impulse point (i.e., $\theta=0$).

Figures 2-3 present comparisons between data^{14,19} and model predictions for aluminum and steel targets. The agreement is quite good and ensures the validity of the model.

Plasma Regime

In this regime, the phenomenology of the laser-solid interaction is quite different from that of the thermoelastic regime and is dominated by the presence of plasma.^{1,4} Extensive theoretical and experimental research has led to detailed modeling of the plasma characteristics and effects.^{1,3-6} Combining the above information, the displacements a distance x away from the impulse point are:

$$\Delta \ell^L = \frac{p_D \sqrt{2Kt_p}}{E} \frac{d_s}{x} e^{a_L x} \frac{F_0}{\mu}, \quad \Delta \ell^S = \frac{p_D \sqrt{2Kt_p}}{E} \frac{d_s}{x} e^{a_s x} \frac{G_0}{\mu} \quad (2)$$

where F_0 , G_0 account for the directivity pattern at $\theta = 0$ (epicenter) and p_D is the pressure delivered to the target surface by the plasma.

Figure 4 presents a comparison between model prediction and data.²⁰ The agreement is sufficient for the purpose of this simple model. High inaccuracies can be observed in the transition regime right before the plasma formation due to the inability of the plasma

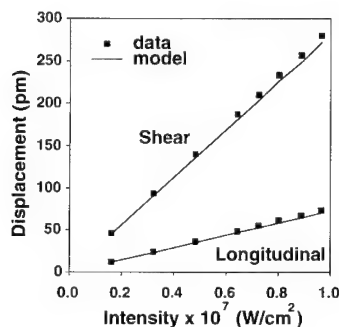


Figure 2. Comparison between data and model predictions for a 25 mm thick aluminum target.

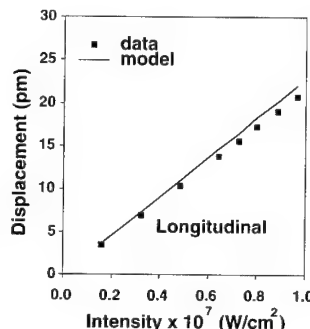


Figure 3. Comparison between data and model predictions for a 25 mm thick steel target.

model to predict thermoelastic effects. The model predicts a change in the slope of the displacement curve at about $26 \times 10^7 \text{ W/cm}^2$, but it does not show any decrease in the amplitude of the displacements. These phenomena are a direct consequence of the interaction between two competing factors, i.e., the increase of the surface plasma pressure with laser flux⁴ and the decrease of the delivered pressure to the workpiece as the plasma confinement time⁴ increases. Another comparison between data and model prediction is also presented in Figure 5. The agreement is within the experimental error and is

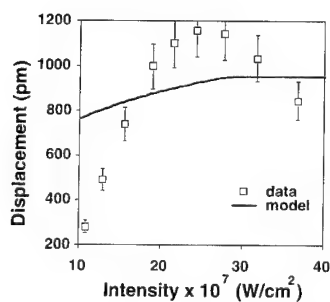


Figure 4. Comparison between data and model for a 25 mm thick aluminum target with constant impulse laser energy (33 mJ).

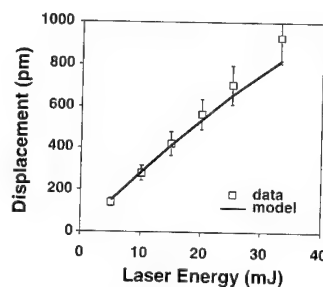


Figure 5. Comparison between data and model for a 25 mm thick aluminum target with constant impulse laser intensity (180 MW/cm^2).

considered satisfactory. Typical displacement achieved through a 25 mm thick aluminum is about 1100 pm or 11×10^{-10} m in the plasma regime, while for a similar steel specimen this value drops down to 55 pm or 55×10^{-12} m.

ANALYTICAL MODEL FOR THE POLARIZING INTERFEROMETER

The purpose of this model is to determine the minimum detectable displacement due to the arrival of ultrasonic waves. In describing the model of the PI, we will refer to Figure 6, where a schematic illustration is presented.

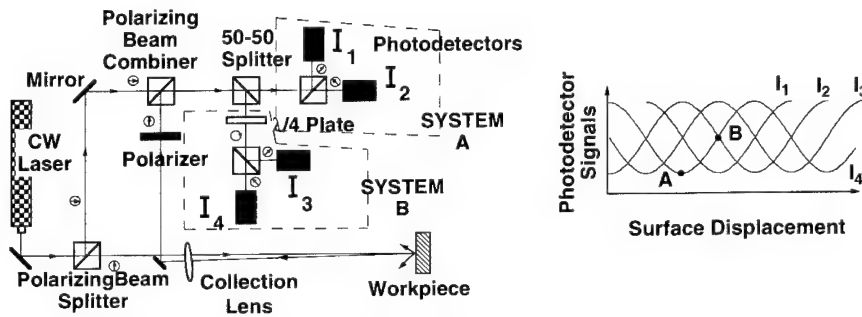


Figure 6. Polarizing Interferometer (PI) configuration and characteristic response curves.

Consider an ultrasonic displacement ξ of amplitude Δ and frequency ω_s as $\xi = \Delta \sin(\omega_s t)$. The corresponding light phase shift is $\Delta\phi = 2(2\pi\Delta/\lambda) \cdot \sin(\omega_s t)$ where λ is the light wavelength and the factor 2 is due to the double path for beam reflection. The signal beam from the workpiece and the reference beam are first linearly polarized, then combined and taken through a 50-50 splitter into systems A and B (Figure 6, dashed lines). After the 45° polarizing beam splitters and the $\lambda/4$ plate in system B, a set of signals 90° apart are generated from the four detectors, I_1, I_2, I_3, I_4 . Signal differences $(I_1 - I_2, I_3 - I_4)$ are then performed to generate two signals in quadrature, which are subsequently taken through high pass filters, followed by squaring and adding operations. A square root operation completes the signal processing. The final current, i , is given as:

$$i = \sqrt{\frac{I_R I_S}{2}} \left[\frac{4\pi\Delta}{\lambda} (RC) \omega_s \right] \cos(\omega_s t) \quad (3)$$

where RC is the time constant of the high-pass filter and I_R, I_S the light intensities in the reference and signal legs.

The minimum detectable displacement is determined by the level of photocurrent noise (shot noise) of the detector, its RMS value being, $\tilde{i}_N = \sqrt{2e\eta I f}$ where f is the detector bandwidth, e the electronic charge, η a quantum efficiency, and I the average light on the photodiode. By setting the RMS signal-to-noise ratio \tilde{i}/\tilde{i}_N equal to 1, the minimum detectable displacement Δ_{min} can be calculated, as:

$$\Delta_{\min} = \frac{\lambda}{\pi(RC)} \frac{\sqrt{ef(I_R + I_S)}}{\omega_s \sqrt{2\eta I_R I_S}} \frac{1}{\sqrt{N}} \text{ for } N \text{ laser shots} \quad (4)$$

According to the model, minimum detectable displacements as small as 30 pm are theoretically feasible.

The signal processing procedure described above makes the interferometer insensitive to external vibrations (usually low frequency) and provides constant sensitivity, independent of the operating point. Since the ultimate goal of this effort is the development of a simple, rugged, low-cost detection scheme, a one-detector configuration has been assembled by eliminating three detectors, with some penalty to the signal-to-noise ratio. The insensitivity to low frequency external vibrations is again achieved through high-pass signal filtering, but the system relies upon multiple laser pulses. The presence of external vibrations (furnace environment) forces the PI to operate at random points, including those of minimum (point A) and maximum (point B) (Figure 6) sensitivity. Several algorithms have been developed to process the multiple signals (typically 10 to 50 laser pulses).

EXPERIMENTAL RESULTS

The objective of these tests was the demonstration of the WPA's ability to detect ultrasonic velocity changes due to temperature or metallurgical state (phase change) of a heated target.² A double-sided WPA configuration was used with a tube furnace rated for 1900°F. No paint or any type of coating was applied to the surface of the samples before or during the tests. A witness piece inside the furnace with an embedded thermocouple was used to monitor the sample temperature. Ultrasound was generated by an Excimer XeCl laser operating at 308 nm with a pulse duration of approximately 20 nsecs and typical energy per pulse of approximately 80 mJ. A CW, 10 mW He-Ne laser was used in the PI configuration.

Temperature tests were conducted with 1" thick 2" diameter samples of various types of carbon and stainless steels, aluminum, and brass. The thickness selection was driven by the need to formulate a data base representative of the most promising heat treating markets. A representative sample of the processed waveforms is shown in Figure 7 for stainless steel (Figure 7a) and brass (Figure 7b) samples. The highest temperature shown (1875°F) represents the limits of the furnace. The digitizer used throughout these tests had a 10 nsec resolution. Although the attenuation at high temperature levels increased, the signal-to-noise ratio was still adequate for the detection of the ultrasonic arrival.

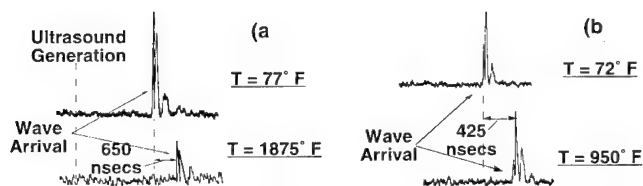


Figure 7. Processed waveforms from 1" thick (a) steel (b) brass samples.

Given the time-of-flight, the ultrasonic velocity can be measured if the sample thickness is known (assumed constant linear coefficient of expansion). Figure 8 presents a representative sample of the results for 1" thick 1010 carbon and 316 stainless steel samples. For the final WPA product, such curves will be generated during calibration with known samples, stored into the computer's memory and used to calculate the temperature of heat-treated workpieces. The discontinuity at 1250-1400°F represents the phase transformation of carbon steel from ferrite to austenite and should be accounted for in the data reduction scheme. However, this observation is a unique feature of the WPA concept

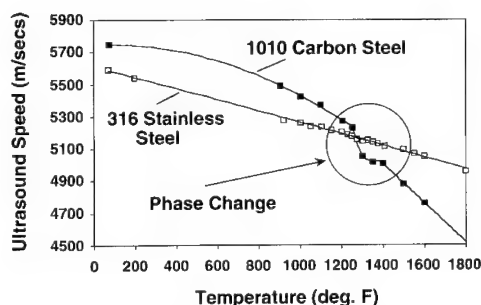


Figure 8. Phase transformation detection on 1010 carbon steel sample.

and can be used to detect the onset and completion of this phase transformation. Excessive soak times can thus be avoided during heat treating cycles. Data validation has been provided by the results of the stainless steel sample which does not go through such phase transformation and, hence, exhibits no curve discontinuity in that temperature range.

BENEFITS AND FUTURE APPLICATIONS

The WPA technology development has been driven by the market potential and the many benefits from the use of this instrument. The measurement is remote and noncontact with large standoff (at least 5 ft.) and the instrument can be placed outside the furnace, avoiding the harsh operating environment. Temperature and phase transformations can be measured on-line with moving workpieces, like those found in walking beam furnaces, continuous casters or continuous strip lines. The temperature readings are independent of the emissivity of the surface of the workpiece. Thus, the WPA can be effectively used for processes where emissivity variations during processing (like galvaneal lines) or low emissivity (like aluminum) hinder the temperature readings. Both bulk and surface temperatures can be monitored simultaneously, providing critical information on temperature gradients (especially with steel workpieces). A single instrument can be used to measure temperature at various points on a workpiece through scanning mirror arrangement for determination of temperature or phase transformation uniformity. Under the simple single detector configuration of the PI, the external low frequency vibrations encountered in normal industrial furnaces have no effect on the measurement. If only surface temperature readings are needed, as in thin strips or aluminum workpieces, then

the WPA can be made into a very small and inexpensive unit, because the energy and cost of the impulse laser can be reduced. The TDS/SC team is currently developing a WPA prototype and pursuing its near-term commercialization.

ACKNOWLEDGMENTS

This work was supported by the U.S. Department of Energy, Office of Industrial Technologies, under the supervision of Mr. Robert N. Chappell (DoE Idaho Operating Office) and Mr. Joseph G. Keller (EG&G, Idaho). The authors wish to thank Mr. Paul Gozewski, Dr. Peter Rostler, Mr. Richard Gannon, and Dr. Daniel Klimek for their support.

REFERENCES

1. U.S. Department of Energy, Phase 1 Final Report, Development and evaluation of a Workpiece Temperature Analyzer for Industrial Furnaces (1990).
2. U.S. Department of Energy, Phase 1-A Final Report, Development and evaluation of a Workpiece Temperature Analyzer for Industrial Furnaces (1991).
3. J.P. Reilly, A. Ballantyne, and J.A. Woodroffe, Modeling of momentum transfer to a surface by laser-supported absorption waves, *AIAA J.* 17:1098 (1979).
4. J.A. Woodroffe, Pulsed-laser material interaction, in: "Gas Flow and Chemical Lasers," Michele Onorato, ed., Plenum Publishing Co., New York (1984).
5. J.A. Woodroffe, J.C. Hsia, and A. Ballantyne, Thermal and impulse coupling to an aluminum surface by a pulsed KrF laser, *Appl. Phys. Lett.* 36:14 (1980).
6. C. Duzy, J.A. Woodroffe, J.C. Hsia, and A. Ballantyne, Interaction of a pulsed XeF laser with an aluminum Surface, *Appl. Phys. Lett.* 37:542 (1980).
7. J.F. Ready, "Industrial Applications of Lasers," Academic Press, New York (1978).
8. H. Kolsky, "Stress Waves in Solids," Dover Publications, Inc., New York (1963).
9. A.E.H. Love, "A Treatise on the Mathematical Theory of Elasticity," Dover Publications, Inc., New York 4th ed. (1944).
10. I.A. Victorov, "Rayleigh and Lamb Waves," Plenum Press, New York (1967).
11. A.M. Aindow, R.J. Dewhurst, and S.B. Palmer, Laser-generation of directional surface acoustic wave pulses in metals, *Opt. Commun.* 42:116 (1982).
12. R.M. White, Generation of elastic waves by transient surface heating, *J. Appl. Phys.* 34:3559 (1963).
13. D.A. Hutchins, R.J. Dewhurst, and S.B. Palmer, Directivity patterns of laser-generated ultrasound in aluminum, *J. Acoust. Soc. Am.* 70:1362 (1981).
14. C.B. Scruby, R.J. Dewhurst, D.A. Hutchins, and S.B. Palmer, Quantitative studies of thermally generated elastic waves in laser-irradiated metals, *J. Appl. Phys.* 51:6210 (1980).
15. W. Kaule, Method and apparatus for receiving ultrasonic waves by optical means, U.S. Patent 4,388,832 (1983) (assigned to Krautkramer-Branson, Inc.).
16. J.P. Monchalin, Optical detection of ultrasound, *IEEE Trans. on Ultrasonics, Ferroelectrics and Frequency Control* 33:485 (1986).
17. G.S. Darbari, R.P. Singh, and G.S. Verma, Ultrasonic attenuation in carbon steel and stainless steel at elevated temperatures, *J. Appl. Phys.* 39:2238 (1968).
18. E.P. Papadakis, L.C. Lynnworth, K.A. Fowler, and E.H. Carnevale, Ultrasonic attenuation and velocity in hot specimens by the momentary contact method with pressure coupling, and some results on steel to 1200°C, *J. Acoust. Soc. Am.* 52:850 (1972).
19. A.M. Aindow, R.J. Dewhurst, D.A. Hutchins, and S.B. Palmer, Laser-generated ultrasonic pulses at free metal surfaces, *J. Acoust. Soc. Am.* 69:449 (1981).

SENSOR SYSTEM FOR INTELLIGENT PROCESSING OF HOT-ROLLED STEEL*

A.V. Clark, M.G. Lozev, B.J. Filla and L.J. Bond¹

Materials Reliability Division
National Institute of Standards and Technology
Boulder, Colorado 80303

¹ Center for Acoustics, Mechanics and Materials
University of Colorado at Boulder
Boulder, Colorado 80309-0427

ABSTRACT

Microstructural engineering offers a means of reducing cycle time and improving product quality with reduced energy cost. Process modelling of hot-rolling of steel has advanced to the point where key metallurgical parameters (e.g. austenite grain size) can be predicted from computer models if other process parameters such as temperature are known. However, a need still remains to develop on-line sensors because sensors can rapidly acquire data for model validation, and could be combined with a process control strategy in feedforward or feedback loops.

We report a study to develop an on-line sensor for austenite grain size measurement at temperatures up to 1000°C. We are developing a system for measurement of attenuation in ultrasonic waves propagating through hot steel samples. Existing theories allow us to infer grain size for attenuation measurement. Our system consists of a high temperature transducer acoustically coupled to a high strength, low loss buffer rod. The rod is to be pressed against a hot steel specimen to achieve sufficiently good contact to transmit ultrasound into the specimen. To avoid plastic deformation of the specimen, we implement computer control of the load applied to the buffer rod.

Attenuation measurements were performed at room temperature on specimens of known grain size. Good agreement with optically measured grain size was obtained. The system is now being assembled for measurement at elevated temperatures.

*Contribution of US National Institute of Standards and Technology, not subject to copyright.

INTRODUCTION

To improve quality of steel plate there is a recognized need to improve the control of the various system and material parameters in the hot rolling process [Cook and Frock (1986)]. Improved control requires the availability of on-line measurements for parameters such as the mean austenite grain size. If the grain size can be measured early in the manufacturing process and these data combined with a process model [Cook and Frock (1986)], feedback systems can in principle be developed to give adjustments to process variables. This will result in reduced product variability, reduced reheating requirements, and a reduced need for post-processing heat treatment.

Ultrasonic techniques have been demonstrated in the laboratory to give a relationship between attenuation and grain size [Papadakis (1981, 1984)]. Excellent correlations have been shown in ferrous materials [Goebbels (1980)], and in-line monitoring measurements for grain size in steel mills have been performed near room temperature [Takafuji et al. (1985); Yada and Kawashima (1987)]. The measurements show a clear relationship between ultrasonic attenuation and an "ultrasonic mean grain diameter" which can be related to the optically measured mean grain size, if the sample microstructure is known. Several grain size instruments are already in use using these concepts [Takafuji et al. (1985), Yada and Kawashima (1987)].

This study considers the development of an ultrasonic attenuation measurement system. From this we propose to determine of the austenite grain size in hot-rolled steel at temperatures above 700°C. Here we envision an ultimate application in which a sensor system would measure austenite grain size during, for example, finish rolling. Ultrasonics may therefore become a practical tool for grain size measurement in the 10-200 μ m range, which can then become a process control parameter [Bridenbaugh et al. (1987)].

THEORY

The theory of the scattering of a wave propagating in a polycrystalline medium has been presented in a number of publications [Papadakis (1981, 1984)]. For a plate with a gradation of grain sizes, the attenuation is dominated by the contributions of the largest grains [Papadakis (1981)]. Steel above the austenite temperature is a single phase equiaxed polycrystalline metal. Measurements suggest that scattering contributes the greater part of the attenuation in this temperature range [Papadakis et al. (1971)]. Therefore, only a limited frequency range may be required for our purposes. This is in contrast to room temperature measurements, where a large frequency range is often necessary to separate the effect of scattering from other contributions to attenuation (such as internal friction).

The solution for the attenuation coefficient for the case of cubic crystallites, in the Rayleigh scattering (long-wavelength) was provided by Merkulov (1956) in a simplified form as:

$$\alpha = Tf^4S \quad (1)$$

where f is the ultrasonic frequency, S is a parameter of the material which is dependent on density and elastic moduli, and T is a measure of the average grain size, with the dimensions of volume. Values of S can be determined theoretically from single-crystal moduli or for other morphologies from experimental data [Takafuji et al. (1985)]. The functional dependence of the attenuation upon and grain size has been given by Papadakis (1984), and it is a weighted function depending on the grain size distribution.

MEASUREMENT METHOD AND SYSTEM DESIGN

Our experimental system employs the pulse-echo technique. Waves are generated by a LiNbO_3 crystal and are propagated down a buffer rod. LiNbO_3 was chosen because of its high Curie temperature and because it has an acoustic impedance close to that of the buffer rod. A hydraulic actuator presses the rod against the sample, which is heated (at temperature up to 1000°C) inside a furnace. This simulates the temperature range in hot rolling.

Three signals are required because there are three unknowns: amplitude of wave generated by the transducer; reflection coefficient R from buffer rod/sample interface; attenuation coefficient. Various echoes can be recorded: the buffer rod/air echo (A'); buffer rod/sample interface echo (A); first and second back wall echoes in the sample (B, C echoes). Two pulse-echo methods for attenuation determination have been considered. These methods are conventionally identified as the $A'AB$ and ABC methods [Mak (1991)], and each employs three signal amplitudes.

A critical parameter in the evaluation of an attenuation measurement scheme is an "attenuation variance-noise number" ($N\alpha$) defined as the product of the (normalized) variance of the attenuation measurement σ_α/α and the signal to noise ratio S : $(\sigma_\alpha/\alpha)S$. This parameter is calculated using relationships given by Mak (1991) and is used to compare the two measurement schemes. The resulting values are plotted against total attenuation T_α in the sample ($T_\alpha = 2\alpha L$, where α is the attenuation coefficient and L the sample thickness). The results are shown in Fig. 1. The $A'AB$ method has better precision for given signal-to-noise ratio.

Fig. 1 can also be used to define a suitable operating frequency. Experimental uncertainty is minimized when T_α is approximately unity; for given sample thickness, this gives a "best" value of α . In practice, the expected grain size, thickness, and temperature are all approximately known. This allows us to calculate α from Equation (1), with frequency as a parameter. The frequency is then chosen so that $2\alpha L$ is approximately 1. In this study an optimized operating frequency between 4 and 5 MHz was determined, for grain sizes of about $50\text{ }\mu\text{m}$, and specimen thickness about 50 mm; these values are typical of industrial practice.

To provide the measurement capability needed to operate at temperatures up to 1000°C , two designs of transducers are being considered. Both are based on a novel cooled buffer-rod design. The cooling is required to protect both the piezoelectric element and the hydraulics. The transducers are set onto the cooled end of the buffer rod.

The first design is a variation on a commercial unit which has been used for acoustic emission monitoring at elevated temperature [Arakawa et al. (1992)]. This has a lithium niobate transducer brazed to the buffer rod. This design is mechanically robust; however, its electrode thickness is fixed by brazing requirements and hence has a limited bandwidth. The second transducer has a more flexible design. (However, its long-term reliability at elevated temperatures is not well-established yet.) It employs a "sandwich" consisting of: a pressure plate, backing, gold foil electrodes and a lithium niobate crystal set onto the buffer rod. The electrode thickness can be chosen to give a wider bandwidth.

The response of these two transducers has been modelled [Clark et al. (1993)], and the expected output voltages are shown in Fig. 2. The larger bandwidth of the second design is clearly evident. These calculations will be compared with experimental data.

The buffer rod must take a significant mechanical load [Lu et al. (1990)] because the acoustic coupling into the sample is achieved using pressure coupling. The buffer rod must have low internal losses due to attenuation. This requires a small grain size. Grain growth must also be minimized. Mechanical strength must not be degraded at elevated

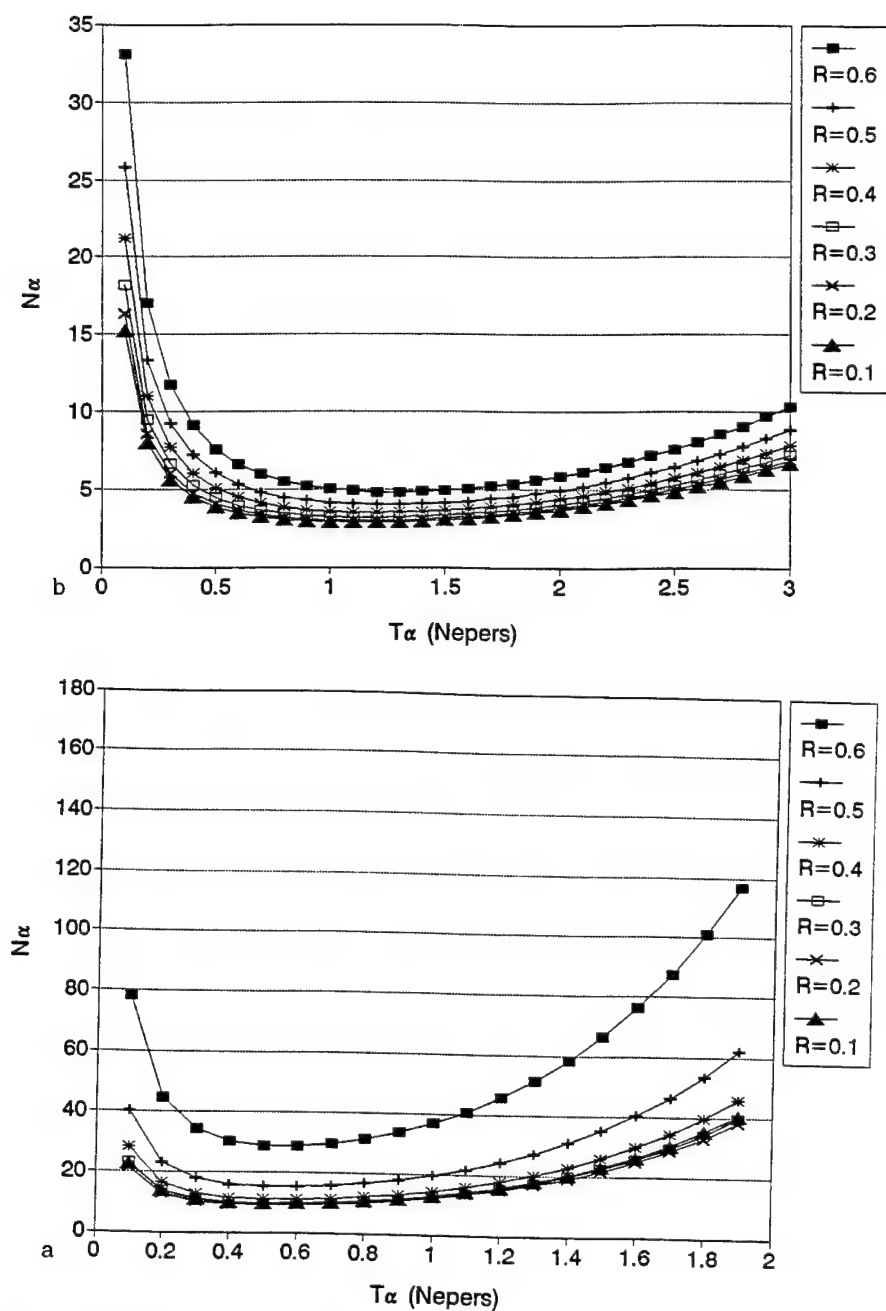


Figure 1. Attenuation variance-noise number, N_α , against total attenuation, T_α , (nepers). Calculations were done for case of 50 mm sample thickness with a 5 MHz, 25 mm diameter transducer is modelled for various interface reflection coefficients, R . Corrections for diffraction have been made.

(a) For A'AB method.

(b) For ABC method.

temperature, and oxidation must be minimized. Conventional stainless steels are not satisfactory, since they have large grain sizes for good mechanical properties at elevated temperatures (plastic deformation occurs by grain boundary motions at these temperatures, rather than by dislocation motion). To meet the various mechanical design requirements a nickel-based mechanical alloy was selected for the buffer rod material.

At elevated temperatures the stress-strain characteristics of the sample become highly dependent on the rate of strain. Typical data for microalloyed steel is shown as Fig. 3. Clearly, contacting the buffer rod to the sample for more than a few seconds at low strain rates will cause plastic deformation of the sample surface. (Momentary contact has been used by Papadakis et al., (1971) for attenuation measurements, with buffer rod

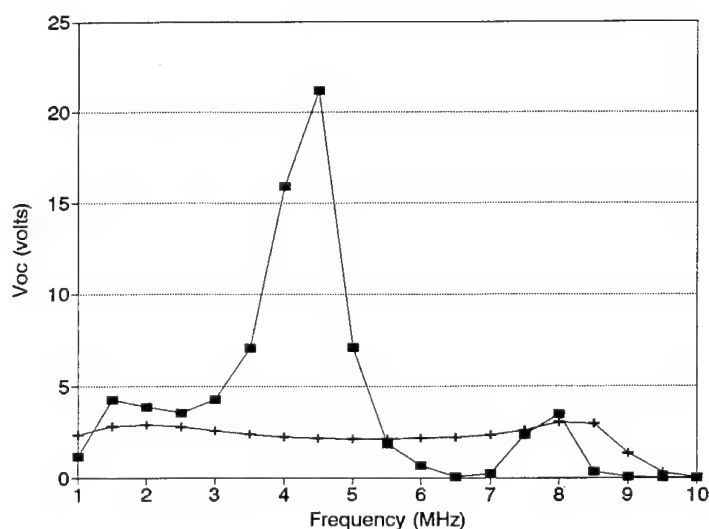


Figure 2. Theoretical transducer response characterized by output voltage (Voc) against frequency. The transducer is assumed driven by a 12 Ω pulser with toneburst of 10 V amplitude. A series inductance of 2.5 μ H is used for tuning. The transducer response of brazed transducer indicated by squares; response of pressure plate transducer by crosses. Thickness of brazed Al electrodes is 200 μ m. Pressure plate transducer has top and counter-electrodes of Au foil, thickness 100 μ m.

completely removed from the furnace after attenuation measurement. The buffer rod is essentially at room temperature. However, this method does not appear feasible in a steel mill.) To avoid excessive plastic deformation computer control of the load applied to the buffer-rod-sample interface is being implemented.

The complete transducer/buffer rod/cooling jacket system, set in the furnace is shown as Fig 4. A methodology using a preheated buffer rod, computer controlled hydraulics to avoid sample deformation, and repeated measurements of the A'AB echoes is to be employed [Clark et al. (1993)].

Room temperature measurements have already been performed on the samples prepared for the high temperature study. The measured values of attenuation were in close agreement to values calculated from the optically measured grain sizes for the sample set [Lozev et al. (1993), Clark et al. (1993)].

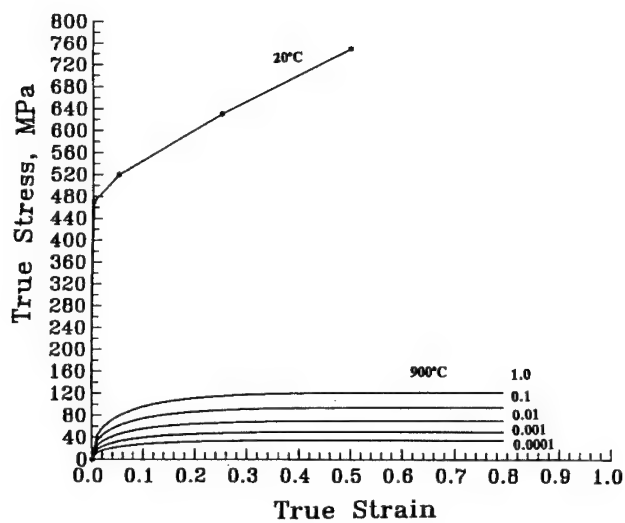


Figure 3. Stress-strain response for microalloyed steel at 20°C and 900°C with strain rate as parameter.

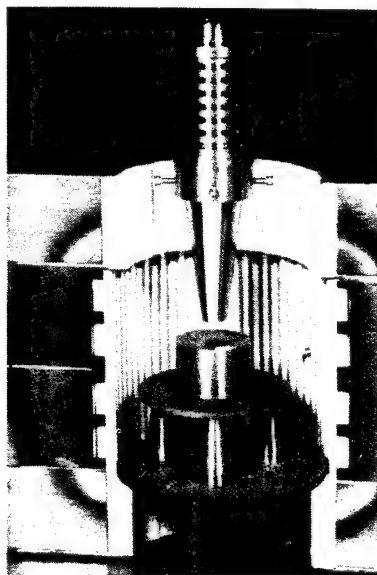


Figure 4. High temperature grain-size measurement system, showing open furnace with (top to bottom): cooling jacket, transducer/buffer rod assembly held above sample.

CONCLUSIONS

A prototype measurement system has now been designed, with the goal of high temperature measurements of attenuation in steel samples. From these attenuation measurements, the austenite grain size can be characterized.

The system consists of: a high temperature transducer acoustically coupled to a buffer rod; hydraulics (under computer control) to pressure-couple the buffer rod to the sample; a cooling jacket to protect the hydraulics from heat conducted through the buffer rod; a furnace to heat samples above the austenite temperature. The components have been chosen based on optimization studies. The system will be tested on hot steel specimens heated up to 1000°C. If these tests are successful, a sensor system with potential for on-line grain size estimation in a hot rolling mill would appear to be possible.

ACKNOWLEDGEMENTS

This work was supported in part by the Office of Intelligent Processing of Materials of the National Institute of Standards and Technology. We are grateful for many useful discussions with our colleagues Drs. Y. Cheng and C.M. Fortunko.

REFERENCES

- Arakawa, T., Yoshikawa, K., Chiba, S., Muto, K., and Atsuta, Y. (1992), Applications of brazed-type ultrasonic probes for high and low temperature uses, Nondestructive Testing and Evaluation, Vol 6 pp. 263-272.
- Bridenbaugh, P.R., Shabel, B.S., and Govada, A.K. (1987), Material characterization for process control for aluminum alloys and advanced materials, in "Nondestructive characterization of materials II," Ed. J.F. Bussiere et al., Plenum Press (New York), pp. 179-194.
- Clark A.V., Lozev, M.G., Bond, L.J., Filla, B.J., and Reed, H. (1993), Austenite grain size characterization in hot rolled steel plate, Research in NDE (in preparation).
- Cook, R.J., and Frock, B.G. (1986) Process control and materials characterization within the steel industry, in "Materials characterization for system performance and reliability" Ed. J.W. McCauley and V. Weiss, Plenum Press (New York) pp. 293-309.
- Goebbels, K., (1980) Structure analysis by scattered ultrasonic radiation, in "Research Techniques in NDT" Vol. 4, ed. R.S. Sharpe, Academic Press (London) pp. 87-158.
- Lozev, M.G., Bond, L.J., Clark, A.V., and Reed, H. (1993), Attenuation of ultrasonic waves in stainless steel at room temperature (in preparation).
- Lu, G.L., Li, S.H., Chu, M.J. and Wang, B.X. (1990), The effect of pressure on ultrasonic testing sensitivity of hot steel blooms by pressure contact method, IEEE Trans. Ultrasonics, Ferroelectrics and Frequency Control 37 (6) pp. 587-589.
- Mak, A.K. (1991), Comparison of various methods for the measurement of reflection coefficient and ultrasonic attenuation, British J. NDT 33 (9) pp. 441-449.
- Merkulov, L.G. (1956), Sov. Phys-Tech. Phys. 1 (1) pp. 59-69.
- Papadakis, E.P. (1981) Scattering in polycrystalline media, in Methods of Experimental Physics, Vol. 19, Ultrasonics, ed. P.D. Edmonds, Academic Press (New York) pp. 237-298.
- Papadakis, E.P. (1984), Physical acoustics and microstructure of iron alloys, Int. Metals Reviews 29 (1) pp. 1-24.

- Papadakis, E.P., Lynnworth, L.C., Fowler, K.A., and Carnevale, E.H. (1971), Ultrasonic attenuation and velocity in hot specimens by the momentary contact method with pressure coupling, and some results on steel to 1200°C, J. Acous. Soc. Amer. 52 (3) pp. 850-857.
- Takafuji, H., Sekiguchi, T., Iuchi, T., and Matsuda, S. (1985), A new measurement method of the grain size of steel by ultrasonic attenuation technique, Proceedings, Ultrasonics International '85, Butterworth Scientific (Guildford) pp. 195-200.
- Yada, H., and Kawashima, K. (1987), Important metallurgical parameters that must be determined to control the properties of steels during processing, in "Nondestructive characterization of materials II," ed. J.F. Bussiere et al., Plenum Press (New York) pp. 195-209.

ON-LINE ULTRASONIC CHARACTERIZATION OF POLYMER FLOWS

L. Piché, D. Lévesque, R. Gendron, and J. Tatibouët

Industrial Materials Institute, National Research Council Canada
75 de Mortagne, Boucherville, Qc, J4B 6Y4, Canada

INTRODUCTION

Although ultrasonic techniques have proven useful for investigating elasticity of solids and viscosity of fluids and gases¹, they have seldom been used for polymer studies. Notwithstanding, all reports^{2,3,4} point out the distinctive behavior of ultrasound in polymers and suggest numerous prospects for fundamental studies, and industrial applications^{5,6}. Thermomechanical properties of polymers are usually measured at low frequencies between 0.01 and 100 Hz, with deformations $\epsilon \approx 10^{-4}$, while ultrasonic techniques involve frequencies in the MHz range and strains near $\epsilon \approx 10^{-7}$. Whilst rheology measures global properties associated to long range diffusion of molecules, ultrasonic waves probe the mobility of short chain segments. In an attempt to relate the different measurements, we described experiments^{7,8} using an apparatus⁹ that measures the complex ultrasonic modulus with close control of the thermodynamic history. Although successful, the technique involves no macroscopic flow of molecules.

Processing, on the other hand, implies macroscopic flows; therefore there is a need for investigating the effect of large scale molecular movements on the short scale mobility. Here we describe an experiment for characterizing flowing polymer melts during processing. In continuum hydrodynamics, it is assumed that the component of the fluid velocity vanishes along a solid surface. This "no-slip" boundary condition may be argued intuitively since internal drag due to viscosity slows down the fluid near the interface. In the case of usual Newtonian fluids, this "no-slip" assumption is usually successful. Non-Newtonian fluids are different and for polymer melts it may be conjectured that near walls, the flow curves are modified due to alignment of molecular chains. In turn, this may lead to slippage at the walls, resulting in flow irregularities that are manifested by so-called melt fracture. This line of reasoning suggests that melt fracture is related to peculiarities of the polymer/wall interface region, which mostly agrees with experimental observations^{10,11,12} from rheology. Recently, we described^{13,14,15} an ultrasonic approach for investigating polymer/metal interfaces. We adapt this method to extrusion of polymer melts. We demonstrate that ultrasonic results correlate with materials properties obtained in rheology, and provide unique information on polymer/wall interactions that condition flow behavior. We conclude that the technique is a powerful tool for monitoring and controlling industrial processes.

METHODOLOGY

Ultrasonics and Fluid Mechanics

The Navier-Stokes equation is the basis for describing the movement of viscous fluids. For the one-dimensional case, the time evolution for the particle velocity, u is given through:

$$\rho \frac{\partial u}{\partial t} + \rho u \frac{\partial u}{\partial z} = -\frac{\partial p}{\partial z} + (\eta_B + \frac{4}{3}\eta) \frac{\partial^2 u}{\partial z^2} \quad (1)$$

where ρ is the density, p the pressure, η the shear viscosity and η_B the bulk viscosity. Solving Eq.(1) in an unbounded medium for small periodic displacements polarized along the z axis and having angular frequency ω , one recovers the usual wave equation, where the velocity of sound, v , and the attenuation, α , are given by:

$$v = \sqrt{\frac{\partial p}{\partial \rho}} \quad \text{and} \quad \alpha = \frac{1}{2\rho v^3} (\eta_B + \frac{4}{3}\eta) \omega^2 = \frac{1}{2\rho v^3} \eta_L \omega^2 \quad (2)$$

However, it is often more useful to describe materials properties of the supporting media in terms of a complex longitudinal modulus, $L^* = L' + iL''$, such that:

$$L' = \rho v^2 \quad \text{and} \quad L'' = 2 \alpha \rho v^3 / \omega \quad (3)$$

For macroscopic displacements, such as laminar flow between two parallel planes, one usually assumes zero flow velocity at the walls. Solving Eq.(1) in the case of incompressible fluids, leads to a parabolic profile for particle velocity. Also, the shear stress is zero at mid-plane and reaches its maximum value at the walls:

$$\sigma_{12} = \frac{e}{2} \Delta p \quad \text{with} \quad \Delta p \equiv \frac{\partial p}{\partial x} \quad (4)$$

where e is the separation between plates and Δp the pressure drop per unit length along the flow channel. In application of Newton's law for fluids, σ_{12} may be related to the volumetric flow rate, Q through:

$$\sigma_{12} = -\eta \dot{\gamma} \quad \text{where} \quad \dot{\gamma} = \frac{\partial u}{\partial z} = 6Q / we^2 \quad (5)$$

is the rate of shear, and w is the breadth of the channel. In principle therefore, ultrasonic measurement of viscosity of fluids can be correlated to properties of macroscopic flows.

Materials and Properties

We experimented on a commercial grade of polypropylene (PP) resin, that was provided by Himont Canada under the designation 6631FB. Specifications were given for the density, $\rho = 890 \text{ kg/m}^3$, and the melt flow rate $\text{MFR} = 2.0 \text{ g/10 min}$. We performed additional rheological measurements with capillary rheometry and dynamic mechanical spectrometry in order to characterize molecular weight, $M_w = 415\,000 \text{ g/mole}$, and determine the constitutive law for the viscosity. The results depended on temperature in

accordance to an Arrhenius process. For illustrative purposes, at a temperature $T = 220^\circ\text{C}$ corresponding to our present experiments on extrusion, we found a Carreau dependence:

$$\eta = 9.9[1 + (0.905\dot{\gamma})^2]^{-0.325} \quad (6)$$

with η in kPa.s. The fact that viscosity was shear rate dependent is in line with the trend for polymer fluids, which usually deviate from Newton's law.

Using an apparatus specially developed in our laboratory⁹, we measured the specific volume, V_c , velocity of sound, v_c , and attenuation, α_c , of the confined material, in the absence of macroscopic flow. Operating at the ultrasonic frequency $f = 5$ MHz, the results in the range of pressure, $p = 0$ to 200 MPa and temperature $T = 175$ to 220°C , could be described through the following fitting functions:

$$V_c(p,T) = 1.115 \cdot 10^{-3} - 7.269 \cdot 10^{-7} p + 1.119 \cdot 10^{-6} T - 5.029 \cdot 10^{-9} pT \quad (7a)$$

$$v_c(p,T) = 1.383 + 3.781 \cdot 10^{-3} p - 2.077 \cdot 10^{-3} T + 1.288 \cdot 10^{-5} pT \quad (7b)$$

$$\alpha_c(p,T) = 8.31 - 0.018 T - 0.071 p \quad (7c)$$

where V_c is expressed in m^3/kg , v_c in km/s , α_c in dB/cm , p in MPa, and T in $^\circ\text{C}$.

For $T = 220^\circ\text{C}$, and $p = 1.0$ MPa, one finds $\eta_L \approx 0.05$ Pa.s, while in the limit of low shear stress, Eq.(6) leads to $\eta \approx 9.9$ kPa.s. The large difference between both values has its origin in the peculiar nature of the polymer liquid, where the long molecules form an entanglement network. The rheology measurement involves large displacements compared to those in ultrasonics so that, while η involves reptation of chains through entanglements, η_L mainly relates to small scale mobility of short molecular segments.

ULTRASONIC PROBE OF FLOWING POLYMERS

Technique

For the experiments on flowing melts, we used a single screw extruder (Flag 25D30V, with 6.35 cm diameter barrel, and length to diameter ratio 30) that we equipped with a slit die, Fig.1, enclosed in a thermostat sleeve for controlling the die temperature, T_D . The entrance channel of the die contained an immersion thermocouple for monitoring melt flow temperature, T_M . The slit section (length, $l = 14.6$ cm, width, $w = 3.8$ cm) had a thickness, e , that could be adjusted between 2.0 and 3.5 mm by means of calibrated spacers. Four pressure transducers(p), installed along the length of the slit served for rheological characterization of the flow by use of Eqs (4) and (5). Two identical ultrasonic probes(US), each consisting of a steel buffer rod with a transducer, were mounted in opposition, approximately at midstream and perpendicular to the slit, so the ultrasonic beam was normal to the flow channel. The free ends of pressure transducers and ultrasonic probes were flush with the die walls, in order not to disturb the flow. We used longitudinal ultrasonic broadband transducers, with a center frequency $f = 5$ MHz and $1 \mu\text{s}$ pulse width that we operated with a repetition rate ≈ 100 Hz. The signal from the receiving transducer was sent to a broadband amplifier connected to a fast digitizer. The numerized signals were then processed in a personal computer where attenuation and velocity were obtained by use of Fast Fourier Transforms and correlation techniques. The time duration for this routine was of the order of 1 s.

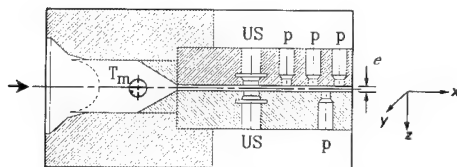


Figure 1. Schematic of slit die. Left hand part is convergence channel with immersion thermocouple for melt temperature, T_m . Right hand portion is instrumented slit having length 14.6 cm, breadth 3.8 cm, and adjustable thickness, e between 2.0 and 3.5 mm. Drawing shows position of pressure transducers, p , and ultrasonic probes, US .

Measurements and Results

In Figs 2a and 2b, we investigate the velocity, v_F , and attenuation, α_F , of sound in the polymer flowing through a slit of thickness $e = 2.00$ mm, and we plot the data as function of pressure, p (MPa), evaluated at the location of the ultrasonic probes. The squares, circles and triangles correspond to die temperatures $T_D = 210, 220$ and 230°C , respectively. The solid lines in Fig.2 are results of a model that will be described later on. For a given pressure, the velocity changed with temperature at a rate $[\partial \ln v_F / \partial T]_p \approx -2.15 \times 10^{-3}/^\circ\text{C}$, close to $[\partial \ln v_C / \partial T]_p \approx -2.10 \times 10^{-3}/^\circ\text{C}$ obtained from Eq.(7b) for the confined melt. On the other hand, for a given set of temperature and pressure, we observed that v_F always exceeded v_C . Also, at low pressure, the rate of change, $[\partial \ln v_F / \partial p]_T \approx 3.0 \times 10^{-8} \text{ Pa}^{-1}$, was more important than for the confined polymer, $[\partial \ln v_C / \partial p]_T \approx 0.69 \times 10^{-8} \text{ Pa}^{-1}$. Finally, instead of increasing steadily with p , the velocity would tend to level off near $p \approx 3.0$ MPa.

At low pressures, corresponding to small flow rates, the attenuation, α_F in Fig.2b, behaved similarly to that in the confined polymer: up to $p \approx 3.0$ MPa, $\alpha_F \approx \alpha_C$ and $[\partial \ln \alpha_F / \partial T]_p \approx [\partial \ln \alpha_C / \partial T]_p \approx -4.4 \times 10^{-3}/^\circ\text{C}$. However, as pressure increased due to higher flow rate, the behavior of α_F contrasted noticeably with that of α_C . Manifestly, temperature effects were more pronounced and $[\partial \ln \alpha_F / \partial T]_p \gg [\partial \ln \alpha_C / \partial T]_p$. Moreover, the attenuation increased with pressure instead of decreasing slightly, as in the confined melt, from Eq.(7c).

The results in Fig.2 cannot be interpreted on the basis of Eqs(7). Obviously, the ultrasonic measurements contain information related not only to pressure and temperature, but also to the hydrodynamics of the macroscopic flow. This was confirmed in other experiments with different slits, which showed that v_F and α_F are dependent on the thickness, e . Although pressure, p , is a relevant parameter for describing flow behavior, one can choose to parametrize v_F and α_F in terms of any of the other variables in Eqs(4) or (5). However, the representation in Fig.(2) has the advantage of being more closely related to the ultrasonic data in Eq.(7) that are described in terms of p and T . On the other hand, given the geometry for the experiment, in Fig.2 one may use the approximation: $p \approx \sigma_{12}$.

BOUNDARY LAYERS

Our measurements on the confined melt, Eqs(7), indicate that attenuation is not highly dependent on pressure, p , or temperature, T . Then, one may suspect that the excess

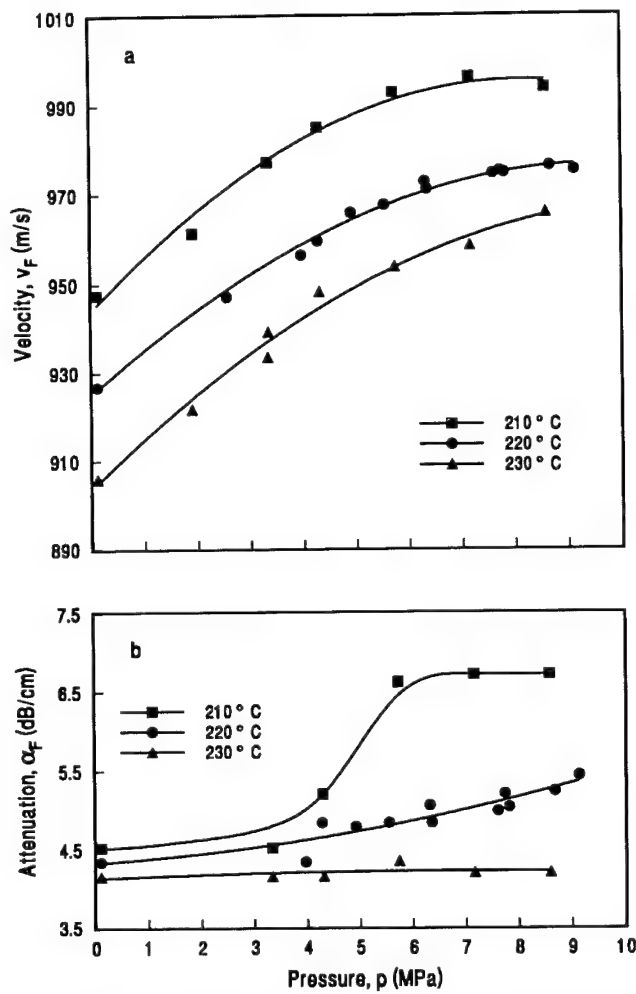


Figure 2. (a) Sound velocity, v_F (m/s) and (b) attenuation, α_F (dB/cm), for flow in slit with thickness $e=2.00$ mm. Temperature on the die was constant : $T_D=210$ (squares), 220 (circles) and 230°C (triangles), and data were plotted versus pressure, p (MPa), related to flow rate.

attenuation in the flowing melt is related to effects due to shear stress, σ_{12} . These effects should be more important near the walls of the flow channel because of the larger shear stress. One is led to propose that the polymer morphology is modified by the flow process. Finally, it is well recognized that near interfaces, polymers exhibit distinctive features, whether or not they are undergoing flow. This brings up the idea of an interface layer where the material has properties different from those of the bulk polymer. This interfacial layer serves to transfer mechanical load between the channel walls, with which the polymer molecules interact, and the bulk polymer in the core, where the molecules arrange into an assembly of random coils.

Following along those lines, we make the hypothesis for two identical layers one adjacent to each wall. There results a multilayer structure for the propagation of sound and, because of changes in acoustic impedance between constituents, calculation of ultrasonic velocity and attenuation develops into a complex problem. In a previous report¹³, we presented a complete description for the ultrasonic response of multilayered absorbing media and discussed this relative to other approaches in the literature. The scheme is based on a recurrence relation for transferring stresses and displacements from one interface to another using the so-called Transfer Matrix Approach. The solution involves a great deal of analytical work, but the final operational result can only be obtained numerically.

We may now map the ultrasonic properties associated with the confined polymer onto the pressure and temperature profiles¹⁶ for the different flow conditions. Both the thickness, d_i , and the (complex) modulus, L_i^* , of the interfacial material are unknown, and and constitute adjustable parameters. However, it may be shown¹³ that, provided d_i is smaller than the acoustic wavelength, $\Lambda = v/f \approx 200\mu\text{m}$, the thickness and modulus are not independent parameters. Instead, the longitudinal specific stiffness, $S^* = L_i^*/d_i$, becomes the relevant variable. At this point however, we need to satisfy conditions of continuity, so that for vanishingly small flow rates the interfacial material and the confined melt have similar properties. For this, we set $L_i''/L_i' = L''/L' \approx 3 \times 10^{-3}$, in which case $S^* \approx S' = L_i'/d_i$ is a real quantity.

We adjusted values of L_i^* and d_i in order to obtain the best fit to the data. The results for the velocity and attenuation are shown as solid lines in Fig.2. We found that this best fit corresponded to small values $d_i \ll \Lambda$, so that S' was the sole parameter of interest. Also, the best fit indicated that the relevant temperature in the problem was that of the melt T_M , which may exceed that for the die, T_D , by several degrees depending on flow rate¹⁶. The results at low flow rates show that the ultrasonic response is correlated to usual rheology. At high flow rates, the stiffness of the polymer in the boundary layer, S' , gradually depreciates. There results a weak link between the core of the flow and the channel walls which acts to regulate flow behavior through feedback.

Conversely, one would like to use the ultrasonic measurements as a means of monitoring melt viscoelasticity during the process. However the results in Fig.2 for the velocity or the attenuation are not single valued in terms of pressure and temperature. For applications, one needs a unique parameter that may serve as a reference to describe or at least compare flow behavior. In this respect, our multilayer model suggests that flow behavior is actually regulated by the properties of the interface layer. In Fig.3 we plot the excess losses due to flow conditions, $A = 2e(\alpha_F - \alpha_C)$, versus the interface parameter, S' . The results, which pertain to numerous experiments over a wide range of flow conditions, demonstrate a unique power law correlation between A and S' . Such scaling behavior is characteristic of universality and constitutes a strong indication for the reality of an interfacial layer that controls the rheology. Also the power law correlation suggests an intervening critical behavior associated with the boundary layer, that may well be the origin of macroscopic flow instabilities, leading to so-called as melt fracture.

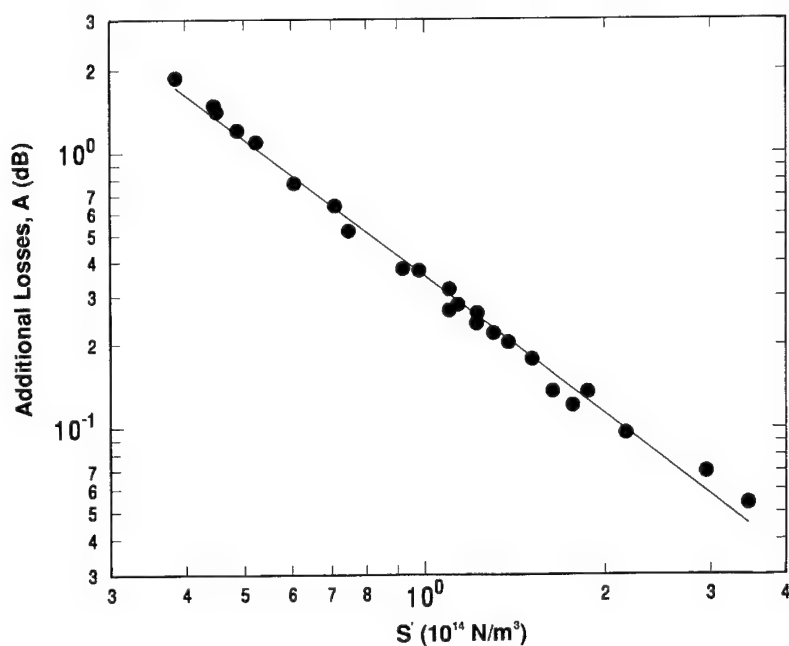


Figure 3. Universal master curve of additional acoustic losses due to flow conditions, $A = e(\alpha_F - \alpha_C)$, versus interface stiffness parameter, S' .

CONCLUSION

Through ultrasonic measurements as function of pressure and temperature we showed that velocity and attenuation of sound in a confined polymer melt correlated to the p,V,T equation of state and to the viscosity associated with small molecular moieties. We adapted the technique for measurements on melts during extrusion through a slit, under well controlled conditions. Compared to the confined melt, the ultrasonic behavior in the flowing polymer were quite anomalous. Making the assumption of a thin viscoelastic boundary layer with complex modulus, L_i^* and thickness d_i , we described the propagation in terms of the specific stiffness of the interface material $S^* \approx S' = L_i^*/d_i$. Finally, our different results exhibit universal behavior which suggests that the interface layer governs flow behavior. A great more work is required and forthcoming reports will concern: i) interfacial mobility in relation to shear stress; ii) the influence of polymer architecture; iii) the non-linear flow regime where melt fracture occurs. Also, a theory is needed to describe the physical origin of the scaling behavior. The present work is open ended and leads to new avenues for novel developments in the field of hydrodynamics and applications. Indeed the technique provides a direct measurement of the "slip factor" that is needed for building representative models of polymer melt flows. On the other hand, the technique is non-invasive and may be easily implemented for on-line monitoring of polymer properties, during manufacturing of raw materials, compounding of blends and alloys, or processing for end-use purposes.

REFERENCES

1. R.T. Beyer, and S.V. Letcher, "Physical Ultrasonics", Academic Press, New York (1969).

2. B. Hartmann, Ultrasonic Measurements in "Methods of Experimental Physics", edited by R.A. Fava, Vol. 16-c, Chap. 12.1, pp. 59-90, Academic Press, New York (1980).
3. R.A. Pethrick, Acoustical Properties in "Comprehensive Polymer Science", edited by C. Booth, and C. Price, Vol. 2 : "Polymer Properties", Chap. 17, pp. 571-599, Pergamon, Oxford (1989).
4. L. Piché, *IEEE Ultrasonics Symposium*, 599-608 (1989).
5. L. Piché, "Ultrasonic density of polymers", Can. Pat.: 1,268,536 (1990); US Pat.: 4,754,645 (1988), ASTM standard D.4883.
6. L. Piché, Ultrasonic characterization of polymers under simulated processing conditions, in "Nondestructive Characterization of Materials IV", Ruud C.O. et al. (Eds), pp.151-158, Plenum Press, New York (1991).
7. F. Massines, L. Piché, and C. Lacabanne, *Makromol. Chem., Macromol. Symp.*, 23: 121-137 (1989).
8. J. Tatibouët, and L. Piché, *Polymer*, 32: 3147-3152 (1991).
9. L. Piché, F. Massines, A. Hamel, and C. Néron, "Ultrasonic technique for characterizing polymers under simulated processing conditions", Can. Pat.: 1,264,195 (1990); US Pat.: 4,677,482 (1987).
10. S.G. Hatzikiriakos, and J.M. Dealy, *J. Rheol.*, 35: 497-523 (1991).
11. N. El Kissi, and J.M. Piau, *J. Non-Newtonian Fluid Mech.*, 37: 55-94 (1990).
12. A.V. Ramamurthy, *J. Rheol.*, 30: 337-357 (1986).
13. D. Lévesque, and L. Piché, *J. Acoust. Soc. Am.*, 92: 452-467 (1992).
14. D. Lévesque, A. Legros, A. Michel, and L. Piché, *J. Adh. Sci. Tech.*, (in press May 1993).
15. L. Piché, D. Lévesque, P. Deprez, A. Michel, and J. Tatibouët, *these Proceedings*.
16. **Note:** Due to shear heating, the true local temperature in the melt may be different from that which is measured on the die (T_D). As will be reported elsewhere, accurate determination of true melt temperature involves finite element analysis of the flow problem in order to solve the complete Navier-Stokes equation coupled with the equation for heat transport. Instead of a uniform temperature for the flow (T_D), the results demonstrate a temperature profile.

AN ULTRASONIC TESTING TECHNIQUE FOR MONITORING THE CURE AND MECHANICAL PROPERTIES OF POLYMERIC MATERIALS

E. C. Johnson, J. D. Pollchik and S. L. Zacharius

The Aerospace Corporation, M2/248
P. O. Box 92957
Los Angeles, CA 90009

INTRODUCTION

Large space booster solid rocket motors (SRMs) contain composite propellant materials based on either a hydroxyl terminated polybutadiene (HTPB) or the terpolymer of butadiene, acrylic acid, and acrylonitrile (PBAN) polymer matrix. Mechanical tests have revealed significant batch-to-batch variances and age related changes in the propellant moduli¹ probably due to continued crosslinking of the system. This paper documents a work in progress directed toward testing the feasibility of using ultrasonic measurements of the propellant mechanical properties to monitor the condition and the degree of cure of the propellant. If the ultrasonic shear and longitudinal velocities, c_s and c_L , and the density, ρ , of the propellant are known, the Young's modulus, shear modulus, bulk modulus, and Poisson's ratio, E , μ , K and σ , respectively, can be calculated via the familiar relations,

$$E = \frac{\rho c_L^2(1-2\sigma)(1+\sigma)}{1-\sigma}, \mu = \rho c_s^2, K = \frac{E}{3(1-2\sigma)} \text{ and } \sigma = \frac{c_L^2 - 2c_s^2}{2c_L^2 - 2c_s^2}. \quad (1)$$

Considerable effort under the NASA Solid Propulsion Integrity Program (SPIP) has been directed along a similar vein.² The work presented here is unique in that a simple ultrasonic resonance technique which permits measurement of the acoustic velocities of thin adhesive material specimens is employed. The technique incorporates a slight modification of what was presented in earlier work³ in that Fast Fourier Transforms (FFTs) are used to process the signals. The technique is characterized by a number of advantages. The same specimen and transducer pair are used to determine both the shear and longitudinal response. In addition, a fluid medium is employed to couple sound into the specimen, thereby eliminating many of the problems associated with the bonding of transducers. Preliminary SPIP results suggest that measurements of the propellant shear velocity are important, but difficult to perform, as the propellant material is very attenuative to shear waves. The hope is that use of thin specimens will serve to mitigate this difficulty.

TECHNIQUE

To understand the technique, consider first a thin medium having acoustic impedance, Z_2 , sandwiched between two semi-infinite media of acoustic impedance, Z_1 , as depicted in

Fig. 1. Assuming a continuous plane wave stimulation in one of the semi-infinite media, the coefficient of acoustic power transfer, P_T , across the thin medium can be calculated;

$$P_T = \frac{4Z_2^2Z_1^2}{\left(Z_1^2 + Z_2^2\right)^2 \sin^2\left(\frac{2\pi x_2 f}{c}\right) + 4Z_2^2Z_1^2 \cos^2\left(\frac{2\pi x_2 f}{c}\right)}, \quad (2)$$

where f is the frequency of the plane wave, c is the acoustic velocity (either shear or longitudinal) and x_2 is the thickness of the thin medium (see Ref. 3).

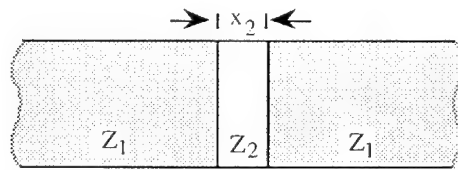


Figure 1. A thin medium of acoustic impedance, Z_2 , and thickness, x_2 , sandwiched between two semi-infinite media of acoustic impedance, Z_1 .

In Fig. 2, P_T is plotted as a function of frequency for the case where $Z_1 = 17$ Rayls (aluminum) and $Z_2 = 1.48$ Rayls (water). It can be seen that the condition of maximum power transmission occurs when $f = f_R = nc/2x_2$, where n is an integer. Note that the thin medium was assumed to be lossless in the derivation of Eqn. 2. Taking attenuation into account, one would expect the amplitude of the local maxima to decrease with increasing n .

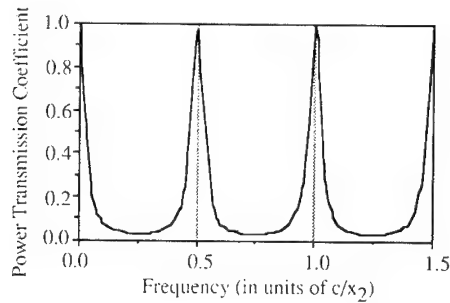


Figure 2. The coefficient of acoustic power transmission across the thin medium as a function of frequency (Eqn. 2) for the three layer system depicted in Fig. 1, where $Z_1 = 17$ Rayls (Al) and $Z_2 = 1.48$ Rayls (water).

The experimental apparatus is depicted in Fig. 3. Two aluminum blocks were cut from square rod stock, each having a 74° and 90° face with respect to one side of the block. A milled finish was determined to be adequate on the 74° faces. The 90° faces were lapped to insure that the surfaces were flat. A thin uniform layer of the specimen being tested was sandwiched between the 90° faces. The spacing between these faces and hence, the specimen thickness, was determined by two identical, stainless steel wire spacers. To hold this Al/specimen/Al sandwich together, a small rubber O-ring was stretched over a set of

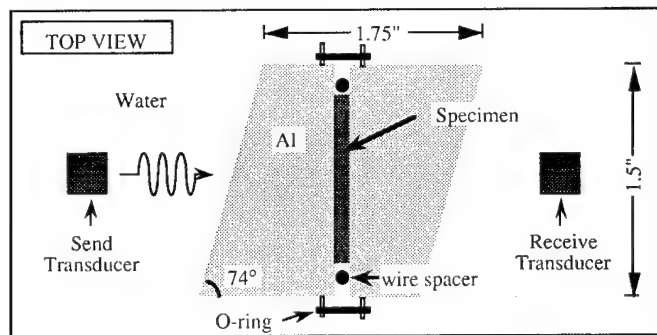


Figure 3. The experimental apparatus as described in the text. As indicated, this is a top view. The Al/specimen/Al sandwich extends 1.5 inches from top to bottom into the page. The transducers and O-ring are bisected by a plane parallel to that of the page and 0.75 inches into the page.

threaded pegs located on each of two opposite sides of the sandwich as shown. The depth of thread for these pegs was less than 0.125 inches. The resultant Al/specimen/Al sandwich was set upon a fixture (not included in Fig. 3 for clarity) and submerged in a water tank so as to be centered between a pair of plane wave, through-transmission, ultrasonic transducers. The fixture was designed to permit rotation of the specimen with respect to the transducers. The apparatus is designed to approximate the conditions leading to the derivation of Eqn. 2. The Al blocks correspond to the semi-infinite media, the specimen to the thin medium.

To perform measurements, the send transducer was stimulated with a spike pulse. The fixture was aligned so that this pulse would strike the first 74° face of the Al/specimen/Al sandwich at a particular angle of incidence, θ_i , to its normal, giving rise to both a longitudinal and a shear wave pulse within the aluminum. The longitudinal and shear wave emergence angles for a particular θ_i can be determined using Snell's law.

In the first phase of the experiment, θ_i was set at $\sim 3.7^\circ$ so that the longitudinal pulse transmitted through the first 74° face would strike the Al-specimen interface at normal incidence, and then travel through the remainder of the Al/specimen/Al sandwich to produce a pulse at the receive transducer. This pulse will be referred to as the longitudinal response. Because the longitudinal velocity in Al exceeds that of the shear, the longitudinal response was the first pulse detected after each drive pulse. This first pulse was followed by others due to the shear wave transmitted through the first 74° face and various internal reflections within the sandwich. Upon reception by the receive transducer, the longitudinal response was isolated and its FFT computed. To isolate the effect of the specimen, this FFT was divided by an FFT of the longitudinal response for a reference block comprised of solid Al and having the same dimensions as the Al/specimen/Al sandwich. The corrected data set was then normalized and stored for analysis. A computer was used to automate the system so that the longitudinal response could be measured repeatedly as a function of a specimen's cure time, t . Peaks in the longitudinal response FFT, which in accordance with Eqn. 2, occur when $f = f_{RL} = nc_L/2x_2$ could then be used to determine c_L , the longitudinal acoustic velocity of the specimen for each measurement.

In the second phase of the experiment, θ_i was set to $\sim 7.5^\circ$ so that the direction of the transmitted shear wave was normal to the Al-specimen interface. The first received pulse resulting from this normal shear wave will be referred to as the shear response. Following each drive pulse, the shear response was preceded by not only the longitudinal response, but also other signals resulting from internal reflections involving the faster longitudinal pulse. To positively identify the shear response, one could increase θ_i beyond the critical angle for longitudinal wave production in the aluminum so that the shear response would be the first remaining pulse. One could then track this signal while decreasing θ_i to the appropriate value. The FFT of the shear response was then computed, normalized and stored in the same manner as that of the longitudinal response. Peaks in the shear response

FFT, occurring when $f = f_{RS} = nc_S/2x_2$, could then be used to determine the shear acoustic velocity of the specimen, c_S .

RESULTS

Three materials were tested: water; EPON 828, a Shell bisphenol-A/epichlorohydrin-based epoxy system, cured with diethylenetriamine (TETA); and an inert HTPB propellant mixture with sodium chloride substituted for the ammonium perchlorate found in live propellant.

Water was tested first to provide an end-to-end system check, as its acoustic velocity is well known. An Al/H₂O/Al sandwich with wire spacers of diameter $x_2 = 6$ mil was prepared. The longitudinal response for the 6 mil water specimen and its FFT are plotted in Figs. 4a and 4b, respectively. The longitudinal response and its FFT for the reference block under the same conditions are plotted in Figs. 4c and 4d. The FFT for the reference block (Fig. 4d) reflects the fact that 5 MHz transducers were used for the measurement. Comparison of Fig. 4a with Fig. 4c (and Fig. 4b with 4d) reveals that the 6 mil water specimen functioned like a bandpass filter for the input pulse. Dividing the reference block FFT (Fig. 4d) into that of the 6 mil water specimen (Fig. 4b) and normalizing the result yielded the plot depicted in Fig. 5. Note that as expected (compare with Fig. 2), multiple, equally-spaced peaks of diminishing amplitude are present. The results for frequencies outside the active range of the transducer, $\sim 2 - 7.5$ MHz (Fig. 4d), however, should be accepted with caution. From the position of the first non-zero maxima one can calculate; $c_L = 2f_{RL}x_2 = 0.056$ in/ μ s which compares favorably with the literature value for water of 0.058 in/ μ s. The slight difference was traced to the fact that the reference block was not cut from the same Al stock as the blocks used for the 6 mil water specimen.

Secondly, tests were performed on the system consisting of a 10:1 mixture of EPON 828 and diethylenetriamine (TETA) hardener. A typical plot of the longitudinal FFT for this system is presented in Fig. 6a. This plot was produced from data acquired following a cure time of $t = 14.5$ min. Three maxima are clearly evident. The third peak is distorted, but it occurs beyond the normal operating range of the 5.0 MHz transducers employed. The thickness of the longitudinal specimen was 10.25 mils. The position of the first maxima

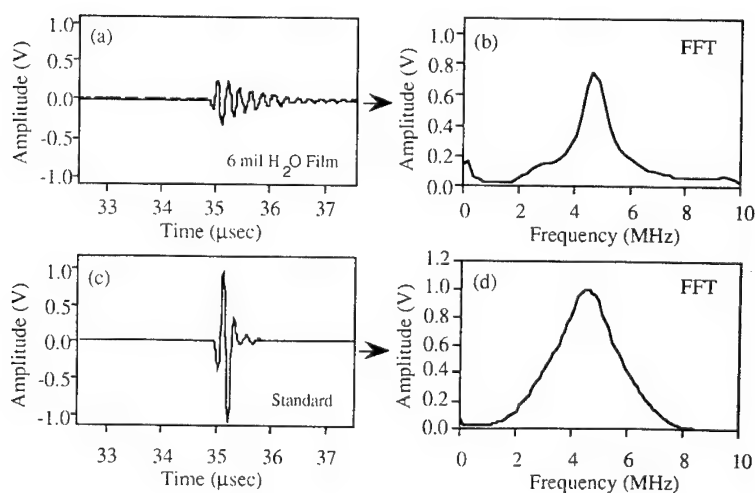


Figure 4. System check: (a) Longitudinal response of the Al/H₂O/Al sandwich. (b) FFT of the Al/H₂O/Al sandwich longitudinal response. (c) Longitudinal response of Al reference block. (d) FFT of the reference block longitudinal response.

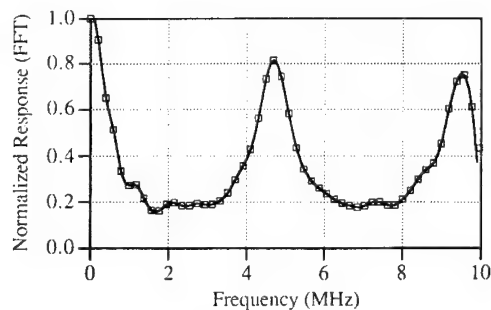


Figure 5. System check: Normalized results from division of the FFTs in Figure 4b and 4d. The first non-zero maxima occurs at 4.69 MHz.

implies that $c_L = 0.062$ in/ μ s. Measurements of the shear response for the EPON 828 system were more difficult. The FFTs obtained varied erratically during the early part of the cure. This is not surprising as liquids do not support shear waves, but at some point a transition must take place. The shear response FFT for $t = 2$ days is plotted in Fig. 6b. A pair of 2.25 MHz transducers were used to accumulate this data. Again, as expected, multiple peaks of diminishing amplitude are observed. The thickness of this specimen was 10.25 mils. The position of the first non-zero maxima implies that $c_S = 0.022$ in/ μ s. More work involving the shear response will be required before consistent trends can be identified.

The value of c_L for the EPON 828/TETA system changed significantly as the specimen cured, so that the peak positions shifted as depicted in Fig 7a, where plots for $t = 6.3$ min. and $t = 96.3$ min are presented. The position of the primary longitudinal peak as a function of cure time is plotted as a solid line in Fig. 7b. It can be observed that the peak position and hence, longitudinal velocity, increased by $\sim 45\%$ during the first 6 hours of cure. The amplitude of the longitudinal FFT peaks also changed as a function of cure as indicated by the curve with open boxes in Fig. 7b. The amplitude change is not evident in Fig. 7a, because the data have been normalized. It can be seen that during the first 1.5 hrs of cure, the amplitude decreased, suggesting that the specimen became more attenuative to sound. The amplitude then rebounded, increasing to slightly above its original value before decreasing abruptly to a value which remained essentially constant for the last hour recorded.

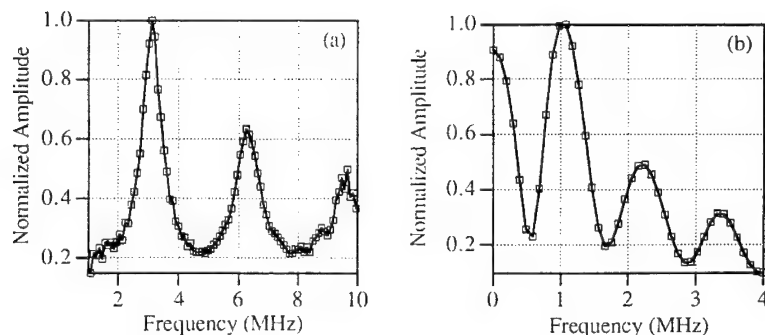


Figure 6. (a) Longitudinal response FFT of EPON 828/TETA mixture at $t = 14.5$ min. (b) Shear response FFT of EPON 828/TETA mixture at $t = 2$ days.

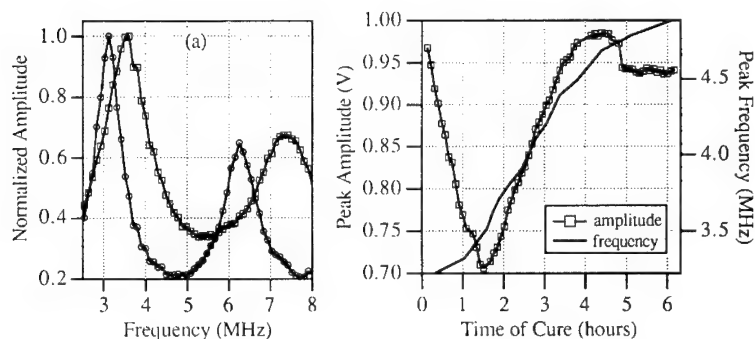


Figure 7. (a) Longitudinal response FFT at $t = 6.3$ min (circles) and $t = 96.3$ min (squares) and (b) the change in amplitude and resonant frequency as a function of t for an EPON 828/TETA specimen.

For comparative purposes, differential scanning calorimetry (DSC) was performed on a number of EPON 828 samples. By measuring the heat of reaction (ΔH) as a function of time beginning with the mix, one can estimate the degree of cure. The ΔH measured for a sample at $t = 0$ corresponds to 0% cure and when $\Delta H = 0$ the system is considered 100% cured. Thus a plot of ΔH versus time provides a correlation between the degree of cure and time which can then be applied to the peak amplitude and frequency versus time data (Fig. 7b). The ΔH measurements were performed on a Mettler DSC 30 with a Mettler TC 10A TA processor. The DSC results for a sample taken from the same mix as that which led to Fig. 7 are plotted in Fig. 8. Each data point in Fig. 8 was measured on a separate sample and represents the residual heat of reaction remaining in the sample at time x . For the EPON 828/TETA system there is a significant amount of heat generated as the two oxirane groups of the EPON 828 react with the amine group of the TETA (an aliphatic polyamine) to produce a three-dimensional, crosslinked network. This reaction occurs at room temperature (RT) and requires several days (at RT) or one to two hours at 100 °C to reach complete cure.

In addition to DSC, a Rheometrics RDA II was employed to measure the epoxy system's viscosity, elastic modulus (G'), viscous modulus (G'') and damping or loss tangent ($\tan \delta = G''/G'$) as a function of time from initial mixing. The RDA measures these viscoelastic parameters in dynamic shear using a parallel plate fixture. The measurements were made at a constant temperature of 27 °C. The RDA II results, which are presented in Fig. 9, give insight into the behavior exhibited by the peak amplitude curve of Fig. 7b. As expected,

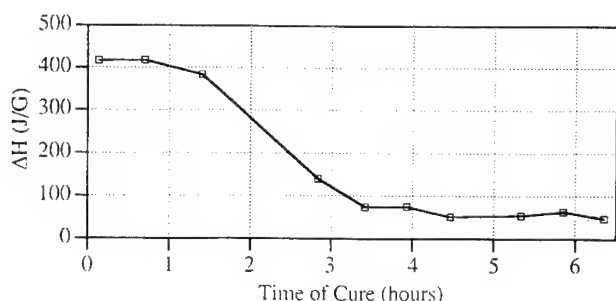


Figure 8. Heat of Reaction (ΔH) versus Time of Cure for the same EPON 828/TETA mixture as that used for the data of Fig. 7.

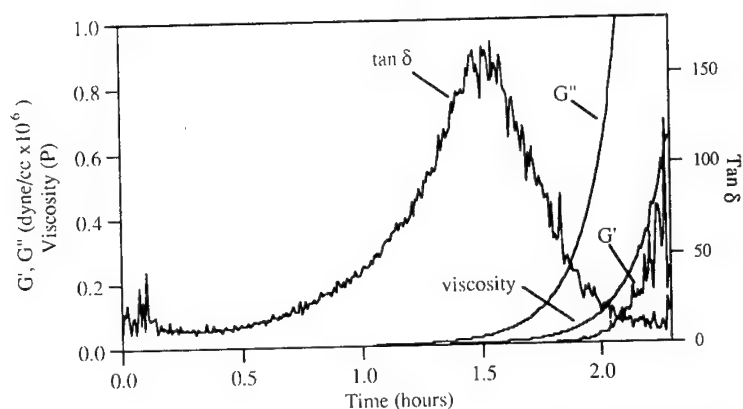


Figure 9. Viscosity, G' , G'' and $\tan \delta$ vs Time for the EPON 828/TETA mixture.

the viscosity increases with time. This is due to the constant increase in molecular weight of the epoxy as crosslinking occurs. Similarly, G' and G'' (the real and imaginary parts of the dynamic shear modulus) increase with time. The G' begins its ascent at approximately the same time that the peak amplitude curve of Fig. 7b exhibits a minimum. The slight difference in time is probably related to fact that the ultrasonic measurements were performed at RT as opposed to 27° C. This same phenomenon is reflected as a maximum in the $\tan \delta$ curve and is most likely associated with the onset of crosslinking for the epoxy. The gel point is traditionally defined as the point at which G' and G'' cross.⁴ The dynamic mechanical testing was terminated at ~ 2.2 hours as the viscosity of the sample exceeded the torque limits of the instrument.

Finally, measurements were performed on HTPB inert propellant specimens. The first difficulty encountered was that it was difficult to compress the material to form samples thinner than 10 mils. The longitudinal response FFT for a 10 mil specimen is plotted in Fig. 10a. Two peaks are clearly visible; the second riding on the tail of the first. The position of the primary peak implies that $c_L = 0.043$ in/ μ s, a value ~ 20% slower than that of water. This value remained essentially constant as a function of cure, perhaps a reflection of the high solid content of the inert propellant. The amplitude of the primary peak did, however, vary significantly with cure time as indicated by the plot depicted in Fig. 10b. The form of the plot is similar to that of the EPON 828/TETA mixture in that the amplitude decreases during the beginning stages of the cure and then rebounds to nearly its initial value. The results differ in that following the rebound, the signal drops monotonically, except for a curious upswing at $t_c \sim 30$ hrs, to a lower value than that achieved in the early stages of the cure. Preliminary attempts to perform a DSC of the inert propellant were unsuccessful. This is attributed to the high filler content. For the purposes of thermal analysis, the filler, which has a high specific heat, absorbs energy and reduces the exotherm temperature. Additionally, because the DSC sample size is small, on the order of 20 mg, the filler has the effect of reducing the amount of material involved in the curing reaction and thus reducing the exotherm. Measurements of the shear response of the inert propellant were less successful than those for the EPON 828/TETA mixture. Again, more work involving the shear response will be required before consistent trends can be identified.

DISCUSSION

The ultrasonic resonance technique described in this work exhibits potential as a means of monitoring the degree of cure as well as cure and age related mechanical property changes

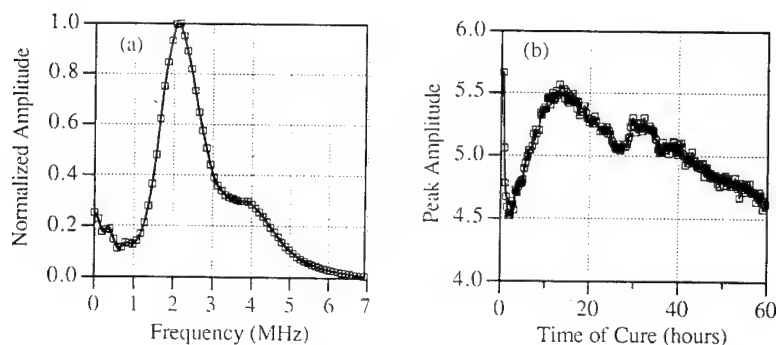


Figure 10. (a) Longitudinal response FFT and (b) the change in amplitude as a function of cure time for a HTPB inert propellant specimen.

in polymers. Preliminary results indicate that the changes in the peak frequency (ultrasonic velocity) data can be correlated with the degree of cure and that the changes in the peak amplitude can be related to the results of dynamic mechanical tests. The results presented in this report suggest that SRM propellants are particularly difficult materials to characterize, especially in the frequency range employed in these tests. Much of the difficulty probably stems from the high solid content of the propellant. It may be prudent to perform similar tests on unfilled HTPB specimens. In addition, future tests (particularly for the shear mode) should be performed at lower frequencies and, perhaps, different temperatures.

ACKNOWLEDGMENTS

The authors gratefully acknowledge the assistance of (1) R. C. Savedra with sample preparation and data acquisition, (2) R. M. Castaneda with the DSC measurements and (3) R. J. Zaldivar with the dynamic mechanical tests.

REFERENCES

1. P. H. Graham, "Analysis of the Variability of HTPB Propellant Mechanical Properties," Annual report for NASA Marshall Space Flight Center under Contract No. NAS8-37802, Report No. 443/1290/36, 12 Dec. 1990.
2. M. Rooney, C. L. Friant, C. V. O'Keefe, and W. M. Ferrell, "Determination of Modulus of HTPB Solid Rocket Propellant using Longitudinal and Shear Ultrasonic Waves," Annual report for NASA Marshall Space Flight Center under Contract No. NAS8-37802, Report No. 443/1291/37, pp. 4.3-55.
3. E. C. Johnson, J. D. Pollchik and J. N. Schurr, "An Ultrasonic Testing Technique for Measurement of the Poisson's Ratio in Tin adhesive Layers," Review of Progress in Quantitative Nondestructive Evaluation (edited by D. O. Thompson and D. E. Chimenti, Plenum Press, New York, 1992), Vol 11B, 1291 - 1298 (1992).
4. C. M. Long, and P. J. Dynes, "Relationships Between Viscoelastic Properties and Gelation in Thermosetting Systems," J. App. Poly. Sci., Vol 27, 569 - 574 (1982).

ELASTICITY OF SINGLE-CRYSTAL Al_2O_3 (SAPHIKON) FIBER TO 1000°C BY BRILLOUIN SPECTROSCOPY

Murli H. Manghnani,¹ Vahid Askarpour,¹ and James A. DiCarlo²

¹School of Ocean and Earth Science and Technology,
University of Hawaii, Honolulu, Hawaii 96822

²NASA Lewis Research Center, Cleveland, Ohio 44135

INTRODUCTION

Continuous fiber-reinforced metal and ceramic matrix composites have received wide applications in industry, engineering and medicine^{1,2}. The mechanical and thermal performance of ceramic matrices in monolithic forms are enhanced by the addition of reinforcing fiber. The choice of the fiber material is very important in the deformation behavior of the composite particularly at high temperatures. In this study, we have characterized the elastic properties of single-crystal Al_2O_3 fibers (160 μm diameter) at elevated temperatures using the technique of Brillouin spectroscopy. Al_2O_3 fibers are employed to demonstrate the feasibility of such experiments on small diameter fibers where other methods to measure fiber elastic properties may not be conveniently available or larger specimen may not be readily accessible.

Single-crystal elastic properties of Al_2O_3 have been previously reported by both Brillouin spectroscopy³ to 1800°C and ultrasonic interferometry⁴ to 1500°C . However, no elasticity data for this material in fiber form and at high temperatures are available. Brillouin spectroscopy is perhaps, the only available technique at present for small sample elastic characterization at elevated temperatures.

THEORY

Brillouin scattering is the inelastic scattering of light by fluctuations in the optical dielectric constant of the scattering medium due to the propagation of thermally excited sound waves⁵. In solids, there are three acoustic bulk waves propagating in an arbitrary direction, one longitudinal (L) and two transverse (T_1 and T_2) acoustic modes.

When light interacts with the acoustic waves, the frequency of the incident light

is Doppler shifted. The frequency shift $\Delta\nu$ in the incident light is related to the sound velocity, V , and q (the magnitude of the phonon wavevector \mathbf{q} as defined by the scattering geometry) by $\Delta\nu = Vq$. In this study, platelet geometry (see Figure 1) was employed to study the elastic properties of Al_2O_3 fibers.

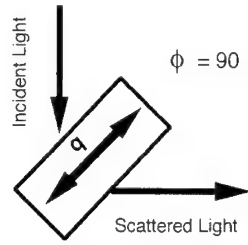


Figure 1. q is the phonon wavevector and represents the direction of acoustic wave propagation.

In platelet geometry, the acoustic velocity is given by:

$$V = \Delta\nu \cdot \lambda_o / \sqrt{2} \quad (1)$$

where, λ_o is the wavelength of the incident laser (514.5 nm in this study). The elastic constants are calculated from:

$$C_{ij} = \rho \cdot V^2 \quad (2)$$

where ρ is the density and C_{ij} are appropriate combinations of elastic constants. The elastic constants are summarized in Table 1.

Table 1. The elastic constants of hexagonal symmetry.

q	Longitudinal	Transverse
[100]	C_{11}	C_{44}
[001]	C_{33}	C_{44}
[011]	C_{13}^1	C_{12}^2
$^1 \{C_{11} + C_{33} + 2C_{44} - [(C_{11} - C_{33})^2 + 4(C_{13} + C_{44})^2]^{1/2}\} / 4$		
$^2 (2C_{44} + C_{11} - C_{12}) / 4$		

EXPERIMENTAL METHOD

Details of the experimental set up can be found elsewhere^{6,7}. Briefly, an argon laser beam was incident on the sample in the platelet geometry. The scattered light was analyzed by a high-contrast high-resolution Brillouin spectrometer consisting of a 6-pass tandem Fabry-Pérot interferometer, designed by J. R. Sandercock, and photon

counting units. The spectra were stored in a 1024 channels of a multichannel analyzer. Further analysis of the spectra were performed by a curve-fitting routine to calculate the frequency shifts. Due to the uncertainties in the frequency shift measurements (better than 0.5%) and the scattering angle ($\sim 0.5\%$), the estimated error in the calculated acoustic velocities were $\sim 1\%$. The fibers were heated in a resistive heating furnace to temperatures of up to 1400 K (with an uncertainty of ± 2 K).

The Al_2O_3 single-crystal (Saphikon) fibers of $\sim 160\text{ }\mu\text{m}$ diameter were coated with a thin platinum coating and embedded in a Al_2O_3 ceramic matrix with the fibers aligned in one direction. Typically the orientation of the c -axis deviated from the fiber axis $\pm 3^\circ$. Figure 2a shows a cross section of a fiber reinforced ceramic composite. Two samples for the present work were prepared. The first sample (A) was polished normal to the fiber length in the form of a $100\text{ }\mu\text{m}$ thick disc as shown in Figure 2b. The $[100]$ axis was not known in this case and hence an estimate of C_{11} was obtained. The second sample (B) was polished with two faces parallel to the fiber length as shown in Figure 2c. This second sample allowed C_{33} and C_{44} to be determined.

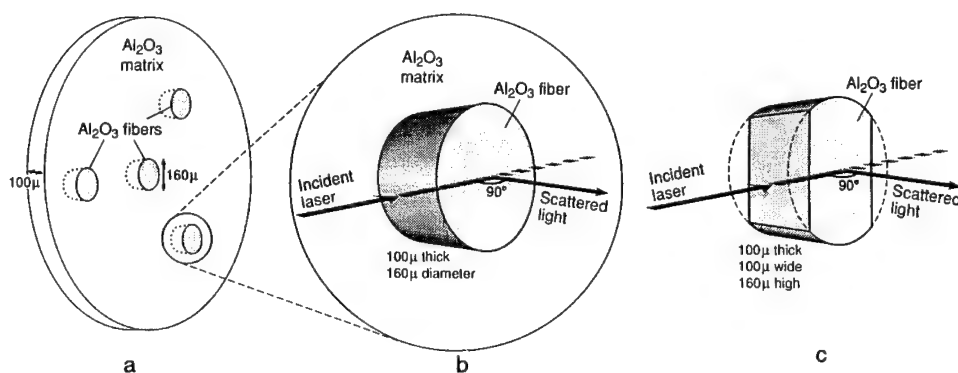


Figure 2. Al_2O_3 fibers in a ceramic matrix composite (2a). Sample (A) was polished normal to $[001]$ axis (2b). Sample (B) was polished parallel to the fiber length (2c).

RESULTS

A typical Brillouin spectrum of the Al_2O_3 fiber is shown in Figure 3. The intense feature at the center of the spectrum is the elastic scattering from the fiber. A pair (upshifted and downshifted in frequency due to Doppler effect) of longitudinal (L) and two pairs of transverse components (T_1 and T_2) were observed. It is noted that the longitudinal peak has a doublet structure, indicating the presence of two crystals of slightly different orientations each contributing separately to the scattering process (i.e., the fiber is not completely single crystal).

Sample (A) was then mounted in the high-temperature furnace in platelet geometry (orientation of the a -axis is arbitrary). The Brillouin spectra of the fiber were recorded to 1000°C in intervals of 100°C . Brillouin spectra were also recorded for sample (B) to 900°C . From the measured velocities in $[100]$ and $[001]$, three elastic constants

C_{11} , C_{33} and C_{44} were determined (2 to 3% error). The temperature dependence of the density for Al_2O_3 needed for this calculation was obtained from Goto et al. (1989)⁴.

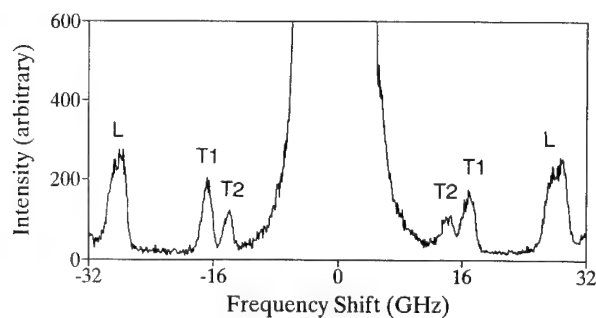


Figure 3. Brillouin spectrum of Al_2O_3 fiber. L and T's represent the longitudinal and transverse components of the spectrum, respectively.

The temperature dependences of the C_{11} , C_{33} and C_{44} are shown in Figure 4. The ultrasonic data⁴ on large crystals are also shown by open squares. Since our fibers were not entirely single crystalline, we have plotted the elastic constants corresponding to all the observed peaks. It is noted that there is about 10% difference in the C_{11} values determined from the longitudinal doublet in Figure 2.

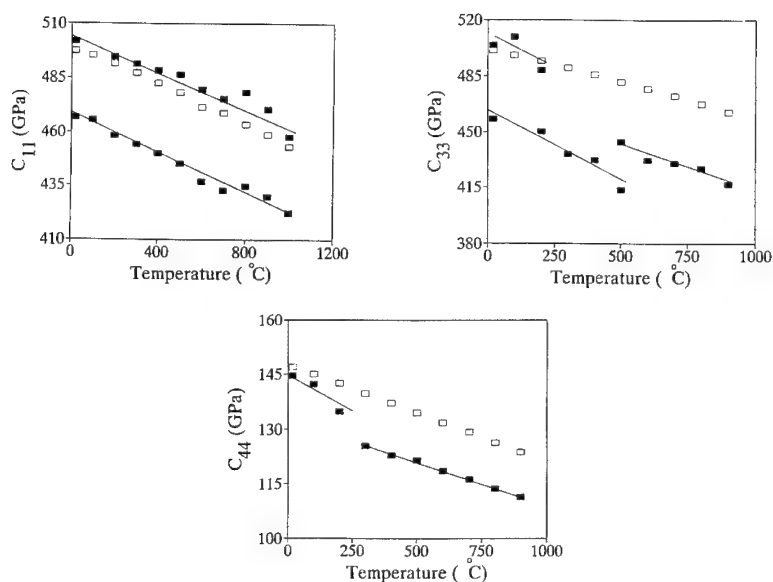


Figure 4. Temperature dependence of the three elastic moduli determined in this study.

DISCUSSION

It is noted from Figure 4 that there is good agreement (within 2-3% error) between our values of the elastic moduli and those determined by ultrasonic technique for appropriate fiber orientation. Crystal orientation and lack of perfect single-crystallinity along the fiber length are causing some discrepancies in the elastic moduli. For example, due to nonhomogeneity of the fiber, there is up to 10% difference in the elastic properties of the constituent microcrystals of the fibers in reinforced ceramic composites (see Figure 4) parallel and perpendicular to the fiber axis in the temperature range of this study. Such variations in the elastic properties are important factors in predicting their high-temperature performance.

SUMMARY

In this study, we have demonstrated the feasibility of carrying out Brillouin scattering measurements on Al_2O_3 single-crystal fibers (Saphikon) as a function of temperature to 1000°C. The results are in good agreement with previous resonance and Brillouin scattering measurements on large crystals.

The observed discrepancies as well as the variations in the C_{ij} values as a function of temperature are attributed to the departure of the fiber axis from true c -axis ($\pm 3^\circ$) and due to the fiber not being truly single-crystalline along the fiber length.

Brillouin scattering is the only available experimental method for investigating the elastic properties of fibers at high temperatures.

ACKNOWLEDGEMENT

The support for the facilities was provided by the W. M. Keck Foundation and the National Science Foundation (Grant 8720404). We are grateful to J. Balogh and O. Matthews for technical assistance and T. Bier for polishing the fiber samples. The composite samples were obtained from M. Jaskowiak at NASA Lewis Research Center. This is School of Ocean and Earth Science and Technology Contribution no. 3240.

REFERENCES

1. J. Doychak, Metals and intermetallic matrix composites for aerospace propulsion and power systems, *JOM* 44:46 (1992).
2. M.A. Karnitz, D.F. Craig, and S.L. Richlen, Continuous fiber ceramic composite program, *Ceram. Bull.* 70:430 (1991).
3. E.S. Zouboulis and M. Grimsditch, Refractive index and elastic properties of single-crystal corundum ($\alpha\text{-Al}_2\text{O}_3$) up to 2100 K, *J. Appl. Phys.* 70:772 (1991).
4. T. Goto and O.L. Anderson, Elastic constants of corundum up to 1825 K, *J. Geophys. Res.* 94:7588 (1989).

5. G.B. Benedek and K. Fritsch, Brillouin scattering in cubic crystals, *Phys. Rev.* 149:647 (1966).
6. V. Askarpour, M.H. Manghnani, S. Fassbender, and A. Yoneda, Elasticity of single-crystal MgAl_2O_4 spinel up to 1273 K by Brillouin spectroscopy, *Phys. Chem. Miner.* 19:511 (1993).
7. J-A. Xu and M.H. Manghnani, Brillouin scattering studies of a sodium silicate glass in solid and melt conditions at temperatures of up to 1000°C, *Phys. Rev. B* 45:640 (1992).

CHARACTERIZATION OF SHEET STEELS IN THE DEVELOPMENT OF ON-LINE SENSORS FOR QUALITY CONTROL MONITORING OF MECHANICAL PROPERTIES

L.J. Swartzendruber¹, Y. Rosenthal², and G.E. Hicho¹

¹National Institute of Standards and Technology
Gaithersburg, MD 20899

²Nuclear Research Center - Negev, P.O. Box 9001
Beer Sheva 84190, Israel

ABSTRACT

Magnetic and mechanical measurements of rolled sheet steel were performed as a part of a study on the feasibility of using magnetic measurements to supplement and improve the determination of sheet steel properties. Three low carbon steel sheets, having different mechanical properties, were selected and their microstructure, hardness, and grain size characterized. Each sheet was tested using tensile specimens cut from locations parallel, perpendicular, and 45° to the rolling direction in order to determine the extent of scatter in mechanical properties within each sheet. Additional specimens cut from these sheets adjacent to the tensile specimens were used for magnetic measurements. The results showed very low scatter (less than 10%) in the traditional mechanical properties as well as in the strain hardening parameters and in the plastic strain ratios within each sheet. Some correlations between the various mechanical parameters and between the magnetic and mechanical properties are shown.

INTRODUCTION

Both the mechanical and the magnetic properties of a material such as ferritic sheet steel depend sensitively on the microstructure. Thus magnetic properties may provide a probe for the nondestructive characterization of mechanical properties (see, for example, references 1-6). The magnetic properties which are sensitive to structure include initial permeability, maximum permeability, coercive force, remanance, and the Barkhausen effect. Some of these properties, such as coercive force and Barkhausen signal, may lend themselves to rapid on-line measurement as the steel is being processed.

In order to be useful, statistically valid correlations must be established between mechanical and magnetic properties that apply to specific types of steel. Establishing such correlations requires sets of well characterized samples that span a range of mechanical properties. Sets of sheet steel samples were obtained from a steel mill. Three sheets each from three different steels were obtained. The objective here is to determine the extent of mechanical property variation for samples within and between the sheets, and then to determine the same for the magnetic properties. Ultimately, it is desired that reproducible correlations between a mechanical property, or several mechanical properties, and selected magnetic properties be obtained. To achieve this goal, mechanical properties were determined for specimens that were parallel and perpendicular

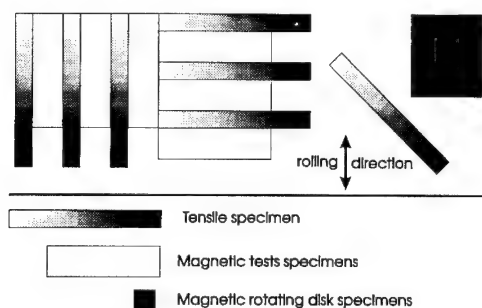


Figure 1. Schematic of relative locations of specimens taken. Three sets were taken from each sheet.

to the rolling direction, and 45° to this direction. Standard ASTM test methods were used to evaluate the mechanical properties of the three different steels. Additional specimens, adjacent to those used for the mechanical property measurements, were sectioned from the sheets and used for the magnetic property measurements. Chemical analysis, hardness, and microstructure evaluation were also performed on each sheet.

EXPERIMENTAL PROCEDURE

Materials

In order to be able to determine any mechanical parameters correlation with magnetic properties it was necessary to characterize the scatter in mechanical properties across a given steel sheet. Three different low-carbon steel sheets were used for this purpose: Cold rolled, interstitial free, Ti stabilized, coded as IF-18 (0.89 m x 0.91 m, 0.83 mm thick); cold rolled, interstitial free, coded as U-4 (0.84 m x 0.66 m, 1.12 mm thick); and cold rolled, electrogalvanized, coded as EI-2 (0.89 m x 0.91 m, 0.93 mm thick). These steels were chosen primarily because their yield strengths were uniquely different. The chemical composition of each steel is shown in Table 1.

TABLE 1. The chemical composition (in w/o) of the steel tested.

	C	Mn	P	S	Si	Al	N	Nb	Ti
IF18	0.004	0.17	—	0.007	—	0.048	0.0099	<0.002	0.72
U-4	0.0016	0.36	0.016	0.0088	0.007	0.077	0.0044	<0.002	0.002
E-I2	0.057	0.17	—	0.018	—	<0.004	0.0024	—	—

Mechanical Test Program

Twenty 50 mm gage standard ASTM flat tensile specimens were machined, eighteen magnetic testing specimens (50 mm x 150 mm), and three specimens for rotating disc magnetic measurements (150 mm x 150 mm) were cut from each sheet. In addition, specimens used for standard chemical analysis and microstructure evaluation were cut from each sheet. The location of the various specimens is shown in Fig. 1. It is emphasized that two tensile specimens were cut 45° to the rolling direction and the others were cut both parallel and transverse to the rolling direction.

Tensile testing was conducted using a universal mechanical testing machine. A fast personal computer and high-level data acquisition software were used to upgrade the existing mechanical testing system. The upgrading enables us to get a fully detailed set of mechanical parameters for any specimen immediately after each test. A loading rate of 2 mm min⁻¹ was used for all the tensile tests.

The data acquisition procedure and analysis consists of four major steps: (1) The test itself during which instantaneous load and displacement (measured using an extensometer attached to the tensile specimen)

data points are acquired at any desired rate and then saved in an ASCII stress-strain data file; (2) Determination of the mechanical elastic parameters (Young's modulus, proportional limit) using linear regression with a different graphics computer program having curve fitting capabilities; (3) Determination of the engineering elastic/plastic and the plastic deformation parameters (0.2% yield stress, ultimate tensile stress, uniform elongation, and elongation at fracture) and, the plotting of engineering stress-strain curve; and (4) Evaluation of the true stress-strain curve and determination of the strain hardening exponent and the strength coefficient as well as the plastic strain ratio.

Calibration of the testing machine's load cell and the extensometer used were conducted prior to the mechanical testing. The load was calibrated using a proving ring (traceable to NIST calibration apparatus) in accordance with section 6 of ASTM Method E74. The load average deviation was 0.2% in the range used for the mechanical testing.

The following equations were used for the evaluation of mechanical parameters:

Determination of Young's Modulus

Equation 1 below was used for linear regression fit to the first part of the stress-strain curve for the determination of the elastic modulus:

$$S = Ee \quad (1)$$

where E is Young's Modulus, S is the engineering stress (equal to P/A_0 , where P is the applied load and A_0 is the initial cross sectional area), e is the engineering strain (equal to $\Delta l / l_0$, where Δl is the displacement increment, and l_0 is the initial gage length).

Determination of strain hardening parameters

The empirical Hollomon equation (Equation 2) was used for the evaluation of strain hardening parameters:

$$\sigma = K\epsilon^n \quad (2)$$

where σ is the true stress (equal to $S(1 + e)$), K is the strength coefficient, i.e. the Y intercept, ϵ the true strain (equal to $\ln(1 + e)$), and n is the strain hardening exponent. The value of n was calculated using linear regression fit for the $\ln \sigma$ vs. $\ln \epsilon$ curve. This fit can be applied only to a certain range of the stress/strain curve starting from small plastic strains (that is beyond the yield point, and then any discontinuous yielding, where applicable) and ending at the ultimate tensile stress.

Determination of plastic strain ratio

The plastic strain ratio (according to ASTM Method E517) is considered a measure of sheet metal drawability and is obtained using Equation 3:

$$r = \frac{\ln(w_0 l_0)}{\ln\left(\frac{l_f w_f}{l_0 w_0}\right)} \quad (3)$$

where r is the plastic strain ratio, w_0 is the initial width of the tensile specimen, w_f is the width of the specimen as measured just before the maximum load, l_0 is the initial gage length (also the extensometer gage length), and l_f is the gage length as measured before the maximum load is reached.

The average plastic strain ratio r_m is calculated as follows:

$$r_m = \frac{r_0 + 2r_{45} + r_{90}}{4} \quad (4)$$

where r_0 is the plastic strain ratio parallel to the rolling direction, r_{45} is the plastic strain ratio 45° to the rolling direction, and r_{90} is the plastic strain ratio perpendicular to the rolling direction.

Determination of Magnetic Properties

The Barkhausen signal and hysteresis loops were obtained on representative samples using the apparatus illustrated in Fig. 2. The Barkhausen signal coil is a surface probe fabricated from a ferrite core. Its output is bandwidth limited to a range of 1 to 100 kHz. The pickup coil is a 300 turn encircling coil. A Hall probe is used to measure H , the tangential field at the surface of the sample. As the energizing yoke sweeps the sample through a hysteresis loop, the signal from the Hall probe, the pickup coil, and the signal coil are digitized and stored in computer memory. The output of the pickup coil is integrated to obtain the magnetic induction, B , as a function of the tangential field. The algorithms used to analyze the Barkhausen signal is discussed in detail in reference 6. Two types of curves will be shown here, the integrated Barkhausen intensity, and the Barkhausen signal emission rate, which is the derivative of the integrated signal after some smoothing has been performed.

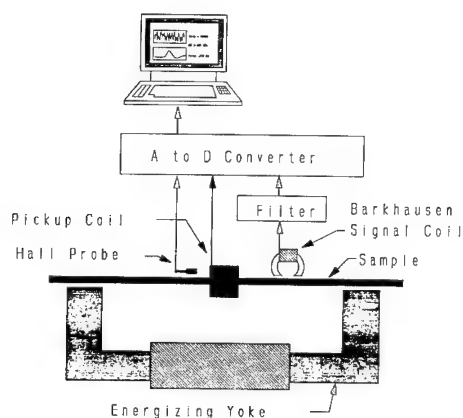


Figure 2. Schematic drawing of the magnetic property measurement system.

RESULTS AND DISCUSSION

Microstructure

The microstructures of three different sheet steels were examined, and Figures 3, 4, and 5 show the general microstructure over the full thickness, and at the quarter-thickness location. Figure 3, the cold rolled, interstitial free and titanium stabilized steel identified as IF-18, consists primarily of fine grained ferrite. The absence of any pearlite is noted, Figure 3a, but this is due to the rather low carbon content of 0.004 weight percent. Figure 4 shows the microstructure of the other cold rolled, interstitial free steel U-4, which was not titanium stabilized. The steel consists of uniform ferrite grains throughout the thickness, Figure 4a. The absence of any significant amount of pearlite is again noted. Interstitial free steels are melted in a way that

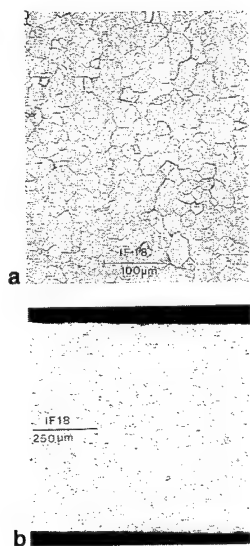


Figure 3. IF-18 microstructure: (a) 1/4 thickness, (b) entire thickness.

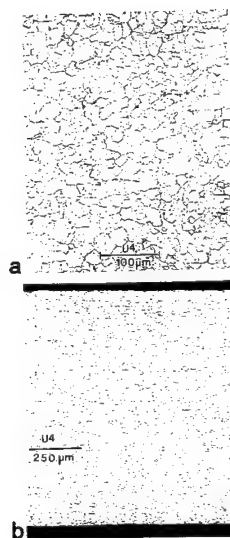


Figure 4. U-4 microstructure: (a) 1/4-thickness, (b) entire thickness.

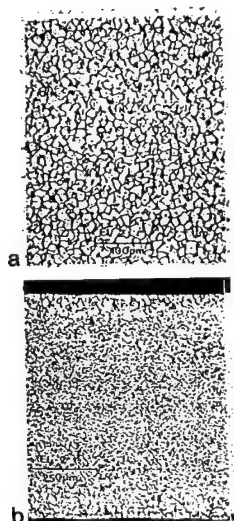


Figure 5. EI-2 microstructure : (a) 1/4 thickness (b) entire thickness.

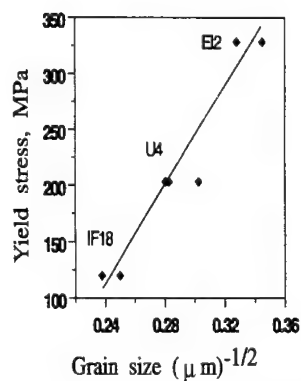


Figure 6. Yield stress vs. grain size relation as obtained for the sheets tested.

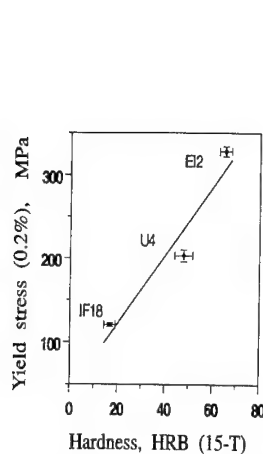


Figure 7. Linear fit of yield stress vs. hardness.

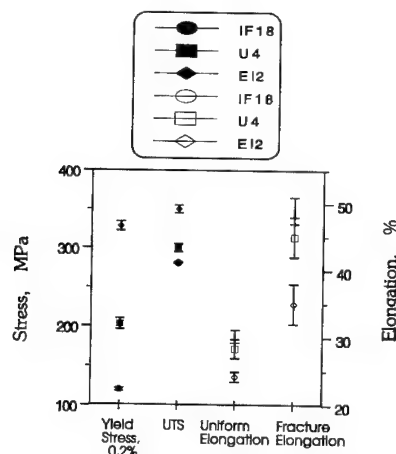


Figure 8. A summary of the differences in mechanical properties among the steels tested.

the levels of the interstitial free elements, carbon and nitrogen, are reduced to small amounts. The steel is normally deoxidized with aluminum and the residual aluminum in the melt ties up the nitrogen by forming nitrides. The residual carbon and nitrogen are removed by the addition of titanium, niobium, or zirconium to the melt. These elements, reportedly form stable carbides and nitrides that remove the interstitials from solid solution and therefore remove the yield point elongation, characteristic of interstitial carbon and nitrogen steels. The third steel examined in this study was a cold rolled, electrogalvanized steel that contained 0.057 weight percent carbon. Figure 5 shows the through thickness microstructure for this sheet that was coded EI-2. The figure shows that the microstructure near the surfaces was devoid of carbon and this was probably due to the galvanizing procedure on the sheet. The galvanizing temperature was such that it removed the carbon from the outside surfaces, essentially decarburizing these sheets. The microstructure of EI-2, Figure 5a, was also primarily ferrite with packets of pearlite dispersed throughout the ferrite and located along the grain boundaries.

The grain sizes of the steel sheets are shown in Table 2. A relation was obtained for the yield stress vs. grain size (Figure 6). The yield stress vs. hardness is plotted in Figure 7. Because of the sheets thickness hardness values were converted from the Rockwell 15 kg. 15-T scale to Rockwell scale B (HRB).

Mechanical Properties

The mechanical properties of the steel sheets are summarized in Table 3 and in Figures 8 (yield stress 0.2%, UTS, uniform elongation, and the total elongation at fracture) and 9 (strain hardening exponent and the strength coefficient). It can be seen that the steels differ in their properties, but the variations in the individual mechanical parameters within each sheet are very small. For example, standard deviations of 1.7%, 3.5%, and 1.8% were obtained for the yield stress values of IF-18, U-4, and EI-2 respectively. The standard deviations were 0.4%, 1.7%, and 1.4% as obtained for the ultimate tensile stress values of these steels. Considering the number of tensile specimens used, these standard deviations are very low suggesting that the sheets have uniform mechanical properties. Furthermore, the 20%-40% average differences in the yield stress and the UTS values (beyond the scatter within each sheet) among the sheets also suggest that they can be used in the search for any possible correlation with magnetic properties as the minimum desired sensitivity of the sensor developed was determined by its ability to reveal 10% changes in mechanical properties.

The plot of the yield stress vs. plastic strain ratio is shown in Figure 10. Because of the correlation between the magnetic characteristics of the steels and the yield stress, to be shown below, the plastic strain ratio, which is used as a measure of sheet metal drawability, can be related to the magnetic characteristics through its linear relation to the yield stress.

TABLE 2. Grain sizes in different locations within the sheets.

* Coarse surface grains, 100-150 μm in depth.

** Grains uniform through thickness.

*** Finer grains near surface, 50 μm in depth.

Sheet	Position	Grain Size, μm	ASTM #
EI-2	1/4 Thickness	8.4	10.5
	Parallel	14.1	9.0 *
	Perpendicular	9.3	10.2
U-4	1/4 Thickness	12.5	9.3
	Parallel	10.9	9.7
	Perpendicular	12.7	9.3 **
IF-18	1/4 Thickness	17.7	8.3
	Parallel	16.0	8.6
	Perpendicular	16.0	8.6
	Parallel	13.5	9.1 ***
	Parallel	12.8	9.3 ***

TABLE 3. Average mechanical properties in tension for the steel sheets tested.

* U.T.S. Uniform Strain

** Fracture Strain, Total in 50 mm

Property	EI-2	U-4	IF-18
Young's Modulus, GPa	234	228	195
(standard deviation)	38	14	11
Yield Stress 0.2%, GPa	331	203	120
(standard deviation)	4	7	2
U.T.S., MPa	351	300	281
(standard deviation)	6	5	1
U.T.S.* , %	23.9	28.3	30.2
(standard deviation)	0.8	1.4	0.9
Fracture Strain **, %	36	45	49
(standard deviation)	3	3	2
n	0.18	0.21	0.26
(standard deviation)	0.003	0.007	0.003
K, MPa	580	519	518
(standard deviation)	7	8	3
r	0.61	0.86	1.06
(standard deviation)	0.05	0.31	0.11

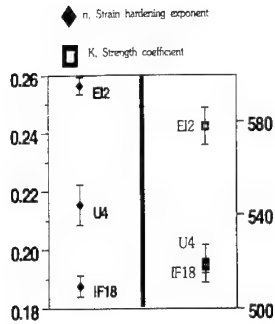


Figure 9. The average strain hardening results and their standard deviations for the steel tested.

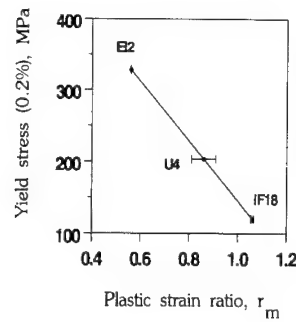


Figure 10. The yield stress vs. plastic strain ratio with a fitted linear regression line.

Yield stress related equations

Three linear equations were fitted to some of the parameters checked suggesting a correlation with the yield stress of the steels tested. The first correlation was found between the yield stress and the grain size, Figure 6, as follows:

$$S_y = 2157.7 (d)^{-1/2} - 411 \quad (5)$$

Where S_y is the yield stress in MPa, and d is the grain size in μm .

A second linear correlation found between the yield stress and the hardness of the steels (Figure 7):

$$S_y = 4.1 (HRB) + 39.5 \quad (6)$$

where HRB is the hardness on the Rockwell B scale.

The third linear relation is between the yield stress and the plastic strain ratio, r_m (Figure 10):

$$S_y = -416 r_m + 561 \quad (7)$$

All these three parameters (d , HRB, and r_m) might be useful, along with the actual values obtained for the traditional mechanical parameters, to evaluate quality control sensors of potential use in the rolling mill. The goal is to develop sensors which can rapidly evaluate when the process is out of control and enable rapid correction of the problem, thereby reducing scrap and enabling the production of a more uniform product.

Magnetic Measurements

The hysteresis loops obtained on the three different sheets, taken with the tangential field, H , parallel to the rolling direction, are shown in Figures 11, 12, and 13. Also plotted on these curves are the incremental permeabilities (the slope of the B vs H curve, dB/dH , in dimensionless units) and a small central loop taken at low applied field. The slope of the small loop gives a good estimation of the initial permeability. (An eddy current type measurement would be most affected by the initial permeability value). The field at which the value of B on the full hysteresis curve passes through zero is the coercive force (H_c) of the

material. The coercive force and the width of the dB/dH curve will be affected by the presence of domain wall pinning centers, grain orientation, residual stresses, and the uniformity of these properties on a microscopic scale. The U-4 sample, which is from the material with the lowest carbon content, has a dB/dH curve with a very small width.

In the dB/dH curve for EI-2 (Figure 13) two nearly resolved peaks are evident. We attribute the peak occurring at a lower tangential field (i.e. the field closest to zero) to the surface of the sample, and the larger peak at a higher tangential field to the bulk of the material. This interpretation is consistent with the metallographic examination (see Figure 5) which shows a larger grain size and lower carbon content on the surface, resulting in a lower coercive force for the material at the surface.

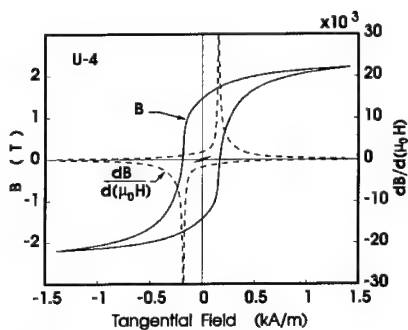


Figure 11. U-4 hysteresis curve, incremental permeability (peaked curve), and small minor loop.

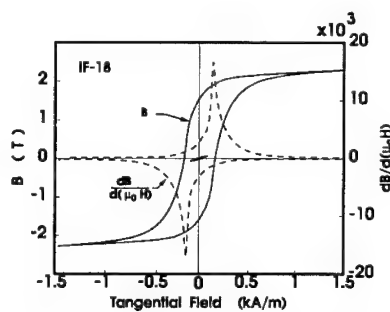


Figure 12. IF-18 hysteresis loop, incremental permeability (peaked curve), and small minor loop.

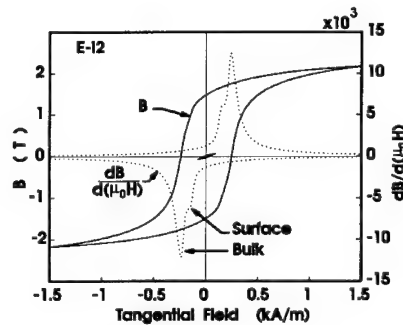


Figure 13. EI-2 hysteresis loop, incremental permeability (peaked curve), and small minor loop.

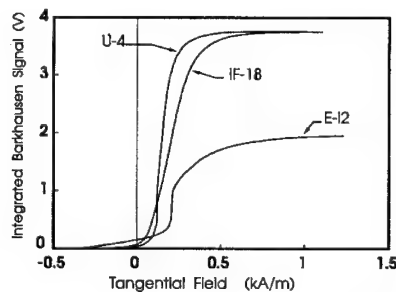


Figure 14. Integrated Barkhausen signals vs. applied tangential field for the three samples.

The integrated Barkhausen signal from the three samples is shown in Figure 14. Note that the signal from sample U-4 rises more sharply than from IF-18 or EI-2, consistent with the sharper incremental susceptibility seen for U-4 in the hysteresis loop curves. The total integrated intensity for EI-2 is much lower than for U-4 or IF-18. This is because the higher carbon - higher strength EI-2 contains a higher density of higher strength domain wall pinning centers. This configuration results in a large number of low intensity Barkhausen jumps which fall below the noise level of the signal coil and hence are not included in the total integrated signal.

The Barkhausen signal emission rates are plotted in Figure 15. The emission rate is the derivative of the filtered integrated Barkhausen signal. The filtering is performed by averaging over approximately 1 A/m to remove the fluctuations inherent in the Barkhausen jumps. For sample EI-2 the contributions from the surface and bulk contributions, which were clearly apparent in the incremental permeability curves of Figure 13, can be seen. In the Barkhausen signal, the contribution from the surface is enhanced because this measurement is more sensitive to the surface. Small additional peaks for U-4 and IF-18 are also evident and these also may be due to a surface layer which has different magnetic (and mechanical) properties than the bulk of the material. For U-4 and IF-18 these surface layers make a much smaller contribution and are not clearly evident in the micrographs.

The magnetic measurements made thus far show some interesting qualitative features. Quantitatively, the best correlation between magnetic and mechanical properties seen in these results is between the coercive force and the yield stress. This is displayed in Figure 16. In the same Figure it can be seen that any correlation between initial susceptibility and yield stress is poor. From Figure 14 it can be seen that the total Barkhausen signal clearly distinguishes the higher strength 0.06 w/o C steel EI-2 from the very low carbon U-4 and IF-18 samples. The total Barkhausen signal does not distinguish between the different strengths of the latter two steels. The higher strength of the U-4 sample is due to its finer and more uniform grain size. This finer, more uniform, structure is clearly reflected in both the Barkhausen signal and the hysteresis curves which give smaller widths and higher peaks for the U-4 sample.

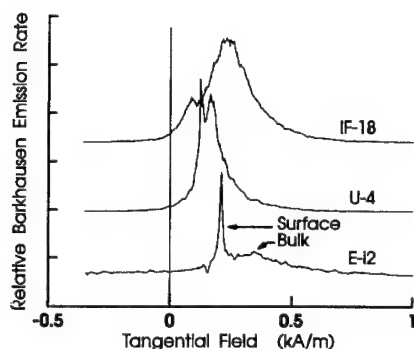


Figure 15. Barkhausen signal emission rates (relative units) vs tangential field. (Curves displaced for clarity).

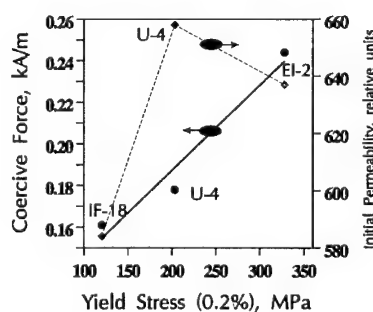


Figure 16. Coercive force and initial permeability vs. yield stress for the three samples.

CONCLUSIONS

(1) Three different low-carbon steel sheets were selected as the source materials for testing specimens in the evaluation of possible correlation between mechanical and magnetic properties.

(2) Mechanical properties and microstructures of the steels were characterized using a large number of specimens for each sheet. The amount of scatter in the parameters checked was found to be very small within each sheet.

(3) The steels differ from each other in their properties, much beyond the scatter within each steel, and as such can be used to obtain the magnetic response for different strength level materials.

(4) Best-fit methods were used in order to obtain the linear Correlations between the yield stress of the steels and other metallurgical parameters such as grain size, hardness, and the plastic strain ratio. Any correlation found between the yield stress and the magnetic properties can be used also as a measure of these other metallurgical parameters which have great importance during the production of steel sheets.

(5) The magnetic and mechanical properties are found to be clearly correlated but not in a simple way. The best magnetic indicator for this set of steels was found to be the coercive force. To obtain practical correlations it will be necessary to determine more than a single property.

ACKNOWLEDGMENTS

The authors would like to acknowledge Mr. Leonard C. Smith for metallographic assistance, Mr. Denzil Mathews for technical assistance, and Drs. R. Fields and R. DeWit for helpful discussions. We would also like to recognize the support of Dr. H. Thomas Yolken, Chief of the Intelligent Processing of Materials Division.

REFERENCES

- [1] R. Ranjan, D.C. Jiles, O. Buck, and R.B. Thompson, *J. Appl. Phys.* **61**, 3199 (1987).
- [2] K. Tiito, *Nondestr. Test. Eval.* **5**, No. 1, 27-37 (1989).
- [3] G.L. Burkhardt and H. Kwun, Review of Progress in Quantitative NDE **8**, D.O. Thompson and D.E. Chimenti, eds., Plenum Press, New York, (1989), p. 2043.
- [4] D.C. Jiles, Review of Progress in Quantitative NDE **9**, D.O. Thompson and D.E. Chimenti, eds., Plenum Press, New York, (1990), p. 1821.
- [5] I. Altpeter and P. Holler, Review of Progress in Quantitative NDE **9**, 1837 (1990).
- [6] L.J. Swartzendruber and G.E. Hicho, *Res. Nondestr. Eval.* **5**, 41 (1993)

QUANTITATIVE ULTRASONIC CHARACTERIZATION OF INTERFACIAL ADHESION IN METAL-POLYMER-METAL MULTILAYER COMPOSITES

L. Piché,¹ D. Lévesque,¹ P. Deprez,² A. Michel,² and J. Tatibouët¹

¹Industrial Materials Institute, Mortagne, Boucherville, Qc, J4B 6Y4, Canada

²Laboratoire Matériaux Organiques, CNRS, BP 24, Vernaison 69390, France

INTRODUCTION

Recent theoretical advances in adhesion science^{1,2} have been accompanied by the development of new analytical tools³ with sufficient resolution and sensitivity to probe structural details and forces near interfaces. These techniques, however, are not applicable to the characterization of adhesion in real structures. Indeed, for polymer adhesion^{4,5}, instead of only an interface plane, the adhesive and the adherend also interact through an interphase region where the homogeneous phases blend into one another. Interfacial adhesion therefore involves interplay of interface and interphase behavior. On the other hand, practical adhesion is defined by the energy required to separate the adherend and the adhesive and relates to complex nonreversible processes that concern the interface and the interphase, but also the bulk materials themselves. Obviously, nondestructive methods that could probe interfaces and interphases in situ, would constitute a great asset. Also, provided they discriminate between interfacial and bulk regions, these techniques could serve to correlate small scale properties near interfaces and large scale behavior in practical adhesion. In this context, ultrasonics stands out as most promising⁶. Although, ultrasonic techniques are well established for detection of delaminations and flaws⁷, it is only recently that efforts were made at characterizing interfaces. Recently, the "Journal of Nondestructive Evaluation" devoted a complete issue at ultrasonic evaluation of microdefects near interfaces⁸, and the "Journal of Adhesion Science and Technology" presented a series on probing mechanical properties of bonded joints⁹. Surprisingly however, few works addressed the question of materials physics, except for effects related to thickness or curing in epoxy joints¹⁰⁻¹⁴. Epoxies and thermosets constitute a major class of structural adhesives, but in this case, polymerization introduces an additional dimension not clearly related to adhesion per se. Likewise important for applications, thermoplastics also undergo structural changes but here the process occurs near interfaces and is intrinsic to the adhesion problem.

Recently^{3,15}, we presented an ultrasonic method for the quantitative and nondestructive characterization of interfacial adhesion that incorporates recent theories for polymers near surfaces. We demonstrated the method through experiments on metal/polymer/metal samples, where we modified interfacial adhesion by chemical action

on the polymer and on the substrates. We showed that the specific stiffness of the interphase, served as a materials constant for describing interfacial properties. Here we investigate adhesion in metal/polymer/metal multilayers with respect to materials properties. We discriminate between interfacial and bulk properties and identify interface and interphase behavior in relation to processing parameters and practical adhesion.

METHODOLOGY

The making of bonds

Adhesion is commonly taken in a broad sense to describe the sticking together of materials. Layered composites, where two materials are bonded through an intermediate layer of polymer adhesive, involve two interfaces prone to adhesive failure and three regions to cohesive failure. Here, we consider adhesion in reference to bonding at the interface between two materials in intimate contact: the adherend and the adhesive. We shall be concerned with the adhesion of thermoplastic polymers, namely polypropylene (PP). These are large molecules composed of $N \approx 1000$ monomer units having a length $a \approx 0.3\text{nm}$, that are covalently linked in a chain. Adhesives are applied as melts, where the molecules form interpenetrated Gaussian coils with average radius $R_g \approx a N^{1/2} \approx 10\text{nm}$. Intermolecular forces are associated with van der Waals interactions, but also with entanglements of the long chains. The polymer liquids may contour surfaces and, through capillary pressure, they may penetrate into pores, creating mechanical keying. Efficiency of mechanical interlocking depends on wetting, since unwetted areas cause stress concentration that initiate breakage. Wetting is related to interfacial tension which is determined by the nature of atomic/molecular binding. Metals feature ordered lattices, while polymers have disordered, entangled morphologies, resulting in complex interactions whereby the antagonistic structures accommodate. Molecules must diffuse or reptate (with characteristic times $\tau_D \propto N^2$ for short chains or $\tau_R \propto N^{3.4}$ for entangled chains)¹⁶ so that segments become anchored on the substrate. At low grafting density, Σ , the anchored molecules form coils near the surface, with average thickness $d_i \approx R_g$. As Σ increases, the coils overlap and interchain stresses associated with attractive osmotic forces and repulsive entropic forces cause the molecules to stretch out, away from the surface. Finally, the hydrodynamic layer in the melt is frozen in during solidification, as suggested from results¹⁷⁻¹⁹ with the surface force apparatus (SFA). This bonding layer serves to transfer mechanical load between the adherend and the adhesive per se.

Materials

Substrates made from sheets of stainless steel with thickness $d_s = 400\mu\text{m}$, were cleansed and etched in an acid solution. In some cases this was followed by anodizing in a sulfochromic solution. The rugosity was $\approx 200\text{nm}$ and, whilst we could not observe pores on the cleansed only substrates, we identified mesopores with diameters between 4 and 10nm on the anodized surfaces. Also anodized surfaces were enriched with Cr and O and OH. Here, adhesion mostly relates to the chemical properties of the surfaces. Substrates made from aluminum sheets, $d_{Al} = 318\mu\text{m}$, were pretreated by etching in sodium dichromate acid and anodizing in phosphoric acid. The process removed original oxides and produced a new, cellular-like, oxide layer with a thickness $\approx 400\text{nm}$ and pore diameters $\approx 50\text{nm}$. Molecular segments may penetrate the large pores and become embedded in the oxide layer, so that mechanical keying also contributes to adhesion.

Polypropylene (PP) is a non-polar and chemically non-reactive molecule with low wettability and very weak adhesion to metals. We investigate changes in adhesion consequent to grafting with 6.5% weight of glycidyl methacrylate (MAG), containing ester and epoxide functional groups. Films of PPMAG were prepared by molding at constant pressure, $p=1.0\text{MPa}$, and temperature, $T=190^\circ\text{C}$, during 5min. The multilayer assemblies were pressed also at $p=1.0\text{MPa}$ and $T=190^\circ\text{C}$ during 5min. The thickness of the polymer adhesive were measured carefully, but on the average $d_p \approx 80.0\mu\text{m}$.

Ultrasonic Techniques

First, we investigated²⁰⁻²² the ultrasonic properties of the PPMAG material with regards to viscoelasticity. Indeed, the ultrasonic strain modifies thermal equilibrium in the polymer, and irreversible internal processes occur on a time scale, τ , during which the system relaxes towards equilibrium, causing dissipation due to increased internal entropy. The small ultrasonic strains, probe small movements of segmental units in the polymer chains. Therefore τ is a Rouse relaxation time²³, quite different from that in usual rheology experiments, which is closer to τ_D , or τ_R . The steady state solution for the generalized complex dynamic modulus, $M^*(\omega) = M'(\omega) + iM''(\omega)$, is :

$$\frac{M'(\omega) - M_0}{M_\infty - M_0} = \frac{(\omega\tau)^2}{1 + (\omega\tau)^2} \quad \frac{M''(\omega)}{M_\infty - M_0} = \frac{\omega\tau}{1 + (\omega\tau)^2} \quad (1)$$

where ω is the angular frequency, M_0 the relaxed modulus in the zero frequency limit and M_∞ the unrelaxed modulus at infinite frequency. In turn, M^* is related to the density, ρ , the sound velocity, v , and the attenuation, α , through :

$$M' = \rho v^2 \quad M'' = 2\rho \omega \alpha^3 / \omega \quad (2)$$

Depending on polarization $M^*(\omega)$ represents the longitudinal, $L^*(\omega)$, or the shear, $G^*(\omega)$, modulus for longitudinal (P-wave) or transverse (S-wave) respectively. Measurements for density, sound velocity and attenuation were carried out at constant pressure, $p=1.0\text{MPa}$ in the temperature range from $T=0$ to 220°C . We observed a strong relaxation feature with a maximum near 60°C corresponding to $\omega\tau \approx 1$. There was evidence of a broad distribution of relaxation times, but near $T=23^\circ\text{C}$, the results could be described through Eq. (1) using the nominal values from Table 1.

For the multilayers, we used a water immersion technique. The temperature was

Table 1. Ultrasonic data for bulk materials, in terms of complex modulus.

	Density, $\rho \text{ kg/m}^3$	Real Modulus Longitudinal $L' \text{ GPa}$	Real Modulus Shear $G' \text{ GPa}$	Loss Modulus Longitudinal $L'' \text{ GPa}$	Loss Modulus Shear $G'' \text{ GPa}$
Water	1000	2.20	—	≈ 0	—
Aluminum	2700	110.4	25.9	$2.2 \cdot 10^{-9} f$	$0.8 \cdot 10^{-9} f$
Steel	7930	263.6	75.42	$43.5 \cdot 10^{-9} f$	$18.5 \cdot 10^{-9} f$
PP relaxed	926	1.80	$0.5 \cdot 10^{-3}$	$\tau = 500 \text{ ns}$	
PP unrelaxed	"	7.53	2.00		

constant, $T=23\pm0.5^\circ\text{C}$, and samples were protected from infiltration of humidity. We used broadband transducers with frequencies from $f=5$ to 50 MHz; effects due to diffraction were minimized and the beams were Gaussian, with 2.0mm half-widths. Transducers were energized with high voltage spikes and a broadband (100 MHz) amplifier served as a receiver. Signals were digitized in a computer and Fourier-transformed into the frequency domain. The resulting spectrum was deconvolved with a reference, which produced the true transfer function for the sample proper. We also used this technique to measure the P-wave and S-wave ultrasonic properties of the substrates, in Table 1.

MEASUREMENTS AND RESULTS

Specific Stiffness of the Boundary Layer

In Fig. 1, the heavy line illustrates the experimental frequency spectrum for the transmission coefficient at normal incidence, T_p (24dB between tick marks). Propagation of sound in multilayers is complex due to changes in acoustic impedance between layers. We accounted for boundary conditions and solved the equations²⁴ for the acoustic field in each layer. The solution^{3,15} involves a great deal of analytical work, but the operational

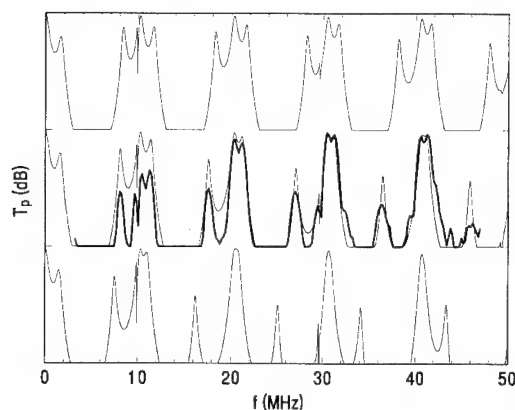


Figure 1. Transmission coefficient, T_p , (longitudinal waves) in Aluminum/PPMAG/Aluminum multilayer. Upper trace is a simulation relating to rigid bonding; center trace: light line is a simulation for an interface layer with $S_p = 11.2 \times 10^{14} \text{ N/m}^3$ and heavy line is an experimental spectrum; bottom trace is a simulation for an interface layer with $S_p = 5.0 \times 10^{14} \text{ N/m}^3$.

result is obtained numerically by using the Transfer Matrix Approach. For this, we built a computer code that is efficient, yet very robust. Based on data in Table 1, the top trace in Fig. 1, describes simulation results assuming that the layers are welded together. This approach cannot duplicate the experimental spectrum, and this is definitely not attributable to faulty values of bulk properties in Table 1. In line with theoretical ideas for

polymers near interfaces, we add interfacial layers with unknown thickness, d_i , and modulus, M_i^* . However, we find that, whenever d_i is smaller than the wavelength, the thickness and modulus are not independent, instead, the specific stiffness, $S^* \equiv (M_i^* / d_i)$, is the only relevant variable in the problem. To ensure continuity between the boundary layer and the bulk polymer, we set $M_i'' / M_i' = M'' / M' \approx 10^{-2}$, in which case, $S^* \approx S \equiv (M_i' / d_i)$ is a real quantity. With only $S_P \equiv L_i' / d_i$ and $\tau_{i,P}$ as fitting parameters, the light line superimposed on the experimental spectrum in Fig. 1, corresponds to simulation results with $S_P = 11.2 \times 10^{14} \text{N/m}^3$ and $\tau_{i,P} = \tau$. The bottom trace in Fig. 1 is a simulation with $S_P = 5.0 \times 10^{14} \text{N/m}^3$ to illustrate weak bonding. In other experiments with shear waves, we found: i) $S_s = (G_i' / d_i) = (G' / L') S_P$, pointing out that adhesion is related to elongational forces, and not only to shear behavior, ii) $\tau_{i,S} \approx \tau_{i,P} \approx \tau$, suggesting that the details for small molecular movements of confined molecules remain essentially the same for longitudinal and shear waves, due to the random nature of the structure.

Interfacial Adhesion

Ultrasonic measurements provide average properties and therefore the specific stiffness parameter, $S^* = M_i^* / d_i$, is a mean field quantity that serves to match the different properties in the substrate and the adhesive. Near the interface, the modulus reflects the strength of chemical bonding of MAG moieties and the number density of grafted molecules, Σ , but also the monomer-wall interactions that may be attractive or repulsive. In Table 2, we show results using the same polymer but different substrates. For stainless steel substrates, changes in adhesion are governed by chemical properties of the interface which condition probabilities for grafting, i.e. Σ . In comparison the results for aluminum demonstrate the efficiency of mechanical interlocking in enhancing interfacial adhesion. When relating to interfaces, the natural length scale is $d_i \approx R_g \approx 10 \text{nm}$, and we found that this also corresponds to the thickness of residue films after delamination. The results for L_i' calculated for $d_i \approx R_g \approx 10 \text{nm}$ in Table 2 represent very small moduli, but are within realistic bounds: i) L_i' remains larger than the van der Waals limit for adhesion forces, ii) L_i' compares well with SFA measurements¹⁷⁻¹⁹ in confined molecular systems. Because all materials characteristics are constant, changes in adhesive behavior are essentially linked to the different surface properties of the substrates.

Table 2. Effect due to nature of substrate on interfacial adhesion parameter, S_P ; and longitudinal modulus, L_i' calculated for the distance from the interface $d_i \approx R_g \approx 10 \text{nm}$.

	Cleansed Steel	Anodized Steel	Aluminum
$S_P \equiv L_i' / d_i, \text{N/m}^3$	1.5×10^{14}	7.0×10^{14}	39.0×10^{14}
$L_i'(d_i \approx R_g), \text{MPa}$	1.5	7.0	39.0

The Interphase Region

After attachment to the substrate, the arrangement of molecules near the surface slowly evolves until an equilibrium entanglement network is formed. This involves interdiffusion of molecules, with a time scale, τ_R , that is mostly governed by reptation of chains through entanglements. Compared to Rouse type relaxation, $\tau = 10^{-9} \text{s}$, the time scale for reptation is much longer, $\tau_R \approx 10^2 \text{s}$, depending on temperature. While keeping the

temperature constant at $T=190^{\circ}\text{C}$, we prepared several multilayers using different processing times from 30.0 s to 45 min., above which the polymer would start degrading. In Fig. 2, we show the evolution of specific stiffness, S_p , as function of time, t , and the solid curve is a best fit to a classical Fickian diffusion equation. The comportment for $t > \tau_R$ refers to the cooperative movement of chains and describes the build up of the entanglement network in the interphase, a short distance away from the interface. In order to evaluate the thickness, δ of the interphase region, we assume continuity of stress, σ , at a short distance, d_i , from the wall. If x is the deformation, we may write $\sigma = L'_i x / d_i$, and correspondingly, for the bulk material $\sigma = L' \epsilon$, with ϵ being the strain. Then $x = \delta \epsilon$, where $\delta = L' / S_p$ is a linear interpolation length that describes the thickness of the interphase. In practice, we found $5.0 \times 10^{14} < S_p < 100 \times 10^{14} \text{ N/m}^3$ for the limits of weak and strong adhesion; in turn, this serves to set bounds for the thickness: $15 > \delta > 0.7 \mu\text{m}$. Thus, for short processing times, the small values of S_p reflect the loose arrangement of molecules in the interphase material, hence the large density gradient near the substrate. At long times, the molecular density near the interface increases, and the interphase network more closely matches that in the bulk polymer.

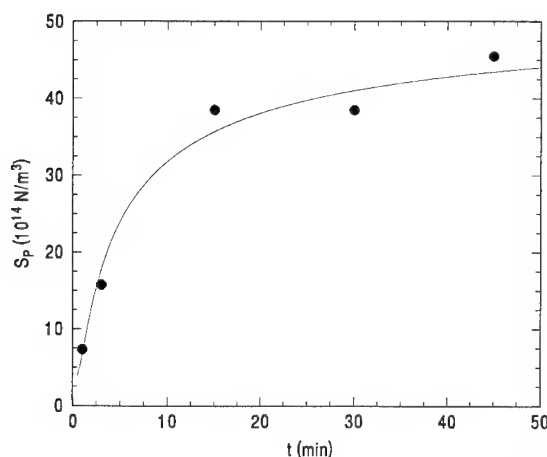


Figure 2. Specific stiffness of intermediate layer, S_p , in Aluminum/PPMAG/Aluminum multilayer as function of contact time during processing at $T=190^{\circ}\text{C}$. Solid curve is best fit to a diffusion equation.

Practical Adhesion

The energy, for separating the adhesive from the substrate relates to complex phenomena, which can in principle take place without breaking of primary bonds. Intuitively, one expects values of the same order as typical surface energies, about 0.025 J/m^2 , instead of about 10 J/m^2 for breaking chains. In practice, however one measures values that are much larger, by orders of magnitude. Also, adhesion energy is found to vary with the rate of separation. Therefore, adhesion is enhanced by energy dissipation within the adhesive, mostly because inelastic effects within the material help reduce stress intensity near crack tips. We performed "near-equilibrium" destructive peeling tests on the

samples described above. The work, W , for separation per unit area of interface, was calculated from the peel force per unit width of the sample. In Fig. 3 we plot the results for the work of detachment, W , versus the specific stiffness, S_p . As seen, there exists a definite correlation between both quantities: from a best fit to the data, we found $W \propto S_p^2$, as illustrated by the dotted line in Fig. 3. Tentatively, we write the strain energy density near the interface as: $U \approx \sigma^2 / 2L'_i$. Then, as described above, the stress may be written: $\sigma \approx S_p x$, leading to $U \approx S_p^2 (x^2 / 2L'_i)$. The stored elastic energy may be used, for example, to pull the chain out from the interphase. Here, with the hypothesis that failure was mainly due to chain pullout, x is a criterion for detachment, such a chain length, and since the same material was used throughout, x is a constant for our samples. On the other hand, L'_i characterizes the region of $d_i \approx R_g \approx 10\text{nm}$ near the substrate, and is independent of contact time. Also we may use the approximation that L'_i remained constant during delamination. Then $x^2 / 2L'_i$ is a constant for the experiment, so that the condition for chain pullout is simply $W \propto U \propto S_p^2$, in agreement with the results in Fig.3. Obviously, our approach is simplified, however, it satisfies intuitive reasoning and other more elaborate findings^{25,26}.

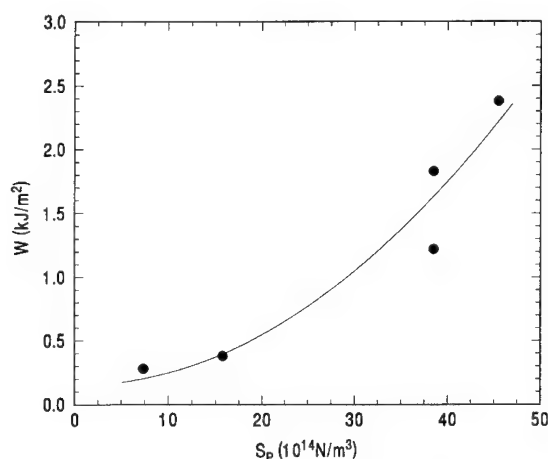


Figure 3. Detachment energy in peel test, W , versus specific stiffness of intermediate layer, S_p , for samples described in Fig. 2.

CONCLUSION

We presented a nondestructive technique for the quantitative characterization of interfacial adhesion. The method hinges on mapping data from ultrasonic measurements on a newly developed model for the propagation of sound in multilayered media. We included recent concepts for polymers near interfaces by allowing for a viscoelastic interface layer with a complex modulus, M_i^* , and a thickness d_i . We showed that the specific stiffness, $S^* = M_i^* / d_i$, was the true materials properties for describing interfacial behavior. Through experiments with different substrates we showed that S^* was related to

surface forces with ranges of the order $d_i \approx R_g \approx 10$ nm. Measurements on multilayers made by varying the processing time, suggested the presence of an interphase region with a thickness $\delta \approx 0.5$ to $10 \mu\text{m}$, where the molecular network accommodates the different properties of the substrate and the bulk polymer. Finally, we demonstrated that small scale behavior, described by S^* , was correlated to practical adhesion, defined by the detachment energy, W , measured in peel tests. Here we mention that the problem for curing of epoxies¹⁰⁻¹⁴ is different and more complicated, because most materials properties depend on the advancement of the crosslinking reaction. The present work is open ended and is expected to lead to novel applications for nondestructive evaluation. Already, the method has been successful for characterizing adhesive seals in the food packaging industry; in this case, S^* was directly correlated to processing parameters. However, a great deal of more fundamental work needs to be done, to fully understand the true meaning of S^* , with respect to interfacial energy.

REFERENCES

1. P.G. de Gennes, *Macromolecules* 13:1069-1075 (1980).
2. J.M.H.M. Scheutjens, and G.J. Fleer, *J. Phys. Chem.* 84: 178-190 (1980).
3. D. Lévesque, A. Legros, A. Michel, and L. Piché, *J. Adhes. Sci. Tech.*, in press.
4. J.D. Miller, and H. Ishida, Adhesive-adherend interface and interphase, in "Fundamentals of Adhesion", Chap. 10, pp. 291-324, L.-H. Lee (Ed.) Plenum Press, New York (1991).
5. K.L. Mittal, *Polym. Eng. Sci.* 17: 467-473 (1977).
6. G.M. Light, and H. Kwun, "Nondestructive Evaluation of Adhesive Bond Quality", Nondestructive Testing Analysis Center, Southwest Research Institute, San Antonio, TX. (1989).
7. R.B. Thompson, and D.O. Thompson, *J. Adhes. Sci. Tech.* 5: 583-599 (1991).
8. *J. Nondestr. Eval.* 11: 109-250 (1992).
9. *J. Adhes. Sci. Tech.* 5: 601-666 (1991).
10. P.B. Nagy, *J. Adhesion Sci. Technol.* 5: 619-630 (1991).
11. D. Jiao, and J.L. Rose, *J. Adhesion Sci. Technol.* 5: 631-647 (1991).
12. W. Wang, and S.J. Rokhlin, *J. Adhesion Sci. Technol.* 5: 647-666 (1991).
13. R.E. Challis, R.P. Cocker, A.K. Holmes, and T. Alper, *J. Appl. Polym. Sci.* 44: 65-81 (1992).
14. P. Fraisse, F. Schmit, and A. Zarembowitch, *J. Appl. Phys.* 78: 3264-3271 (1992).
15. D. Lévesque, and L. Piché, *J. Acoust. Soc. Am.* 92: 452-467 (1992).
16. P.G. de Gennes, "Scaling Concepts in Polymer Physics" Cornell University Press, Ithaca, NY, (1979).
17. A.M. Homola, H.V. Nguyen, and G. Hadziioannou, *J. Chem. Phys.* 94: 2346-2351 (1991).
18. J. Van Alsten, and S. Grannick, *Macromolecules* 23: 4856-4862 (1990).
19. J.C. Israelachvili, S.J. Kott, and L.J. Fetters, *J. Polym. Sci.: B: Polym. Phys.* 27: 489-502 (1989).
20. Massines, F., Piché, L. and Lacabanne, C., *Makromol. Chem. Macromol. Symp.* 23: 121-137 (1989).
21. Piché, L., Massines, F., Hamel, A. and Néron, C., "Ultrasonic technique for characterizing polymers under simulated processing conditions", Can. Pat. N° 1,264,195 (1990); US Pat. N° 4,677,482 (1987).
22. J. Tatibouët, and L. Piché, *Polymer* 32: 3147-3152 (1991).
23. J.D. Ferry, "Viscoelastic Properties of Polymers", John Wiley, New York (1980).
24. L.M. Brekhovskikh, "Waves in Layered Media", Academic Press, New York (1980).
25. P.G. de Gennes, *Can. J. Phys.* 68: 1049-1054 (1990).
26. A.N. Gent, *Int. J. Adh. Adhes.* April issue, 175-180 (1981).

SURFACE ROUGHNESS AND ULTRASONIC MATERIALS CHARACTERIZATION

Peter B. Nagy,¹ Gabor Blaho,¹ and James H. Rose²

¹Department of Welding Engineering
The Ohio State University
Columbus, Ohio 43210, U. S. A.

²Center for NDE
Iowa State University
Ames, Iowa 50011, U. S. A.

INTRODUCTION

Ultrasonic materials characterization relies primarily on measurements of three quantities: (1) backscattered power from the microstructure, (2) frequency-dependent attenuation of the transmitted coherent wave, and (3) shifts in the sound velocity. Surface roughness tends to randomize the phase of the reflected and transmitted waves, which can significantly distort the ultrasonic measurements. For example, uncorrected surface roughness effects can cause substantial underestimation of the porosity in cast aluminum samples.¹ There are three basic effects of surface roughness which should be accounted for in evaluating the data measured by an unfocused transducer. First of all, the coherent reflection and transmission through the interface are attenuated by scattering at the rough surface. Second, the incoherent background scattering from inherent material inhomogeneities in the sample is relatively weakly affected by surface roughness. It does not decrease in proportion to the coherent signals and sometimes even increases slightly. Third, incoherent backscattering at the rough interface produces a slowly decaying tail in the reflection from the front surface, which adds to the incoherent background scattering, especially at small depths below the surface. It has been shown that, for the purposes of NDE, all three effects can be accurately described by the so-called phase-modulation technique. In this simple approximation, explicit analytical results can be derived for (i) the surface roughness induced attenuation of the coherent signals, (ii) the incoherent material noise, and (iii) the level of the additional incoherent surface noise. In this paper, we shall review the above mentioned three main effects of random surface roughness on ultrasonic materials characterization and present simple theoretical predictions and experimental data in order to quantify the resulting changes in the measured parameters.

COHERENT REFLECTION AND TRANSMISSION

Surface roughness tends to randomize the phase and to alter the magnitude of the transmitted and reflected waves. For roughnesses of relatively small curvature, i. e., where the r.m.s. height, h , of the roughness is small compared to its variation (correlation length) along the surface, the randomization of the phase primarily determines the effect on the transmission process.² The roughness induced change in the local wave amplitude across the interface is relatively unimportant. This insight leads us to examine our experimental results in terms of a method that considers only the phase variation, the so-called phase-screen approximation.³ The experiments that will be reported in this section measure the loss (or attenuation) induced by the rough surface in the coherently transmitted and reflected waves. For the longitudinal transmitted wave, the loss is defined as the ratio of the transmission coefficients of the rough and a smooth, but otherwise identical, interface:

$$A^L(\omega, \theta_I) = \ln \frac{T_o^L(\theta_I)}{T^L(\omega, \theta_I)}, \quad (1)$$

where ω is the angular frequency, θ_I denotes the angle of incidence measured with respect to the normal, and the superscript refers to the type of the transmitted wave (longitudinal) and the zero subscript indicates a smooth reference surface. The loss of the transmitted shear wave, A^T , and the reflected pressure wave in water, A^R , are defined in analogy with (1). In the phase-screen approximation, these losses can be written as⁴

$$A^{R,L,T} = h^2 \omega^2 C^{R,L,T}, \quad (2)$$

where

$$C^R = 2 [\cos(\theta_I)/c_w]^2, \quad (3)$$

$$C^L = \frac{1}{2} [\cos(\theta_L)/c_L - \cos(\theta_I)/c_w]^2, \quad (4)$$

and

$$C^T = \frac{1}{2} [\cos(\theta_T)/c_T - \cos(\theta_I)/c_w]^2, \quad (5)$$

where c_w , c_L , and c_T are the compressional wave velocity in the water and the longitudinal and shear velocities in the solid, respectively. θ_L and θ_T denote the longitudinal and shear refraction angles, which can be easily calculated from Snell's law.

Equations 1-5 provide simple explicit formulas for the scattering induced loss of the coherent reflection and transmission coefficients of a slightly rough interface in the phase-screen approximation. In order to verify the accuracy of these results, the same coefficients were numerically evaluated using the second-order approximation of Kuperman and Schmidt.⁵ This approximation is expected to be good if the r.m.s. roughness is sufficiently small. The results of the second-order approximation can be cast in the same form as Eq.(2). However, the multiplicative functions $C^{R,L,T}$ now have to be changed to reflect the

more complex nature of the calculations. We define the reduced losses (in the second-order approximation) by

$$A^{R,L,T} = h^2 \omega^2 K^{R,L,T}. \quad (6)$$

Explicit formulas cannot be given for the K 's, rather they must be evaluated from certain integrals given in Ref. 5. Detailed calculations show that $K^{R,L,T}$ weakly depend on the ratio of the density of water to that of the solid and the ratio of the r.m.s. height to the surface-roughness correlation length (h/L).

Equations 2 and 6 show that the different losses depend on the r.m.s. height and the frequency as simple quadratics. This dependence can be removed naturally by normalizing the angular-dependent reflection and transmission losses to the reflection loss at normal incidence:

$$N^{R,L,T}(\omega, \theta_I) \equiv \frac{A^{R,L,T}(\omega, \theta_I)}{A^R(\omega, \theta_I=0)}, \quad (7)$$

where

$$A^R(\omega, \theta_I=0) = 2 \frac{\omega^2 h^2}{c_w^2}. \quad (8)$$

In order to study the problem of surface roughness induced attenuation of the transmitted longitudinal and shear waves, we prepared a series of 5" x 5", 1/2"-thick aluminum plates roughened on one side by different surface preparation techniques. This large area facilitated more extensive spatial averaging, while the smaller thickness was necessary so that transmission measurements could be made at relatively high angles of incidence. Table I shows the list of the aluminum samples that we used to study the effects of surface roughness on the coherently transmitted components. Details of our experimental procedure are described in Ref. 4.

Figure 1 shows the surface roughness induced attenuation of the reflected ultrasonic wave at normal incidence as a function of frequency for the eight rough samples listed in Table I. In good agreement with our expectations, the measured attenuation seems to be proportional to the square of frequency. The best fitting f^2 curves (plotted with solid lines in Fig. 1) were used to estimate the r.m.s. surface roughness listed in Table I by using the attenuation coefficient of Eq. (8) at normal incidence. Figure 2 shows typical examples for the surface roughness induced attenuation of the transmitted longitudinal and shear waves at different angles of incidence as functions of frequency for sample #2. Again, the measured attenuation seems to be proportional to the square of frequency, but its value is significantly lower than the reflection loss at normal incidence, which is also shown for easier comparison. It is interesting that the transmission loss of the shear wave is somewhat lower than that of the longitudinal wave. This is due to the fact that the shear velocity is much closer to the compressional velocity in the fluid than the longitudinal velocity of aluminum. As a consequence, the scattering at the irregular liquid-solid interface is also smaller for the shear wave.

The main purpose of these experiments was to verify a single conclusion of great practical importance that follows from our theoretical results. Namely, the ratio of the surface roughness induced transmission loss at oblique incidence to the reflection loss at normal incidence is basically a single, universal function of the angle of incidence, which

Table I List of the aluminum samples used in this study.

Sample	Surface Preparation	Estimated Roughness (micron, r.m.s.)
#1	2 mm steel balls	45.6
#2	10 mm miller head	25.6
#3	>2 mm sand	15.2
#4	>2 mm quartz	12.8
#5	1.8 - 2 mm sand	11.4
#6	1 - 1.8 mm sand	9.9
#7	1 - 1.8 mm quartz	8.7
#8	1 mm steel balls	5.6
#9	smooth (reference)	0

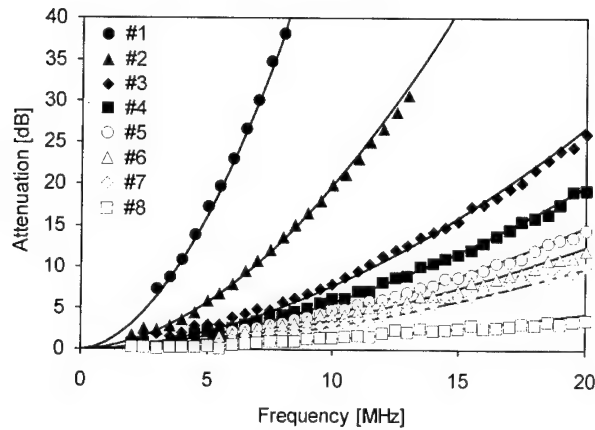


Figure 1 Surface roughness induced attenuation of the reflected wave at normal incidence (solid lines are best fitting f^2 curves).

is determined by the sound velocities in the fluid and the solid. The normalized transmission losses are independent of both frequency and r.m.s. roughness. They are also almost entirely independent of the densities of the fluid and the solid. In the two angular ranges of high practical importance in ultrasonic NDE, they are weakly sensitive to the auto-correlation length of the surface topography and to the angle of incidence.

INCOHERENT MATERIAL SCATTERING

Ultrasound backscatters from the microstructure of the sample. Acoustic backscatter can be used to characterize various material properties of structural solids but it is also the major source of noise in many ultrasonic inspections. In everyday practice of ultrasonic material characterization, we often take advantage of the fact that the average

backscattered signal only weakly depends on the misalignment of the probe or on the shape and curvature of the sample. It has been shown experimentally that surface roughness attenuates the backscattered incoherent noise much less than the coherent transmission.⁶ This lack of sensitivity can be readily explained by using the phase-screen approximation.⁴ Interestingly, this simple theory also predicts that scattering at a rough surface can slightly

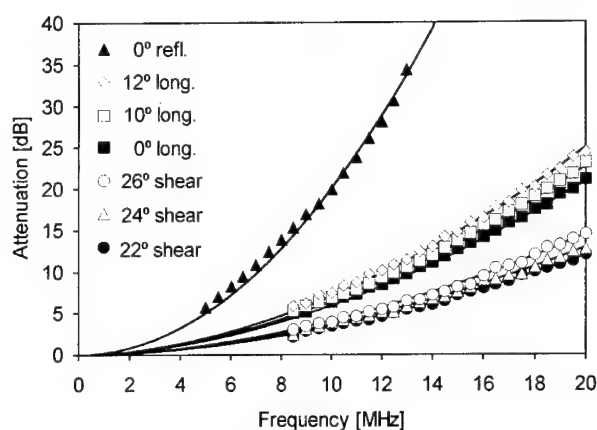


Figure 2 Surface roughness induced attenuation of the double-transmitted longitudinal and shear waves at different angles of incidence for Sample #2. (solid lines are best fitting f^2 curves).

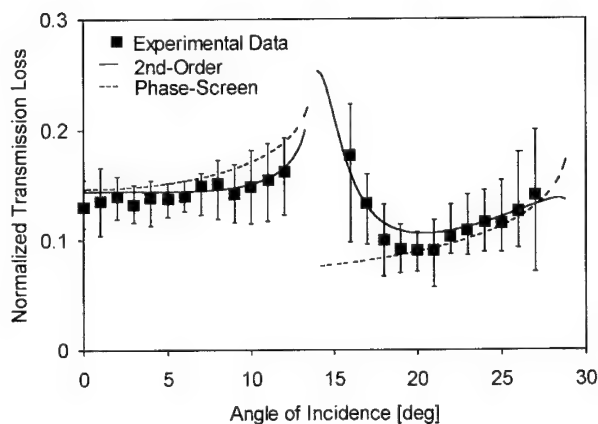


Figure 3 Normalized transmission loss versus angle of incidence averaged for all eight samples listed in Table 1 (in the 2nd-order approximation, $h/L = 100$ was assumed).

increase the incoherent material noise, which has been also experimentally observed.⁷ However, as a general rule, surface roughness has a relatively weak effect on the incoherent backscattering from material inhomogeneities, which can be neglected in most typical applications.

Figure 4.a shows the frequency-dependent attenuation of the longitudinal wave backscattering due to the surface roughness at normal incidence in brass. Most of the apparent "attenuation" is due to the remanent random modulation. Although this ripple is greatly reduced by spatial averaging, the relatively small area available for such averaging limited our ability to further smooth the spectra. As can be seen, the attenuation is negligible throughout the whole frequency range of 4-22 MHz. In comparison, the coherently transmitted wave is attenuated by as much as 15 dB at the center of this range and by more than 40dB at the upper end of it. In order to study the surface roughness

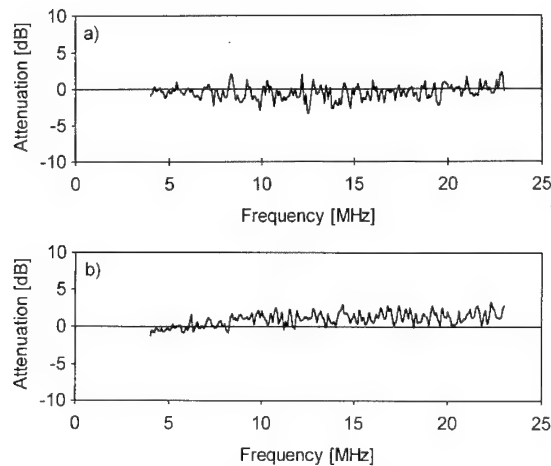


Figure 4 Surface roughness induced attenuation of grain noise in a brass sample of 40 μm roughness at normal (a) and 45° (b) angle of incidence.

induced attenuation of the incoherently transmitted shear component, a similar experiment was carried out above the first critical angle, too. Figure 4.b shows the frequency-dependent attenuation of shear wave backscattering from brass at 45° angle of incidence. Again, the surface roughness effect is negligible with respect to the much stronger attenuation of the coherently transmitted component. At low frequencies, the attenuation seems to be negative corresponding to an actual gain in the grain noise. This effect might be partially due to direct scattering at the surface, which produces an elongated "tail" in the front surface reflection. This "tail" can be observed at normal incidence, too, but there it is much easier to separate it from the grain scattering emanating from the interior of the specimen by proper time gating. This adverse effect of incoherent scattering from the surface on our ability to characterize the material at small depths below the rough interface will be discussed in more detail in the next chapter.

INCOHERENT SURFACE SCATTERING

When the material noise is relatively weak, in a shallow region below the rough surface, the incoherent background noise is dominated by direct backscattering from the surface. This effect is demonstrated in Figure 5 showing the r.m.s. noise level in a low-carbon steel specimen as a function of propagation time. Both the grain size and the surface roughness were approximately $20\text{ }\mu\text{m}$. The measurement was made by averaging the square of the received rf signal over a 1"-by-2" area in a 3 MHz wide frequency range centered around 10 MHz. From the smooth side of the specimen, the material noise slightly decreases between the front- and back-wall echoes, which is partly due to the spread of the acoustic beam and partly to scattering induced attenuation in the sample. From the rough side, the overall noise level is much higher. Close to the surface, the additional surface noise is significantly stronger than the inherent material noise. Due to its faster decay, surface noise becomes negligible with respect to the material noise at large depths.

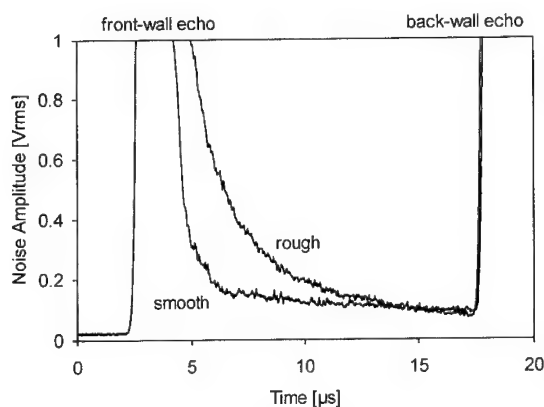


Figure 5 Example of increased near-surface noise in a low-carbon steel specimen.

The excess surface noise produced by direct ultrasonic backscattering from a rough liquid-solid interface was recently studied by both analytical and experimental means.⁸ In weakly scattering materials and near the surface, this excess noise can easily overshadow the intrinsic material noise. At oblique incidence, the surface noise is primarily due to strong first-order scattering. At normal incidence, the first-order scattering is strong but very short and the excess noise observed at larger "depth" in the material is primarily due to higher-order scattering. The time-decay of the excess surface noise can be determined from purely geometrical considerations. For small roughness, the absolute level of the surface noise can be easily calculated as a function of frequency and angle of incidence from the r.m.s. surface roughness and the auto-correlation length assuming that the type of the correlation function is known.⁸ The r.m.s. roughness is most easily assessed from the surface roughness induced loss of the coherent reflection at normal incidence. Finally, the correlation length and the most appropriate correlation distribution model can be estimated from the angular-dependence of the backscattered signal at a given frequency.

CONCLUSIONS

Three main effects of surface roughness on ultrasonic materials characterization by unfocused transducers were identified and discussed. First and most importantly, the coherent reflection and transmission through the interface are attenuated by scattering at the rough surface. The losses of all three coherent components are proportional to the squares of the r.m.s. roughness of the surface and the inspection frequency. Interestingly, the transmitted wave is usually much less attenuated than the reflected one. Experimental results from samples with r.m.s. roughness between 5 and 50 μm were found to be in good agreement with the predictions of the suggested phase-modulation approximation in the 2 to 20 MHz frequency range. Second, we found that the incoherent background scattering from inherent material inhomogeneities in the sample is relatively weakly affected by surface roughness. Third, incoherent backscattering at the rough surface adds a slowly decaying tail to the front surface reflection, which increases the incoherent background scattering, especially at small depths below the surface. These adverse effects should be taken into consideration in the optimization of ultrasonic characterization methods as well as during the quantitative evaluation of material properties of samples with rough surfaces.

ACKNOWLEDGMENT

This work was supported by the National Science Foundation under grant No. ECO-9008272 and the Center for NDE at Iowa State University. The authors greatly appreciate the valuable contributions of S. Meng, C. Pecorari, M. Bilgen, and L. Adler.

REFERENCES

1. P. B. Nagy, D. V. Rypien, and L. Adler, "Surface roughness effects in porosity assessment by ultrasonic attenuation spectroscopy," *in*: Review of Progress in Quantitative Nondestructive Evaluation, Eds. D. O. Thompson and D. E. Chimenti, Plenum, New York, 6B: 1435-1442 (1987).
2. J. A. Ogilvy, Theory of Wave Scattering from Random Rough Surfaces, Adam Hilger, Bristol (1991).
3. C. Eckhart, "The scattering of sound from the sea surface," J. Acoust. Soc. Am. 25: 556 (1953).
4. P. B. Nagy and J. H. Rose, "Surface roughness and the ultrasonic detection of subsurface scatterers" J. Appl. Phys. 73: 566 (1993).
5. W. A. Kuperman and H. Schmidt, "Self-consistent perturbation approach to rough surface scattering in stratified elastic media," J. Acoust. Soc. Am. 86: 1511 (1989).
6. P. B. Nagy and L. Adler, "Scattering induced attenuation of ultrasonic backscattering," *in*: Review of Progress in Quantitative Nondestructive Evaluation, Eds. D. O. Thompson and D. E. Chimenti, Plenum, New York, 7B: 1263- 1271 (1988).
7. M. Bilgen, J. H. Rose, and P. B. Nagy, "Ultrasonic inspection, material noise and surface roughness," *in*: Review of Progress in Quantitative Nondestructive Evaluation, Eds. D. O. Thompson and D. E. Chimenti, Plenum, New York, 12B: 1767- 1774 (1993).
8. P. B. Nagy, L. Adler, and J. H. Rose, "Effects of acoustic scattering at rough surfaces on the sensitivity of ultrasonic inspection," *in*: Review of Progress in Quantitative Nondestructive Evaluation, Eds. D. O. Thompson and D. E. Chimenti, Plenum, New York, 12B: 1775- 1782 (1993).

MICROSCOPIC DETERMINATION OF SURFACE WAVE VELOCITIES IN HEAT TREATED STEELS BY ULTRASONIC REFLECTIVITY MEASUREMENT

Ikuro Ihara,¹ Tatsuhiko Aizawa,² and Junji Kihara ²

¹ Department of Mechanical Engineering
Nagaoka University of Technology
1603-1 Kamitomioka, Nagaoka, Niigata 940-21, Japan

² Department of Metallurgy
University of Tokyo
7-3-1 Hongo, Bunkyo-ku, Tokyo 113, Japan

INTRODUCTION

The measurement of mechanical properties on a microscopic scale is the key technology for the characterization of inhomogeneous materials, as well as small scale materials such as used for a micromechanism. Recently, many investigations on mechanical properties at a small area by surface waves have been carried out using an acoustic microscope and others. The surface wave provides useful information on the character near the surface of the materials. Generally, in investigations by the surface wave, it is very important to measure precisely the surface wave velocity because the velocity is closely related to the mechanical properties such as elastic properties and the state of stress. Since most wave-materials interaction is frequency dependent, an ultrasonic spectroscopy technique is particularly effective for such investigations. Authors have applied the spectroscopy technique based on the ultrasonic reflectivity measurement^{1,2,3} for the microscopic characterization of mechanical properties on a surface layer.^{4,5} However, basic research on the microscopic measurement by this technique is not yet sufficient. For practical applications of this technique, it is necessary to obtain the fundamental knowledge on the sensitivity and the reliability of the velocity measurement, and a clear physical interpretation for the measured value.

In the present paper, the resolution and the accuracy of the velocity measurement by the present technique are examined. Secondly, based on the investigations of the reflection coefficients for angles in the vicinity of the Rayleigh critical angle and the experimental results with various kinds of heat treated steels, the influence of absorption losses in materials on the measured velocity are considered. Finally, the paper closes with a discussion of problem associated with the microstructure of materials on the microscopic determination of the surface wave velocity of the polycrystalline materials.

DETERMINATION OF SURFACE WAVE VELOCITY AT A SMALL AREA

Measurement Principle of Surface Wave Velocity

We suppose that the upper half space on a semi-infinite solid is filled with fluid, typically water, and an ultrasonic plane wave is injected on the solid with an incident angle θ . In general, the reflection coefficient for the liquid-solid interface can be given^{6,7} as

$$R(k_x) = \frac{[(2k_x^2 - k_t^2)^2 - 4k_x^2 \{(2k_x^2 - k_t^2)(2k_x^2 - k_l^2)\}^{1/2}] - i(\rho_w/\rho_s)k_l^4 \{(2k_x^2 - k_t^2)/(2k_w^2 - k_x^2)\}^{1/2}}{[(2k_x^2 - k_t^2)^2 - 4k_x^2 \{(2k_x^2 - k_t^2)(2k_x^2 - k_l^2)\}^{1/2}] + i(\rho_w/\rho_s)k_l^4 \{(2k_x^2 - k_t^2)/(2k_w^2 - k_x^2)\}^{1/2}}, \quad (1)$$

where ρ_s and ρ_w are densities of the solid and the liquid, k_w is wavenumber in the liquid, k_l and k_t are wavenumbers for longitudinal and transverse waves in the solid, and k_x is tangential component of the wavevector in the fluid which matches the propagation vector of the surface wave. The effects due to absorption losses in materials can be incorporated into $R(k_x)$ by introducing the complex wavenumber k_l and k_t as defined below. Denoting d_l and d_t as attenuation per wavelength for the longitudinal and transverse waves in the solid, each wavenumber can be written as

$$\left. \begin{aligned} k_w &= \omega/v_w \\ k_l &= (\omega/v_l)(1 + id_l/2\pi) \\ k_t &= (\omega/v_t)(1 + id_t/2\pi) \\ k_x &= (\omega/v_w)\sin\theta \end{aligned} \right\}, \quad (2)$$

where v_w is the sound velocity in the liquid, v_l and v_t the velocities for the longitudinal and transverse waves in the solid, and ω the angular frequency. As the incident angle increases, the reflection coefficient exhibits a phase change of nearly 2π and a minimum of a modulus in the vicinity of a critical angle. These phenomena are due to the generation of a leaky Rayleigh wave at the critical angle. For most liquid-solid interface, the angular position at which the phase change is π or the modulus is minimum is very closely equal to the so-called Rayleigh critical angle θ_c , when the absorption losses in materials are a small quantity.⁷ With a known value for v_w , the Rayleigh wave velocity v_{sw} can then be determined by Snell's law:

$$v_{sw} = v_w / \sin\theta_c. \quad (3)$$

When the absorption losses in materials are significant, the angular position at which the phase change is π or the modulus is minimum is not always agree precisely with this Rayleigh critical angle.

Measurement of Reflection Coefficient at a Small Area

Figure 1 shows a block diagram of the equipment used for the measurement of the reflection coefficient.³ The equipment has an ultrasonic sensor consisted of a transmitter with a planar lens and a receiver with a spherical lens. In this equipment, a broadband impulsive wave is incident on a specimen surface through water, and only a reflected wave component from the specimen surface in focus area of the spherical lens is selectively

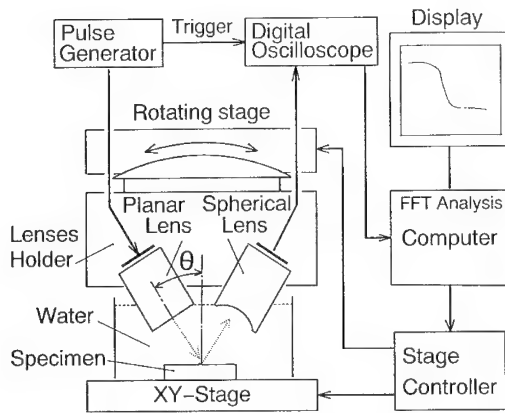


Figure 1. Block diagram of ultrasonic reflectivity measurement system.

received as an effective electrical signal. An output signal of the sensor is proportional to the reflection coefficient of the material even near the Rayleigh critical angle;³ therefore, we can get the reflection coefficient at an arbitrary incident angle with high spatial resolution by the spherical lens. In the present measurement, the specimen surface held in the horizontal is precisely positioned at a focal point of the spherical lens; and tilting the sensor unit round the focal point, the reflected waves at the incident angle from 22° to 38° are measured at intervals of 0.1° . Applying fast Fourier transform (FFT) analysis to the received waveforms, then, phase and modulus of reflection coefficient at each incident angle are obtained in a frequency range from 40 to 120MHz.

MATERIALS

Cylindrical specimens(diameter 10mm, length 20mm) of structural carbon steel(JIS type S45C: 0.45% carbon content) were procured for this experiment. After homogenizing by heat treatments, nine types of specimens were prepared: quenched, tempered at various temperature and annealed. The specimen surface for the reflectivity measurement was buffed after grinding. Young's modulus and poisson's ratio of each specimen were calculated from the theory of elasticity for isotropic materials using longitudinal and transverse wave velocities measured by the pulse-echo method at 10MHz.

RESULTS AND DISCUSSION

Measurement Accuracy

In determining the Rayleigh wave velocity v_{sw} through the present technique, it is seen from Equation(3) that the measurement accuracy of the velocity v_{sw} is affected by the velocity v_w and the angle θ_c . The measurement error of the Rayleigh wave velocity δv_{sw} is, since v_{sw} is a function of v_w and θ_c , approximately given by

$$\delta v_{sw} = \left| \frac{\partial v_{sw}}{\partial v_w} \right| \delta v_w + \left| \frac{\partial v_{sw}}{\partial \theta_c} \right| \delta \theta_c = v_{sw} \left(\left| \frac{\delta v_w}{v_w} \right| + \left| \frac{\delta \theta_c}{\tan \theta_c} \right| \right). \quad (4)$$

Where δv_w and $\delta \theta_c$ are measurement errors of v_w and θ_c , respectively.

Experiments were made in order to estimate the $\delta\theta_c$; that is, the reflection coefficient measurements on the steel tempered at 973K were repeated 20 times under the same conditions (the temperature in water was maintained at 296.4 ± 0.1 K) and the Rayleigh critical angles were determined from the phase change of the reflection coefficient, where an incident angle at which the slope of the phase curve became steepest was defined as the Rayleigh critical angle. The standard deviation of the Rayleigh critical angle obtained from the above experiments had a tendency to increase with frequency. We regarded the standard deviation at 120MHz, 3.3664×10^{-4} , as the $\delta\theta_c$ in Equation(4).

In general, the sound velocity in water was functional in temperature. In a temperature range from 293K to 299K, the variation of the velocity in water with temperature is about $2.83 \text{ms}^{-1}\text{K}^{-1}$. Therefore, fractional variation of the velocity is approximately given by $\delta v_w/v_w \approx 0.0019\delta T$, where δT is the variation of the temperature. Substituting $\delta v_w/v_w$ and $\delta\theta_c$ determined above into Equation(4), we obtain

$$\delta v_{sw} = v_{sw} \left(0.0019\delta T + \left| \frac{3.3664 \times 10^{-4}}{\tan\theta_c} \right| \right) \quad (5)$$

In measurements on steels, putting $\theta_c=30^\circ$, $v_{sw}=2980 \text{ms}^{-1}$, and $\delta T=0.1$ K as an error in the temperature measurement, then δv_{sw} is about 2.31ms^{-1} from Equation(5). Accordingly, in the results presented hereafter, It is considered that the measured velocities contain about $\pm 2.31 \text{ms}^{-1}$ of error.

Measurement Resolution

In measuring the velocity at a small area, it is important to understand quantitatively the spatial resolution of the measurement because the spatial resolution depends on the operating frequency and the degree of focusing ability of the spherical lens. To estimate the spatial resolution, an experiment was made using the quenched steel with a sharp edge; that is, the sensor was linearly scanned crossing the edge of the specimen at $5 \mu\text{m}$ intervals keeping the incident angle at the Rayleigh critical angle (30.37°), and the reflected wave received at each scanning position was analyzed by the FFT analysis. Figure 2 shows the changes in the amplitude of the reflected wave with the displacement of the sensor. The rapid change in the amplitude curve means that the edge of the steel passed over the focusing area of the spherical lens. Since the slope of the curve in the rapid change region becomes steeper with increasing the frequency, it is clear that the spatial resolution becomes higher with the frequency. The sweep distances over which the amplitude increased from 15% to 85% were about $85 \mu\text{m}$, $38 \mu\text{m}$ and $26 \mu\text{m}$ for frequency at 40MHz, 80MHz and 120MHz, respectively. Thus, the frequency dependence of the spatial resolution was approximately estimated from the sweep distance.

Reflection Coefficients for Heat Treated Steels

Figure 3 shows the phase curves of the reflection coefficients measured for the quenched steel. The phase changes by 2π rad at a Rayleigh critical angle and no frequency dependence of the phase curve is observed; therefore, Rayleigh wave velocity at each frequency can be precisely determined from the phase curves. Results for tempered steels were almost the same as that obtained for the quenched. On the other hand, the phase curves for the annealed steel shown in Figure 4(a) are anomalous at frequency region higher than about 90MHz; that is, the phase does not fully change 2π rad but only wobbles at the

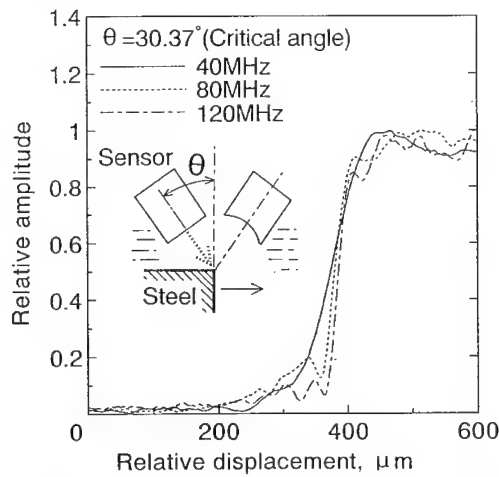


Figure 2. Changes of amplitude for the reflected wave when the sensor was scanned over the edge of steel.

Rayleigh critical angle. This is because the attenuation of the Rayleigh wave is significant at such high frequency owing to absorption losses in the solid.^{6,7} In this case, we have difficulty in determining precisely the velocity from the phase curves at high frequency region. However, we can fortunately determine the velocity from the modulus curve of the reflection coefficient even at the high frequency region, because the modulus curves in the entire frequency region exhibit a sharp dip at the critical angle as shown in Figure 4(b).

Before examining the effect of the absorption loss, let us here estimate the attenuation coefficient of the annealed steel. In generally, the behavior of the reflection coefficient in the vicinity of the critical angle is determined by poles and zeros of $R(k_x)$ close to the real axis in a complex k_x plane;⁷ and the value of the zero changes with the loss parameter d which is attenuation per wavelength. When the zero crosses the real axis of the complex plane, the loss parameter becomes the critical value d_c ; and because the loss parameter d is a function of frequency, the critical value d_c corresponds to the critical frequency f_c which is the frequency of least reflection.⁷ Then, the critical loss parameter for longitudinal wave d_{lc} is written as

$$d_{lc} = \lambda_{lc} \alpha_l = v_l \alpha_l / f_c. \quad (6)$$

Where λ_{lc} is wavelength corresponds to the critical frequency and α_l is the attenuation of the longitudinal wave. The frequency of least reflection f_c is about 86MHz from Figure 4(b); and the loss parameter d_{lc} was calculated to be 0.03328 on conditions that $v_l=5900\text{ms}^{-1}$, $v_t=3200\text{ms}^{-1}$, $v_w=1495\text{ms}^{-1}$ and $\alpha_l=4\alpha_t$. Thus, α_l is calculated to be 485m^{-1} using Equation(6); and assuming that the attenuation coefficient is proportional to the forth power of the frequency, the attenuation coefficient can be estimated as $8.8664 \times 10^{-30} \text{ s}^4 \text{ m}^{-1}$.

Figure 5 shows behaviors of the phase curve and the modulus curve calculated with the above estimated attenuation coefficient. These figures are similar in frequency dependence to those shown in Figure 4. This means that the estimated attenuation coefficient is adequate. The Rayleigh wave velocity calculated with an angular position of the minimum in Figure 5(b) agreed precisely with the theoretical value⁸ calculated with elastic constants for isotropic material and density; therefore, it is considered that the Rayleigh wave velocity of the annealed steel determined from the modulus curve is independent of the absorption losses in the material.

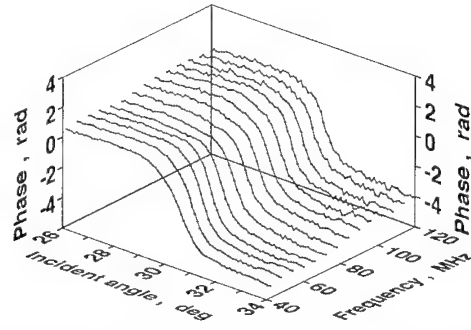


Figure 3. Measured phase curves of the reflection coefficients for the quenched steel.

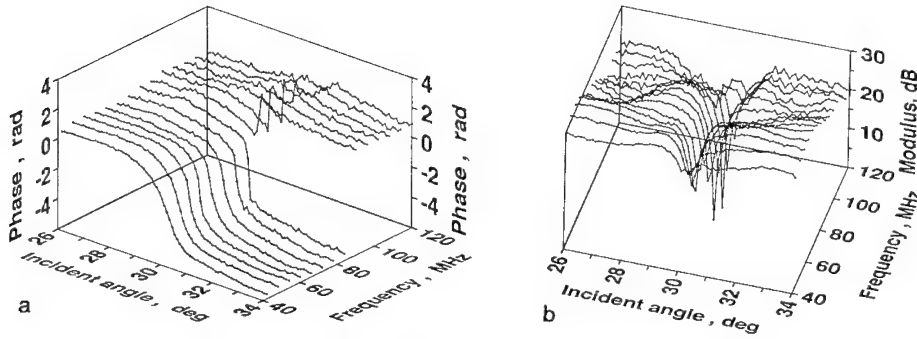


Figure 4. Measured reflection coefficients for the annealed steel: (a) phase curves; (b) modulus curves.

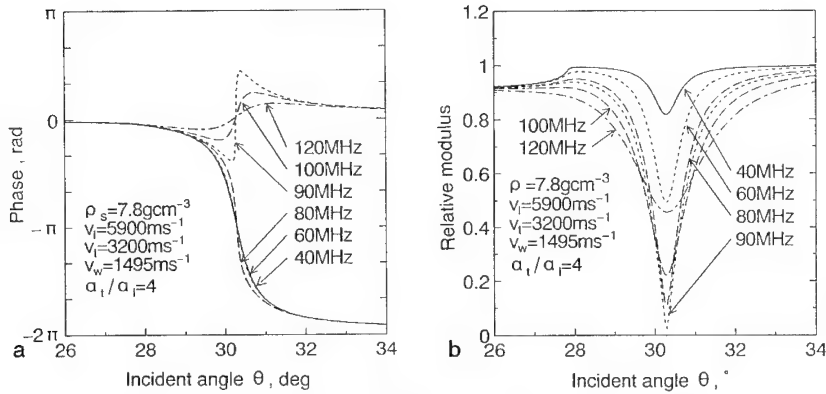


Figure 5. Frequency dependence on reflection coefficients calculated for the annealed steel: (a) phase curves; (b) modulus curves. Longitudinal wave attenuation coefficient of $8.86 \times 10^{-30} \text{ s}^4 \text{ m}^{-1}$ was used.

Rayleigh Wave Velocities for Heat Treated Steels

Figure 6 shows Rayleigh wave velocities measured at 120MHz for various kinds of heat treated steels. Theoretical values calculated by using Equations(1), (2) and (3) with

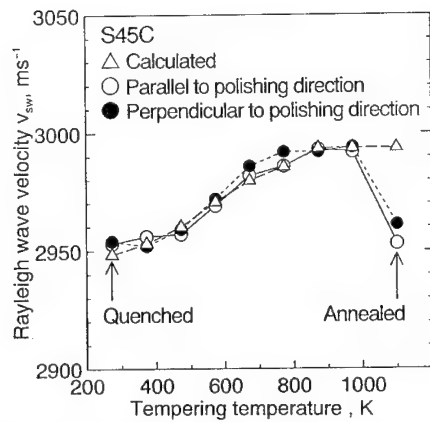


Figure 6. Measured at 120MHz and calculated results of Rayleigh wave velocities for heat treated steels.

macroscopic elastic constants for isotropic materials and densities also shown in Figure 6. For the quenched and the tempered steels, the measured values well agree with the theoretical values. This means that the velocities measured on these steels characterize exactly the macroscopic elastic properties of the materials. For the annealed, however, the measured and calculated value differ remarkably from each other. This suggests that the microstructure of materials should have great influence on the measured velocities. Figure 7 shows typical micrographs of heat treated steels. The quenched and the tempered steel have the fine structure which is composed of martensite or tempered structure with finely dispersed carbides; on the other hand, the annealed steel has the dual-phase structure of ferrite and pearlite. In the measurement at 120MHz for the annealed steel, where the spatial resolution or the size of the measurement area is comparable with the size of each phase, it is considered that effects of a difference in the velocity of each phase and/or an elastic anisotropy on the measured velocity should be remarkably enhanced. Figure 8 shows that changes of the measured velocity with the measuring position for the annealed steel and its frequency dependence. The velocity fluctuates with the measuring position and the fluctuation becomes larger with frequency. This is partially because the large fluctuation at high frequency was caused by inhomogeneity of the coarsely mixed structure as mentioned above. At frequency less than 60MHz, on the contrary, the velocities remain almost constant. This result indicates that the effect of the inhomogeneity of the dual-phase structure disappeared because the spatial resolution at such low frequency is larger than the size of each phase or the grain size.

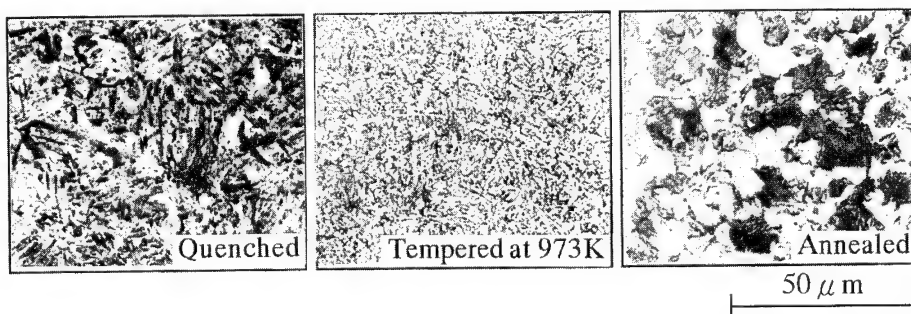


Figure 7. Typical microstructures of steel quenched, tempered at various temperatures and annealed.

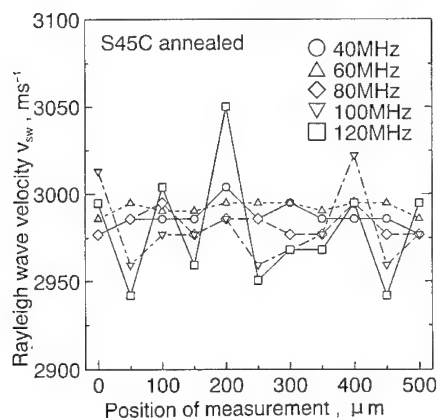


Figure 8. Variations in Rayleigh wave velocities of annealed steel with measuring position.

CONCLUSIONS

The Rayleigh wave velocity obtained by analyzing the ultrasonic reflectivity measured at a small area was found to be a useful parameter for the estimation of mechanical properties at the small area. For the quenched and the tempered steel specimens, the measured velocities characterized exactly macroscopic elastic properties of materials, and were independent of absorption losses of materials. Improving the resolution by using the higher frequency, it might be possible to estimate acoustic properties and mechanical properties of a fine grain by measuring the reflectivity.

Acknowledgements

The authors would like to thank Dr. Tsukahara, Mr. Nakaso and Mr. Ohira of Toppan Printing Co., Ltd for valuable advice. This work was supported by a Grant-in Aid for Science Research from Iketani Science and Technology Foundation and the Ministry of Education, Science and Culture, Japan.

REFERENCES

1. F.R. Rollins, Jr., Ultrasonic Reflectivity at a Liquid-Solid Interface near the Angle of Incidence for Total Reflection, *Appl. Phys. Lett.*, 7-8, 212 (1965).
2. G.L. Fitzpatrick and B.P. Hildebrand, Near Surface Flaw Detection by Ultrasonic Critical Angle Imaging, *Journal of Nondestructive Evaluation*, 3-4, 201 (1982).
3. Y. Tsukahara, N. Nakaso and K. Ohira, Angular Spectral Approach to Reflection of Focused Beams with Oblique Incidence in Spherical-Planar-Pair Lenses, *IEEE Trans. Ultrason. Ferroelec. Freq. Contr.*, 38-5, 468 (1991).
4. T. Aizawa and J. Kihara, Ultrasonic Microscopic Evaluation of PVD/CVD Coated Hard Materials, in: "Residual Stress III: Science and Technology Vol.1," H. Fujiwara, ed., Elsevier Science Publisher, London (1992).
5. I. Ihara, A. Shimamoto, K. Tanaka, T. Aizawa and Y. Tsukahara, Microscopic Characterization of Elastic Property on Surface Damaged Layer of MnZn Ferrite by using an Ultrasonic Micro-Spectrometer, *Proc. 70th JSME Fall Annual Meeting Vol. B*, 522 (1992).
6. F.L. Becker and R.L. Richardson, Influence of Material Properties on Rayleigh Critical-Angle Reflectivity, *Journal of the Acoustical Society of America*, 51-5, 1609 (1972).
7. H.L. Bertoni and T. Tamir, Unified Theory of Rayleigh-Angle Phenomena for Acoustic Beams at Liquid-Solid Interfaces, *Appl. Phys.*, 2, 157 (1972).
8. I.A. Viktorov, "Rayleigh and Lamb Waves, Physical Theory and Applications," Plenum Press, New York, (1967).

ULTRASONIC BACKSCATTERING AS A FINGERPRINT TECHNIQUE FOR IDENTITY AND INTEGRITY VERIFICATION OF COMPONENTS

Herbert H. Willems¹ and Esther Wogatzki²

¹Fraunhofer-Institute for Nondestructive Testing
University, Building 37
D-66123 Saarbrücken, Germany

²GNS Gesellschaft für Nuklear-Service
Lange Laube 7
D-30159 Hannover, Germany

INTRODUCTION

During the interim storage of spent fuel rods the verification of the identity as well as of the integrity of special shielding casks containing final disposal packages has to be guaranteed by applying appropriate safeguards measures over a period of up to 50 years until a geological repository goes into operation. The casks to be verified are made of cast iron (GGG 40) and consist of the actual final disposal package and a cylindrical shielding cask with a height of about 6 m and a diameter of about 1.5 m which is closed with a screwed-on lid. It is planned to link the lid to the cask by a short weld seam, so that the lid can only be removed by destroying the weld. The identification of the weld allows for statements on the integrity of the cask as well as on its identity. The latter is, in addition, supported by non-reproducible cask characteristics.

As the smooth surface of the cask without any openings prevents the application of conventional sealing methods like, for example, metal cap seals, other techniques have to be developed. In the case of storage cans (wall thickness: 1mm) for special nuclear material previously investigated¹, the use of guided ultrasonic waves was proposed using reflections signals obtained from a weld and its individual geometry as a fingerprint. Our approach is based on the material's microstructure as characterized by its grain and precipitation structure, which represents a non-reproducible fingerprint². The microstructural characteristics can be converted into an ultrasonic signal using the backscattering technique. Backscattering signals provide an unambiguous representation of the microstructure considered and hence allow the recording of microstructural fingerprints in a reproducible way. In this contribution we present results on the influence of various parameters on the reproducibility of ultrasonic backscattering signals enabling us to define the conditions under which the backscattering technique can be used for the verification task.

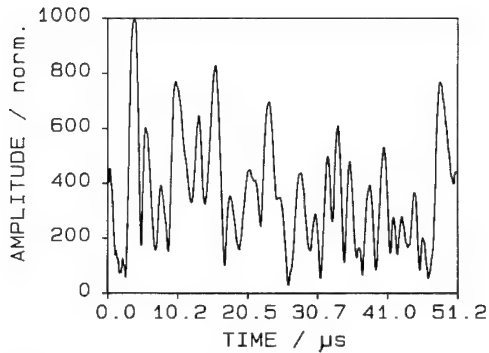


Figure 1. Ultrasonic backscattering signal from cast iron GGG 40 (2.5 MHz T-wave).

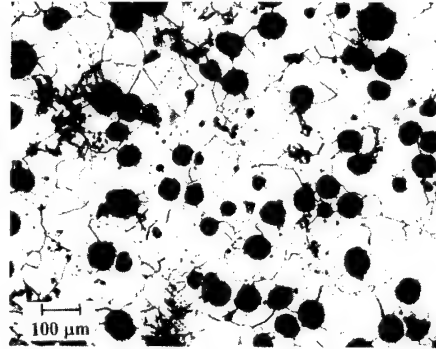


Figure 2. Metallographic image of the cast material GGG 40.

ULTRASONIC APPROACH

Background

In polycrystalline and/or multiphase materials ultrasonic scattering occurs at grain boundaries and phase boundaries due to a local mismatch in the acoustic impedance. Amplitude, phase and sound field characteristic of the scattered wavefield depend, apart from the microstructure, in particular on the frequency and the wave mode of the ultrasonic pulse. If the grain d is small compared to the ultrasonic wavelength λ , i.e., $d / \lambda \ll 1$, Rayleigh scattering is the dominant scattering mechanism. Then the scattering coefficient α_S is given by $\alpha_S \sim d^3 \cdot f^4$ with f being the ultrasonic frequency. A rectified ultrasonic backscattering signal (Figure 1) measured in pulse-echo technique may be expressed in the form

$$A_S(x, z, t) = A_N(t) + A_S(x, z = 0) \cdot \exp(-\alpha \cdot z) \cdot M(z). \quad (1)$$

$A_S(x, z, t)$ is the backscattered ultrasonic amplitude as a function of position x , of the sound path z and of time t . $A_N(t)$ is the contribution due to electronic noise which is negligible in case of sufficient signal amplitude ($A_S \gg A_N$). Apart from the noise contribution the backscattering signal is stationary, i.e., independent of time. $A_S(x, z = 0)$ is the initial amplitude of the backscattering signal at position $x = 0$. The term $\exp(-\alpha \cdot z)$ accounts for the ultrasonic attenuation along the sound path z where the attenuation coefficient α comprises both the scattering losses and the absorption losses. The function $M(z)$ in Eq. 3 describes the modulation pattern of the backscattering signal which is caused by the interference of all the backscattered waves (see Figure 1). This pattern represents an acoustic image of the microstructure along the sound path and thus a microstructural fingerprint of the measuring position which may be used for the verification of its identity. Any signal recorded under the same conditions at the same position will always show the same interference pattern whereas signals recorded at different positions will look more or less different. Therefore, the problem of identification basically requires a method which allows the evaluation of the similarity (or non-similarity) of two backscattering signals. This can be achieved by correlation analysis.

Signal Evaluation

The similarity of two digitized signals i, j each with p sampling points can be numerically

evaluated using their correlation coefficient CC. The correlation coefficient of two signals A_i , A_j is defined as⁴

$$CC_{ij} = \frac{\sum_{k=1}^p A_{ik} A_{jk} - \sum_{k=1}^p A_{ik} \sum_{k=1}^p A_{jk}}{\sqrt{\left[\sum_{k=1}^p A_{jk}^2 - \left(\sum_{k=1}^p A_{jk} \right)^2 \right] \left[\sum_{k=1}^p A_{ik}^2 - \left(\sum_{k=1}^p A_{ik} \right)^2 \right]}} \quad (2)$$

Here, A_{ik} is the amplitude of signal i at sample point k . For similar signals the correlation coefficient is close to 1. For uncorrelated signals the correlation coefficient lies around zero.

Even otherwise uncorrelated backscattering signals show some similarity due to the exponentially decaying shape of the signals which is accounted for by the attenuation term $\exp(-\alpha \cdot z)$ in Eq. 2. This leads to an offset contribution in the correlation coefficient which can be compensated by multiplying the recorded signals with the correction term $\exp(+\alpha \cdot z)$. The attenuation coefficient α is obtained from a regression analysis.

EXPERIMENTAL PROCEDURE

Samples

In order to prove the suitability of the backscattering technique with regard to the verification task, it was necessary to determine the influence of the parameters which are relevant to the interference structure of the ultrasonic signal. Therefore, the dependence of the signal on the frequency, the pulse length, the transducer (including the probe wedge in the case of angular transmission) and the measuring position has been studied. The experiments were performed using longitudinal waves (L) in perpendicular transmission, shear (transversal) waves (T) in 45° and 60° transmission and surface waves also called Rayleigh waves (R). The nominal frequencies of the (commercially available) transducers used for the experiments were 2.5 MHz and 5 MHz.

For the experiments, a sample of the original cask material, with a size of 190 mm x 100 mm x 40 mm, was provided. The material is ductile cast iron GGG 40. A metallographic image of its microstructure is shown in Figure 2. The mean grain size of the ferrite phase is about 90 μm , the mean diameter of the graphite spheres is about 50 μm . The volume fraction of the graphite amounts to approximately 20 %. The graphite phase having a particle size comparable to the ferrite phase essentially contributes to the ultrasonic scattering because of the large difference in acoustic impedance between graphite and ferrite (impedance ratio 1:9). Additionally, experiments were performed using a sample of comparable size containing a weld seam.

Measuring Set-Up

The backscattering measurements were performed with an ultrasonic test device developed⁵ at the IzfP. The system enables the generation of ultrasonic pulses with defined frequency and pulse-length. The frequency range is 2.5 - 30 MHz adjustable in steps of 0.1 MHz. The pulse-length can be set between 5 λ - 15 λ adjustable in steps of 1 λ .

The signals received are rectified, amplified and finally digitized at a sampling rate of 20 MHz using an 8 bit A/D-converter. One signal consists of 1024 data points resulting in a ultrasonic time-of-flight 50.12 μs . This time-of-flight corresponds to an ultrasonic sound path of about 78 mm for shear waves and about 141 mm for longitudinal waves, respectively, in

the material considered. In a subsequent averaging unit up to 1024 single signals can be added up for signal averaging in order to improve the signal-to-noise ratio. After recording the backscattering signals are transferred from the ultrasonic device to a personal computer in order to perform the signal evaluation. The total measuring time takes only a few seconds.

RESULTS

Frequency and Pulse-Length Variation

The excitation frequency of the ultrasonic pulse was varied in steps of 100 KHz in the range from (center frequency - 0.5 MHz) to (center frequency + 0.5 MHz). Figure 3a shows the signal decorrelation as a function of the frequency change Δf . For all test series a similar behaviour is obtained. Here, a frequency change of about 0.4 MHz leads to a decrease of the correlation coefficient from 1 to about 0.8.

The pulse-length of the excitation burst was varied in steps of one wavelength between 5λ and 15λ . The result of the pulse-length variation ΔP is shown in Figure 3b. ΔP refers to the initial pulse-length of 5λ . A decrease of the correlation coefficient below 0.8 is found for $\Delta P > 3\lambda$. By changing the pulse-length the volume of the microstructure contributing to the backscattered amplitude $A(t)$ at the same time is changed as well. As a result the interference pattern changes, leading to the observed decrease in the correlation.

Position Variation

From Figure 4 follows that a change in position of 1 mm already causes a distinct decorrelation. This means that the interference pattern strongly depends on the measuring position. The decorrelation takes place the faster the higher the frequency because the wavelength and thus the spatial coherence length decreases with increasing frequency. A decrease of the correlation coefficient below 0.8 is obtained at a position change of 1/3 mm in the case of both 5 MHz longitudinal wave and 5 MHz shear wave whereas at a frequency of 2.5 MHz a change of about 0.5 mm is required.

Influence of Transducer and Wedges

In order to assess the impact of individual transducer characteristics, backscattering signals were recorded at the same position with up to 6 transducers of the same type and then compared to each other. Measurements were performed with 2.5 MHz respectively 5 MHz

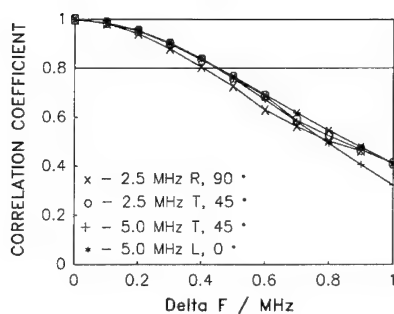


Figure 3a. Influence of frequency variation on the decorrelation of ultrasonic backscattering signals.

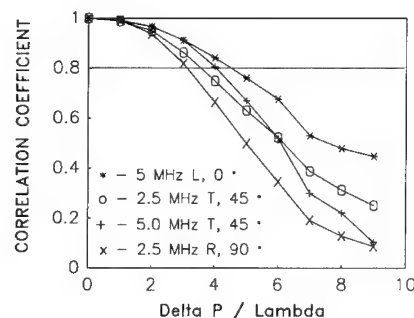


Figure 3b. Influence of pulse-length variation on the decorrelation of ultrasonic backscattering signals.

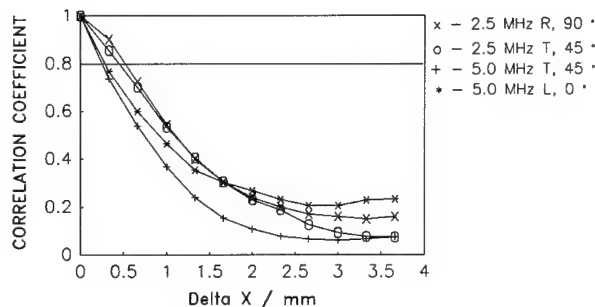


Figure 4. Decorrelation of ultrasonic backscattering signals by position variation.

T-waves using 45° transmission and with 5 MHz L-waves using perpendicular transmission. Only for the 2.5 MHz /45° T- wave transducers all correlation coefficients lie above 0.8. For the 5 MHz L-wave transducers, however, all values are below 0.8 indicating a large scatter of the individual transducer characteristics which may be attributed to variations in center frequency, radiation characteristic and sound field symmetry.

Additionally, the impact of the wedges to which the ultrasonic transducers are screwed on for angle transmission on the signal reproducibility was investigated for the case of 2.5 MHz / 45° - T-waves. Therefore, signals were recorded with the same transducer at the same position using five different wedges of the same type and all possible combinations of two signals were evaluated. The lowest correlation coefficient obtained was 0.926 (mean: 0.956) indicating that the wedges are almost identical in their ultrasonic properties.

Reproducibility and Individuality of the Backscattering Signal

In order to evaluate their reproducibility 20 signals were recorded at the same position. All possible signal combinations were evaluated resulting in 190 correlation coefficients for each test series. For every single measurement, the transducers were newly positioned. A precise positioning was ensured by using a stop bracket fixed to the sample. Mean, maximum, minimum and standard deviation of the correlation coefficient distribution of the individual testing modes are shown in Table 1. The reproducibility is excellent for the 2.5 MHz R- and T-wave as well as for the 5 MHz T-wave. All correlation coefficients are above 0.85. Only for 5 MHz L-waves in perpendicular transmission some data are below 0.8. This is attributed to the fact that in the case of perpendicular transmission the signals are much more influenced by small coupling variations than in the case of angular transmission.

The measurement and signal evaluation for the assessment of the signal individuality corresponds to the procedure described before with the difference that the backscattering signals were recorded at 20 different positions. The results are also given in Table 1. As expected, the mean values are now close to zero and the maximums are all below 0.51.

Tests of reproducibility and individuality were also performed on a sample containing a weld of 2 cm depth and 2 cm width. Ultrasound using 2.5 MHz T-waves was transmitted perpendicularly to the weld from the cask material across the weld (measuring geometry A) as well as in the weld direction along the weld (measuring geometry B). In order to obtain a sufficiently long sound path within the weld, 60° transmission was used. For both measuring geometries the results are essentially comparable to those obtained for the cask material as can be seen from Table 1.

Table 3. Statistical parameters obtained from the evaluation of the correlation coefficients for the tests with respect to reproducibility (R) and individuality (I).

Measuring Mode	Sample*	Mean		Standard Deviation		Minimum		Maximum	
		R	I	R	I	R	I	R	I
2.5 MHz R 90°	CM	0.980	0.033	0.013	0.13	0.935	-0.30	0.996	0.45
2.5 MHz T 45°	CM	0.991	0.046	0.005	0.12	0.967	-0.27	0.998	0.47
5.0 MHz T 45°	CM	0.954	0.093	0.026	0.09	0.856	-0.15	0.990	0.35
5.0 MHz L 0°	CM	0.885	0.115	0.079	0.15	0.614	-0.37	0.992	0.46
2.5 MHz T 60°	WS - A	0.969	0.090	0.010	0.15	0.938	-0.27	0.990	0.43
2.5 MHz T 60°	WS - B	0.954	0.083	0.022	0.14	0.892	-0.24	0.989	0.51

*CM - Cask Material, WS - Weld Seam (A, B: measuring geometries, see Text).

Statistical Reliability

In order to evaluate the reliability of the ultrasonic technique with respect to misinterpretations, it is necessary to know the number of independent characteristics contained in a backscattering signal. Obviously, the number of features is proportional to the total length of the signal (here 50 μ s) on the one hand, and on the other it depends on the bandwidth of the electronic signal demodulation. The latter is 2.5 MHz corresponding to a time resolution of 0.4 μ s. This means that, at most, 125 independent signal features can be expected within 50 μ s. The real number is actually smaller due to the fact that the spatial coherence length of the ultrasonic pulse, that is the spatial region which contributes to the scattered signal at the same time and thus limits the time interval between independent scattering indications, is about half the pulse-length. At 2.5 MHz T-waves, the wavelength is 1.24 mm in the considered material. At a total pulse-length of 5λ used for the measurements half the pulse-length comes to 3.1 mm corresponding to a time-of-flight of 1 μ s yielding approximately 50 independent features.

To substantiate these considerations a computer programme was written enabling the simulation of backscattering signals. By means of a random number generator, 50 signals with a defined but variable number of independent characteristics were generated during each run providing 1225 signal combinations and the standard deviation σ of the distribution of the resulting correlation coefficients was determined. In Figure 5, σ is shown as a function of the number of independent characteristics which was varied between 5 and 100. If one compares the experimentally determined standard deviations ranging from 0.12 to 0.15 with the

simulated data, one obtains in fact about 50 to 60 independent characteristics in agreement with the estimations given above.

Using the 2.5 MHz/45° - signals recorded at the cask material, the actual dependence of σ on the number of independent characteristics was checked for the measured signals. By taking only a part of the signals for the calculation of the correlation coefficients the number of independent characteristics was stepwise reduced assuming that the number is proportional to the signal length. As can be seen from Figure 5, the agreement with the result of the simulation is very good. The best fit is obtained assuming 53 independent characteristics for the full signal.

Based on these considerations it is possible to estimate the reliability of the ultrasonic technique with respect to the verification task in a more quantitative way. In all tests of individuality the experimentally determined standard deviation of the distribution of the correlation coefficients, which is found to be a normal distribution (Figure 6), lies below 0.15. Let us assume that a correlation coefficient ≥ 0.8 is required for correctly identifying a cask. Then, the gap between the required threshold value of 0.8 and the mean (≈ 0) becomes larger than 5σ . Assuming a Gaussian distribution the probability P_I that another cask or an another location gives a signal similar to the identification signal of the cask under consideration comes to less than $5.7 \cdot 10^{-7}$, i.e., the probability that a cask or a weld is wrongly identified or mistaken ('false acceptance') is negligible.

A similar consideration holds for the signal reproducibility. In this case, the correlation coefficients are, strictly speaking, not normally distributed since the distribution is asymmetric with regard to its mean. In the range below the mean, however, the actual distribution may be approximated by a Gaussian. Except for one test series, the gap between the mean and the threshold of 0.8 amounts to $> 6\sigma$ (see Table 1). This means that the probability P_{II} of not identifying a cask or a weld, i.e., 'false alarm', is less than $2.0 \cdot 10^{-9}$. Consequently, the probability P_C of a correct identification is given by the complement to the sum of P_I and P_{II} yielding $P_C = 1 - (P_I + P_{II}) = 0.99999943$.

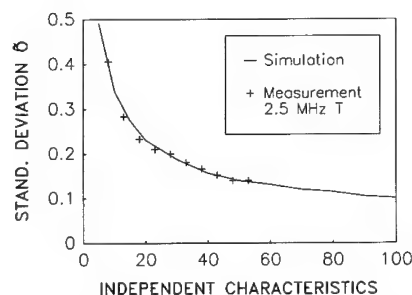


Figure 5. Standard deviation of the distribution of correlation coefficients as a function of independent signal characteristics.

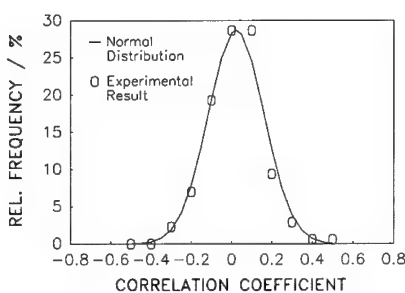


Figure 6. Distribution of correlation coefficients as obtained from individuality test.

DISCUSSION

The results presented allow for the assumption that the ultrasonic backscattering technique is suitable for the task considered. Proof of the cask integrity is achieved by the identification of the weld seam since a newly applied weld would give a different backscattering signal. Thus the proof of integrity would mean, if positive, a proof of identity

at the same time, i.e., both requirements are met by just one measurement. A negative test result, however, implies the possibilities that either the weld seam has been tampered with or that the cask has been replaced. To avoid such ambiguity, it would seem useful to record two signals per cask, one from the cask and one from the weld. According to Figure 4 the positioning of the transducer must be as precise as 0.3 mm in order to reproduce the signal correctly. This can be attained easily by providing, for example, a stop bracket or a snug fit, thus forcing an exact positioning.

The results of frequency variation as well as pulse-length variation show the necessity of using well-defined electrical pulses for the ultrasonic excitation. The realization of suitable ultrasonic transmitters is state-of-the-art. Some development, however, would be needed in order to set up a portable, battery driven system. The effects of equipment aging, which may play a role in long-term applications, can be dealt with by using digital techniques for signal generation and signal processing.

Though transducers of the same type have led to comparable signals in some of the tests one has to ensure in any case that the transducers to be used are interchangeable. Therefore, it is proposed that the correlation coefficient of signals recorded with different transducers at the same position should be at least > 0.9 . This requirement can be achieved by applying appropriate selection criteria. The same argument holds for the angle wedges.

CONCLUSION

This work demonstrates that the ultrasonic backscattering technique is suitable for the identification and verification of components made of polycrystalline materials. Backscattering signals provide a non-reproducible fingerprint of the material's microstructure, which can be considered as absolutely proof against tampering. As a threshold value for the correct identification of a fingerprint signal, a correlation coefficient with the reference signal of at least 0.8 is recommended. In order to obtain reproducible signals a well defined excitation signal as well as precise positioning of the ultrasonic transducer is required. In the considered case of cast iron the use of 2.5 MHz shear waves in angular transmission turned out most appropriate. Apart from the high reliability, the ultrasonic technique provides easy operation and fast measuring times. It is planned now to develop a portable prototype system for inspection purposes.

ACKNOWLEDGEMENT

The work presented in this article was part of a feasibility study commissioned by GNS within the framework of a project sponsored by the German Ministry of Research and Technology under contract # KWA 7908/5.

REFERENCES

1. K.D. Bones, C.C. Holt, and R.P. Holt, Verification of nuclear material (SNM) containers by means of ultrasonic inspection and fingerprinting, Proc. of the 5th Annual Symp. on Safeguards and Nuclear Material Management, Versailles (1983).
2. P. Höller, German Patent DE 33 19 102 C2 (1987).
3. A.B. Bhatia, "Ultrasonic Absorption", Clarendon Press, Oxford (1967).
4. E. Walpole and R. H. Myers, "Probability and Statistics for Engineers and Scientists", The Macmillan Company, New York (1972).
5. Willems, R. Neumann, S. Hirsekorn, and K. Goebbels, Gefügeanalyse an Stählen mittels Ultraschall-Streuung, IzfP-Report # 820520-TW (1982).

AIR-COUPLED ULTRASONIC SYSTEM FOR DETECTING DELAMINATIONS AND CRACKS IN PAINTINGS ON WOODEN PANELS

A. Murray¹, E.S. Boltz², M.C. Renken², C.M. Fortunko²,
M.F. Mecklenburg³, and R.E. Green, Jr.¹

¹Department of Materials Science and Engineering and the Center for
Nondestructive Evaluation, The Johns Hopkins University, Baltimore, MD,
21218

²National Institute of Standards and Technology, Boulder, CO, 80303

³The Conservation Analytical Laboratory, The Smithsonian Institution,
Washington, D.C., 20560

ABSTRACT

It has been established that the risk of damage to paintings on wood ("panel paintings") increases with the presence of cracks, delaminations, and their associated stress concentrations. Such flaws can originate and increase in size as a result of fluctuations in temperature and relative humidity, as well as shock and vibration. Many internal flaws cannot be detected either visually or by traditional testing techniques, and it is difficult, therefore, to assess the risk transportation poses to panel paintings.

Air-coupled ultrasound has been used to assess the condition of two panel paintings (*Parental Admonition* [a copy of the original] and *Women Gathering Yucca Plants*), in a non-contact, non-intrusive manner; this method provides information complementary to that given by radiography. It has been demonstrated that the ultrasonic system is clearly more suitable for detecting specific types of flaw, such as in-plane cracks and delaminations. The system enables measurements to be easily made of highly anisotropic and inhomogeneous materials such as wood.

The ultrasonic system used in this study has a superior signal-to noise ratio because it uses efficient transducers, low noise pre-amplifiers, and a phase-sensitive superheterodyne ultrasonic system that has analog signal averaging and filtering components. The signal can be exploited to yield both amplitude and phase information. The ultrasonic system also incorporates a mechanical scanner to produce easily interpreted two-dimensional images of large areas of paintings to give a clear indication of their condition. The results can be further enhanced by using image processing techniques.

INTRODUCTION AND BACKGROUND

Wood has often been used for a support for paintings. The structure of a typical panel painting may include the following layers: the wooden support (often oak or poplar); the

ground or gesso layer (gesso is rabbit skin glue and calcium carbonate or calcium sulfate), which sometimes includes linen; the underdrawing; the paint layer; the varnish; and any retouchings. Later artists used both solid wood and wood products such as hardboard for supports, with surface layers that include gesso, gesso and linen, and paper. Throughout the centuries, some works of art and furniture, such as marquetry pieces, have a top surface of veneer (a thin layer of wood).

Catastrophic failure is much more likely in panels with severe stress concentrations caused by cracks and delaminations. For this reason it is imperative to detect, locate, and treat these flaws. By maintaining constant relative humidity, the lifetime of these artifacts can be prolonged; however, this high-maintenance environment cannot be achieved in all circumstances, for example during the transportation of works of art. If flaws can be detected, repairs can be made and predictive computer models (using finite element analysis) can anticipate the conditions that could lead to failure of the object. These conditions, including temperature and relative humidity changes and certain shock and vibration impacts, can then be avoided. It is possible to use computer models to predict the stresses in the individual components and in the entire painting, once any flaws have been detected.¹

Detecting flaws in panels is not a trivial technical problem because wood is a highly anisotropic and inhomogeneous material and because conventional techniques cannot always locate cracks and delaminations. Moreover, working with art objects imposes restrictions that are not necessary when testing industrial materials. For example, contact ultrasonic methods should be avoided because they require pressure to transmit and receive the ultrasonic signals.

Air-Coupled Ultrasound

Much has been written about nondestructive testing methods used to examine paintings.² Flaws such as delaminations and cracks at certain angles have not been detected with traditional techniques such as radiography because the density change at these flaws is too small to be seen. The ultrasound technique is very useful in detecting delaminations and cracks oriented perpendicular to the sound beam because the signal is stopped by any delaminations and the amplitude is registered as zero. When a crack is at an angle, both ultrasonic and radiographic techniques can be used to advantage.

Air-coupled ultrasound uses air as a couplant, which does not saturate the material being examined, change its properties, or leave residues and therefore brings no danger of damage or contamination as other couplants do. This is true as long as the power or amplitude of the sound-wave is not too great.

The background and previous air-coupled ultrasound work has been discussed before.³ The low signal-to-noise which is one of the major limitations of the air-coupled ultrasound technique, can now be overcome through the judicious selection of the critical components, including transducers, transmitting and receiving electronics, and the use of appropriate signal processing methods. Because of transducer limitations, operation is not possible in the pulse-echo mode, where only one transducer is used to send and receive the signal; this means that both sides of the painting or sample need to be accessible.

Materials with low acoustic impedances are more easily examined with air-coupled ultrasound because the acoustic impedance mismatch with air is low. Examples of materials that can be examined include: ligneous materials, foams, fibre-reinforced composites, rubber, paper, and non-metallic composites. Using non-contact ultrasound, the wood industry has made distance measurements and has located cracks and holes in wood, decay in lumber, and blows (delaminations) within hardboard, insulation board, and

particle board.⁴ Air-coupled ultrasound would be extremely advantageous in this field because of the coupling difficulties between the transducer and wood.⁵

The present work differs from past ultrasonic work on art objects, which used contact techniques with gels or pressure to examine stone, metal, and waterlogged wood, making measurements at specific points rather than over complete areas.⁶ The technique used here allows entire paintings to be examined and comparisons to be very easily made between local and adjacent points, thus enabling contextual information to be obtained. This paper is the culmination of research in which air-coupled ultrasound has successfully examined samples used to mimic panel paintings. The samples were made with different flaws (delaminations and cracks), supports (oak, poplar, and hardboard), and surfaces (paint, gesso, gesso and linen, paper, and veneer); each sample varied one of these parameters at a time.

EXPERIMENTAL SET-UP

The main component of the air-coupled ultrasound system in this work was the phase-sensitive superheterodyne measurement system that generated and processed the ultrasonic signals.⁷ It was linked to a commercial C-scan system which controlled the position of the two transducers on either side of the painting in the XY-plane. During the experiment, computer programs controlled the ultrasonic measurement and scanning systems. They also stored the data for the amplitude, phase, x and y positions, and the measurement system settings.

The system operated between 50 kHz and 5 MHz. The ultrasonic measurement system had modules that contained different components including: an IF oscillator and quadrature phase-sensitive detectors; a direct digital synthesizer; a high power gated RF amplifier; a broadband RF receiver; a mixer and IF amplifier; gated analog integrators; a coherent timer; and a 12-bit analog to digital converter (A/D converter).

The piezoelectric transducers used operated at 0.5 MHz and were spherically focused at around 5.08 cm (2.0 inches). During the experiments, the generating transducer was brought very close to the back surface of the sample, and was therefore focused within the wooden panel. The receiving transducer was focused on the sample-air interface of the front surface. This configuration ensured that the maximum energy entered the painting, to obtain the best resolution possible while maintaining the safety of the painting.

SAMPLES

The first painting examined came from the private collection of Dr. Hans Goedicke of Baltimore, Maryland. The painting, *Parental Admonition*, also known as *The Brothel Scene*, was a studiopiece (a copy from the same studio as the original). The original was painted by Gerard Terborch around 1654-55. The panel was oak and had a thickness of 3.6 mm (0.14 inches). Photographs of the front and back of the painting are shown in Figures 1a and 1b. The painting was of interest because of cracks in the wooden support, the craquelure or cracks in the paint layer, and because the painting had been "cradled". Cradling is an intrusive conservation treatment, used from the late 18th century until the early 20th century, where a secondary wooden support was added to constrain the panel dimensionally.

The second painting, *Women Gathering Yucca Plants*, is owned by the National Museum of American Art, the Smithsonian Institution (accession number 1969.64.9). It



Figure 1. (a) Photograph of the painting *Parental Admonition*, (b) verso

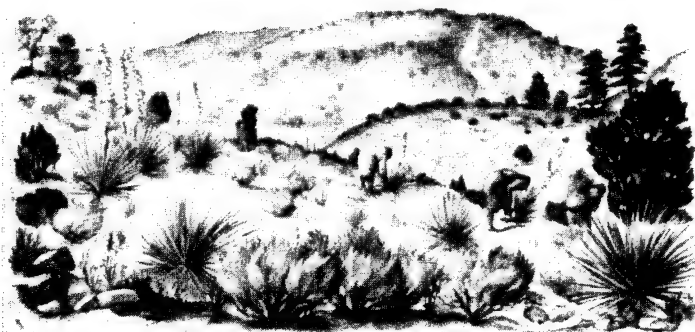


Figure 2. Photograph of the painting *Women Gathering Yucca Plants*, National Museum of American Art, Smithsonian Institution, transfer from the U.S. Department of the Interior

was painted by an unidentified artist in the 20th century and is shown in Figure 2. It is a watercolour and ink painting on illustration board (laminated paper board with paper layers glued to its surface) mounted on hardboard. The painting was approximately 6 mm (0.24 inches) thick. The illustration board had delaminated from the hardboard in certain, hard-to-determine areas.

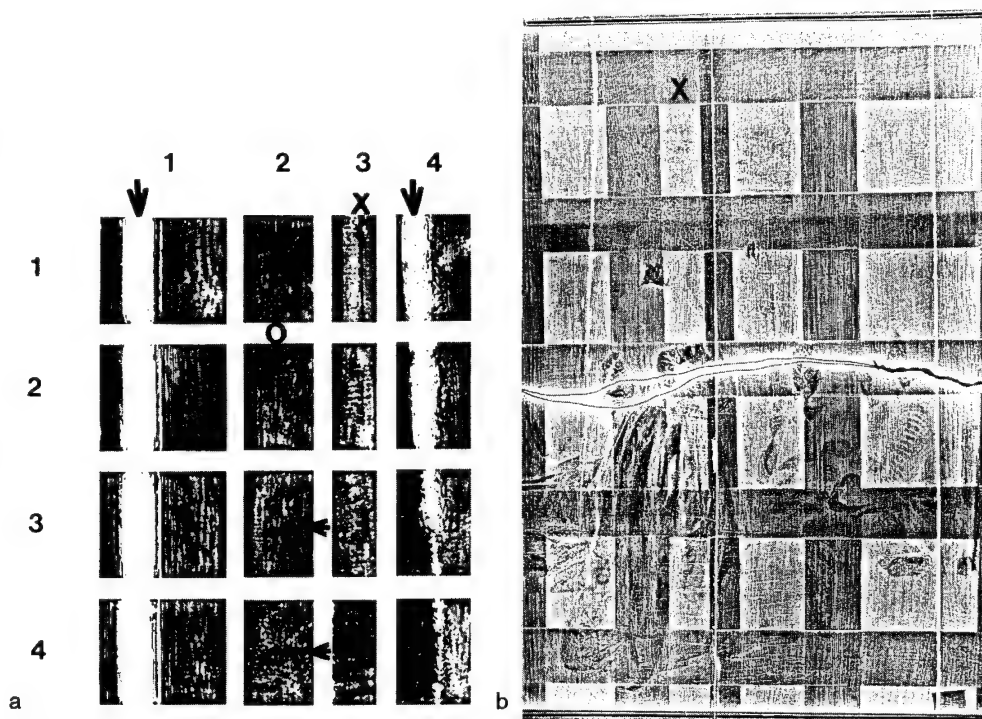


Figure 3. (a) Amplitude results from ultrasound scan of painting *Parental Admonition*, (b) xeroradiograph of the painting *Parental Admonition*: X is near closed crack which is hardly visible, and other features seen are the open cracks, the cradle, the hanging wire, and the image from the paint layer (x-ray tube was 130 cm or 51.2 inches above film, settings were between 40 and 60kV, 5 mA, and exposure time was one minute)

RESULTS

The results of air-coupled ultrasound investigations are shown using two-dimensional representations known as C-scans. Four ultrasonic parameters possible are: amplitude, phase, "processed" amplitude, and "processed" phase, where "processed" refers to the image processing technique of thresholding, where all the pixels above a certain grey level are shown as black and the pixels below the level are white. The first two types of amplitude scans will be shown in this paper. In the unprocessed amplitude images, the light areas indicate regions where the ultrasonic signal was easily able to penetrate the sample and the darker areas show where the signal was not been able to penetrate. Gradations of this can be seen in the unprocessed amplitude scan with the different grey levels. In the processed amplitude images, the light areas show regions where ultrasound has not been able to penetrate through.

Parental Admonition

Investigations were made of the cradled painting *Parental Admonition*. In this case, the cradle on the painting had not adhered well to the panel so that the signal-to-noise ratio was insufficient to allow an investigation of the entire painting. Thus ultrasonic scans could be performed only in the 16 areas between the battens of the cradle. A variety of artifacts can be seen in the ultrasonic C-scan of the amplitude results shown in Figure 3a.

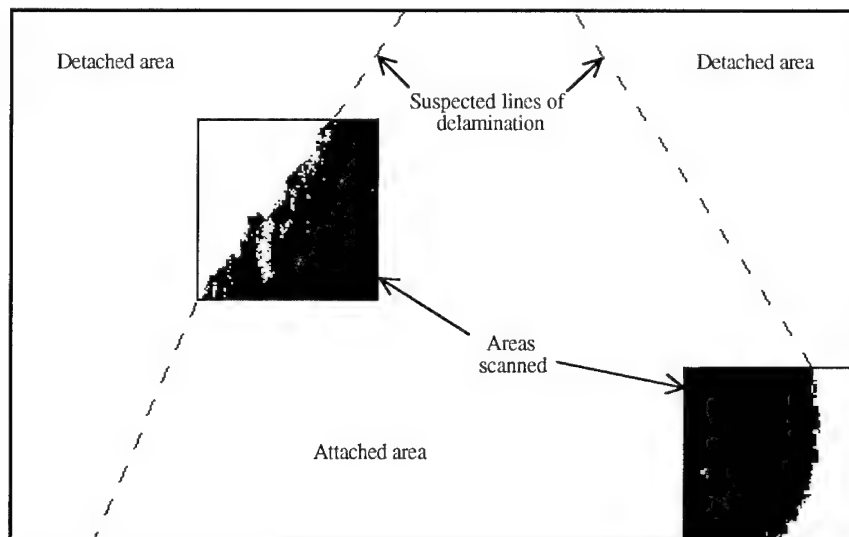


Figure 4. Outline of the front of the painting *Women Gathering Yucca Plants*, showing processed amplitude ultrasonic results from scanned areas (dotted lines show places at which it is suspected that the paperboard has become delaminated)

Two types of cracks exist: open cracks, where there is a visible opening to the other side, and closed cracks, where this is not the case. The open cracks appear as white lines (indicated by large arrows) and are larger on the ultrasonic image because of diffraction effects. Open cracks may mask other nearby artifacts, such as other cracks or paint craquelure. The closed cracks are dark lines (one is indicated by an "X").

Many of the vertical lines correspond to grain and closed cracks in the wood. Using the ultrasonic data only, it is difficult to distinguish the lines due to grain and those due to cracks. For example, in the two areas located in the second column and first and second rows, the lines could be indicative of either grain or cracks (adjacent to the circle).

The horizontal lines in the two areas in columns two and three and rows three and four are the craquelure running perpendicular to the grain. Some of the craquelure is identified by small arrows. Knots can also be seen in the first column, first row.

The closed crack marked by the X is detected with the ultrasound, but could not be detected visually or by xeroradiography (Figure 3b). In the positive xeroradiograph, the high density areas appear dark and those of low density appeared light. Visually it is very difficult to determine if the line indicates a crack running all the way through the panel, or merely an indentation in the wood.

Women Gathering Yucca Plants

Figure 4 shows the outline of the painting *Women Gathering Yucca Plants* (Figure 2), and the results from ultrasonic imaging of two areas within the painting. The processed amplitude scans are used as they show the delaminations most clearly.

The regions where the paperboard is detached from the hardboard are white. The dotted lines show the places at which it is suspected that the paperboard has become delaminated. The entire painting would need to be scanned to validate these lines. As expected, the xeroradiography (which is not shown) does not detect any delaminations.

IMPORTANCE AND FUTURE DIRECTIONS FOR ART CONSERVATION

Previous work has shown that air-coupled ultrasound can detect cracks and delaminations in panel paintings. The ultrasound can penetrate typical thicknesses of panel paintings, the thickest oak panel being 1.6 cm (0.63 inches), the thickest poplar panel being 2.0 cm (0.79 inches), and the thickest hardboard panel being 0.6 cm (0.24 inches). Thicker panels of all materials could probably be examined with additional signal processing such as time signal averaging.

The different ultrasonic results (amplitude, processed amplitude, phase, and processed phase) can be used to advantage to display certain types of flaws more clearly. Delaminations are most effectively shown with the processed amplitude scans, even when the paint layer has uneven thicknesses, while the amplitude scans show the degree of delamination. The amplitude scans better define cracks in radially cut panels, while the phase scans isolate them better in the tangentially cut panels. It is therefore useful to take both amplitude and phase measurements.⁸

Air-coupled ultrasound could also be used to examine paintings on canvas as the ultrasound easily penetrates paint, linen, and gesso layers. Flaws similar to those detected in panel paintings, such as delaminations between layers, could be found. Furniture pieces could also be investigated. It is conceivable that three-dimensional objects could be examined, although the results would be more complex and would need more interpretation.

As well as detecting delaminations and certain cracks, air-coupled ultrasound has other advantages over radiographic techniques. X-ray radiography and xeroradiography sometimes show the paint layer which may obscure other information found in a radiographic image. Also radiographic techniques cannot be used to examine a support with a lead white paint layer as x-rays aren't able to penetrate it, and therefore any information about the painting is masked. Image-processed ultrasonic amplitude scans, however, are not affected by changing paint layer thicknesses and ultrasound can penetrate the lead white paint layer.

The unique features of this system that make it of value in the conservation field should be emphasized. Ultrasonic components, such as the transducers, do not touch the material being examined. There is no evidence that the ultrasonic wave causes any damage. Moreover, a portable version of the system could be designed quite cheaply; for example, it could use less expensive transducers and a simpler transducer holder than were used in the experiments described here.

CONCLUSIONS AND FUTURE WORK

An air-coupled ultrasonic imaging system has been assembled for inspecting wooden panels. This system operates in the through-transmission mode, using two transducers, one on either side of the object; one transducer sends an ultrasonic signal and the other receives it. The signal has sufficient signal-to-noise and can be exploited to yield both phase and amplitude information, as well processed amplitude and phase versions using the image processing technique of thresholding where all the pixels above a certain grey level are black and the pixels below that level are white. Two-dimensional scans of samples are generated.

The ultrasound system reliably detected flaws in the panel paintings *Parental Admonition* and *Women Gathering Yucca Plants*. Cracks, delaminations, craquelure in the paint layer, wood grain, and knots found within the samples were all clearly imaged by the system.

The system maps flaws in wooden panel paintings that cannot be detected by other

techniques such as radiography. The ultrasonic system was clearly shown to be more suitable for detecting certain flaws, such as in-plane cracks and delaminations.

Further work is needed in the area of image recognition in order to improve the reliability and ease of use of the air-coupled ultrasound system. In particular, it is important to develop methods that will distinguish between images of natural anomalies (grain) and flaws (cracks). Incorporation of information from visual examination and from other nondestructive techniques, such as radiography, will be useful here. As new transducers become available, the same transducer will be able both to send and to receive signals; this will remove the need to access both sides of the art work. Using more image processing may also be useful.

Air-coupled ultrasound is a potentially important, non-intrusive inspection method. The technique can yield information that will improve the long-term care of paintings on wood and, by implication, other works of art.

Acknowledgements

We would like to thank the Conservation Analytical Laboratory, the Smithsonian and the Center for Nondestructive Evaluation, The Johns Hopkins University for their financial support. We also grateful to Dr. Hans Goedicke and the National Museum of American Art, the Smithsonian Institution for lending us the paintings.

REFERENCES

1. Mecklenburg, M.F., and C.S. Tumosa, "Mechanical Behavior of Paintings Subjected to Changes in Temperature and Relative Humidity," *Art in Transit - Studies in the Transport of Paintings*, (Washington, D.C.: National Gallery of Art, 1991) 173-216.
2. Mairinger, F., and M. Schreiner, "Analysis of supports, grounds and pigments," *Art History and Laboratory Scientific Examination of Easel Painting, in the Journal of the European Study Group on Physical, Chemical and Mathematical Techniques Applied to Archaeology*, (Strasbourg, France: Council of Europe, Parliamentary Assembly, 1986) 13, 171-184.
- Wainwright, Ian N.M., "Examination of Paintings by Physical and Chemical Methods," *Shared Responsibility Proceedings, National Gallery of Canada, 26 to 28 October 1989* (Ottawa, Canada: National Gallery of Canada, 1990).
- Murray, A., R.E. Green, M.F. Mecklenburg, and C.M. Fortunko, "NDE Applied to the Conservation of Wooden Panel Paintings," edited by C.O. Ruud, J.F. Bussière, R.E. Green, Jr., *Nondestructive Characterization of Materials IV*, (New York: Plenum Press, 1991).
3. Murray, Alison, "Air-Coupled Ultrasound Used to Detect Flaws in Paintings on Wooden Panels," Ph.D. dissertation, The Johns Hopkins University, 1993.
- Fortunko, C.M., M.C. Renken, and A. Murray, "Examination of Objects Made of Wood Using Air-Coupled Ultrasound," *IEEE Ultrasonics Symposium 1990* (IEEE, 1991), 1099-1103.
- Fortunko, C.M., D.E. Chimenti, "Characterization of Pre-Impregnated Graphite Epoxy Lamina with Gas-Coupled Ultrasound," *IEEE Ultrasonics Symposium 1993* (IEEE, to be published).
- Fortunko, C.M., D.P. Dubé, J.D. McColskey, "Gas-Coupled Acoustic Microscopy in Pulse-Echo Mode," *IEEE Ultrasonics Symposium 1993* (IEEE, to be published).
4. Birks, A.S., "Particleboard Blow Detector," *Forest Products Journal* 22.6 (1972): 23-26.
5. Beall, F.C., "Acoustic Emission and Acousto-Ultrasonic Characteristics," *Wood Encyclopedia*, 1-2.
6. Murray, A., C.M. Fortunko, M.F. Mecklenburg, and R.E. Green, Jr., "Detection of Delaminations in Art Objects Using Air-Coupled Ultrasound," *Materials Issues in Art and Archaeology III*, Materials Research Society Volume 267, (Materials Research Society, 1992), 371-377.
7. Murray, Ph.D. dissertation, 1993.
- Murray, A., E.S. Boltz, C.M. Fortunko, M.F. Mecklenburg, R.E. Green, Jr., "Air-coupled Ultrasonic System for Nondestructive Evaluation of Wooden Panel Paintings," *3rd International Conference on Non-Destructive Testing, Microanalytical Methods and Environmental Evaluation for Study and Conservation of Works of Art, Viterbo, Italy, 4-8 October 1992*.
8. Murray, Ph.D. dissertation, 1993.

MODEL-BASED CALIBRATION OF ULTRASONIC SYSTEM RESPONSES FOR QUANTITATIVE MEASUREMENTS

Lester W. Schmerr, Jr.¹, Sung-Jin Song², and Huilian Zhang³

¹Center for NDE and Dept. of Aerospace Engineering
and Engineering Mechanics

²Control and Instrumentation Dept.
Research Institute of Industrial Science and Technology
Pohang, 790-600 Korea

³Dept. of Electrical Engineering
Iowa State University
Ames, IA 50011

INTRODUCTION

In order to perform quantitative ultrasonic NDE measurements, it is necessary to make those measurements independent of the characteristics and settings of the pulser-receiver used and the choice of the transducer employed. The combined effects of those parts of the ultrasonic system on the measured signal can be described mathematically in terms of a single system "efficiency" factor.

Here, we will show that ultrasonic system efficiency factors can be experimentally determined with the use of recently developed ultrasonic models for a variety of calibration scatterers, including plane front and back surfaces, flat-bottom holes, and solid cylinders. Because of the generality of the models employed, these scatterers can be in either the near or farfield of a planar transducer. It is also demonstrated that the system efficiency factor determination can be made independent of the choice of the material in the sample being considered provided that suitable material attenuation corrections are made.

EFFICIENCY FACTOR DETERMINATION

First, consider a general ultrasonic immersion setup for making flaw or material measurements. In any of these applications, an input voltage pulse, $V_i(t)$, drives a

piezoelectric transducer in a fluid which converts the electrical energy into mechanical motion. Here, we assume the motion generated is a spatially uniform velocity, $v_o(t)$, over the face of the transducer face (planar piston transducer model) whose frequency components, $v_o(\omega)$, are proportional to the frequency components of the input voltage, $V_i(\omega)$, i.e.

$$v_o(\omega) = \beta_i(\omega) V_i(\omega) \quad (1)$$

where ω is the frequency (in radians/sec) and $\beta_i(\omega)$ is an input proportionality factor. This motion generates a beam of ultrasound which interacts with the material or scatterer under examination and is partially scattered back to the same transducer, now acting as a receiver. If we also assume that the frequency components, $V_m(\omega)$, of the voltage pulse received are proportional to the spatially averaged velocity received at the transducer as a function of frequency, then we may write

$$V_m(\omega) = \beta_r(\omega) \langle v_m(\omega) \rangle \exp\left(-\sum_{i=1}^n \alpha_i(\omega) d_i\right) \quad (2)$$

where $\beta_r(\omega)$ is a receiving proportionality factor and $\langle v_m(\omega) \rangle$ represents the spatially averaged velocity received over the face of the transducer if the incident and scattered waves travel in ideal (non-attenuating) media. The exponential terms in eq.(2) account for the presence of material attenuation through the attenuation coefficients, $\alpha_i(\omega)$, of the i th media and the corresponding pathlengths, d_i . Combining eqs(1) and (2) we find

$$V_m(\omega) = \beta(\omega) \langle v_m(\omega) \rangle \exp\left(-\sum_{i=1}^n \alpha_i(\omega) d_i\right) / v_o(\omega) \quad (3)$$

in terms of a single total "efficiency" factor $\beta(\omega) = \beta_r(\omega)\beta_i(\omega)V_i(\omega)$. For the moment, assume that we can, through a combination of models and measurements, obtain both $\beta(\omega)$ and the attenuation coefficients and pathlengths in eq.(3). Then the measurement of the voltage frequency components of a particular material measurement, $V_m(\omega)$, can be used to directly obtain, through eq.(3), the normalized average velocity, $\langle v_m \rangle / v_o$. Thompson and Gray¹, for example, have shown how further modelling of $\langle v_m \rangle / v_o$ and the concept of deconvolution can be used to directly determine the far-field response of a flaw. In contrast, Tang et al.² have shown how measurements and models can be used to obtain both $\langle v_m \rangle / v_o$ and $\beta(\omega)$ so that measurements of $V_m(\omega)$ can be used to determine the unknown attenuation of the material under inspection. In both cases, $\beta(\omega)$ is obtained through the use of a separate reference experiment where the voltage frequency components, $V_r(\omega)$, are measured in a setup with the same transducer and system settings (so that β_i, β_r , and V_i are the same as in the original measurement setup) and where the normalized average velocity and attenuation terms are known. Figs 1a-d, for example, show four different possible reference calibration setups. For any of these cases we have a relationship entirely similar to eq.(3), i.e.

$$V_r(\omega) = \beta(\omega) \langle v_r(\omega) \rangle \exp(-\sum \alpha_i D_i) / v_o(\omega) \quad (4)$$

In principle, then, $\beta(\omega)$ can be obtained from this reference experiment through a simple division process. However, when V_r and $\langle v_r(\omega) \rangle / v_o(\omega)$ are both small, noise contaminates this division process, making it unreliable. To overcome this difficulty, one approach has been to use the concept of a Wiener filter³. Using such a filter, we obtain

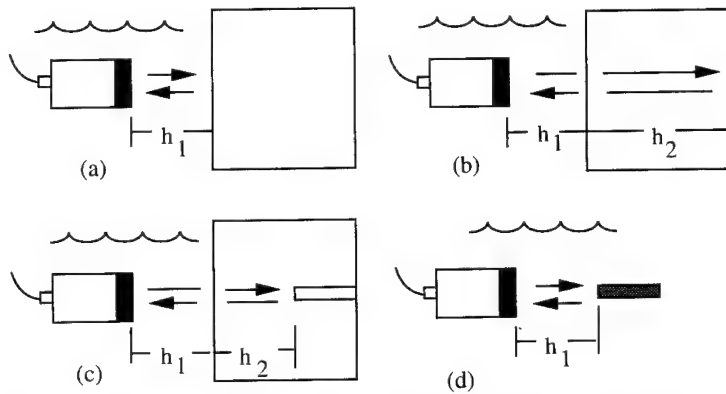


Fig. 1. Reference scattering geometries using (a) the reflection from the plane front surface of a specimen, (b) the reflection from the plane back surface of a specimen, (c) the backscatter response of an on-axis flat-bottom hole in a ASTM specimen, (d) the backscatter response of an on-axis solid cylinder in a fluid.

$$\beta(\omega) = \frac{V_r}{\langle v_r \rangle / v_o \exp(-\sum \alpha_i D_i)} \left[\frac{|\langle v_r \rangle / v_o \exp(-\sum \alpha_i D_i)|^2}{|\langle v_r \rangle / v_o \exp(-\sum \alpha_i D_i)|^2 + \epsilon^2} \right] \quad (5)$$

where ϵ is a small constant whose value is chosen so as to desensitize the division process. Since the use of such filters have been described elsewhere ^{3,4}, we refer the reader to those sources for further details.

PLANE SURFACE REFERENCE MODELS

Front Surface Model

To turn eq.(5) into a useful expression for the determination of $\beta(\omega)$, it is necessary to have an explicit expression for the normalized average velocity received by the transducer, i.e. an explicit reference scattering model, and a knowledge of the material attenuation coefficients. One commonly used reference scattering configuration is that of a plane front surface (Fig. 1a) of a specimen oriented parallel to the face of the transducer. For the waves reflected once from the front surface and received by the transducer, we have⁵:

$$\langle v_r \rangle / v_o = \langle v_{f.s.} \rangle / v_o \quad (6)$$

where

$$\langle v_{f.s.} \rangle / v_o = R_{12} \exp(2ik_1 h_1) C(k_1 a^2 / 2h_1) \quad (7a)$$

and

$$C(k_1 a^2 / 2h_1) = \left\{ 1 - \exp(ik_1 a^2 / h_1) \left[J_0(k_1 a^2 / 2h_1) - iJ_1(k_1 a^2 / 2h_1) \right] \right\} \quad (7b)$$

C is a diffraction coefficient and R_{12} is the ordinary plane wave reflection coefficient (at normal incidence) for the interface between the water and the specimen, k_1 is the wavenumber of the water, a is the radius of the transducer, and J_0, J_1 , are Bessel functions. Although eq.(6) is strictly speaking only an approximate high frequency solution for the response from the interface between two fluid media, several studies^{6,7} have validated its use for the fluid-solid interface. It should be noted that nothing in the derivation of eq.(6) restricts the location of the interface⁵. Thus, eq.(6) is applicable when the interface lies in either the near- or far-field of the transducer radiation field.

For this case the propagation distance in eq.(5) is $D_1 = 2h_1$ (Fig. 1a) and the attenuation term is that of water, i.e. $\alpha_1 = \alpha_w$. For water at room temperature we have⁸:

$$\alpha_w = 25.3 \times 10^{-15} f^2 \quad \text{m}^{-1} \quad (8)$$

where the frequency, f , is in Hz.

Back Surface Model

In a similar manner, one can use the plane back surface of a specimen as a reference. Here⁹

$$\langle v_r \rangle / v_0 = \langle v_{b.s.} \rangle / v_0 \quad (9)$$

where

$$\langle v_{b.s.} \rangle / v_0 = T_{12} R_{21} T_{21} \exp(2ik_1 h_1 + 2ik_2 h_2) C(k_1 a^2 / 2h_1) \quad (10)$$

and $h = h_1 + c_2 h_2 / c_1$ (Fig. 1b). Here, c_1 and c_2 are the wavespeeds for the water and solid, respectively, and the R_{21} and T_{12}, T_{21} are the plane wave reflection and transmission coefficients. In this case one needs to know both the attenuation of the solid, α_s , as well as that of the water. In eq. (5), then, $\alpha_1 = \alpha_w$ and $D_1 = 2h_1, D_2 = 2h_2$. The water attenuation term can again be obtained from eq.(8). For the solid, we can use the ratio of measurements of the front and back surface echoes to eliminate the efficiency factor, β , and the common water attenuation coefficient to yield, from eqs. (4), (6), and (9), an expression that can be solved for the attenuation of the solid. Formally, we obtain

$$\exp(-2\alpha_s(\omega)h_2) = |B(\omega)| / |F(\omega)| \quad (11)$$

where

$$|F(\omega)| = |V_{b.s.}(\omega) R_{12} C(k_1 a^2 / 2h_1)| \quad (12)$$

and

$$|B(\omega)| = |V_{f.s.}(\omega) T_{12} R_{21} T_{21} C(k_1 a^2 / 2h)| \quad (13)$$

In eqs. (12),(13) $V_{b.s.}$ and $V_{f.s.}$ are the frequency components of the voltage pulses received from the back and front surface echoes, respectively. The division process of eq. (11), however, is also contaminated by noise at both high and low frequencies so that again using the Wiener filter approach, we replace eq.(11) by

$$\exp(-2\alpha_s(\omega)h_2) = \frac{|B(\omega)|}{|F(\omega)|} \left\{ \frac{|F(\omega)|^2}{|F(\omega)|^2 + \epsilon^2} \right\} \quad (14)$$

which is now a well-behaved expression for the determination of α_s .

FLAT-BOTTOM HOLE MODEL

Equation (6) together with eq. (8), or eq. (9), together with eqs.(8) and (14), provide all the basic terms needed in eq.(5) to obtain the efficiency factor from either the plane front of back surface of a specimen. In a similar manner, other reference reflectors can, of course, be considered. A common calibration setup used in ultrasonic NDE involves a block containing a flat-bottom hole (Fig. 1c). In this case Song, Schmerr, and Sedov⁶ have obtained an explicit expression for the received average velocity, which we write symbolically as:

$$\langle v_r \rangle / v_0 = \langle v_{fbh} \rangle / v_0 \quad (15)$$

Space does not permit us to give the rather lengthy expression for the normalized average velocity here so we refer the reader to Song, Schmerr, and Sedov⁶ where the explicit form is given. The attenuation terms in this case are $\alpha_1 = \alpha_w$ and $\alpha_2 = \alpha_s$ and the propagation distances in eq.(5) are $D_1 = 2h_1, D_2 = 2h_2$. As in the case of the back surface response, the water and solid attenuation coefficients can be determined, if needed, from eqs.(8) and (14), respectively.

SOLID CYLINDER MODEL

The flat-bottom hole is a popular reference scatterer since it represents a highly specular reflector, like a crack, when viewed at normal incidence. However, when using the flat-bottom hole to obtain $\beta(\omega)$ through eq.(5), it is necessary, as just described, to measure the attenuation of the solid. This extra step can be eliminated if we use instead the flat end of a solid cylinder in an immersion setup (Fig. 1d). In this case, a high frequency Kirchhoff-like approximation for the scattering problem¹⁰ gives the average received velocity symbolically as:

$$\langle v_r \rangle / v_0 = \langle v_{cyl} \rangle / v_0 \quad (16)$$

Again, for space reasons we do not write down the explicit form here but refer the reader to Sedov, Schmerr, and Song¹⁰ where an explicit expression is given. The solid cylinder, like the flat-bottom hole, is a highly specular reflector but in this case the only

attenuation coefficient needed is α_w , which can be obtained from eq. (8), and the propagation distance in eq.(5) is $D_1 = 2h_1$ (Fig. 1d).

EXPERIMENTAL TESTS

The previous sections have discussed a variety of reference scatterers that can, in principle, be used in making system efficiency measurements. Here, we will demonstrate that consistent $\beta(\omega)$ measurements are possible with any of these configurations by the use of the appropriate attenuation corrections as described previously.

Figure 2, for example, shows the results for the efficiency factor versus frequency for a 10 MHz, 1/4 inch diameter transducer, calculated from either the planar front or back surface of an aluminum specimen, using eqs. (6) and (9) and including the attenuation corrections for the water and aluminum through eq.(8) and eq.(14). As can be seen, there is excellent agreement between the two results, indicating that the efficiency factor can be calculated with either of these reference scattering configurations.

The system efficiency factor, β by definition is not dependent on the properties of the reflector being used. Thus, β should also be independent of the material properties of the reference scatterer being employed. Fig. 3 shows that this is indeed the case for a 10 MHz, 1/4 inch diameter plane transducer, using plane front surface reflections from aluminum, titanium, or steel specimens. Thus, β calculations, can, with careful measurements, also be transferred across materials.

Determination of β should also be independent of the geometry of the scatterer being used. Fig. 4 compares the efficiency factor calculations for a 10 MHz, 1/4 inch diameter plane transducer using four types of reference scattering geometries: 1) the front surface of a steel specimen, 2) the response from a flat-bottom hole in a steel block, 3) the response of a 4/64 inch diameter steel cylinder in water, and 4) the response of a 6/64 inch diameter steel cylinder in water. In each of these cases the appropriate attenuation corrections were included. As can be seen from Fig. 4, there is good consistency

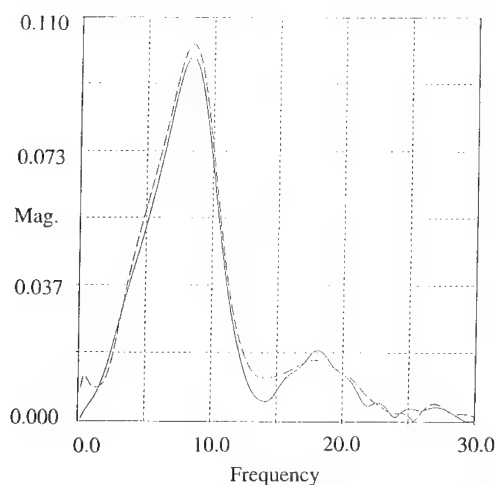


Fig. 2 Efficiency factor versus frequency for a 10 MHz, 1/4 inch diameter planar transducer calculated with (a) a planar front surface response _____, (b) a planar back surface response _____.

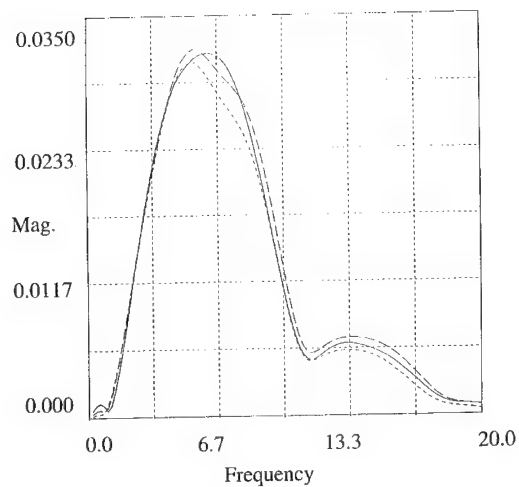


Fig. 3. Efficiency factor versus frequency for a 10 MHz, 1/4 inch diameter planar transducer using the front surface response of a specimen made of (a) aluminum _____, (b) titanium _____ (c) steel _____.

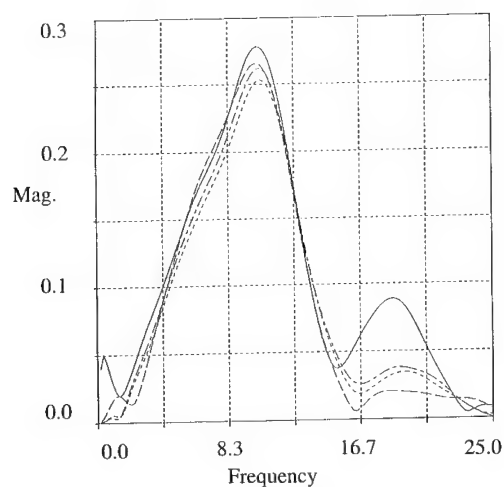


Fig. 4. Efficiency factor versus frequency calculated for a 10 MHz, 1/4 inch diameter planar transducer using (a) the planar front surface of a steel specimen _____, (b) the backscatter response of a 5/64 inch diameter flat-bottom hole in an ASTM 4340-5-0038 specimen _____ (c) the backscatter response of a 4/64 inch diameter steel cylinder in an immersion setup _____ (d) the backscatter response of a 6/64 inch diameter steel cylinder in an immersion setup _____.

(maximum differences are normally 10% or less across the major portion of the transducer spectrum) for all these configurations. Thus, the determination of β by these methods is transferable across different materials and geometric setups.

CONCLUSIONS

We have demonstrated a general procedure for determining the transducer system efficiency factor for an ultrasonic system. This determination requires both a model of the average velocity received by the transducer and measurements of the attenuation corrections for the materials under consideration. Although we have only shown these procedures for planar transducers, similar methods can also be used for focused probes¹¹. We have also demonstrated that the results obtained from one material and geometrical setup can be transferred to a different material and/or geometry.

ACKNOWLEDGMENTS

This work was supported by the Center for NDE, Iowa State University.

REFERENCES

1. R.B. Thompson and T.A. Gray, "A model relating ultrasonic scattering measurements through liquid-solid interfaces to unbounded medium scattering amplitudes," *J. Acoust. Soc. Am.* 74:1279 (1983).
2. X.M. Tang, M.N. Toksoz, and C. H. Cheng, "Elastic wave radiation and diffraction of a piston source," *J. Acoust. Soc. Am.* 87:1894 (1990).
3. D. Elsley, J. Richardson, and B. Addison, "Optimum measurement of broadband ultrasonic data," 1980 Ultrasonics Symposium Proceedings, IEEE, N.Y., 916 (1980).
4. Y.B. Murakami, B.T. Khuri-Yakub, G.S. Kino, J.M. Richardson, and A.G. Evans, "An application of Wiener filters to nondestructive evaluation," *Appl. Phys. Ltrs.* 33:685 (1978).
5. P.H. Rogers and A.L. Van Buren, "An exact expression for the Lommel correction integral," *J. Acoust. Soc. Am.* 55:724 (1974).
6. S.J. Song, L.W. Schmerr, and A. Sedov, "DGS diagrams and frequency response curves for a flat-bottom hole: a model-based approach," *Res. Nondestr. Eval.* 3:201 (1991).
7. D.H. Green and H.F. Wang, "Shear wave diffraction loss for circular plane-polarized source and receiver," *J. Acoust. Soc. Am.* 90:2697 (1991).
8. J.M.M. Pinkerton, "A pulse method for the measurement of ultrasonic absorption in liquids: results for water," *Nature* 160:128 (1947).
9. A. Sedov, L.W. Schmerr, and S.J. Song, "Ultrasonic scattering by a flat-bottom hole in immersion testing: an analytical model," *J. Acoust. Soc. Am.* 92:478 (1992).
10. A. Sedov, L.W. Schmerr, and S.J. Song, "A bounded beam solution for the pulse-echo transducer response of an arbitrary on-axis scatterer in a fluid," *Wave Motion* (to appear), (1993).
11. L.W. Schmerr, T. Lerch, and A. Sedov, "A focused transducer/scatterer model for ultrasonic reference standards," *Review of Progress in Quantitative Nondestructive Evaluation*, D.O. Thompson and D.E. Chimenti, Eds., Plenum Press, N.Y., 12A, 925-931, 1993.

ULTRASONIC CHARACTERIZATION OF TEXTURE IN PURE AND ALLOYED ZIRCONIUM

A. Moreau¹, P.J. Kielczynski², J.F. Bussière¹, and J.H. Root³

¹ National Research Council of Canada
Industrial Materials Institute
75 de Mortagne Blvd.
Boucherville, Québec
Canada J4B 6Y4

² Same as above. Current address:
Research and Productivity Council
921 College Hill Road
Fredericton, New Brunswick
Canada E3B 6Z9

³ AECL Research
Chalk River Laboratories
Chalk River, Ontario
Canada K0J 1J0

INTRODUCTION

Recently, we have developed a method to relate the angular dependence of ultrasonic velocities to the five expansion coefficients of the crystallographic orientation distribution function (CODF) of hexagonal materials with orthorhombic macroscopic symmetry.¹ The ultrasonic velocity measurements are performed with an acoustic microscope on one, two, or three of the principal planes of symmetry using one or more ultrasonic modes. In this paper, the theory of ultrasonic measurement of texture is reviewed, and we present data showing that it can be applied to two-phase alloys, when the primary phase makes up most of the material.

The paper begins with the expansion of the CODF in terms of generalized spherical harmonics and a discussion of the physical significance of the expansion coefficients W_{lmn} , in terms of the crystallite's c-axis orientations. Various methods used to obtain the W_{lmn} ultrasonically are summarized and discussed using a general theory. Results are presented for a sample of pure zirconium and six samples of Zr-2.5%Nb alloys containing 5 to 10 % beta (cubic) phase. The ultrasonic texture coefficients are compared to those obtained by neutron diffraction. A discussion of measurement errors, second phase effects, and averaging methods follows.

THE CRYSTALLITE ORIENTATION DISTRIBUTION FUNCTION

Texture is described by a crystallite orientation distribution function (CODF) that describes the probability of finding a single crystallite in a specific orientation. The crystallite orientation is described by the three Euler angles, ψ , θ , and ϕ . These angles relate the crystallite's internal coordinates to an external system of coordinates. This paper considers the particular case of hexagonal crystallites in an aggregate of orthorhombic symmetry. In this case, ψ and θ represent the "longitude" and the "latitude" of the crystallite's c axis with respect to the aggregate's axes, and ϕ represents the rotation of the crystallite around its own c axis.

The CODF, denoted here by $w(\psi, \theta, \phi)$, may be expanded in terms of generalized spherical harmonics,

$$w(\psi, \theta, \phi) = \sum_{l=0}^{\infty} \sum_{m=-l}^l \sum_{n=-l}^l W_{lmn} Z_{lmn}(\cos \theta) e^{-im\psi} e^{-in\phi} \quad (1)$$

where $Z_{lmn}(\cos \theta)$ is a generalization of the associated Legendre function, and W_{lmn} are the coefficients of the expansion.² The normalization condition for the CODF is

$$\int_0^{2\pi} \int_0^{2\pi} \int_{-1}^1 w(\psi, \theta, \phi) d(\cos \theta) d\psi d\phi = 1 \quad (2)$$

It has been shown that the effective (second order) elastic constants of a polycrystalline aggregate depend only on expansion terms for which $l \leq 4$.³ This very important result implies that fine details of the CODF will not be measurable with linear ultrasonics. Conversely, all linear acoustic properties and all linear mechanical properties of a polycrystalline aggregate only depend on a small number of texture coefficients.

Because of symmetry properties of orthorhombic aggregates of hexagonal crystallites,² the W_{lmn} are real, $W_{lm0} = W_{l\bar{m}0}$ and only the following texture coefficients with $l \leq 4$ are non zero: W_{000} , W_{200} , W_{220} , W_{400} , W_{420} , and W_{440} .⁴ Moreover, Z_{lmn} always satisfies the relation $Z_{lmn} = (-1)^{m+n} Z_{l\bar{m}\bar{n}}$. Using these relations, we can write

$$w(\psi, \theta, \phi) \approx \sum_{l=0,2,4} \sum_{\substack{m=-l \\ m \text{ even}}}^l W_{lm0} Z_{lm0}(\cos \theta) \cos m\psi \quad (3)$$

To better understand the meaning of the non-zero W_{lm0} , we plot $w_{lm0}(\theta, \psi) = Z_{lm0}(\cos \theta) \cos m\psi$ in spherical coordinates in Figure 1. In Figure 1, the vertical axis is the macroscopic z axis and the circle in the xy plane is labeled in degrees from the x axis. The new basis function, $w_{lm0}(\theta, \psi)$, is related to the probability of finding the c axis of a hexagonal crystallite pointing in the (θ, ψ) direction if all other texture coefficients are zero. Note that $w_{lm0}(\theta, \psi)$ can be positive or negative.

The w_{000} function is independent of θ and ψ , is equal to $\sqrt{2}/2$, and is trivially shown as a sphere in Figure 1. It represents an isotropic distribution. It is also the only term that integrates to a non zero value in the normalization integral (2). Therefore, W_{000} is always equal to $\sqrt{2}/8\pi^2$. The w_{200} function is axisymmetric and has two positive lobes in the $\pm z$ directions and a negative ring in the xy plane. Negative values of $w_{lm0}(\theta, \psi)$ are represented as positive radii in the $(\pi - \theta, \psi + \pi)$ direction. However, the $w_{lm0}(\theta, \psi)$ considered have point symmetry and Figure 1 can be thought of as $|w_{lm0}(\theta, \psi)|$. Although negative probabilities are unphysical, the individual w_{lm0} are never observed individually,

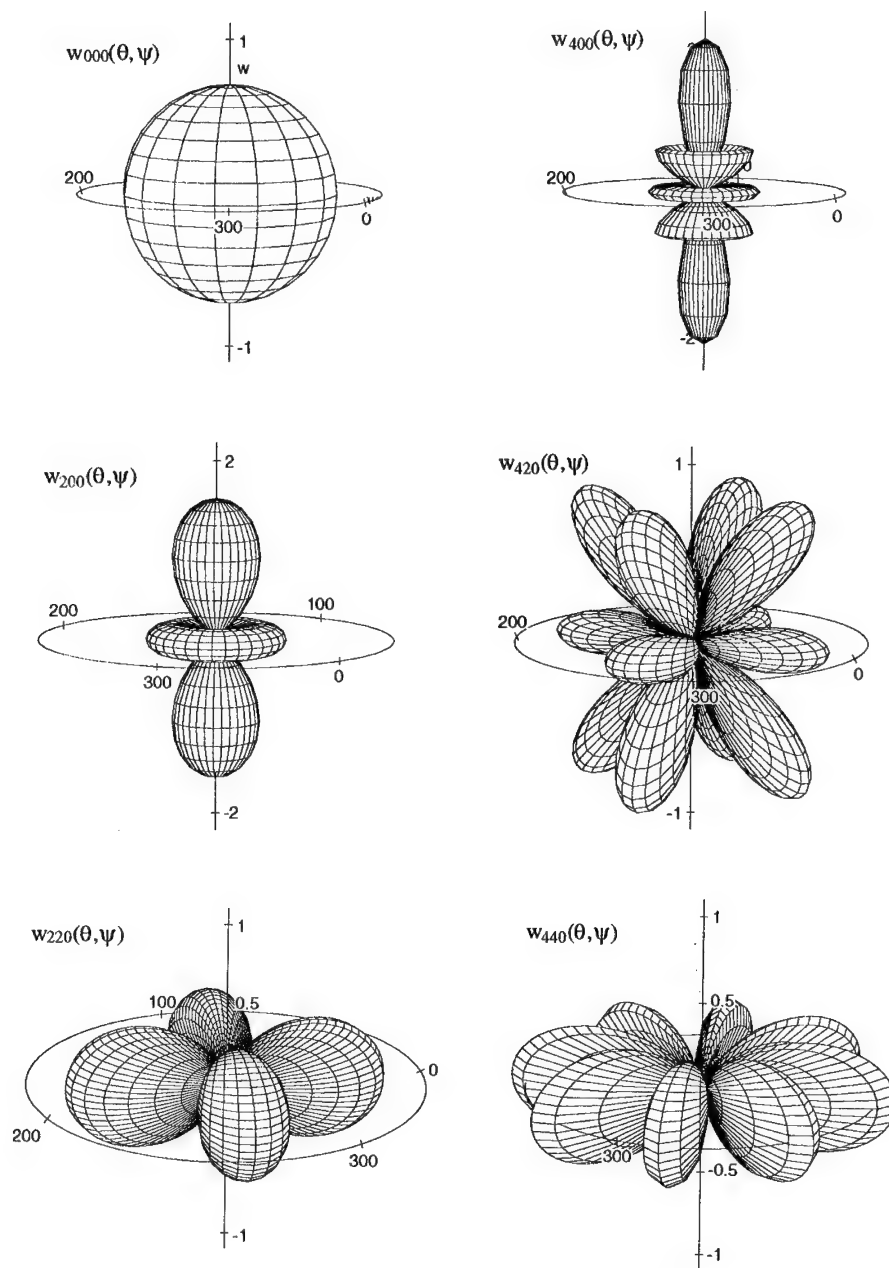


Figure 1. Three dimensional representation of the basis functions $w_{lm}(\theta, \psi)$ for $l \leq 4$ and even values of m . The vertical axis is the z axis and a circle labeled in degrees from the x axis is drawn in the xy plane. The radii of the circles are: 1.0 for w_{000} , w_{420} , and w_{440} , 1.2 for w_{220} , and 2.0 for w_{200} and w_{400} . The sign of each lobe alternates, as described in the text.

but as part of the expansion (1). In particular, they must be added to the constant w_{000} term. Consequently, positive or negative values of W_{200} indicate that the c axes of the hexagonal crystallites are preferentially aligned along the z axis or in the xy plane, respectively. The w_{220} has two positive lobes along the x axis and two negative lobes along the y axis. Consequently, positive or negative values of W_{220} indicate that the c axes of the hexagonal crystallites are preferentially aligned along the x or y axes, respectively. The w_{400} function is axisymmetric and has two positive lobes along the z axis, one positive ring in the xy plane, and two negative "cones" around the z axis. The effect of w_{400} on texture can be quite complex, but one important effect is to sharpen the w_{200} distribution and to increase the probability of finding the crystallite's c axis aligned along the macroscopic z axis. Alternately, negative values of W_{400} may occur with positive values of W_{200} and a non zero value of W_{220} . This results in a twin peak about the z axis. This texture may be observed in Zr rolled plates when the z axis is defined as the direction transverse to the rolling direction. The function w_{420} is considerably more complicated and consists of 12 lobes of alternating sign, with negative lobes along the x axes. The function w_{440} consists of 8 lobes of alternating signs, all located in the xy plane, and with positive lobes along the x and y axes.

From the above representation of the w_{lm0} functions, it is clear that the expansion of the CODF in terms of the generalized spherical harmonics treats the z axis differently from the x and y axes. Although the basis functions form a complete set, the limited number of coefficients that can be obtained by acoustic measurements makes the choice of macroscopic axes important because a better choice can reduce the error sum-of-squares, i.e., the integral of the squares of the difference between the CODF and its truncated expansion. Conventional pole figures of the various basis functions and of the CODF can be obtained using a contour plot of a projection of the above representation. Given that only the probability distribution of the crystallite c axes can be obtained, the (0002) pole figure is the only relevant one. Pole figures of w_{400} , w_{420} , and w_{440} on a xy plane projection have been published elsewhere.⁵

ULTRASONIC MEASUREMENTS OF TEXTURE

Recently, we have shown how to relate the angular dependence of the acoustic velocity of various acoustic modes to the five texture coefficients W_{200} , W_{220} , W_{400} , W_{420} , and W_{440} .¹ The effective elastic constants of the aggregate, \overline{C}_{ij} , are expressed as⁶

$$\overline{C}_{ij} = C_{ij}^0 + \Delta C_{ij}, \quad (4)$$

i.e., as a sum of an isotropic value,

$$C_{ij}^0 = C_{ij}^0(c_{sc}), \quad (5)$$

and a texture dependent term,

$$\Delta C_{ij} = \Delta C_{ij}(c_{sc}, W_{lmn}), \quad (6)$$

subject to the weak anisotropy condition

$$\Delta C_{ij} \ll C_{ij}^0. \quad (7)$$

In (4) and (5), c_{sc} are the single crystal elastic constants. These expressions can be found using either Reuss, Voigt, or Hill averages.⁷

Experimentally, the angular dependence of the acoustic velocity in one to three principal planes of the orthorhombic aggregate is fitted to the approximate equation

$$v(\gamma) \approx v_0 + P + Q \cos 2\gamma + R \cos 4\gamma, \quad (8)$$

where v is the acoustic velocity of the aggregate, γ is the propagation angle in the principal plane, v_0 is the isotropic velocity, and P , Q , and R are the fitted parameters. In the weak anisotropy condition (7), equation (8) is a good approximation to the solution of the Christoffel's equation,⁸ and the fitted parameters can be expressed in terms of the effective elastic constants. Therefore, we can write

$$\begin{aligned} P &= P(\bar{C}) = P(c_{sc}, W_{lmn}) \\ Q &= Q(\bar{C}) = Q(c_{sc}, W_{lmn}) \\ R &= R(\bar{C}) = R(c_{sc}, W_{lmn}) \end{aligned} \quad (9)$$

These expressions have been obtained for bulk longitudinal and shear waves, Rayleigh surface waves, and Lamb symmetric plate waves.¹

If enough acoustic modes are observed in one or several principal planes so that at least five different values of P , Q , and R are known, the W_{lmn} can be found by inverting (9).¹ (Note that if not all W_{lmn} are desired, fewer values of P , Q , or R may be required.) If more than five different values of P , Q , and R are known, equations (9) become overdetermined and a least squares fitting procedure can be used.⁹ However, it has been pointed out that the W_{lmn} evaluated using the P values (absolute velocity measurements) are much more sensitive to errors in the single crystal elastic constants and density than those evaluated using only Q and R values (relative velocity measurements).¹ On the other hand, the R values are usually smaller and more difficult to measure than the Q values. Therefore, the choice of procedure to use for the inversion of (9) is very dependent on the amount and quality of the acoustic data.

THE ACOUSTIC MICROSCOPE

The measurements presented here were made with a 225 MHz line-focus acoustic microscope.¹⁰ This method of measurement has the advantages that only small samples and relatively little machining are needed, and that the acoustic velocity of surface waves may be measured at any angle on the sample surface. However, the acoustic microscope requires careful polishing of the sample surfaces and scans of the elastic properties are made on a relatively small volume near the surface. Therefore, the technique is limited to samples with small grain sizes and it is sensitive to surface texture only. Moreover, the microscope measures leaky Rayleigh waves (LRW) and leaky surface-skimming compressional waves (LSSCW) instead of the pure Rayleigh waves and bulk longitudinal waves described in the above theory. The LRW are thought to behave essentially as pure Rayleigh waves.¹¹ We assume that the LSSCW behave as bulk longitudinal waves, but recent work indicates that this assumption may not always be valid.¹²

RESULTS

Pure Zr sample

To test the validity of the inversion of (9) and of our experimental technique, we have obtained the texture coefficient of a 99.8 % pure Zr rod (Goodfellow Corporation, Malvern,

PA, part #ZR007910) using both acoustic measurements and neutron diffraction. The neutron diffraction measurements were made at the NRU reactor at AECL Research, Chalk River Laboratories. The acoustic measurements were obtained using the LRW and the LSSCW propagating in the $x = 0$ and $y = 0$ planes (Acoustic 1) and in the $x = 0$ and $z = 0$ planes (Acoustic 2). One hundred velocities were measured in intervals of 2° . The single-crystal elastic constants used are from the literature¹³ and the density was measured. The sample grain size was of the order of $20\text{ }\mu\text{m}$ but this large grain size did not seem to affect the quality of the data. The results are shown in Table 1. The numbers in parentheses are the error estimates on the least significant digits. For the neutron diffraction measurements, the errors were deduced from the consistency of five different pole figures. For the acoustic measurements, the errors are obtained from the statistical error of the fitted values of P, Q, and R. To this statistical error, one must add an unknown systematic error resulting from the choice of averaging method. In Table 1, Hill's averaging was used. The choice of averaging method will be discussed further below.

Table 1. Comparison of pure-zirconium texture coefficients obtained using neutron diffraction and acoustic measurements. The acoustic measurements were made using LRW and LSSCW in the $x = 0$ and $y = 0$ planes (Acoustic 1) and in the $x = 0$ and $z = 0$ planes (Acoustic 2). Hill's averaging is used.

	Neutron	Acoustic 1	Acoustic 2
W_{200}	-0.0156 (4)	-0.0147 (4)	-0.0141 (7)
W_{220}	0.0002 (1)	-0.0010 (5)	0.0017 (3)
W_{400}	0.0097 (2)	0.0136 (10)	0.0111 (7)
W_{420}	-0.0001 (1)	0.0006 (5)	-0.0011 (2)
W_{440}	0.0000 (1)	0.0007 (9)	0.0018 (5)

Zr-2.5%Nb alloys

Metals are usually alloyed to tailor various physical properties. Therefore, acoustic texture measurement techniques are of limited use unless they can be applied to alloys. Some complications arising in alloys are the presence of additional phases and possible changes in the single crystal elastic constants caused by the solute. We do not attempt to model each phase separately and obtain texture coefficients for each phase but restrict ourselves to alloys where the primary phase constitutes most of the material, so that the second phase can be ignored in first approximation.

To verify the method's applicability to alloys, we measured six samples of Zr alloyed with 2.5% Nb. The samples are made of 90 to 95% hexagonal α phase and 5 to 10% cubic β phase. The α phase contains up to 1% of Nb in solution and the β phase contains from 30 to 50% Nb. The β phase is known to have a much weaker texture than the α phase.¹⁴ The grain sizes are of the order of $1\text{ }\mu\text{m}$. The samples were annealed to remove possible residual stress effects. The acoustic texture was obtained using the same α -Zr single crystal elastic constants as for pure Zr, and the measured density of the alloy. The acoustic texture coefficients of these six samples and of the pure Zr sample are plotted in Figure 2 as a function of the α phase coefficients obtained by neutron diffraction. For the acoustic measurements, Hill's averaging and the two acoustic waves LSSCW and LRW propagating in the $x = 0$ and $y = 0$ planes are used.

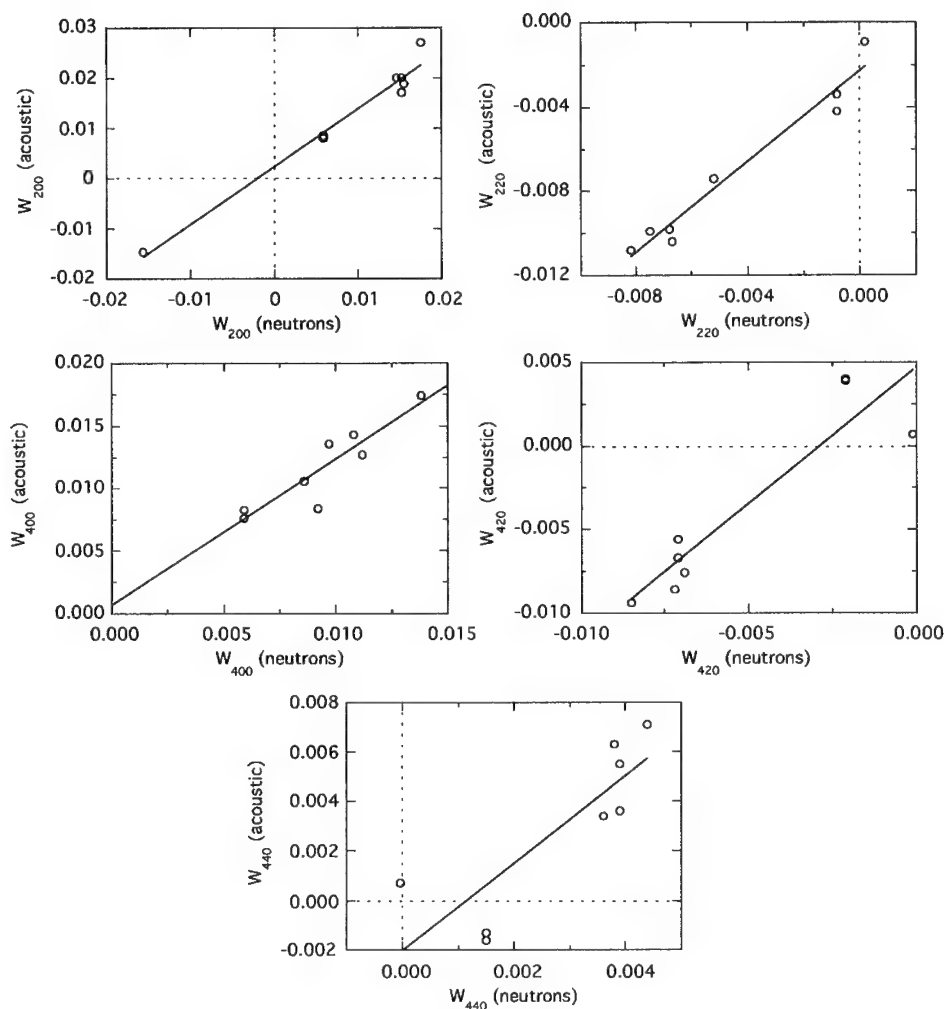


Figure 2. Texture coefficients as measured with ultrasound versus those obtained by neutron diffraction for one pure Zr and six Zr-2.5%Nb samples. The linear least squares fits shown include all data points.

In all cases (Fig. 2) the relation between the acoustic and neutron diffraction measurements is linear, the slope is nearly equal to one, and the y intercept is nearly zero. There occurred measurement difficulties for one sample: the measured acoustic velocities contained abnormally large errors, equation (8) was poorly satisfied, and some of the fitted values of P, Q, and R were unreliable. The measurements were repeated a second time without improvements and we do not know why this sample behaved differently. Consequently, the two points with neutron values of W_{420} near -0.002 and the two points with neutron values of W_{440} near 0.0015 are likely to be outliers. The linear relationship between neutron and acoustic measurements appears best for the W_{200} and W_{220} and, to a lesser extent, the W_{400} coefficients. Perhaps this should not be surprising because their

corresponding basis functions are the simplest ones and have the largest amplitude (see Figure 1). Another reason for the better linearity of W_{200} and W_{220} might be that, because of symmetry, these coefficients must be equal to zero for orthorhombic aggregates of cubic materials² and consequently, the β phase is not expected to contribute.

These results show that the acoustic behavior of the samples is dominated by the texture of the primary α phase. This is not surprising because the effective elastic constants, in the Reuss or Voigt approximations, are volume averages of the individual phases and because the primary α phase represents 90 to 95 % of the material. On the other hand, the elastic constants and density of the β (cubic) crystallites can be substantially different from those of the α (hexagonal) crystallites¹⁵ but because it is weakly textured, the β phase should affect mainly the isotropic component of the sample's effective elastic constants. Only relative velocity measurements were used in the texture measurement; therefore, the β phase is not expected to affect the results significantly. The results also show that the 1% Nb dissolved in the α phase does not affect the elastic properties of the crystallites sufficiently to prevent texture measurements.

Voigt, Reuss and Hill averaging

The influence of averaging method on the texture coefficients obtained using ultrasonic methods is best illustrated by Figure 3. The figure is similar to Figure 2 for the Hill average of W_{200} but, for each acoustic measurement, the Voigt and Reuss values are indicated. In all three cases, the linear relationship is recovered but the three slopes differ somewhat: the slope is equal to 0.97 for Voigt averaging, 1.16 for Hill averaging (Figure 2), and 1.43 for Reuss averaging. The three lines meet in a point at a W_{200} acoustic value near zero and a neutron diffraction value near -0.0025. Therefore, the choice of averaging method introduces a systematic relative error as large as $\pm 23\%$ in the texture coefficient. The systematic absolute error is unexplained but may be due to measurement uncertainties or to the various approximations made: single phase material and LRW and LSSCW instead of pure Rayleigh and bulk longitudinal waves.

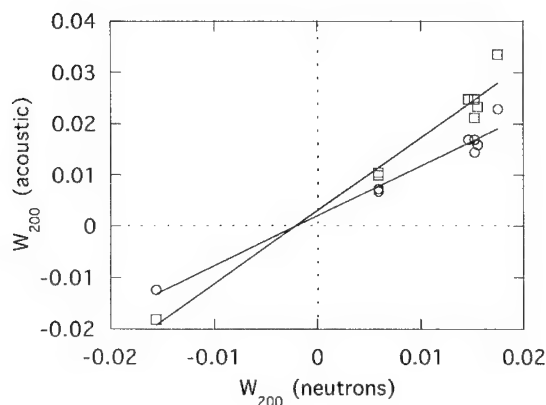


Figure 3. W_{200} as measured with ultrasound for Voigt (circles) and Reuss (squares) averaging methods versus W_{200} obtained by neutron diffraction for one pure Zr and six Zr-2.5%Nb samples.

CONCLUSION

We have used an acoustic microscope to measure the LRW and LSSCW velocities as a function of angle in two principal planes of one pure Zr and six Zr-2.5% Nb samples. The texture measurements of the pure Zr sample agree reasonably well with the neutron diffraction measurement. Discrepancies are related to the statistical error of the fitted P, Q, and R parameters, to the choice of averaging method, and to the use of two types of waves, LRW and LSSCW, that are only an approximation to the pure Rayleigh and bulk longitudinal acoustic modes. A linear relationship was found between the texture coefficients obtained by ultrasonics and those obtained by neutron diffraction for one pure Zr and six Zr-2.5%Nb samples. The presence of a 5 to 10% of a secondary phase and of up to 1% Nb in solution in the primary phase does not invalidate the measurement. This is an important result for the future use of acoustic methods to evaluate the texture of alloys. Our results also show systematic relative errors caused by the choice of averaging method.

ACKNOWLEDGEMENTS

This work was supported in part by the Fuel Channel NDE working party of the CANDU Owners Group.

REFERENCES

- 1 P. J. Kielczynski, A. Moreau, and J. F. Bussière, to be published in *J. Acoust. Soc. Am.*
- 2 Ryong-Joon Roe, *J. Appl. Phys.* **36**, 2024 (1965).
- 3 H.-J. Bunge, *Kristall und Technik* **3**, 431 (1968).
- 4 C. M. Sayers, *Ultrasonics* **24**, 289 (1986).
- 5 M. Hirao, K. Aoki, and H. Fukuoka, *J. Acoust. Soc. Am.* **81**, 1434 (1987).
- 6 C. M. Sayers, *Ultrasonics* **24**, 289 (1986).
- 7 Yan Li and R. Bruce Thompson, *J. Appl. Phys.* **67**, 1 (1990).
- 8 B. A. Auld, "Acoustic Fields and Waves in Solids," vol. 1, Krieger, Malabar, Florida, 1990.
- 9 P. J. Kielczynski, J. F. Bussière, J. H. Root, and D. Juul Jensen, *Nondestruct. Test. and Eval.* **7**, 497 (1992).
- 10 Jun-Ichi Kushibiki and Noriyoshi Chubachi, *IEEE Trans. Sonics Ultrason.* **SU-32**, 189 (1985).
- 11 I. A. Viktorov, "Rayleigh and Lamb waves. Physical Theory and Applications," Plenum Press, New York, 1967.
- 12 Yusuke Tsukahara, Yongshen Liu, Christian Néron, C. K. Jen, and Jun-Ichi Kushibiki, unpublished.
- 13 E. S. Fisher, C. J. Renken, *Phys. Rev.* **135**, A482-A494 (1964).
- 14 J. H. Root and A. Moreau, unpublished.
- 15 E. Walker and M. Peter, *J. Appl. Phys.* **48**, 2820 (1977).

MICROTOMOGRAPHY USING CONVENTIONAL X-RAY SOURCES

Yasushi Yamauchi,¹ Naoki Kishimoto,¹ and Takashi Ikuta²

¹National Research Institute for Metals

Sengen, Tsukuba 305, Japan

²Osaka Electro-Communication University

Hatsumachi, Neyagawa 572, Japan

INTRODUCTION

Microscopies such as optical and electronic types are mostly restricted to surface observation of objects. Information required for material research actually not only arises from a surface but is buried more in the bulk. Computerized x-ray tomography (CT) nondestructively provide us image of any cross section of the object, i. e., three dimensional image of the bulk.

Images of element distribution in objects can be obtained by absorption contrast using two monochromatic x-ray beams which straddle its absorption edge.¹ In order to implement this method monochromatic x-ray beams have been used. Monoenergetic sources are obtained mainly with the combination of SR and monochromator,²⁻⁴ with radioisotopes⁵ or with fluorescence from secondary targets.⁶ The latter two sources are more accessible than SR but their intensity is mostly poor. Therefore we attempted to utilize polychromatic beams other than monochromatic beams of conventional x-ray sources. We have extended this critical absorption technique to polychromatic x-ray with filter modulation instead of crystal monochromators and have demonstrated its capabilities.

In the present paper the basic idea of our filter modulation technique for x-ray microtomography is described at first and the devices used in this study are briefly explained. Then the experimental results obtained through two different data subtraction processes are discussed.

FILTER MODULATION

Conventional x-ray sources such as sealed-off tubes generate a wide band of white radiation superimposed with characteristic lines of target elements. Filters have been used for crystal diffraction studies to select a suitable line from those characteristic lines. A single filter which has an absorption edge on the just higher energy side of K_{α} lines of a target suppresses a K_{β} line and a considerable part of white radiation. This filtered spectrum still contains

continuum in the low energy region and in the far high energy. The remained continuum and the reduced K_{β} can be substantially eliminated by the Ross balanced filter technique, which is a combination of a β filter and an additional filter of proper thickness with an absorption edge on the just lower energy side of K_{α} lines. The difference between the two measurements obtained with each filter is ascribed to the narrow band between the absorption edges of filters, i. e., mainly to the K_{α} lines. We have applied these techniques to microtomography in the simpler condition.

Figure 1 shows schematic representation of continuum x-ray spectra from a conventional source. Characteristic lines are not essential and are omitted for simplicity. As illustrated in the figure, I_0 and I designate the intensities of the incident and transmitted x-ray fluxes, respectively. It is assumed that the object contains an element of an absorption edge at the energy denoted by s and that two filters of different absorption edges at the higher and the lower energies denoted by f_1 and f_2 are employed for the spectrum modulation of the incident beam.

Postreconstruction Subtraction

Spectra (a) are incident and transmitted ones without filtering. One absorption edge at s is illustrated in the transmitted spectrum of I . The contrast corresponding to this absorption should be involved in the CT image reconstructed from projections with these spectra. In the case of f_1 -filter, (b) in the figure, the transmitted spectrum includes a part of absorption curve from the edge s but the transmitted spectrum of f_2 -filter, (c) in the figure, does not contain any absorbed component due to the edge s . The reconstructed tomograph with filter f_1 should have the contrast due to the absorption edge s but the tomograph with f_2 should not. The contrast of reconstructed images are the results calculated from I/I_0 , the ratio of transmitted to incident intensity, where I_0 and I are integrated intensities over the spectra. From the spectra (a), (b) and (c) it can be expected that the contrast due to the absorption edge s in reconstructed tomographs appears to be stronger in (b), moderate in (a) and weak in (c). By comparison of these three images, simply by subtraction between reconstructed images, the possibility for element-selective imaging arises. This may be termed "postreconstruction subtraction".

Prereconstruction Subtraction

The curves of (d), (e) and (f) in Figure 1 are narrow band spectra obtained by direct subtraction of (b) from (a), (c) from (a) and (c) from (b), respectively. This may be called "prereconstruction subtraction". Through this process the low energy envelopes are reduced in the spectra of incident beams. The transmitted spectra of (d) and (e) have to contain the absorption due to the edge s and the fraction of those components are nearly same. The most monoenergetic spectra are (f), which eliminate polychromatic artifact from CT images. This combination of subtractions provide highest contrast if the absorption edge s is equal to f_2 but least contrast will be given if the edge s is equal to f_1 .

EXPERIMENTAL

The microtomography system used in the present study consists of an x-ray source, a filter changer, a sample stage, an image detector (a combination of a fluorescent screen and a cooled CCD still camera) and a computer, as shown in Figure 2. A personal computer (PC) was employed to control filtering the incident beam, rotation of the sample stage and to acquire image data of incident and transmitted x-ray. The PC is connected to a local area network and is able to access other powerful engineering work stations, which was used for the fast reconstruction of the cross section by filtered liner back projection using the Shepp-Logan

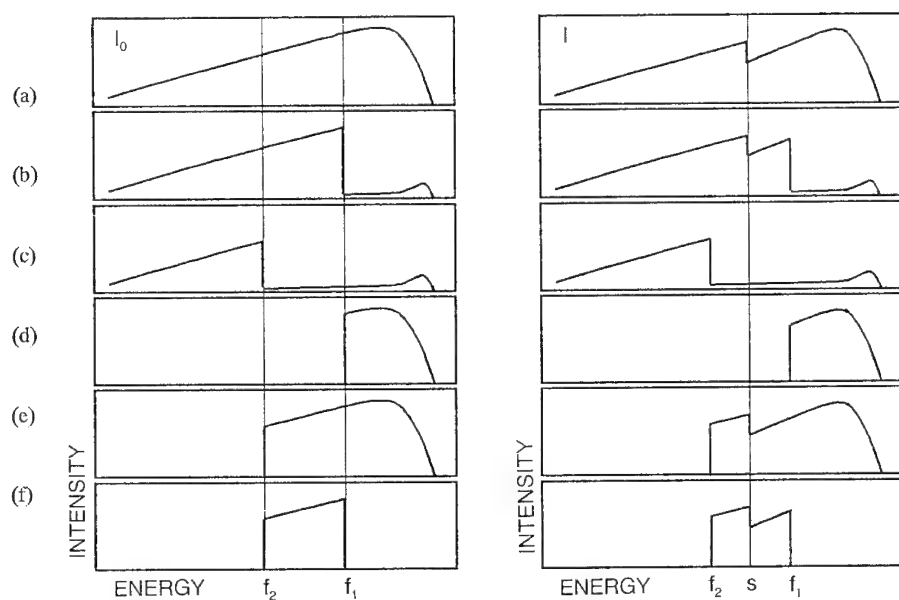


Figure 1. Schematic representation of spectral variation of incident (left) and transmitted (right) white x-ray modulated by filters. The object consists of an element of an absorption edge at s . Filters of different absorption edge at f_1 or f_2 is used in (b) and (c) to modulate incident beams but no filter is used in (a). Subtracted spectra of (a)–(b), (a)–(c) and (b)–(c) are also illustrated in (d), (e) and (f) respectively.

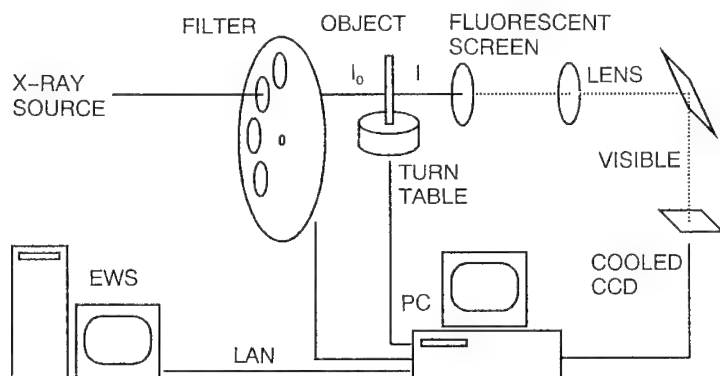


Figure 2. Block diagram of the microtomography system. The filter mechanism controlled by the PC exchanges the filters to modulate the spectrum of the incident x-ray beam.

Table 1. Transmission coefficients of filters.

Material	Thickness(μm)	Transmission coefficient	
		Cu K_{α}	Cu K_{β}
Copper	10	0.624	0.704
Nickel	10	0.668	0.089

These values are estimated from the attenuation coefficients listed in the reference (8).

filter. Most of the system has been described elsewhere.⁷ Only the filter manipulation mechanism is added for this study.

A copper target tube of normal focus was used in the present study and was operated at a power of 20 kV x 40 mA. The equivalent source size was 1 mm or less. Number of pixels of the CCD is 576 x 384 but the data of neighboring two pixels in the vertical and the horizontal direction were joined to one and then they were again summed over 30 pixels in vertical direction along to the CT rotation axis. This data reduction provides a better signal to noise ratio with moderate spatial resolution.

RESULTS AND DISCUSSION

The test sample is made of two coaxial glass tubes of 0.7 mm in outmost diameter. The outer and inner tubes are respectively filled with CuSO_4 and NiSO_4 saturated solutions. Copper and nickel foils of 10 μm in thickness were used for beam modulation filter, whose transmission coefficients are given in Table 1. The combination of this sample and the filters comprises either of the special cases in which absorption edges s are equal to f_1 or f_2 .

The reconstructed cross section of the test sample are shown in Figures 3. 3(a), 3(b) and 3(c) are measured without filter, with the copper filter and with the nickel filter, respectively. At a glance there are no differences among these three photographs, but some difference is found on the CRT. In the original CRT images of 3(a) and 3(b), the nickel solution region appears slightly darker than the copper, while almost the same brightness are seen in 3(c). Information of element distribution are extracted from these delicate deviations by subtraction between the images.

Postreconstruction Subtraction

The image obtained by subtraction of Figure 3(b) from 3(a) is Figure 4(a), Figure 3(c) from 3(a) is Figure 4(b) and Figure 3(c) from 3(b) is Figure 4(c). The copper solution region is darker than the nickel region in Figure 4(a), while it is reversed in (b) and (c). These are in good agreement with the above consideration based on Figure 1(a), (b) and (c). Absorption edges f_1 and f_2 of Figure 1 correspond to copper and nickel, respectively, in this experiment. In the copper solution region the edge s is equal to f_1 and in the nickel solution region s is f_2 .

Both of the copper and the nickel solution regions in Figure 3(a) exhibit characteristic absorption, and in 4(b) only the nickel region shows the absorption but no characteristic absorption occurs in 4(c). Therefore in Figure 4(a) [3(a)-3(b)] the copper solution region is more enhanced and becomes darker than the nickel region. This relation is found to be reversed in Figure 4(c).

Reconstructed absorption intensities in the copper and nickel solution in Figure 3(a) is not the same because nickel strongly absorbs copper K_β line. Since the tomograph is calculated from I/I_0 which includes the characteristic lines, it makes the nickel solution region slightly darker than the copper. This is confirmed in Figure 4(b) [3(a)-3(c)].

Prereconstruction Subtraction

To pick up properly a narrow band of spectra as shown in Figures 1(d), 1(e) and 1(f) intensities of the incident have to be adjusted over the envelope to be eliminated before the subtraction process. Intensities on the lower energy side of absorption edge of filters can be matched by considering transmission factors shown in Table 1.

Figure 5(a) is obtained by tomographic reconstruction after subtracting copper filter data multiplied by a factor of 1.43 from no filter data and is equivalent to a tomograph using x-ray of higher energy than the copper absorption edge. Also the other two images, Figures 5(b) and

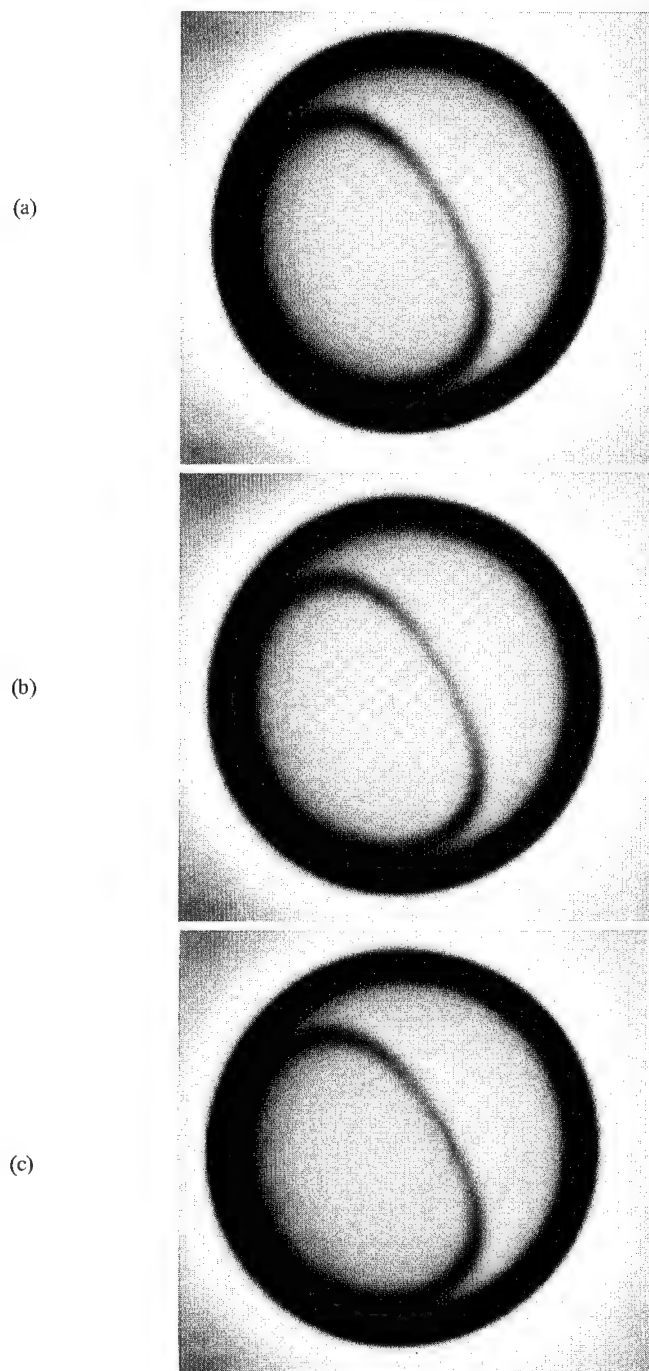
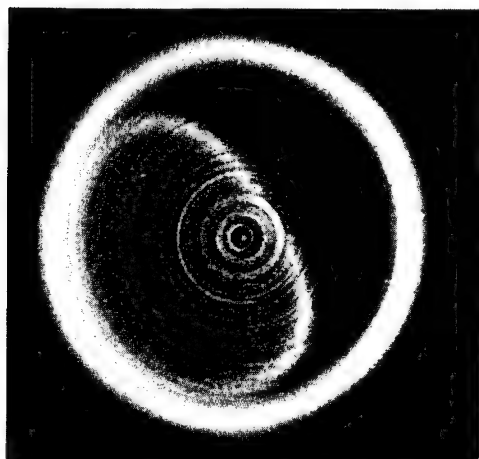
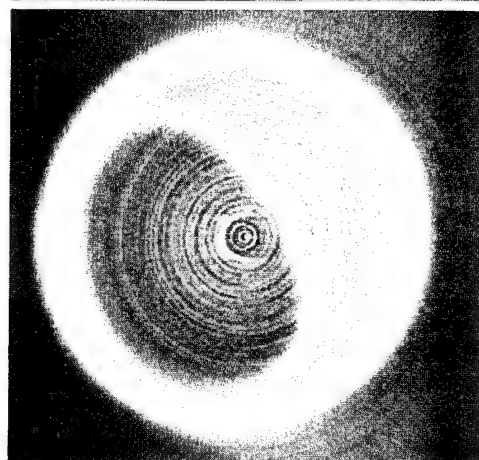


Figure 3. Reconstructed tomographs of the coaxial glass tubes of 0.7 mm in outmost diameter filled with CuSO_4 and NiSO_4 solutions. No filter is employed in (a). The copper and nickel filters are used in (b) and (c), respectively. Transmission coefficients of the filters are listed in Table 1.

(a)



(b)



(c)

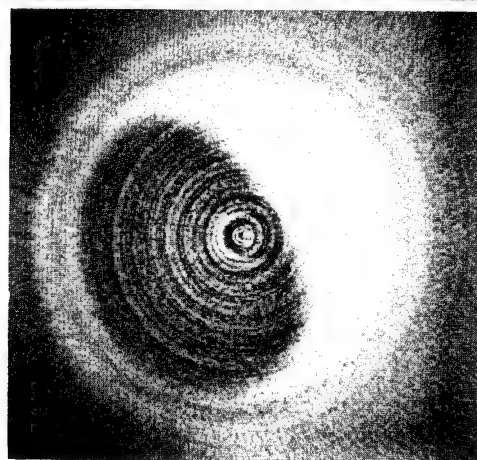
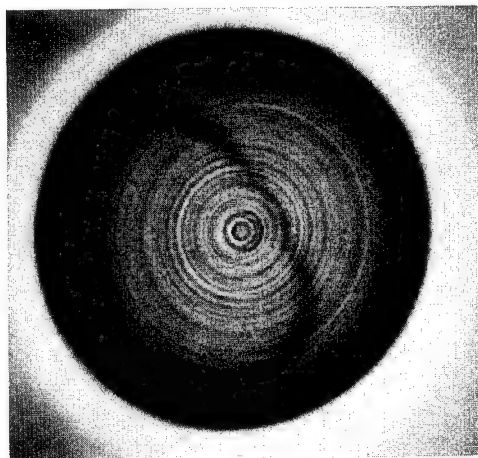
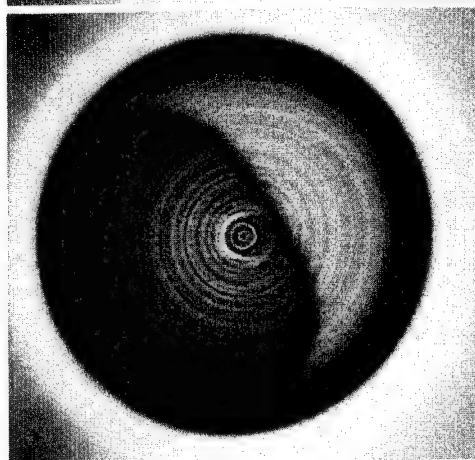


Figure 4. Images obtained by "postreconstruction subtraction" of the reconstructed tomographs in Figure 3. The images (a), (b) and (c) correspond to subtraction of Figure 3(b) from 3(a), of 3(c) from 3(a), and 3(c) from 3(b).

(a)



(b)



(c)

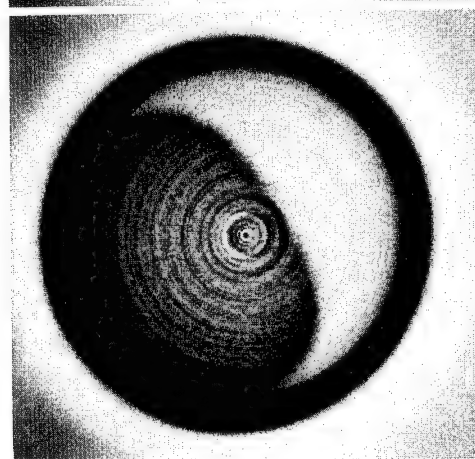


Figure 5. Reconstructed tomographs after "prereconstruction subtraction". The data of transmission images are subtracted each other after multiplied by correction factors which is estimated from the transmission coefficients in Table 1 before the reconstruction process. (a): (no filter) - $1.43 \times$ (copper filter), (b): (no filter) - $1.50 \times$ (nickel filter), (c): (copper filter) - $0.93 \times$ (nickel filter).

5(c), are reconstructed after subtraction of nickel filter by a factor of 1.50 from no filter and after subtraction of nickel filter by a factor of 0.93 from copper filter, i. e., correspond, respectively, to the higher region than nickel edge and the narrow band between copper and nickel edges.

Absorption by the copper and the nickel solution are nearly the same in the higher energy region than the copper edge. Thus no differences between both regions are found in Figure 5(a). The x-ray spectrum of higher energy than the nickel edge contains quite large K_{β} line of copper. This profile gives somewhat darker contrast to the nickel solution than to the copper in Figure 5(b). As for monoenergetic characteristics, high contrast between the nickel and the copper solution is seen in Figure 4(c), because x-ray having energy between copper and nickel edges is strongly absorbed by the nickel solution but not by the copper.

Figures 5(c) and 4(c) are different from each other even though they are obtained from the identical data set of the nickel filter and the copper filter. The "postreconstruction subtraction" extracts elemental information but it drops other contrast such as glass tubes in Figure 4(c). On the contrary, the "prereconstruction subtraction" provides quasimonochromatic CT which clearly exhibit elemental dependence but does not extract only elemental information. It still contains other contrasts such as glass tubes in Figure 5(c).

CONCLUSIONS

We have described an experimental approach to introduce filtering technique into x-ray microtomography using conventional sources for elemental evaluation of objects. Results are summarized as follows:

- Filter modulation of incident beam yields slight modification of contrast in tomographs.
- Postreconstruction subtraction between those tomographs extracts elemental information qualitatively.
- Prereconstruction subtraction with initial projection data provide quasimonochromatic features to polychromatic CT.

In this study incident x-ray contains not only continuum but also characteristic lines which seem to influence tomography both positively and negatively. Further investigation is necessary to generalize this technique for pure continuum spectra. The images processed by "prereconstruction subtraction" can be treated again by the "postreconstruction subtraction". Doubly processed images may be promising to effectively extract the elemental information.

REFERENCES

1. L. Grodzings, Critical Absorption Tomography of Small Samples, Nucl. Instr. and Meth. 206:547(1983).
2. B. P. Flannery, H. W. Deckman, W. G. Roberge, K. L. D'Amico, Three-Dimensional X-Ray Microtomography, Science 237:1439(1987).
3. J. H. Kinney, Q. C. Johnson, R. A. Sarayan, M. C. Nichols, U. Bonse, R. Nusshardt, and R. Pahl, Energy-Modulated X-Ray Microtomography, Rev. Sci. Instrum. 59:196(1988).
4. Y. Suzuki, K. Usami, K. Sakamoto, H. Kozaka, T. Hirano, H. Shinnno, and H. Kohno, X-Ray Computerized Tomography Using Monochromated Synchrotron Radiation, Jpn. J. Appl. Phys. 27:L461(1988).
5. J. Fryar, K. J. McCarthy and A. Fenelon, Differential X-Ray Absorptiometry Applied to Computerized X-Ray Tomography, Nucl. Instr. and Meth. A259:557(1987).
6. R. Cesarco, Principles and Applications of Differential Tomography, Nucl. Instr. and Meth. A270:572(1988).
7. Y. Yamauchi, T. Ikuta, and N. Kishimoto, Three-Dimensional High Resolution Tomography for Small Objects, Nondestr. Test. Eval., 7:309(1992).
8. J. A. Ibers and W. C. Hamilton, "International Tables for X-Ray Crystallography Vol. IV", Kynoch Press, Birmingham (1974).

X-RAY MEASUREMENT OF FATIGUE DAMAGE BY USING IMAGING PLATE

Satoru Yusa,¹ Kazuo Yoshida,² Yasuo Yoshioka³

¹ Research Institute, Ishikawajima-Harima Heavy Industries Co., Ltd.
3-1-15, Toyosu, Koto-ku, Tokyo 135 Japan

² Research and Development Group, Nuclear Power Division
Ishikawajima-Harima Heavy Industries Co., Ltd. 1
Shin-nakahara-cho, Isogo-ku, Yokohama 235 Japan

³ Musashi Institute of Technology
1-28, Tamazutsumi, Setagaya-ku, Tokyo 158 Japan

INTRODUCTION

To improve reliability, safety and economy of structure or plant, needs of life assessment and residual life estimation are increasing. Therefore, the improvement of accuracy and expansion of the application range of damage measuring technique are requested.

Fatigue is one of the most important failure modes as well as corrosion, creep, etc. For the measurement of fatigue damage, various methods have been proposed, and most of them measure change of hardness (hardening or softening), initiation or growth of micro-crack, and change of substructure (dislocation density, subgrain size, total misorientation, etc.) The X-ray diffraction measures the third phenomenon and it is thought that fatigue damage measurement by using X-ray diffraction has the following three characteristics.

- Nondestructive
- Measured at surface
- Measured in small area

By the way, the imaging plate is a newly developed X-ray detector¹. At first, it was used in the medical field instead of a radiographic film. As it was shown that imaging plate has an excellent characteristic and is useful for measurement of X-ray diffraction², the application of imaging plate to the field of material science has been tried recently^{3,4}.

Imaging plate combines following characteristics compared with old X-ray detectors.

- Two-dimensional detector
- High sensitivity
- Wide dynamic range
- Repetitious use
- Quantitative
- Quick development

Then, we measured the X-ray diffraction images of fatigue damaged material by using imaging plate, to study a new damage evaluation method for metallic material.

PRINCIPLE OF IMAGING PLATE

Imaging plate is a flexible plate on which fine particle of photostimulable phosphor crystal are spread uniformly (Figure 1). When the radiation such as X-ray or γ -ray is applied to imaging plate, photostimulable phosphor crystal absorb the energy of radiation and electrons are excited to semi-stable high energy level. After that, when the incitement such as heat or visible ray is applied to imaging plate, electron drop down to the ground

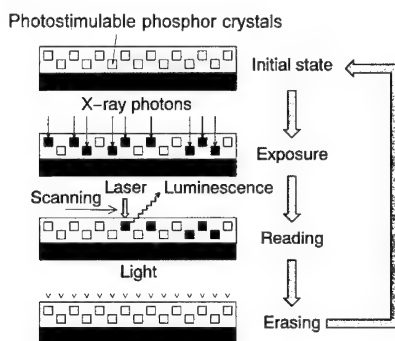


Figure 1. Principle of imaging plate.

level and discharge saved energy as fluorescence. As the number of excited electron is in proportion to the integral strength of applied radiation, the intensity of fluorescence is in proportion to it, too. That is, by measuring the position and intensity of the fluorescence brought by incitement, we can know the distribution of radiation applied to the imaging plate before. After reading X-ray image, imaging plate is erased by the visible ray for a new measurement.

CONSTRUCTION OF READOUT SYSTEM

As readout system is necessary to get the X-ray image from imaging plate, we constructed image reader (Figure 2) and used for the measurement of X-ray diffraction. We adopted the concentric circle type scanning for our image reader, because, we thought that Debye-Scherrer ring can be measured efficiently with this style.

Laser beam to incite the imaging plate passed through the optical filter, shutter, collimator, and was bent in the right angle with a beam splitter. And, laser beam was focused by objective lens to the small area with diameter of 100 μm .

We used the high-resolution type imaging plate with the thickness of 0.15 mm made by Fuji Film Co. The center hole of imaging plate was made to pass through the x-ray collimator through it, and this hole was used to fix the imaging plate on the turntable of image reader. The turntable was rotated by a DC servo motor at a constant speed of 60 rpm. The scanning point was moved 100 μm at a time in radial direction by a slide table that was set up under the turntable.

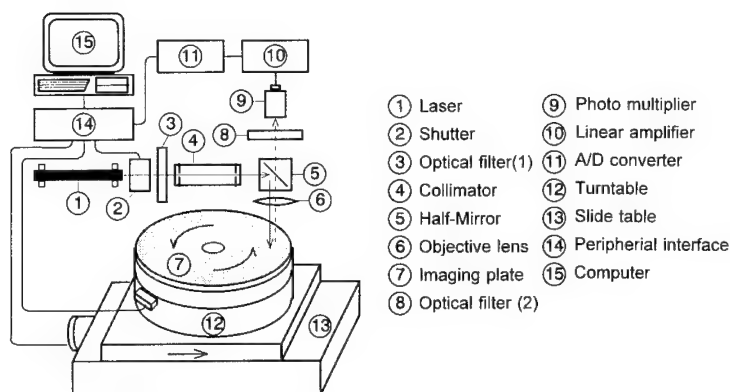


Figure 2. Schematic view of imaging plate readout system.

Fluorescence that the imaging plate emitted passed through the objective lens, beam splitter, optical filter, and was finally detected by the photomultiplier tube. The voltage, which the photomultiplier tube outputs, was amplified by a linear amplifier, converted into digital data by a A/D converter, and logged by a computer.

The movement of the slide table, opening and shutting of the shutter, and the fluorescence intensity logging were synchronized with the rotation of the turntable, and all of them were automatically controlled by a computer. The computer could log the intensity of fluorescence for 4096 point in a rotation of turn table, and the measured intensities of fluorescence were recorded in the form of the digital data of 12 bit.

To confirm the performance, we carried out the experiment using standard γ -ray source. We read out the imaging plate after applying the γ -ray to it for a proper time, and

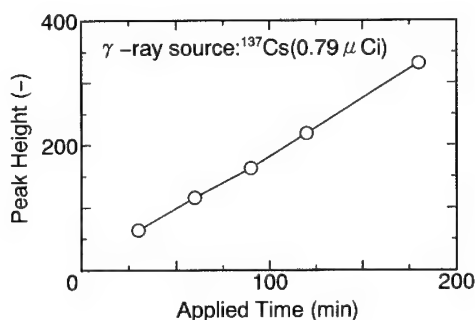


Figure 3. Change of peak height with exposure of γ -rays.

varied exposure time from 30 min to 180 min. As shown in Figure 3, the maximum peak value was in proportion to applying time, and we could confirm that the measured value by the image reader was in proportion to the integral dose of radiation.

EXPERIMENT

At first, we made samples which had already known amount of fatigue damage. Next we measured the X-ray diffraction image of them, and at last we calculated parameters from diffraction images to evaluate fatigue damages by them.

Making of Fatigue Damages Samples

To make the materials that have various fatigue damage, we carried out low-cycle fatigue tests. The specimen for low-cycle fatigue test is shown in Figure 4 and test conditions are shown in Table 1.

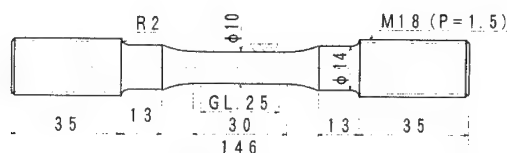


Figure 4. Specimen for low-cycle fatigue test (all dimensions in mm).

Table 1. Condition of low-cycle fatigue test.

Type of loading	Axial
Control mode	Strain
Waveform	Triangle
Strain rate $\dot{\epsilon}$ (%/sec)	0.4
Strain range $\Delta\epsilon$ (%)	1.2
Temperature	R.T.

At first, fatigue test was carried out to determine the fatigue life of the material. After that, other fatigue tests were interrupted with fewer cycle number than fatigue life to make materials that had a different amount of fatigue damage. The result of low-cycle fatigue test is shown in table 2.

Table 2. Results of low-cycle fatigue test.

Cumulated damage(%)	Cycle
100	3174 (failure)
75	2382
50	1588
25	794
10	315
1	31
0.1	3

Samples were cut out from the center of the specimen, polished by mechanical polishing, its surface layer was removed about 100 μm in thickness by electrolyte polishing.

Measurement of X-ray Diffraction

The X-ray diffraction patterns measured in the back reflection mode at the section of the sample. The conditions of diffraction measurement are shown in Table 3. The samples of diffraction image are shown in Figure 5.

Table 3. Conditions of X-ray diffraction.

Characteristic X-ray	Cu-K α
Diffraction line	Fe- γ 420
Tube voltage	40 kV
Tube current	50 mA
Irradiated area	ϕ 1 mm
Exposure time	1 ~ 20 min

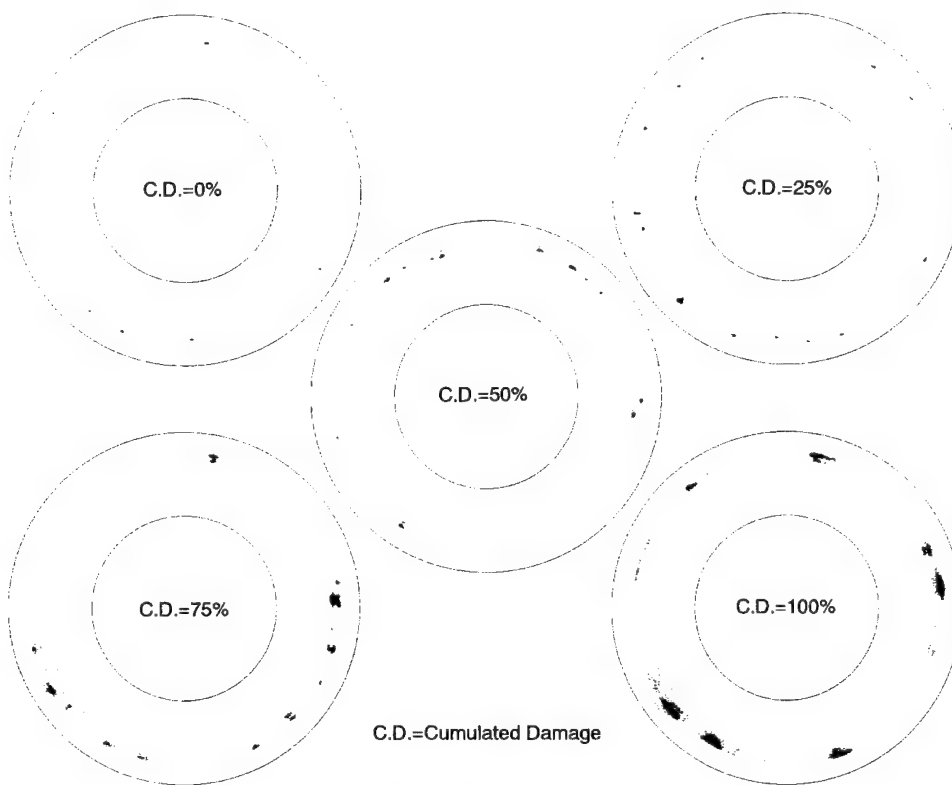


Figure 5. Change of Debye-Scherrer ring with cumulated damage.

All of diffraction images were not continuous rings but formed with diffraction spots. Intensity of each diffraction spot seems to be decreasing, and the size of the spot looks increasing with the increase of damage. And we could observe the separation for some diffraction spots. The typical changes of diffraction spot with the increase of fatigue damage are shown in Figure 6. It was thought that such expansion of a diffraction spot was caused by the distortion of lattice a by large number of dislocations introduced into grain by fatigue, and, the separation was caused by the formation of subgrains. The diffraction image of a sample obtained from a failure specimen is significantly different from the image for other specimens, and it is thought that this big change of diffraction image is caused by the deformation of the sample that was added by the fracture of specimen.

Calculation of Parameter

In this study, we tried to get the parameters that can evaluate the change of diffraction spot, and examine the correlation of these parameters and the fatigue damage.

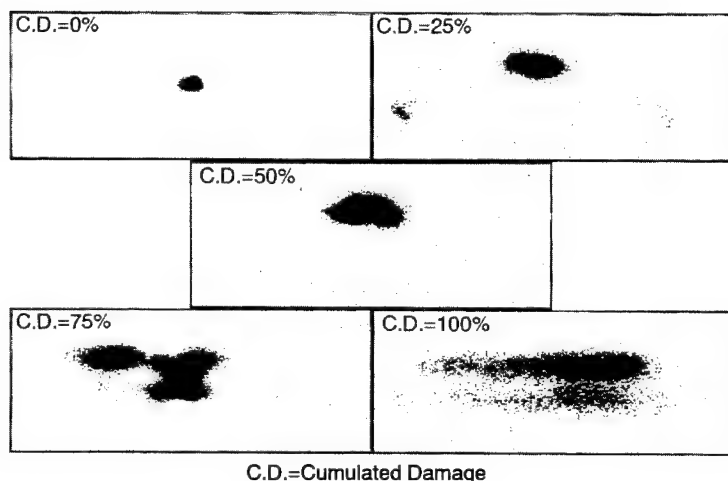


Figure 6. Typical change of diffraction spot.

As diffraction images in this study were not continuous, we could not apply the definition of half value breadth for the diffraction ring that is often used for the evaluation of fatigue damage. Then, we defined the following parameters (Figure 7) and calculated them for each diffraction stop in the Debye-Scherrer ring.

- Half value breadth for the tangential direction
- Half value breadth for the radial direction
- Half value aspect ratio
- Half (50%), 25%, 10% value area

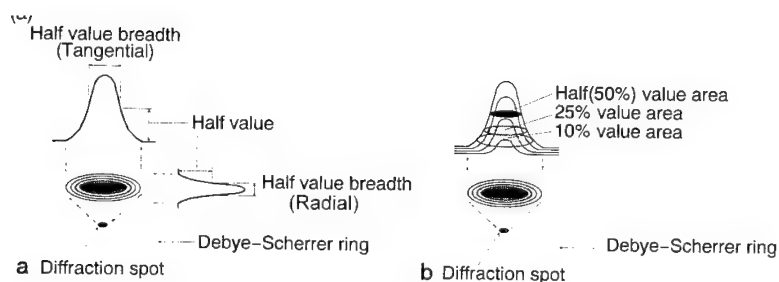


Figure 7. Definition of parameters. (a) Tangential and radial half value breadth. (b) Half(50%), 25%, 10% value area.

Half value breadth for the tangential direction and radial direction were the half value breadth of 2-dimensional peak that were calculated by projection of 3-dimensional intensity diagram of diffraction spot to each direction. Half value aspect ratio was a ratio of the tangential half value breadth and radial half value breadth. Half value area, 25% value area, and 10% value area were defined as area of the part where measured intensity exceeds 50%, 25%, and 10% of peak value respectively.

These values were measured in 100 of diffraction spots or more for each sample. And, the value of the spots that have peak intensity less than 500 was screened out. Next, the measured values were arranged in order, and, the value of 10% from maximum value and 10% from minimum value were screened out. The average of these values were calculated at the end.

RESULTS

The change of the averaged half value breadth for tangential and radial direction with damage is shown in Figure 8.

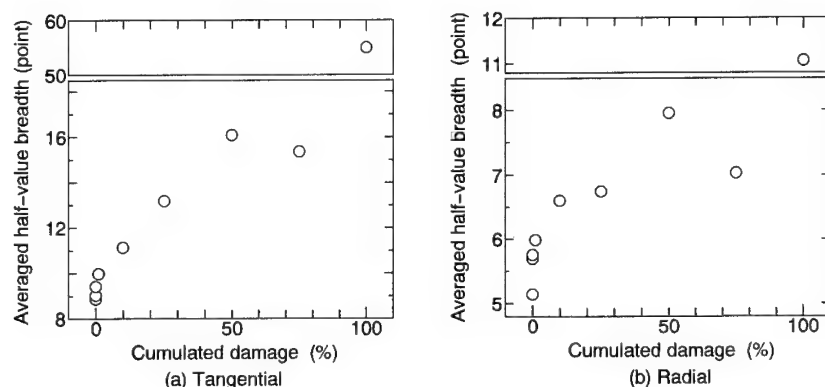


Figure 8. Change of averaged half value breadth with cumulated damage. (a) Tangential half value breadth. (b) Radial half value breadth.

Both half value breadth are increasing with the increase of fatigue damage, and the parameter of 100% damaged sample is larger than other samples. As mentioned in the observation of diffraction spot, it was thought that this difference was caused by the plastic deformation added by failure of sample.

In the comparison of the tangential half value breadth and the radial half value breadth, the tendency of value change is almost similar, but, radial half value breadth have a little larger scattering.

Although, the value for the sample that have 75% damage is less than that of 50% damage, we guessed that this is caused by some errors of low-cycle fatigue test condition such as total strain range etc.

The value change of tangential half value breadth from initial state is larger than that of radial half value breadth.

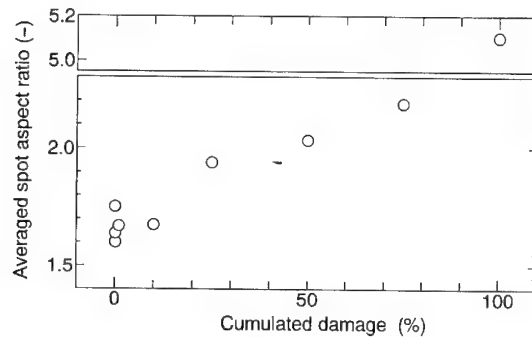


Figure 9. Change of averaged spot aspect ratio with cumulated damage.

The change of aspect ratio of the diffraction spot with the fatigue damage is shown in Figure 9, and the tendency of aspect ratio change looks similar to the change of half value breadths. But, as the statistic scatter of two half value breadth was multiplied, the scattering of the aspect ratio became large. The change of half value area, 25% value area, and 10% value area with fatigue damage are shown in Figure 10. The tendency of their changes are similar to the change of the tangential half value breadths, too. The change of the spot area is surely related to the product of the change of the tangential spot size and the change of the radial spot size. However, as the change of the tangential spot size is

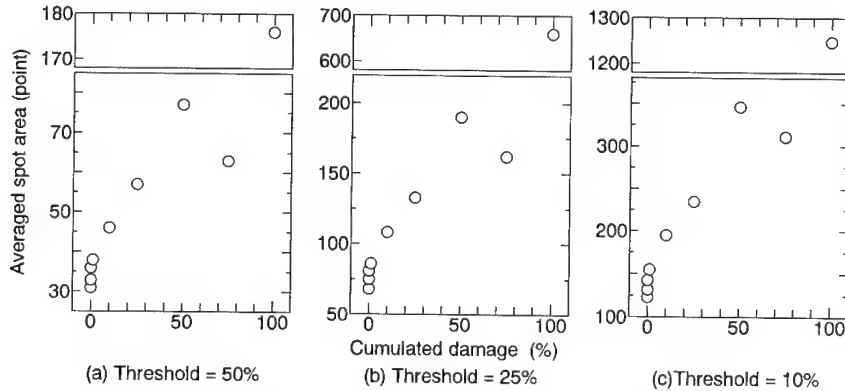


Figure 10. Change of averaged spot area with cumulated damage. (a) Threshold level = 50% of peak height. (b) Threshold level = 25% of peak height. (c) Threshold level = 10% of peak height.

larger than that of radial spot size, the change of tangential spot size affects the change of spot area remarkably.

The tendency of the area change is almost the same in any threshold level. In other words, the diffraction spot expand similarly with the increasing of fatigue damage. When the threshold level is low, as the area change from initial value becomes large, it seems easy to evaluate damage from it. However, when the threshold level is too low, there is the possibility that the background noise affects the value of the parameter, and it becomes difficult to separate the close diffraction spots. Therefore, we have to define the threshold level carefully to calculate these parameters.

As mentioned above, the tangential half value breadth and the area of the diffraction spot are hopeful as parameter to evaluate the change of diffraction spot with fatigue damage. Especially, as area of diffraction spot is easy to get from diffraction image directly by data processing, we thought that it seems suitable for practical use.

CONCLUSIONS

We made an image reader to apply the imaging plate to fatigue damage evaluation by using X-ray diffraction. And, we measured the diffraction image of type 304 stainless steel that had various amount of fatigue damage. As a result, we observed that diffraction spots expanded with the increase of fatigue damage, and it was shown that fatigue damage can be evaluated by a parameter which indicate the change of spot size.

REFERENCES

1. M.Sonoda,M.Takano,J.Miyahara and H.Kato, Computed radiography utilizing scanning laser stimulated luminescence, *Radiography* 148:833(1983).
2. Y.Amamiya,N.Kamiya and J.Miyahara, Application of photostimulable phosphor film to X-ray diffraction studies , " *OYO BUTURI* " 55:957(1986) (In Japanese).
3. Y.Yoshioka,T.Shinkai and S.Ohya, The use of 2-D detector utilizing laser-stimulated luminescence for X-ray diffraction studies on mechanical behavior of materials, *Adv. X-Ray Anal.*33:339(1990).
4. Y.Yoshioka and S.Ohya, X-ray analysis of stress in a localized area by use of imaging plate, *Adv. X-Ray Anal* 35:537(1992).

NONDESTRUCTIVE CHARACTERIZATION OF METALS SUBJECTED TO HIGH-POWER ULTRASOUND

Kirsten A. Green and Robert E. Green, Jr.

Center for Nondestructive Evaluation
The Johns Hopkins University
Baltimore, Maryland 21218

X-ray diffraction topography and infrared imaging techniques were used in situ with aluminum and zinc specimens undergoing high-power insonation using a 20 kHz ultrasonic horn. X-ray topographic techniques allowed for a nonintrusive study of the mechanical alterations in the structure of the metal specimens, while the infrared system allowed for a study of the specimens' thermal properties. It should be noted that all testing was performed in real-time with x-ray and infrared images recorded simultaneously on video tape.

INTRODUCTION

In 1955, Blaha and Langenecker reported a softening effect in zinc crystals which were undergoing tensile deformation with superimposed ultrasonic vibrations [1]. This phenomenon has become known as the "Blaha effect" and has stimulated scientific interest. Subsequent investigators also noted work softening in specimens insonated below a certain sound intensity threshold [2-4]. However, above a certain sound intensity threshold a work hardening effect was observed [4,5]. In addition, application of high-power ultrasound to metal specimens during wire and strip drawing and bar and tube bending has been shown to reduce the internal (volume) and external (surface) frictional forces required to plastically form the specimens [6-8].

Several "theories" have been proposed to explain the above mentioned phenomena. Some investigators believe that work softening occurs due to additional energy supplied by the ultrasonic field which causes dislocations to be created and moved [1]. Others attribute the work softening to localized heating which takes place in regions around dislocations and other imperfections when ultrasonic waves are scattered [3,4]. The high intensity ultrasonic treatment (work hardening) has been likened to fatigue testing [9]. The internal and external friction reductions have been explained in terms of the superposition of alternating ultrasonic stress waves on an externally applied static stress [2,6-8]. For a more detailed account of past work conducted in this field one is referred to a review by Green [10].

Speculation surrounds what is in fact happening to the internal structure of a metal subjected to high-power insonation. It was the objective of this research to arrive at some conclusions regarding this matter. X-ray topographic and infrared imaging techniques were used in situ with aluminum and zinc specimens undergoing high-power insonation using a 20 kHz ultrasonic horn.

BACKGROUND

X-ray topography is the name given to several x-ray diffraction techniques which permit direct observation of lattice defects both on the surface (back-reflection) and in the bulk of single crystals (transmission). Topographic techniques are unique in that they yield information about the defect structure, down to the size of individual dislocations, throughout the volume of fairly thick crystals; these techniques have been reviewed in several publications [13,14]. Among the various possibilities, the Asymmetric Crystal Topography (ACT) technique [15] was used to study the effects of high-power ultrasound on aluminum and zinc single and polycrystalline specimens. In the ACT set-up used in this investigation, a slit collimated, white radiation x-ray source was incident upon a high quality asymmetrically cut silicon crystal. This crystal served as both a monochromator and beam expander, resulting in a x-ray beam of approximate dimensions of 1 1/2 inches high by 1/2 inch wide. Specimens of interest were placed in the path of this monochromated and expanded x-ray beam and diffraction information was detected using an image intensifier with a fluorescent screen faceplate. Due to the relatively weak x-ray source available in the laboratory (copper tube operated at 50 kV, 32 mA), as well as to the thickness of the specimens examined (1/2 inch square or 1/2 inch diameter), the back-reflection mode was utilized in this research. Figure 1 shows a schematic diagram of the ACT experimental arrangement in the back-reflection mode.

In the ACT technique each individual topographic image is essentially a large Laue "spot" generated by diffraction from a particular set of "parallel" lattice planes covering a large area of the crystal. The x-ray beam incident on the specimen illuminates a large area unlike conventional Laue pin-hole techniques and, because of the special beam expanding monochromizing silicon crystal, this large incident beam experiences minimal divergence.

EXPERIMENTAL METHOD

Aluminum and zinc single and polycrystalline specimens of 1/2 inch square (or 1/2 inch diameter) were machined to various lengths depending on whether it was desired for the specimen to be of resonant (a half wavelength) or non-resonant length. Resonance was determined by accounting for the frequency of the ultrasound used (20 kHz) and the longitudinal sound velocity that was measured in each specimen by traditional pulse-echo techniques. Typical specimen lengths were about 4-5 inches; it should also be noted that polycrystalline specimens had a grain size of about 1/2 to 1 inch. The reason for using large grained polycrystalline materials is that a substantial amount of x-ray diffraction information can be gained (as is also true for single crystal specimens) while at the same time studying the influence of grain boundaries.

After specimens were cut to length, they were tapped at one end to facilitate coupling the specimen to the ultrasonic horn. In addition, a series of grinding and polishing clothes were used to polish one side of each specimen to a 5 μ m finish. Surface preparation was completed by chemically polishing the specimen in a Tegtart acid solution. Early testing determined that surface finish plays a role in the quality of the x-ray diffraction topographs one obtains in the back-reflection mode.

Following surface preparation, specimens were photographed at low magnification for documentation purposes. In addition, topographs and Laue x-ray diffraction photographs of specimens were made and recorded on film prior to testing.

Specimens were screwed into a tapped catenoidal 20 kHz ultrasonic horn which was mounted in Newport rotation and translation stages allowing for two degrees of rotation and two translational motions. The third translational motion was controlled by a lab jack on which the

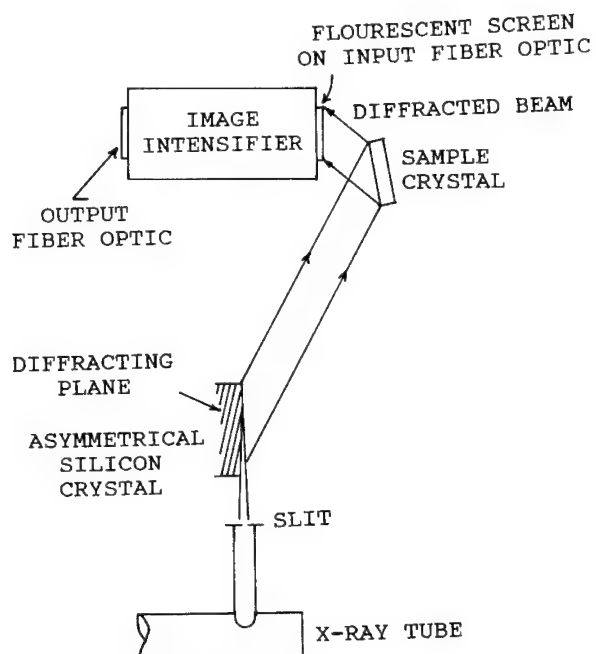


Figure 1. Schematic diagram of the asymmetric crystal topography system in the back-reflection configuration.

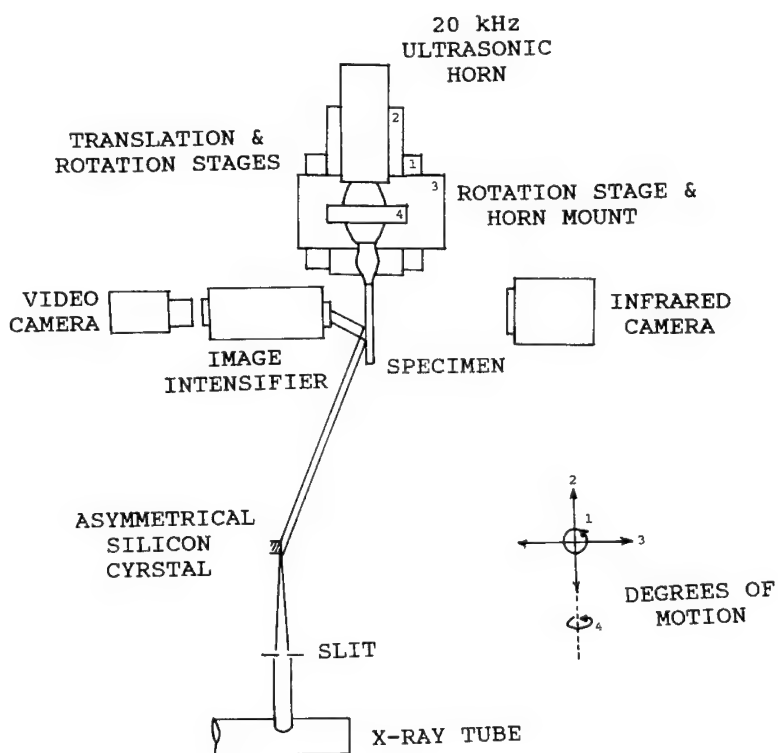


Figure 2. Schematic diagram of the experimental set-up used for analyzing the effects of high-power ultrasound in aluminum and zinc.

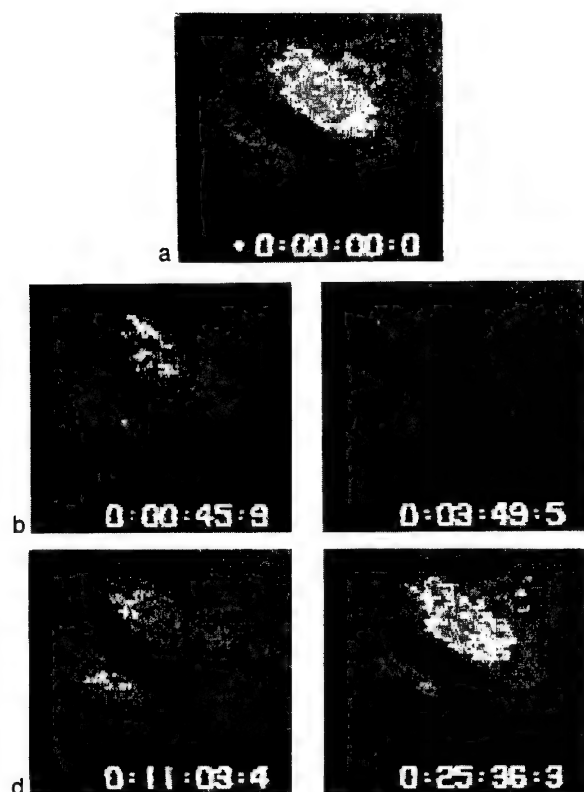


Figure 3. Sequence of frames taken from a videotape of a real-time x-ray run for an aluminum polycrystalline specimen of resonant length. (Only one grain is imaged.)

During Insonation:



After Insonation:



Figure 4. Infrared data for the same resonant length, polycrystalline aluminum specimen shown topographically in Figure 3.

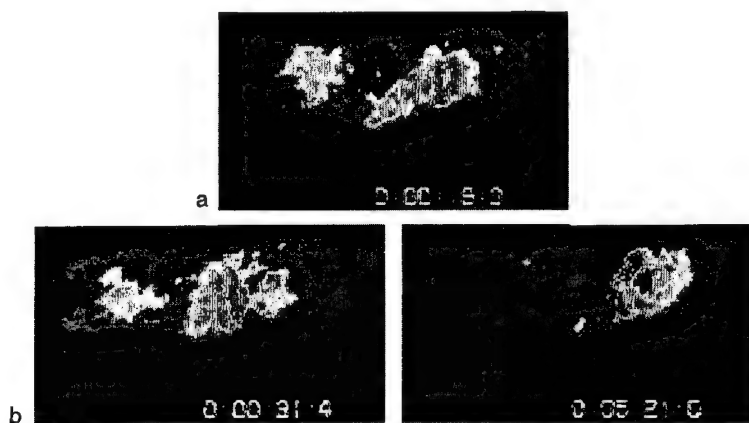
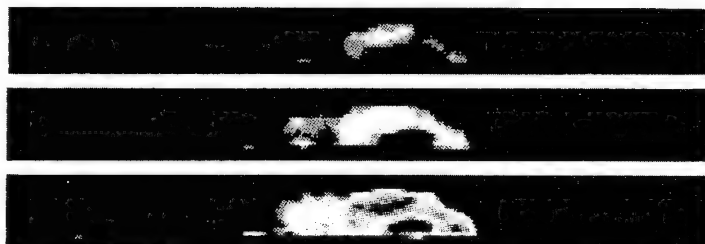


Figure 5. Sequence of frames taken from a video-tape of a real-time x-ray run for an aluminum polycrystalline specimen of non-resonant length. (Only one grain is imaged.)

Before Insonation
Hand-warmth reflection:



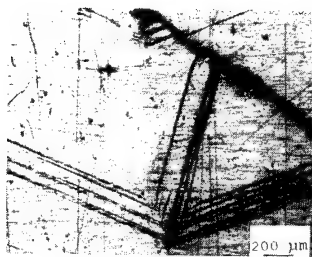
During Insonation (Unpainted):



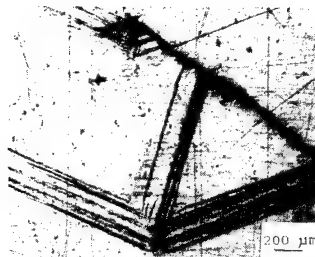
During Insonation (Painted):



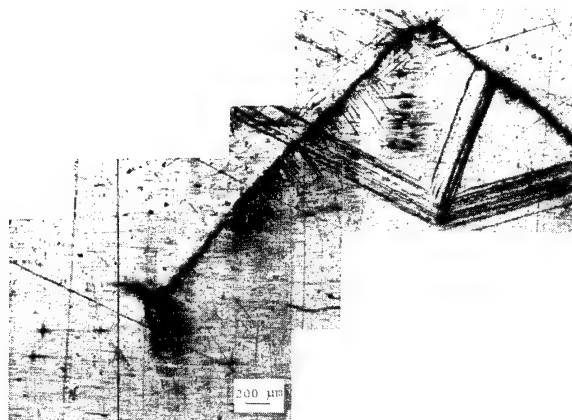
Figure 6. Infrared data for the same non-resonant length, polycrystalline aluminum specimen shown topographically in Figure 5.



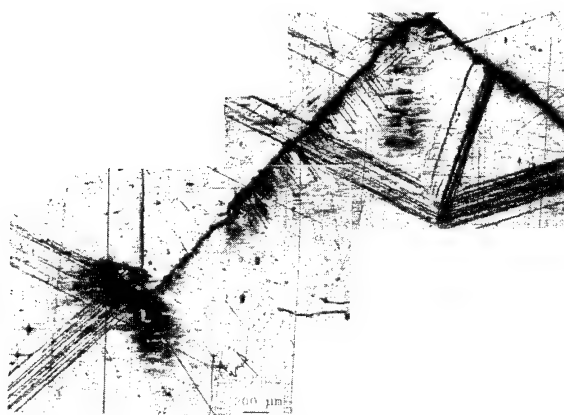
(a)



(b)



(c)



(d)

Figure 7. A series of metallographic montages of a crack propagating in a non-resonant length zinc bicrystal. Total duration of insonation was (a) 198 minutes, (b) 203 minutes, (c) 207 minutes, and (d) 249 minutes.

Newport stages were mounted. The horn-specimen configuration was placed in the asymmetric crystal topography (ACT) set-up such that the specimen was in the path of the expanded, monochromated x-ray beam. An image intensifier with fluorescent screen face-plate was used to detect diffracted x-ray images and these images were recorded by a video camera/VCR which was focused on the output image of the image intensifier. In addition an infrared (IR) camera was placed opposite the image intensifier to detect thermal differences in the specimens undergoing insonation and this information was also recorded on a VCR. In order that the x-ray and IR data recorded on videotape could be directly compared upon analysis it was necessary to have a synchronized event occur which could be detected by both the IR camera and the video camera; therefore, a simple circuit consisting of a light-emitting diode and a light bulb were connected in series with a battery and a push button switch. The light bulb was placed on the front faceplate of the image intensifier in the field of view of the IR camera and the light-emitting diode was placed on the rear faceplate of the image intensifier in the field of view of the video camera. Immediately preceding insonation of a specimen the lights were triggered several times while the VCRs were running and then the horn was turned on. Specimens were insonated for periods of 1 1/2 minutes for the resonant length specimen to as much as 20 minutes for non-resonant length specimens. The resonant specimen was insonated for much shorter time periods due to the 250°C temperature obtained. A schematic diagram of the experimental set-up used for analyzing the effects of high-power ultrasound in aluminum and zinc is shown in Figure 2.

RESULTS AND DISCUSSION

Real-time x-ray topographs of aluminum specimens showed intensity shifts occurring in some areas the instant the ultrasonic horn was turned on. A 3-4°C temperature increase was also detected at the onset of insonation. It is speculated that dislocations are being moved/created by the applied ultrasonic energies as witnessed by the x-ray intensity shift. That is, the x-ray intensity variations in the specimens are likely due to strain fields associated with dislocations, and when these dislocations move so do the associated strain fields. In addition, the temperature increase may be attributed to the fact that it takes more energy to start dislocations moving than it does to keep them moving and this excess energy shows up in the form of thermal energy.

Figure 3 shows a sequence of frames taken from a videotape of a real-time x-ray run for an aluminum polycrystalline specimen of resonant length. Frame (a), at time zero, shows a picture of an x-ray diffraction topographic image of a single grain (dimensions 3/4 inch wide by 1/2 inch high) prior to testing. Frame (b) shows the same grain immediately following the onset of insonation; note the dramatic shift in intensity. Frame (c) shows that after three minutes of insonation the Bragg condition was no longer satisfied (the lattice planes in the crystal had expanded) due to the 250°C temperature reached during testing. Once the ultrasonic horn was turned off and the specimen was allowed to cool down to room temperature the topographic image reappeared, frames (d) and (e).

Figure 4 shows the IR data acquired during and after insonation for the same resonant length, polycrystalline aluminum specimen discussed in Figure 3. As stated above, the resonant length specimen obtained temperatures of 250°C within minutes of the onset of testing. During the insonation process the hot spot was seen to occur at the center of the specimen, as expected in the resonant length specimen, since this is the area of maximum stress (antinode). Upon cooling, it was observed that the specimen did not cool uniformly and may be dependent upon the orientation of the grains within the specimen (there were four grains in this particular specimen).

Figure 5 shows a sequence of frames taken from a videotape of a real-time x-ray run for an aluminum polycrystalline specimen of non-resonant length. Frame (a) shows a picture of an x-ray diffraction topographic image of a single grain (dimensions 1 1/2 inches wide by 1/2 inch high) prior to testing. Frame (b) shows the same grain immediately following the onset of

insonation; note the dramatic shift in intensity. The dramatic shift in intensity at the onset of insonation was similar to that noted in the resonant length specimen, however, topographic images were not observed to disappear as in the case of resonant length specimens even for insonation times of five minutes as is seen in frame (c), as well as for longer time periods of testing (more than 20 minutes). This can be explained because non-resonant length specimens did not reach the temperatures that resonant length specimens achieved (approximately 100°C after 20 minutes of testing versus 250°C after 2 minutes of testing, respectively) and therefore the Bragg condition for diffraction was maintained.

Figure 6 shows the IR data acquired for the same non-resonant length, polycrystalline specimen discussed in Figure 5. The top picture in Figure 6 shows the affect that orientation plays in the emissivity of heat in aluminum specimens; the specimen shown was unpainted and warmed by heat radiated from a hand and clearly shows the four distinct grains in the specimen. The middle sequence of pictures in Figure 6 is the unpainted specimen as a function of heat produced while the specimen was being insonated. From this picture it appears that the grain which was the hottest is the second from the right. In fact, the grain which was the hottest is the one on the far left as shown in the last picture in Figure 6, the painted non-resonant length specimen. These observations indicate the effect of orientation on emissivity and justifies the need for painting specimens black so that discontinuities within the specimen, such as grains of different orientation, are alleviated and results from one grain to another can be compared directly.

Figure 7 shows a series of metallographic montages of a crack propagating in a non-resonant length zinc specimen. The crack formed at a void within the crystal and propagated across one grain to the grain boundary where it was arrested. With further insonation the crack propagated across the second grain and continued to grow until it arrested again. The cause for the second arrest spot is unclear since the specimen was a bicrystal.

CONCLUSIONS

Aluminum specimens of resonant and non-resonant lengths and zinc specimens of non-resonant lengths were studied to determine the effects of high-power ultrasound on the internal structure of the crystals. X-ray topographic and infrared imaging techniques were used in situ with specimens undergoing insonation from a 20 kHz ultrasonic horn. It was determined at the onset of insonation in the aluminum specimens that topographic image contrast was seen to dramatically shift in areas, possibly due to a change in the strain fields associated with dislocation motion. In addition, a 3-4 °C temperature increase was also noted at the onset of testing in these aluminum specimens. The maximum temperature was seen to occur at the antinodal point in the aluminum resonant length specimen, while the position of maximum temperature in the aluminum non-resonant length specimens varied from specimen to specimen and appears to be dependent on crystal orientation.

Deformation in the form of slip bands has been noted in both resonant and non-resonant length specimens of aluminum and zinc. The most striking evidence of deformation occurred in the resonant length aluminum specimen which fractured at the antinodal point (point of maximum stress) due to insonation alone. In addition, stress concentrators aid in the deformation process as witnessed in the zinc specimen where a crack was generated at a void and in a cylindrical aluminum specimen where a possible notch in the threaded region of the specimen caused failure after 2 1/2 minutes of insonation.

REFERENCES

1. F. Blaha and B. Langenecker, "Dehnung von Zinkkristallen unter Ultraschalleinwirkung," *Naturwissenschaften* 42:556 (1955).
2. G.F. Nevill, Jr. and F.R. Brotzen, "The effect of vibrations on the static yield strength of low-carbon steel," *Proc. Am. Soc. Test. Mat.* 57:751 (1957).

3. B. Langenecker, W.H. Frandsen, C.W. Fountain, S.R. Colberg and J.A.M. Langenecker, "Effects of ultrasound on deformation characteristics of structural metals," US Naval Ordnance Test Station, China Lake, California, *NAVWEPS Rept. 8482*, NOTS TP 3447 (March 1964).
4. B. Langenecker, "Effects of ultrasound on deformation characteristics of metals," *IEEE Trans Sonics Ultrasonics* SU-13:1 (1966).
5. B. Lagenecker, "Work hardening of zinc crystals by high-amplitude ultrasonic waves," *Proc. Am. Soc. Test. Mat.* 62:602 (1962).
6. R. Pohlman and F. Lechfeldt, "Influence of ultrasonic vibration on metallic friction," *Ultrasonics* 4:178 (1966).
7. R. Pohlman, The reduction of friction and the forming of metals by generating high frequency bending stresses, in: "Ultrasonics Conference Papers," IPC Science and Technology Press Ltd., Guildford (1971).
8. A.G. Rozner, "Effect of ultrasonic vibration on coefficient of friction during strip drawing," *J. Appl. Phys.* 49:1368 (1971).
9. "Proceedings of the First International Symposium of High-Power Ultrasonics", Graz, Austria, September 1970, IPC Science and Technology Press Ltd., Guildford (1972).
10. R.E. Green, Jr. "Non-linear effects of high-power ultrasonics in crystalline solids," *Ultrasonics* 13:117 (1975).
11. R.B. Mignona and R.E. Green, Jr., "Multiparameter system for investigation of the effects of high-power ultrasound on metals," *Rev. Sci. Instr.* 50:1274 (1979).
12. R.B. Mignona, R.E. Green, Jr., J.C. Duke, Jr., E.G. Henneke II and K.L. Reifsnider, "Thermographic investigation of high-power ultrasonic heating in materials," *Ultrasonics*, 159 (July 1981).
13. R.W. Armstrong and C. Cm. Wu, X-ray diffraction microscopy in "Microstructural Analysis: Tools and Techniques," J.L. McCall and W.M. Mueller, eds., Plenum Press, New York (1973).
14. B.K. Tanner, "X-ray Diffraction Topography," Pergamon Press, New York (1976).
15. W.J. Boettinger, H.E. Burdette, M. Kuriyama and R.E. Green, Jr., "Asymmetric crystal topographic camera," *Rev. Sci. Instrum.* 47:906 (1976).

A STUDY OF SUBSTRUCTURES IN WELDED BETA TITANIUM ALLOY BY MICROBEAM X-RAY DIFFRACTION ANALYSIS

Y. Shirasuna, A. Nozue, T. Okubo¹, K. Kuribayashi²,
S. Ishimoto, H. Sato³ and Y. Yoshioka⁴

¹ Sophia University, 7-1 Kioi-cho, Chiyoda-ku, Tokyo 102, Japan.

² The Institute of Space and Astronautical Science, Sagami-hara,
Kanagawa 229, Japan

³ Nissan Motor Co., Ltd., Momoi, Suginami-ku, Tokyo 167, Japan

⁴ Musashi Institute of Technology, Tamazutsumi, Setagaya-ku,
Tokyo 158, Japan

INTRODUCTION

Ti-15V-3Cr-3Sn-3Al alloy has been used for welded structures such as an upper stage motor case of launch vehicle for space-study satellite [1] because of its good formability and high strength [2]. The fabrication process of the case is as follows: Two half spherical shells, which are formed by cold deep drawing from hot rolled plate, are welded to make a sphere. The welded shell is aged to have desired strength and fracture toughness. The fracture toughness of weld joint is found not to meet the design criterion when the welded case was heat-treated conventionally.

Figure 1 shows a schematic hardness distribution near the weld joint after heat treatment. With the conventional heat treatment process, the hardness of the weld metal is higher than that of base metal. The reason is that the age hardening rate is higher in weld metal than in the base metal. This excessive hardening resulted in low fracture toughness in the weld joint. Two kinds of welding and heat treatment processes have been developed to enhance the fracture toughness of the weld joint by the present authors [3,4]. The idea behind the new methods is to make the hardness of the weld metal a little lower than of the base metal as shown by a solid line in Fig. 1.

Table 1 summarizes heat treatment, welding method and fracture toughness for conventional process, new process I and new process II. The design criterion [5] for the weld joint is also shown at the bottom of this table. The first process is to avoid excessive hardening in the weld metal by two-stage heat treatment [3]. The second process is to suppress the age hardening rate by enriching vanadium in the weld metal [4]. The fracture toughness of the weld joint obtained by the two new processes becomes higher compared with the conventional method, and satisfies the design criterion.

The present paper shows observations on substructures in vanadium enriched weld metal by microbeam X-ray analysis, and discusses the role of the substructures in the age hardening behavior with the results on conventionally welded joints so far reported [6].

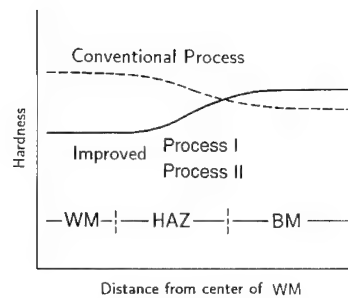


Figure 1. Schematic representation of hardness distribution of welded materials. Hardness distributions of dotted and solid lines are obtained by conventional and new processes. WM, HAZ and BM denote weld metal, heat-affected-zone and base metal respectively.

Table 1. Heat treatment and welding conditions of three processes and fracture toughness K_{IC} obtained.

	Solution treatment	Pre-aging	Welding Filler	Aging	K_{IC} MPam ^{1/2}
Conventional		none	15V-3Cr-3Sn-3Al		25
Process I	1073K 1.8ks	748K 57ks	15V-3Cr-3Sn-3Al	748K 36ks	34
Process II		none	21V-3Cr-3Sn-3Al		38
Design criterion					30

MATERIALS AND METHOD

Materials, Welding and Heat treatment

Hot rolled plates of standard Ti-15V-3Cr-3Sn-3Al alloy were welded by multilayer gas arc method after solution treatment at 1073K. The weld joint was double U-groove shape and vertical to the rolling direction of the plate. A welding current was 100-120A, voltage 11-12V, and speed 2.0-2.5mm/s. The number of the layer was 20 for each side of the plate. The layer temperature was kept below 375K for each layer welding. For welding filler, four titanium alloys with different vanadium content of 15, 17, 21, and 25% were used to enrich vanadium in the weld metal. The amount of Cr, Sn, Al in filler materials was about 3% as in the base metal. The chemical analysis after welding showed that the vanadium content in the weld metal was almost the same as in filler material. After welding, the substructures in the weld metal were studied by an X-ray microbeam diffraction method and an optical microscope. The welds were aged at 738K for 1ks to 360ks and subjected to hardness measurement.

X-ray Microbeam Diffraction Analysis

The X-ray microbeam diffraction method [7] was used to study the substructures in the weld metal. Diffraction spots along Debye ring are obtained from polycrystalline materials when the beam is sufficiently fine as shown in Fig. 2. The shape of each spot reflects the structure of irradiated region of polycrystalline materials. A tangential length of a spot St comes from the orientation scattering in subgrains. A radial length Sr can be correlated to lattice strain in subgrains.

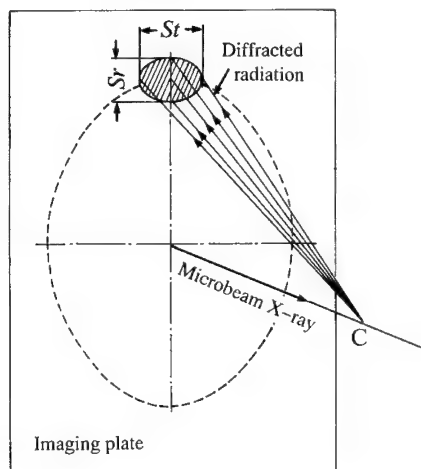


Figure 2. Diffraction spot in microbeam X-ray analysis. Specimen is located at C.

Copper K- α characteristic X-ray was used for the analysis. The diffraction plane is (321) of beta titanium. Imaging plate was used to detect diffraction spots instead of conventional X-ray film. By using the imaging plate, the shape of spots is observed with high resolution under shorter exposure time.

Figure 3 shows the system for the data retrieval from the imaging plate [8]. The photostimulated luminescence on the imaging plate activated by collimated Helium-Neon laser beam was detected with a photomultiplier tube. The signal is sent to a personal computer for data processing.

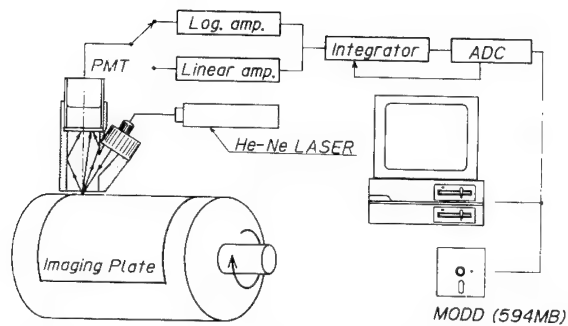


Figure 3. Schematic layout of imaging plate readout system.

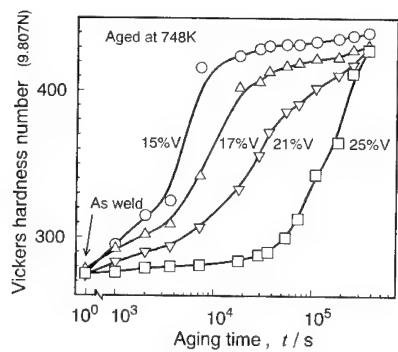


Figure 4. Hardness of weld metal as a function of aging time for different vanadium content.

RESULTS AND DISCUSSION

Aging Hardening Behavior

Figure 4 shows the hardness in weld metal as a function of aging time for four welds of different vanadium content. This clearly shows that the age hardening rate was suppressed by enriching vanadium in the weld metal. The filler of 21% vanadium was found suitable to have desired strength and the fracture toughness as shown in Table 1.

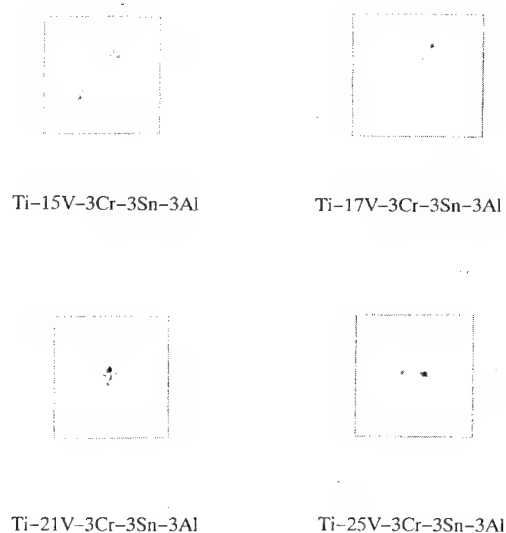


Figure 5. Back-reflection Debye patterns from weld metal of different vanadium content.

Microbeam X-ray Diffraction Patterns

Figure 5 shows X-ray diffraction patterns from the weld metal of different vanadium content. A typical diffraction spot was enlarged and shown in a square at the center of each figure. Diffuse diffraction spots are observed for the case of 15 %V where the vanadium content in weld metal is the same as in base metal. With increasing vanadium content in the weld metal, the diffraction spots become sharper.

Figure 6 schematically shows substructures in a grain formed during welding. Subgrains can be formed by reordering of dislocations which formed under thermal stresses during welding. The orientation of each subgrains differs slightly by introduction of a small angle boundary. Each diffraction spot comes from one grain in

irradiated region. When this grain contains subgrains, the spot is diffused along tangential direction to the Debye ring as shown in Fig. 2. The range of orientation or total misorientation β is estimated from the tangential size of the spot. The accumulation of defects such as dislocations in subgrains causes the distortion of crystal lattice and the scatter in lattice parameter d . The amount of distortion or micro-lattice-strain is estimated from the radial size of the diffracted spot.

The total misorientation and micro-lattice-strain calculated from the size of the spots were plotted in Fig. 7 as a function of vanadium content. The open symbols in these figures are for weld metal and closed symbols are for the solution-treated but not welded material. Both parameters decreased with increasing vanadium content for the weld metal, while remained constant for solution-treated material.

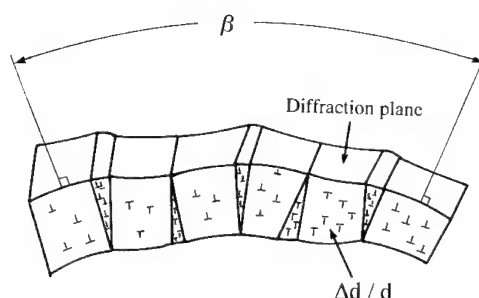


Figure 6. Schematic representation of substructures formed during welding. β and $\Delta d/d$ denote total misorientation and micro-lattice-strain.

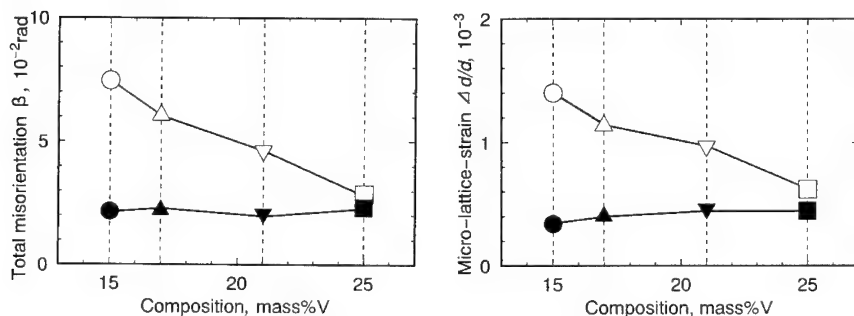


Figure 7. Total misorientation and micro-lattice-strain as a function of vanadium content. Open symbol is from weld metal and closed symbol from material without welding.

Optical Micrographs

Figure 8 shows optical micrographs of the weld metal with different vanadium content. Within the β -grains formed during welding, subgrains are observed. The size of subgrains becomes fine for 15%V and increases with vanadium content. For solution treated but not welded material, subgrains are not observed.

CONCLUSIONS

Table 2 compiles the results of this study so far reported [4]–[6]. The main findings are as follows:

- (1) The age hardening rate of the weld metal becomes higher than that of the base metal when the vanadium content is 15%, which results in the low fracture toughness of the weld joint. The fracture toughness is increased by two-stage heat treatment which suppresses the excessive hardening in the weld joint.
- (2) With increasing vanadium content in the weld metal, the age hardening rate decreases. Using the filler of 21%V, the desired fracture toughness can be achieved by one-stage heat treatment.
- (3) Under the conditions where the enhancement of the age hardening occurs, the microbeam X-ray diffraction spots are diffused and the optical micrograph reveals fine subgrains.
- (4) When the age hardening rate is low, the diffraction spots is sharp and subgrains are coarse or not observed.

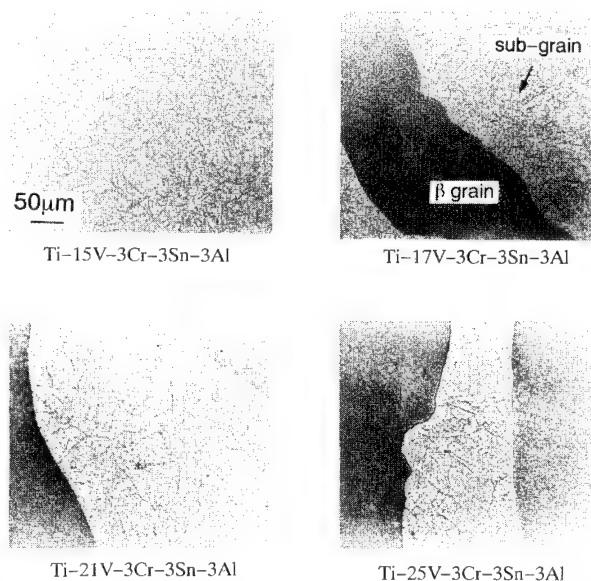


Figure 8. Microstructure of weld metal of different vanadium content.

The consistency of these findings suggests that the age hardening enhancement in the weld metal can be attributed to substructures formed under thermal cycles during welding. The enrichment of vanadium affects the age hardening rate through the suppression of the formation of such substructures. The detailed discussion on the relation between the substructures and the age hardening in the weld metal is left for further studies.

Table 2. Summary of relation between vanadium content, aging characteristics and substructure in weld metal.

	V content	Aging rate	X-ray diffraction pattern	Subgrain
Weld	15%	Rapid	Diffuse	Fine
	25%	Slow	Spotty	Coarse
Base Metal	15%	Slow	Spotty	Not Observed

REFERENCES

1. J. Onoda, N. Watanabe, K. Ichida, Y. Hashimoto and A. Nakata, Reports of The Institute of Space and Astronautical Science of Japan, Special Issue, No.29, 87(1991).
2. P. J. Bania, G. A. Lenning and J. A. Hall, in: "Beta Titanium Alloy in The 1980's", R. R. Boyer and H. W. Rosenberg, ed., TMS / AIME, New York, 209(1984).
3. Y. Shirasuna, A. Nozue, T. Okubo, K. Kuribayashi, R. Horiuchi, S. Ishimoto and H. Sato, TETSU-TO-HAGANE, The Iron and Steel Institute of Japan, 76, 614(1991).
4. Y. Shirasuna, A. Nozue, T. Okubo, K. Kuribayashi, S. Ishimoto, H. Sato, and Y. Yoshioka, Abstracts of the Japan Institute of Metals, 112, 370(1993).
5. Y. Shirasuna, A. Nozue, T. Okubo, K. Kuribayashi, R. Horiuchi, S. Ishimoto and H. Sato, Nondestructive Testing and Evaluation, 9, 1085(1992).
6. Y. Shirasuna, A. Nozue, T. Okubo, K. Kuribayashi, S. Ishimoto, H. Sato, and Y. Yoshioka, Journal of the Society of Materials Science, Japan, 42, 600(1993).
7. K. Hayashi and T. Konaga, in: "X-Ray Studies on Mechanical Behavior of Metals", Committee on Mechanical Behavior of Materials, ed, The Society of Materials Science, Japan, 351(1974).
8. Y. Yoshioka and S. Ohya, in: "Residual Stresses-III", H. Fujiwara, T. Abe and K. Tanaka, ed., Elsevier Applied Science, London, 2, 985(1992).

STUDY OF EFFECT OF METHANE CONCENTRATION IN ARGON PLASMA ON TANTALUM COMPOUND SPUTTERING DEPOSITION PROCESS

S.L. Lee¹ and C.S. Lee²

¹U.S. Army Armament, Research, Development and Engineering Center
Benet Laboratories, Watervliet, NY 12189-4050

²Department of Mechanical Engineering, Rensselaer Polytechnic Institute
Troy, NY 12180

ABSTRACT

There are increasing demands for advanced materials which meet the erosion, corrosion resistant properties, possess desirable thermal and electrical properties, and which can endure the high pressure, high temperature and aggressive chemical environment of the bore in future projectile launchers. In this work, tantalum and tantalum compounds were sputter deposited in argon plasma containing methane of varying concentrations. X-ray diffraction analysis demonstrated that *bcc* alpha tantalum was formed at low methane concentrations, and *fcc* tantalum carbide at high methane concentrations. The steep transition occurred at 22 molar percent of methane and 78 percent argon plasma mixture. As percentage methane in argon increases, drastic changes in coating composition, crystalline structure, particle size and preferred orientations occur. Deposition rate, Knoop hardness and temperature coefficient of resistivity have also been found to be sensitive function of methane concentration. The successful deposition of refractory ceramic constituents, such as tantalum carbide, promises new tough ceramics for future refractory coating applications.

INTRODUCTION

A new generation of advanced refractory bore coating materials are being developed for future launch technology. Coating the bore surfaces with refractory metals and ceramics greatly improves the wear and erosion life of pressure vessel systems. However, in addition to the erosion and corrosion resistant requirements of coating deposition, the new materials must endure the aggressive high temperature, high pressure conditions, possess desirable thermal and electrical properties, and have low reactivity to the plasma environment. Active research programs are being conducted in refractory bore coatings by electrochemical deposition in aqueous solution

and molten salt bath, and by physical vapor deposition through sputtering and evaporation processes. Objectives of the coating project are: (1) to develop refractory metals, alloys, and ceramics of superior physical and chemical properties, (2) to optimize deposition process parameters to obtain strong adhesion, low stress and uniform deposits, (3) to characterize coating processes by nondestructive X-ray diffraction, energy dispersive X-ray analysis, and electron microscopy techniques. Sputtering deposition of tantalum carbide was achieved in a triode sputtering chamber, where the plasma density was controlled by adjusting the electron emission from a hot tantalum filament. Advances in weapon sputtering coating technology have been reported^{1,2}. As methane concentrations increase, Knoop hardness increases, and temperature coefficient of resistivity decreases³.

Melting point temperatures of common refractory metals and alloys above 1000°C are given in Figure 1. Many of the metals and ceramic constituents of Cr, Ta, Mo, W, Re etc. have been considered for advanced coating materials for future projectile launchers. Tough ceramics, such as tantalum carbide and tantalum nitride, are among the most promising. Due to the low atomic weight of carbon in heavy tantalum matrix, energy dispersive X-ray microanalysis of specimens obtained at 0, 22, 33 and 50 percent methane concentrations in argon showed only tantalum, but no carbon peak. In this work, X-ray diffraction determined that *bcc* tantalum was deposited at methane concentrations below 20%, and *fcc* tantalum carbide was deposited at methane concentrations above 25%, and a mixture of tantalum and tantalum carbide at the transitional 22% methane concentration. For the 22% methane specimen, recent wavelength dispersive X-ray fluorescence spectrometer analysis further demonstrated both tantalum and carbon contents in the specimen. Grain size in polycrystalline materials has pronounced effects on strength and hardness, increasing strength and hardness accompanies a decrease in grain size. The introduction of methane (CH₄) gas in argon plasma in the sputtering chamber caused the coating deposits to transform from Ta to TaC. The Ta/TaC deposits consisted of very fine particle sizes. Coating composition, crystalline structure, particle size and preferred orientations were found to be very sensitive to methane concentrations in argon in the sputtering deposition process.

TANTALUM, TANTALUM CARBIDE AND TANTALUM HYDRIDE PHASES

Binary phase diagrams of Ta-C and Ta-H have been compiled by Hansen in 1958, Shank in 1969 and Massalski in 1986⁴. They disclose phase dependence on temperature and atomic percent of the constituents. Tantalum-carbon phase diagram discloses Ta, TaC and Ta₂C phases at temperatures above 1800°C, and tantalum-hydrogen phase diagram is not well defined. Data base search for tantalum/tantalum carbide/tantalum hydride phases in ICDD⁵ results in- two phases of tantalum: alpha-Ta (*bcc*), beta-Ta (*tetragonal*); two phases of tantalum carbides: TaC (*fcc*), Ta₂C (*hexagonal*), and intermediate phases with various degrees of nonstoichiometry- zeta-TaC_{0.47}, metastable zeta-TaC_{0.6}, and xi-C_{0.71}Ta (*rhombohedral-hex*); several phases of tantalum hydrides: beta-TaH (*hexagonal*), Ta₂H (*orthorhombic*), and intermediate phases with various degrees of nonstoichiometry: TaH_{0.8} (*orthorhombic*), TaH_{0.9} (*orthorhombic*).

X-RAY SPECTROSCOPY CHEMICAL ANALYSIS

Our energy dispersive X-ray (EDX) microanalysis of sputtered specimens was not conclusive. Spectra obtained for sputtered deposits at 0, 22, 33 and 50 percent methane concentrations in argon plasma showed only tantalum peak, but no carbon peak. Atomic weight of carbon is 12.01, atomic weight of tantalum is 180.95, it is difficult to detect low Z materials in a heavy matrix. Our Tracor x-ray fluorescence (XRF) analyzer has capability of chemical analysis of low-Z elements down only to sodium. The coating deposit obtained at 22% methane

concentration is of particular interest because it represents a state of co-existence of Ta and TaC. Wavelength dispersive spectrometer measurements were made of the 22% methane, 78% argon deposit during our recent visits to Rigaku USA and Philips Electronics. Strong carbon as well as tantalum peaks were observed.

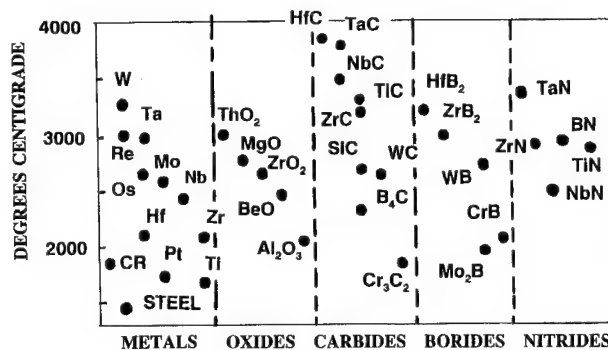


Figure 1. Melting point temperatures of refractory materials for bore coating applications.

X-RAY DIFFRACTION ANALYSIS

X-ray diffraction (XRD) analysis was first performed using a semi-quantitative Philips diffractometer, then with a recently procured Scintag diffractometer. The Philips diffractometer has a LiF crystal monochromator, NaI scintillation detector and strip chart recorder. Molybdenum radiation was used in the study. The four-axis Scintag diffractometer has a Peltier-cooled Si(Li) detector, multi-channel spectrum analyzer, and optimized divergent, receiving and scattering slits. Both molybdenum and copper radiations were used in the study.

In Figure 2, Philips diffractometer scans of sputtering deposits obtained at 0, 22 and 25 percent methane concentrations in argon are displayed along with diffraction scans of tantalum and tantalum carbide powders obtained from Semi-Elements Inc. A sieve with opening of 0.074 mm (0.0029 inch) was used to prepare tantalum and tantalum carbide powders. The tantalum powder pattern is attributed to alpha Ta, and tantalum carbide powder pattern to TaC. Comparison of pattern for deposit obtained at 0% methane in argon (thickness 23.24 microns on 0.05 mm Al foil substrate) with tantalum powder diffraction pattern discloses predominantly alpha-Ta in the sputtered sample. The pattern obtained at 22% methane in argon (thickness 22.73 microns on 3 mm Al₂O₃ substrate) is difficult to interpret because of the very broad and diffused diffraction peaks. The pattern indicates possible co-existence of tantalum and tantalum carbide. Comparison of pattern for deposit obtained at 25% methane in argon (thickness 4.8 microns on 3 mm Al₂O₃) with tantalum carbide powder diffraction pattern discloses predominately TaC phase.

In Figure 3, Philips diffraction scan for sputtered sample obtained at 50% methane, 50% argon (thickness 1.73 microns on 3 mm Al₂O₃ substrate) is displayed along with scans for tantalum carbide powder and aluminum oxide substrate. The pattern is characterized by very broad TaC peaks superimposed on sharp diffraction peaks from Al₂O₃ substrate through TaC layers. When methane concentration in argon plasma varies from 0 to 50%, deposition rate decreases from 2.5 to 0.3 microns/hr. Because of the slow deposition rate at high methane concentration, a long time is required to obtain thicker coatings.

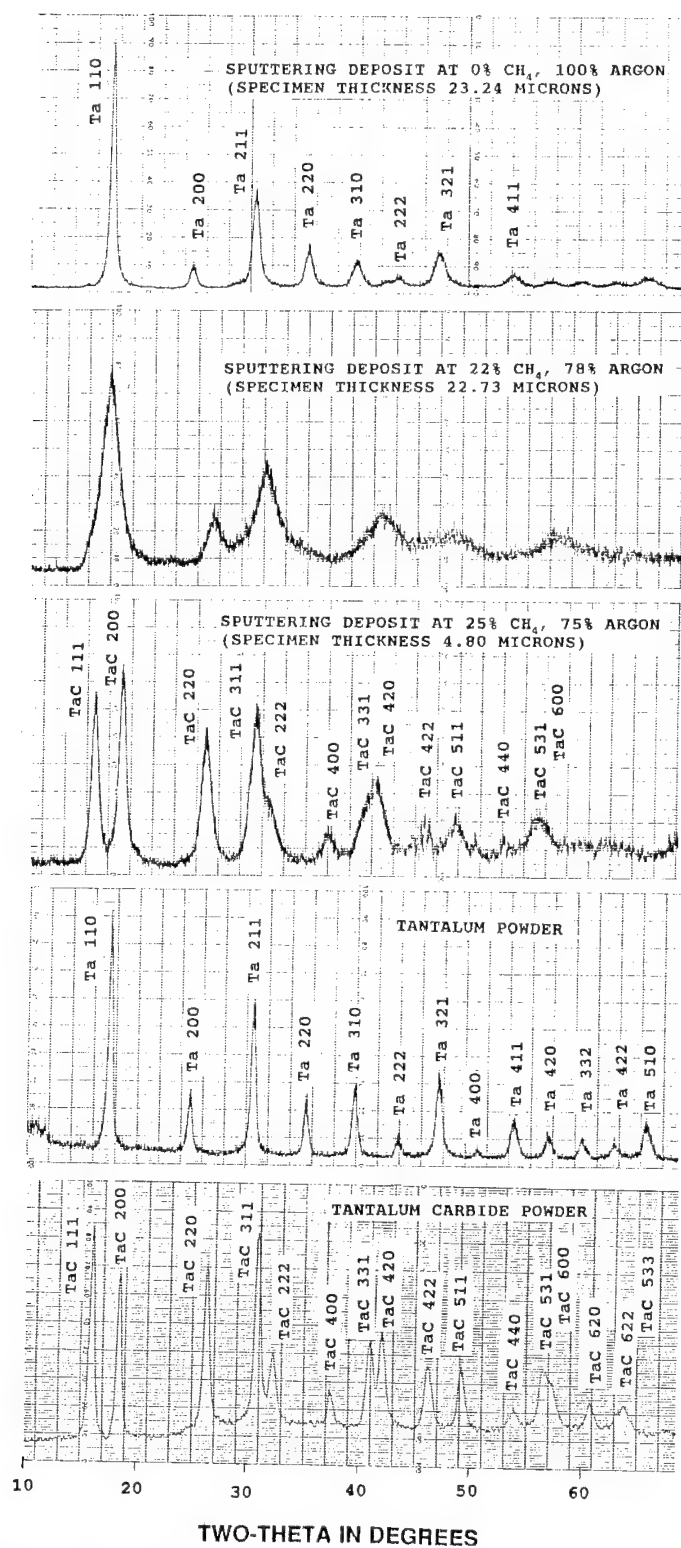


Figure 2. Diffraction scans of sputtering deposits obtained at 0, 22 and 25 percent methane concentrations in argon plasma, compared with scans of tantalum and tantalum carbide powder specimens using Philips diffractometer.

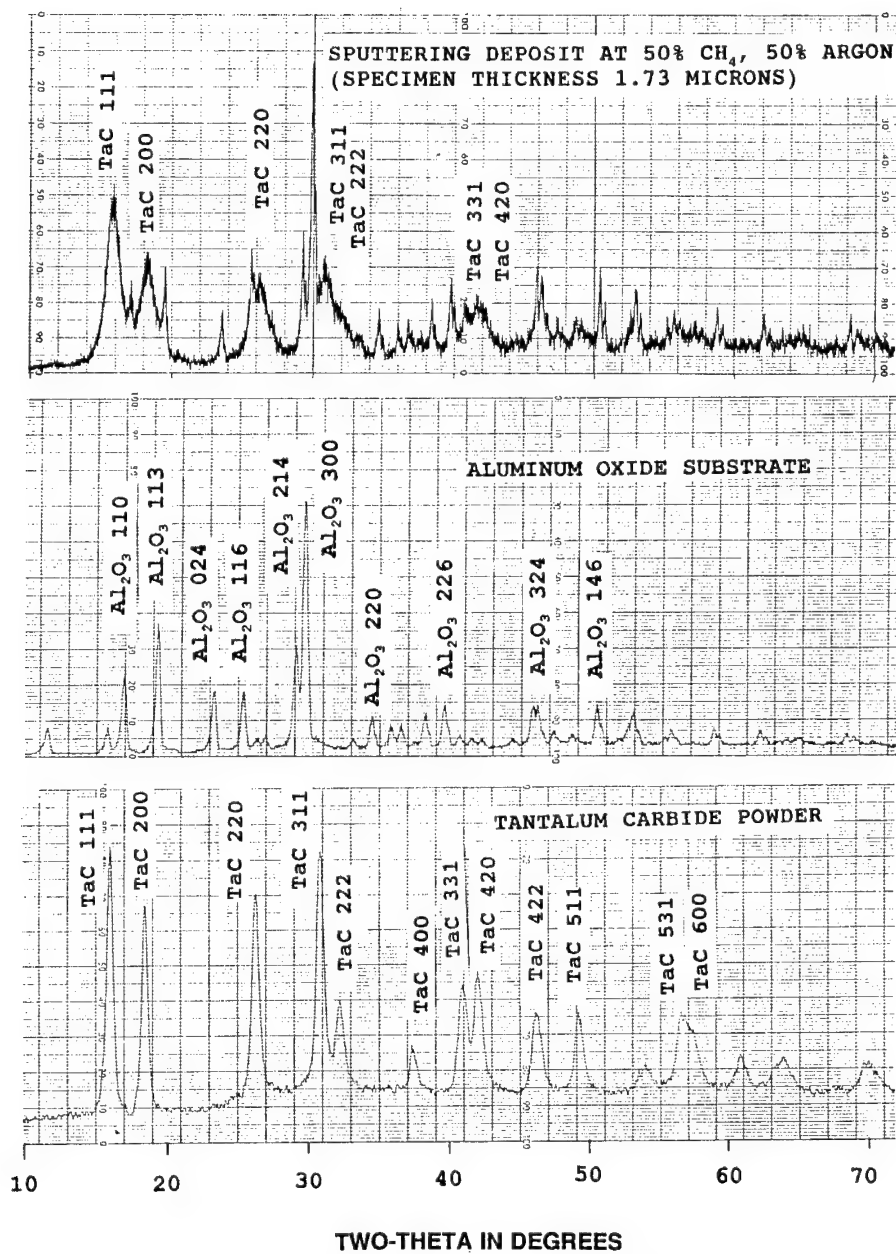


Figure 3. Diffraction scan of sputtering deposit obtained at 50% methane concentration compared to scans of aluminum oxide substrate and tantalum carbide powder specimen.

In Figure 4, Scintag diffraction patterns of tantalum target metal and sputtered specimen obtained at 0 % methane are displayed along with tantalum powder scan and simulated pattern from ICDD diffraction data base. The patterns were background subtracted and K-alpha2 corrected, the simulated pattern included only K-alpha1 peak. The results are summarized: (1) The randomly oriented Ta powder has diffraction peak intensities and peak locations in agreement with the simulated Ta pattern. (2) Tantalum target metal lines are from alpha Ta, with major diffraction peaks shifted 0.2° towards lower two-theta compared to Ta powder. (3) Full width at half maximum (fwhm's) of major peaks in Ta powder range from 0.03° to 0.07° for two-theta from 17° to 50° , Ta target metal peaks fwhm's range from 0.10° to 0.20° in similar two-theta range. (4) Strong texture with preferred $\langle 200 \rangle$, $\langle 211 \rangle$ and $\langle 411 \rangle$ crystalline orientations, and diminished $\langle 110 \rangle$ orientation in the Ta target metal. (5) The 0% methane deposit Ta pattern exhibits a 0.5° shift towards higher two-theta, broadened lines which range from 0.3° to 0.6° in the same two-theta range. The 0% deposit was strongly textured with $\langle 211 \rangle$, $\langle 222 \rangle$, $\langle 321 \rangle$ and $\langle 332 \rangle$ preferred orientations.

In Figure 5, Scintag diffraction scan of sputtering deposit obtained at 25% methane concentration in argon is compared with diffraction scans of tantalum carbide powder and simulated tantalum diffraction pattern. The results are summarized: (1) The diffraction pattern of fine tantalum carbide powder is consistent with pattern for TaC. Diffraction peak intensities and peak locations indicate that TaC powder was randomly oriented with peak intensities and locations identical to TaC from ICDD data base. TaC powder lines have fwhm's of 0.03° to 0.06° in the range of interest. (2) The 25% methane deposit exhibits a 0.2° to 0.3° peak shift towards lower two-theta compared to TaC pattern. (3) The fwhm's of the broadened diffraction peaks range from 0.6° to 0.8° for two-theta range of 15° to 30° . (4) Enhanced $\langle 200 \rangle$ preferred orientation in the 25% methane coating sample.

In Figure 6, Scintag diffraction scan of sputtering deposit obtained at 22% methane concentration in argon is compared to simulated Ta and TaC diffraction data base. The very broad and diffused peaks are difficult to interpret. Co-existence of Ta and TaC is possible, as well as other carbide and hydride phases. The two strongest lines have fwhm's of 0.75° and 0.95° .

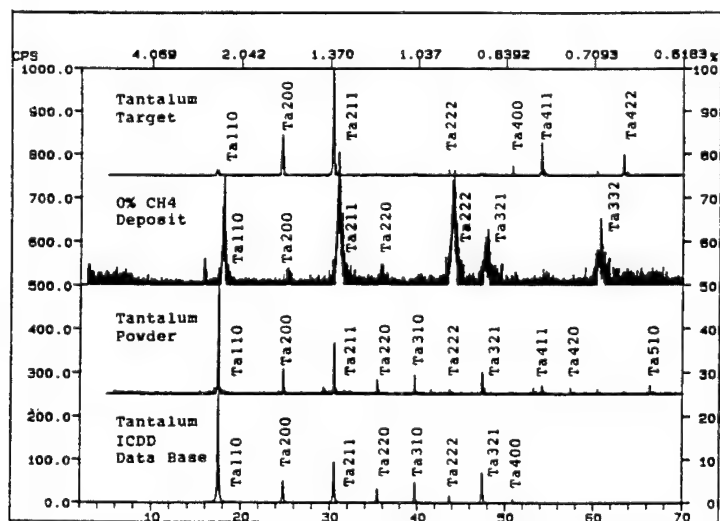


Figure 4. Scintag diffractometer scan of specimen obtained at 0% methane concentration as compared with scan of tantalum powder specimen and ICDD simulated diffraction pattern for tantalum.

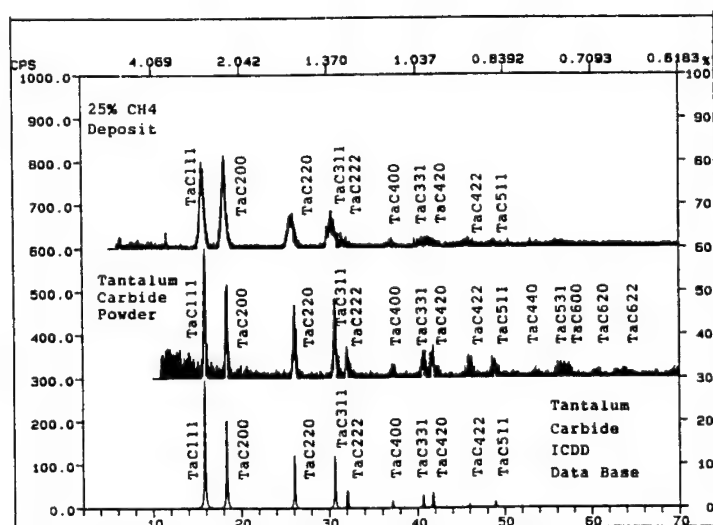


Figure 5. Scintag diffractometer scan of specimen obtained at 25% methane concentration as compared with scan of tantalum carbide powder specimen and ICDD simulated diffraction pattern for tantalum carbide.

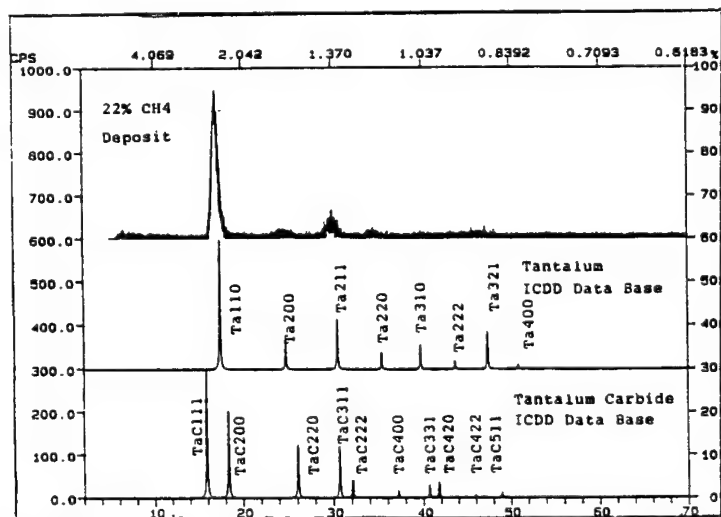


Figure 6. Scintag diffractometer scan of specimen obtained at 22% methane concentration as compared with simulated diffraction patterns for tantalum and tantalum carbide.

Table 1 summarizes major diffraction peaks in tantalum target metal, sputtering deposition specimens obtained at 0, 22 and 25 percent methane concentrations, and tantalum and tantalum carbide powders. Diffraction line shift reflect residual stresses in the specimens, diffraction peak broadening reflects a reduction in crystalline size, by fault of certain *hkl* planes and by microstrains in the coherently diffracting domains⁶. In addition, carbon and hydrogen dissolution interstitially in the Ta/TaC deposits can also cause shifts in the diffraction peaks. In the 0% deposition specimen, peak shifts to smaller d-spacings, which represents tensile stresses. Alpha Ta (*bcc*) has lattice parameter of 3.3058 angstroms, TaC (*fcc*) has lattice parameter 4.4547 angstroms. In the deposit obtained at 25% methane concentration, peak shifts to larger d-spacings, which may be due to the effect of carbon dissolved in Ta/TaC, or compressive residual stresses. In addition to internal residual stresses generated in the deposition process, thermal stresses should also be considered. Furthermore, the 0% deposit was made on Al foil substrate, while the 25% deposit was made on Al₂O₃ substrate, the shifts can be caused by the differences in thermal expansion coefficients of tantalum metal compared to the aluminum substrate, and tantalum carbide ceramic compared to the aluminum oxide substrate. For diffraction peak around 17° two-theta, fwhm for Ta target was 0.16°, for deposition samples at 0, 22% and 25% were 0.5°, 0.9° and 0.5°, while fwhm for Ta and TaC powder samples were of the order of 0.03°. These results suggest small particles sizes were generated during the deposition process, and in particular, very small particles were produced in the 22% transition range. According to Klug and Alexander⁷, when diffraction lines are very broad and diffuse, crystalline size broadening is the major cause of peak broadening. At particle sizes much less than 100 angstroms, the back-reflection lines disappear, the low angle lines become very wide and diffuse. Scherrer and Warren-Auerbach^{8,9} methods for particle size and microstrain broadening analysis have been implemented. Small microstrains and average particle sizes of approximately 85, 55 and 65 angstroms were observed for specimens obtained at 0, 22 and 25 percent methane concentrations.

CONCLUSIONS

Advances in x-ray techniques and instrumentation allow successful characterization of the effect of methane concentration on tantalum and tantalum compound sputtering deposition process. In the investigation of Ta/TaC sputtering deposition, tantalum was formed at low methane concentrations, at the threshold of 22% methane and 78% argon, there was an onset for tantalum carbide formation. As the methane concentration reached 25%, the coating deposit was predominately tantalum carbide. Ta/TaC formation was found to be a sensitive function of methane concentrations, with steep transition at 22% methane concentration.

Summarizing our current and previous investigations of Ta/TaC sputtering deposition, as methane concentration in argon increases from 0, 22, 25 to 50 percent, the following transitions occur in the coating deposits: (1) crystalline structure changes from *bcc* Ta to *fcc* TaC, (2) diffraction peaks change from broad, to very broad and diffused, to broad, (3) fine particle size of the order of 55-85 angstroms are observed, (4) strong deposition and thermal residual stresses, and strong preferred orientations, effect of solid solution are observed, (5) deposition rate decreases from 2.5 to 1 microns thickness per hour, (6) Knoop hardness increases from 820 to 1500, (7) temperature coefficient of resistivity decreases from 1.7 to -0.1 (1/Deg. C. x 10⁻³), and the successful deposition and characterization of tantalum and tantalum carbide demonstrates a new tough ceramic for future refractory coating applications.

ACKNOWLEDGEMENTS

The authors would like to thank Joe Cox for the helpful discussions during the present and previous investigations of refractory coating project.

Table 1. Major x-ray diffraction peaks in the tantalum target, sputtering deposition specimens obtained at 0%, 22% and 25% methane concentrations, tantalum powder and tantalum carbide powder samples.

Sample Ident	Two-Theta (deg)	d-Space (angstrom)	I/I ₀	FWHM (deg)	HKL
Ta target	24.5533	1.6679	26	0.19	Ta 200
	30.2467	1.3593	100	0.14	Ta 211
	53.9819	0.7814	25	0.10	Ta 411
	63.2812	0.6761	16	0.10	Ta 422
0 % methane	17.9943	2.2678	80	0.28	Ta 110
	30.9738	1.3282	100	0.47	Ta 211
	43.9933	0.9469	92	0.53	Ta 222
	47.7592	0.8761	26	0.60	Ta 321
	60.7076	0.7018	29	0.59	Ta 332
22% methane	17.0604	2.3909	100	0.75	
	29.9441	1.3728	9	0.95	
25% methane	15.6740	2.6006	99	0.57	TaC 111
	18.1642	2.2468	100	0.59	TaC 200
	25.7890	1.5893	38	0.80	TaC 220
	30.3966	1.3528	32	0.83	TaC 311
Ta powder	17.4625	2.3363	100	0.03	Ta 110
	24.7859	1.6525	16	0.06	Ta 200
	30.4813	1.3491	35	0.05	Ta 211
	35.3300	1.1687	10	0.03	Ta 220
	39.6631	1.0454	14	0.07	Ta 310
	47.3372	0.8834	15	0.06	Ta 321
TaC powder	15.8675	2.5694	100	0.03	TaC 111
	18.4718	2.2161	73	0.08	TaC 200
	26.0900	1.5712	61	0.03	TaC 220
	30.6388	1.3424	60	0.06	TaC 311

REFERENCES

1. Lee, S.L., Heffernan, W., and Walden, J.A., "Nondestructive characterization of sputtering deposition of tantalum and tantalum carbide by X-ray diffraction", American Society for Nondestructive Testing Paper Summaries of the 1992 Spring Conference Professional Program, Orlando, FL., pp. 185-187 (1992).
2. Walden, J.A., Heffernan, W. and Lee, S.L., "Advances in weapon coating technology by physical vapor deposition", US Army Technical Report in Basic and Applied Research, pp. 2-9 to 2-17 (1993).
3. Heffernan, W. and Walden, J.A., "Sputtering deposition of tantalum and tantalum compound from argon plasmas containing methane", US Army Technical Report in Basic and Applied research, pp. 3-19 to 3-28 (1991).
4. Massalski, T. "Binary Alloy Phase Diagrams", vol. 1 & 2, American Society for Metals, p. 592, p. 1282, (1986); Francis Shunk, "Constitution of Binary Alloys", Second Supplement, McGraw-Hill Book Company, p. 158, p. 409 (1969); Phil M. Hansen, "Constitution of Binary Alloys", McGraw-Hill Book Company, p. 380-381, p. 796-797 (1958).
5. ICDD, International Center for Diffraction Data, Swarthmore, PA (1993).
6. Wagner, C.N.J., Boldrick, M.S., and Keller, L., "Microstructural characterization of thin polycrystalline films by x-ray diffraction", Advances in X-Ray Analysis, Plenum Press, pp. 129-142 (1988).
7. Klug, H.P. and Alexander, L.E., "X-Ray Diffraction Procedures for Polycrystalline and Amorphous Materials", John Wiley and Sons (1974).
8. Noyan, I.C. and Cohen, J.B., "Residual Stress Measurement and Interpretation", Springer-Verlag (1987).
9. Warren, B.E., "X-Ray Diffraction", London: Addison Wesley (1969).

QUANTITATIVE NONDESTRUCTIVE EVALUATION OF DENSITY OF GREEN STATE COMPRESSED PRODUCTS

J. Muller¹, L. Ackermann², D. Babot³, G. Peix³, P. Zhu³

¹PECHINEY CRV, BP 27, 38340 Voreppe (France)

²SINTERTECH, Route des Collines, 38800 Pont de Claix (France)

³INSA DE LYON, Bat.303, 20 av Albert EINSTEIN, 69621 Villeurbanne
Cédex (France)

INTRODUCTION

Industrial P/M products shapes are often complex and do not permit any density measurement by X-ray transmission. The local density at different locations (on several mm³, just after powder compression) is an essential parameter of the process, which governs the future mechanical properties of the final product (after sintering). In order to set up compression presses, operators need rapid assessments after each tool modification that has influenced local density distribution within the compressed piece. Currently, a statistical approach is used on the basis of manual measurements on broken products. Drawbacks are evident : operator dependent results, insufficient accuracy on the density (± 0.05), time consuming procedure (20 minutes).

FUNDAMENTAL APPROACH

There are several types of X-ray interaction process¹, but only four are of concern in industrial radiology. Each of these interaction occurs with a probability depending on X-ray energy and atomic number Z of the interacting material (Figure 1, calculated for iron). In *Rayleigh scattering*, the incident X-ray photon is scattered with no change in energy, and no release of electrons. In *photoelectric interaction*, the X-ray photon is absorbed and its energy is used in removing an electron or electrons from the inner shells of the interacting atom. In *Compton scattering*, the incident X-ray photon is scattered non-elastically and a recoil electron is produced out of the interacting atom. With most of the X-ray energies used in industrial radiology, this is the dominant contribution to total attenuation. The result of this interaction process is a scattering photon of lower energy than the incident photon, travelling in a different direction, and a recoil electron. *Pair production* (electron-positron) occurs only if the primary photon has an energy greater than 1.02 MeV.

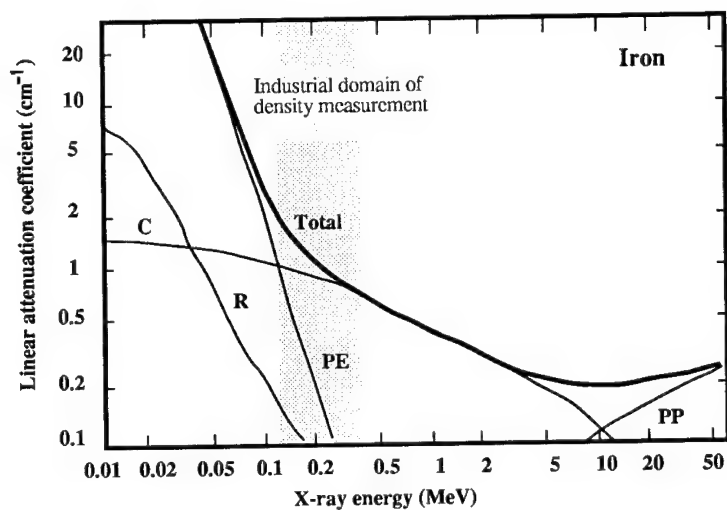


Figure 1 . Linear interaction coefficients for iron, plotted against X-ray energy, showing different components of the total scatter: Compton scatter (C), Photoelectric scatter (PE), Pair production (PP), Rayleigh scatter (R). ¹

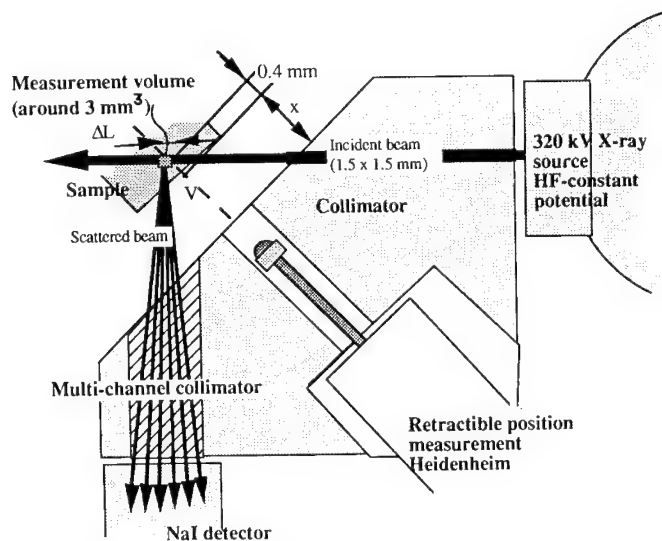


Figure 2 . Principle of Compton radiation scattered measurement. A detector measures all the radiation scattered coming from a small volume (measurement volume V). The main difficulty is to provide enough radiation scattered in a short time and in usual industrial conditions (160 kV), for the required accuracy on the density. The technology of the multi-channel collimators governs the performance of the technique.

mm resolution. Other workers have constructed an apparatus suitable for *thickness measurements* of shells, coatings and intervals between two objects ^{2,15,16,17}.

EXPERIMENTAL APPROACH FOR QUALIFICATION

Ten values of density between 6.10 and 7.30 have been targeted for evaluating quantitative measurements (three samples per value). Compressed test pieces (10x10x50mm) have been made in a classical P/M alloy : Distaloy AB + 0.3%C + 0.7% zinc stearate (Fe-1.5%wt Cu - 1.7%wt Ni - 0.5%wt Mo). The mean density of each sample is measured by the pycnometric method with a resolution of ± 0.05 .

A high stabilized 320 kV X-ray generator (PANTAK HF) has been used (Figure 2), in order to ensure the highest stability of X-ray beam. The detector, a 2" diameter sodium iodide (thallium activated) crystal is connected to a selector and scaler through an amplifier. After the preliminary tests at the 320 kV level, we set the level at 160 kV in order to achieve a compromise between the highest X-ray photon flow and the limited cost of investment for a quality control apparatus. The P/M testpieces are quite small. They are placed on a three axis table, which is controlled by a computer, enabling explorations of samples to be performed automatically.

Since the measurement must be quick and precise, the detector must detect as many scattered photons as possible. The measurement volume has been targeted at a few mm³. We have reached a compromise with a measurement configuration at a 90° Compton angle, and manufacturing of a multi-channel collimator (around 40 channels of ϕ 1.5 mm, all centered on the measurement volume). This particular design permits a high level of counting : 450000 counts in 40 seconds, for a density of 6.7, with standard radiographic conditions (160 kV, 19 mA).

When the sample is moved near the location of the measurement volume, the scattering process follows the law described on figure 3 : the number of photons scattered increases quickly when the measurement volume penetrates into the sample, so reaches its value given by equation (1) and decreases because of the interaction processes within the matter. The abscissa of the maximum radiation scattered is specific to the material tested.

At the beginning of the campaign, a number of test parameters must be fixed : voltage and intensity of the X-ray source (160 kV, 19 mA), minimum counting duration for the required accuracy on the scattered level (around 40 s for $\pm 0.3\%$), optimum depth of the measurement volume according to the mean density to be measured (around 0.4 ± 0.010 mm).

RESULTS : FROM DENSITY STANDARDS TO INDUSTRIAL PRODUCTS

Figure 4 shows the excellent fit of the linear regression between pycnometric densities d and radiation scattered measurements N , made on the ten standard samples (eqn.3) :

$$d = -14,835 + 4,5090 \cdot 10^{-5} \cdot N \quad (R^2 = 0,999) \quad (3)$$

Of course, numerical values are extremely dependent on the configuration and test parameters. In day-to-day use, it is not necessary to verify so completely the calibration, but it must be made as often as possible (every half-hour) on one standard.

Advanced tests have been made on industrial samples, given by SINTERTECH : synchronizing rings for automotive industry. Those products are very representative of the industrial problem : how to measure as fast as possible the density on each tooth (21 teeth) with the best resolution ? We have asked SINTERTECH to modify partially the press in order to create an alteration in the density distribution of teeth. Two samples, one up, the oth-

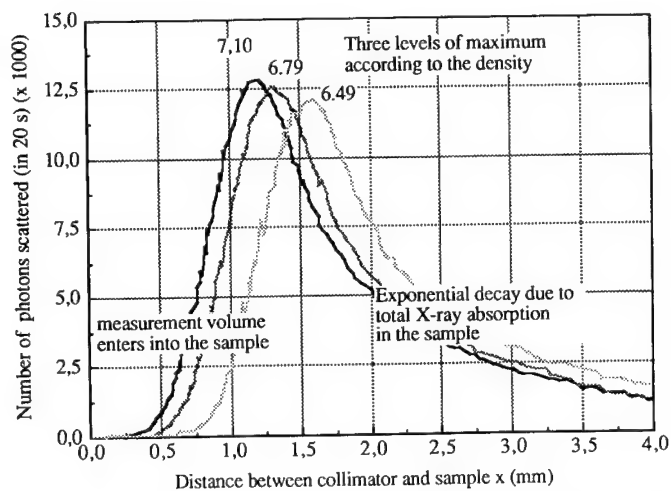


Figure 3 . Experimental curves of radiation scattered vs depth obtained by moving the samples in the x direction before the measurement volume. The level of maximums is reported for density calibration on standard samples.

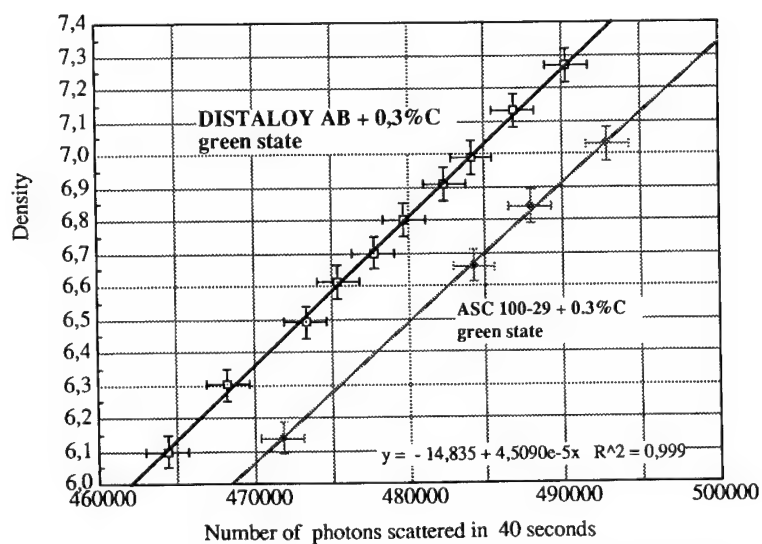


Figure 4 . pycnometric density vs photons scattered number for two P/M alloys.

er one down have been provided. Using an automatic rotating table, the two samples have been completely characterized within half an hour with a accuracy of ± 0.070 for the density ($\pm 0.3\%$ on the scattered radiation). Figure 6 shows these results. It gives the operator the exact locations to be modified to go back to normal press settings.

That example shows that it is not necessary to have the relationship between density and the radiation scattered ; it is enough to calibrate the apparatus with a standard sample (the good ring), and to compare other samples on the basis of the scattered radiation.

DISCUSSION : AN ADVANCED TECHNIQUE FOR A MORE PRECISE AND QUICK MEASUREMENT

The measured dispersion of ± 0.07 on the density is still too large compared with ± 0.05 of the pycnometric method, even if the measurement is considerably quicker. First, we shall outline the main sources of that dispersion, before discussing how to reduce it.

Physical Origins of the Main Sources of Dispersion

Intrinsic Heterogeneity of Standard Samples : green state P/M products always have a relative heterogeneity. It is well known that a density gradient exists according to the direction of compression (this apparatus could characterize it later ...). That is why, each measurement on density standard has been conducted at the same location of the surface.

Multi-scattering Inside the Measurement Volume and Edge Effects : this phenomenon has already been reported¹⁸, up to 47% along the side of the samples when the measurement volume exits the sample. Industrial density evaluation also begins with verifying the integrity of the measurement (no edge effect).

Position Uncertainty and Maximum Counting Location Procedure : Figure 3 shows that it is important to determine very precisely the optimum depth at which the measurement volume is to be placed, corresponding to the maximum scattered radiation. This abscissa is found and fixed at the beginning of the campaign, according to an automatic procedure using a retractable position detector.

Intrinsic Statistical Process of the Photon Production : photon emission is a random phenomenon, well described by Poisson's law (large number of events with weak probability for each). In practice, the number of photons scattered N is related to the number of emitted photons with the same law ; in fact, it can be considered that N is known with the dispersion of $\pm 2\sqrt{N}$; in the case studied, N is around 450 000 counts ± 1341 . The resolution of this measurement is also $\pm 0.3\%$.

X-ray Source Instability : each X-ray tube needs to warm up before use. In spite of the technology used (high frequency and constant potential generator), the incident beam always undergoes some evolution, when a constant flow is needed during a long time ; half an hour is enough to observe a drift of 0.5%, which cannot be due to natural dispersion. So, each campaign is punctuated by calibration on a density standard.

Industrial Tests Are in Progress for a Better Accuracy Than ± 0.05

All the above mentioned sources of dispersion are quite difficult to isolate. In order to evaluate the global accuracy of the technique, we have performed the same operation 150 times on the same sample (d around 6.7) following this procedure : measurement of photons scattered on the three standard samples, calculation of the linear regression law, measurement of the photons scattered number on the sample, calculation of the density. Figure 6 shows the results for the radiation scattered distribution and the calculated density distribution. Dispersion on results is given by :

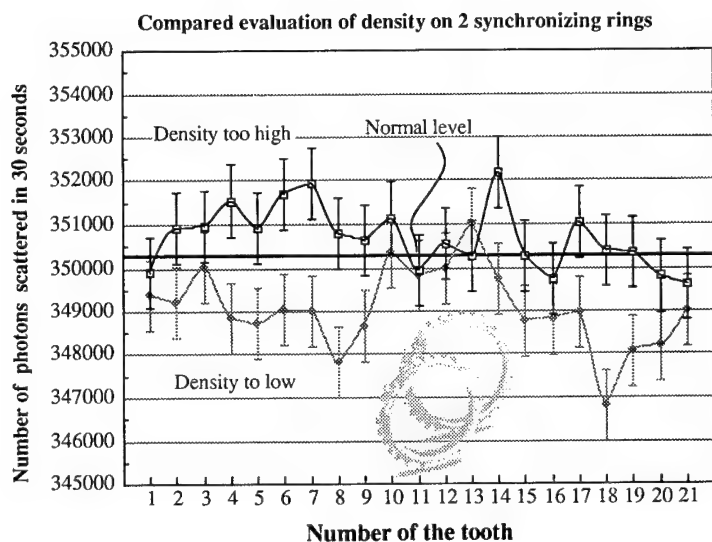


Figure 5 . Example of the sensitivity of the Compton measurement technique on industrial P/M product. (courtesy of SINTERTECH company) : synchronizing ring for the automotive industry. Each tooth of the ring (21 teeth) must satisfy a minimum density, in order to eliminate risk of breakage in normal use. Density characterization by Compton effect takes around 25 minutes, (21 measurements on each tooth) against 20 minutes (5 measurements on 5 teeth). This technique increases quality assurance for the customers. The press parameters have been slightly modified between the two rings (on two sectors). In less than half an hour, all teeth are characterized by the technique and the operator can directly see on which parameter he must act to set up correct production.

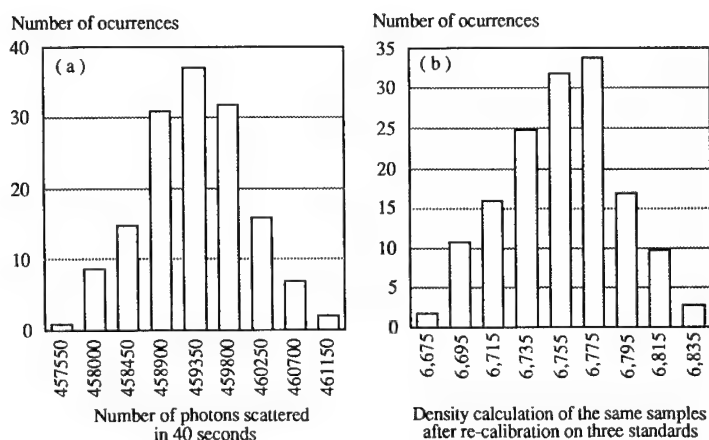


Figure 6 . Characterization of the distribution of radiation scattered measurement (a) and its effect on the evaluation of the density of a same sample (b) . (150 measurements have been made with 150 re-calculations of the linear regression with three standard samples).

$N = 459353 \pm 1407$ counts ($\pm 0.3\%$ like the Poisson statistic)
and $d = 6.757 \pm 0.068$ in density.

The main source of uncertainty is again the photon production governed by the Poisson's law. That means that better accuracy on the density is directly a function of : the flow of incident X-ray photons (already at the maximum level), the increase of measurement duration (from 40 to 60 seconds will give a accuracy of ± 0.055), the increase of the solid angle $\Delta\Omega$ (eqn.2), by changing the size of the detector (from 2" to 3"), and the technological control of multi-channel collimator design, which is the most critical piece in the apparatus. Most of our efforts are targeted on this topic.

In 1993, a MECASERTO prototype, developed from laboratory INSA apparatus, is being tested in France at the SINTERTECH plant.

CONCLUSIONS

This paper has demonstrated a new industrial development of the backscattered Compton effect in the powder metallurgy field. Evaluation of the local density of P/M products (a few mm^3) has been performed with an excellent resolution of ± 0.070 in 40 seconds, with a laboratory apparatus. Industrial developpement is targeting a better resolution than ± 0.050 , based on multi-channel collimator technology. This industrial apparatus is now tested in France as a prototype, and will be available in 1994 for industrial use.

REFERENCES

1. R.Halmshaw, "Non-Destructive Testing", 2nd Edition (1991) pp 22-24
2. G.Berodias, G.Peix, *Materials Evaluation*, n°46, (August 1988), pp 1209-1213
3. "Radiographic inspection" in Nondestructive Evaluation and Quality Control, Metals Handbook 9th ed. Vol.17 (1989) p 309.
4. R.S.Holt, M.J.Cooper, *British Journal of NDT*, (March 1988) pp 75-80
5. C.Le Floch, P.Sarrazin, D.Babot, G.Peix, D.Duvauchelle, 17th Review of Progress in Quantitative NDE, San Diego, California (USA), (15-20 Jul 1990), Ed. D. O. Thompson & D. E. Chimienti, Plenum
6. P.G.Lalc, *Phys.Med.Biol.*, Vol.4 (1959)
7. S.S.Shukla, A.Karellas, I.Leichter, J.D.Craven, M.A.Greenfield, *Medical Physics*, vol.12, n°4 pp 447-448 (Jul-Aug 1985).
8. K.H.Reiss, B.Steinle, *Siemens Forschungs- und Entwicklungberichte*, vol.2 n°1 pp 16-25.
9. H.Olkkonen, P.Karjalainen, *British Journal of Radiology*, N°48 (1975) 594-597.
10. J.T.Stalp, R.B.Mazess, *Medical Physics* vol.7 n°6, pp 723-726 (Nov-Dec 1980)
11. J.A.Stockes, K.R.Alvar, R.L.Corey, D.G.Costello, J.John, S.Kocinski, N.A.Lurie, D.D.Thayer, A.P.Trippe and J.C.Young, *Nuclear Instruments and Methods*, N°193 (1982) pp 261-267.
12. R.H.Rossi, K.D.Fridell, J.M.Nelson, *Mater. Eval.*, Vol.46(1988) pp 1462-1467.
13. B.C.Towe, A.M.Jacobs, *IEEE Transactions on Biomedical Engineering*, Vol.BME-28, (Sep1981) pp 646-654.
14. G.Harding, H.Strecker, R.Tischler, *Philips Technical Review*, Vol.41 N0 2, (1983/84) pp 46-59.
15. C.Bachmann, Report INI-MF-10652 (24 May 1985) Technische Hochschule Aachen.
16. S.Teller, J.Meyer, F.K.Kristofersen, J.M.Farley, 4th European Conference on Nondestructive Testing, London UK (1988) pp 2156-2163.
17. T.Dudzus, C.Segebade, *Materialprüfung*, Vol.18 (Sep 1976) pp 336-338.
18. J.J.Battista, L.W.Santon, M.J.Bronskill, *Physics in Medicine and Biology* Vol. 22, n°2 (1977) pp 229-244.

**A NEURAL NETWORK FOR PREDICTING
ULTIMATE STRENGTHS OF ALUMINUM-LITHIUM WELDS FROM
ACOUSTIC EMISSION AMPLITUDE DATA**

Eric v. K. Hill¹ and Gregory L. Knotts²

¹Embry-Riddle Aeronautical University
Aerospace Engineering Department
600 S. Clyde Morris Boulevard
Daytona Beach, FL 32114

²Acoustic Emission Consultants
13490 Shelley Drive
Madison, AL 35758

ABSTRACT

Acoustic emission (AE) amplitude data have been shown to contain information concerning failure mechanisms and their correlation to ultimate strengths in both metallic and composite materials. As such, AE flaw growth activity was monitored in a set of eleven aluminum-lithium weld specimens from the onset of tensile loading to failure. The amplitude data from the beginning of loading up to 25% of the expected ultimate strength for five of the specimens were used along with the actual measured ultimate strengths to train a backpropagation neural network to predict ultimate strengths. Architecturally, the fully interconnected network consisted of an input layer for the AE amplitude data, two hidden layers for mapping, and an output layer for ultimate strength. The trained network was then applied to the prediction of ultimate strengths in the remaining six specimens where the worst case prediction error was found to be 4.3%.

INTRODUCTION

The 2195 aluminum-lithium alloy is being considered as a replacement material for the 2219 aluminum currently in use on the Space Shuttle External Tank (ET). Both materials exhibit good weldability and strength, but the aluminum-lithium is lighter in weight and stronger, thereby providing extra payload capacity; hence, the incentive for change. Since variable polarity plasma arc welding is the principal method of joining, and the welds are typically the weakest link, weld strength is paramount to ET structural integrity. A method is developed here for predicting ultimate weld strengths at proof loads as

low as 25% of the expected ultimate using acoustic emission (AE) data.

Ultimate strengths have been predicted in both composites (Kalloo, 1988; Hill, 1992; and Walker, 1992) and in metals (Hill and Knotts, 1993) using the acoustic emission (AE) data taken during proof loading. These predictions included the use of AE amplitude, energy, and event rate data in combination with multivariate statistical analysis which in each case resulted in a linear prediction equation. Thus it may be concluded that the AE data contain information concerning failure mechanisms which can be correlated to ultimate strengths in materials. However, it should be noted that these correlations could *only* be obtained using subsets of the original data, e.g., high energy, high amplitude, or low amplitude AE data. No correlation could be obtained using all the energy or amplitude data for a given test. This is, in part, because all the AE data are not equally important to the prediction of ultimate strength.

In fiber reinforced plastic composites, matrix cracks are less damaging than fiber breaks, while delaminations can in some instances provide stress relief and lead to higher strengths (Hill, 1992). Plastic deformation in metals is less damaging than crack growth. Rubbing noises (friction emission) have little or no effect on the ultimate strength and heretofore have had to be removed from the AE data in order to accurately assess damage. In short, the various failure mechanisms contribute in varying degrees to the structural integrity, depending upon the material involved and the geometry of the part. Therefore, in an ultimate strength prediction equation each mechanism must be weighted differently (have a different coefficient). Mechanisms such as rubbing and plastic deformation, that contribute little or nothing to the ultimate strength, would have weighting functions (coefficients) approaching zero, while those that contribute significantly, such as fiber breaks in composites or intermetallic precipitate fractures in alloys, would have large coefficients. One technique for determining these coefficients or weighting functions is neural networks. In this research the input for the neural network was provided by the AE amplitude data.

THEORY

Acoustic Emission Amplitude Distributions

The acoustic emission amplitude parameter, A [dB], is a logarithmic representation of the peak signal voltage, V [V], of the AE waveform:

$$A = 20 \log(V/V_i) .$$

For most applications, $V_i = 1 \mu\text{V}$ at the sensor output is chosen as the 0 dB reference because it is slightly above the noise level of the system electronics. Here the sensor contained a built-in 40 dB preamplifier; therefore, 0 dB was referenced to 100 μV at the preamplified sensor output.

Acoustic emission amplitude distributions have been shown to contain information that allows the identification of failure mechanisms in materials (Pollock, 1981). The typical (differential) amplitude distribution (histogram) can represent peak signal voltages of the AE waveforms from 100 μV (0 dB) to

10 V (100 dB). The various failure mechanisms are grouped together as characteristic humps or bands in the amplitude distribution, and while the amplitude bands for such mechanisms as plastic deformation and crack growth are widely separated, there are other mechanisms whose characteristic amplitude bands overlap. This overlap in the AE failure mechanism amplitude bands is increased by attenuation effects, especially dispersion. However, because the specimens used herein were small, the attenuation effects in the AE waveforms were expected to be minimal. It was therefore hoped that the amplitude distributions would have enough separation in the failure mechanism bands to allow accurate prediction of ultimate strengths in the aluminum-lithium weld specimens.

The amplitude distribution for specimen 01-5 is shown in Figure 1. Note that there are five distinct humps or failure mechanism bands and 307 total AE events. Since the logarithms of measurements can be expected to have normal distributions (Tennant-Smith, 1985), the various failure mechanism humps in the amplitude distribution should be normally distributed. This being the case, the first mechanism probably has amplitudes between 4-12 dB; the second mechanism ranges from approximately 8-20 dB; the third from 20-29 dB; the fourth from 34-35 dB; and the fifth (specimen failure) at 91 dB. It can be seen that there is some overlap between the first and second and the second and third mechanisms; moreover, inasmuch as the first hump does not appear to be normally distributed, there may well be more than one mechanism buried within it. This is where neural networks come into play.

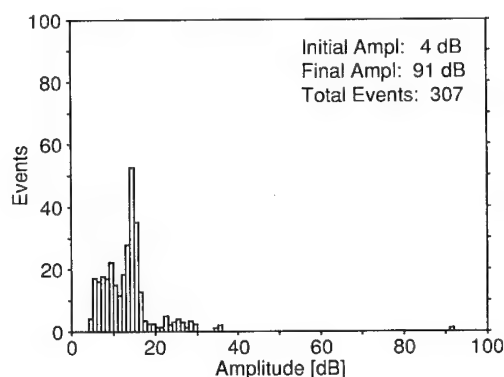


Figure 1. Differential amplitude distribution for aluminum-lithium weld specimen 01-5.

Neural Networks

One of the beauties of neural networks lies in the fact that they can take into account the effects of data overlap from the various failure mechanisms without explicitly identifying and/or isolating them from the rest of the data. Moreover, given the appropriate architecture and input, neural networks can learn all the pertinent data interactions and make accurate predictions using the entire data set, regardless of extraneous data (such as AE from rubbing noises) and without having to resort to multivariate statistical analysis (Kalloo, 1988; Hill, 1992; and Walker, 1992).

In this application the failure mechanism amplitudes were to be used as inputs with the output being the ultimate strength. If all the amplitude distributions were plotted, it could be seen that most of the failure mechanisms occur at amplitudes below 50 dB. Those AE events with higher amplitudes were, in this application, associated with ultimate specimen failure and were therefore not included. Only the amplitudes from 1 to 50 dB were input to the network.

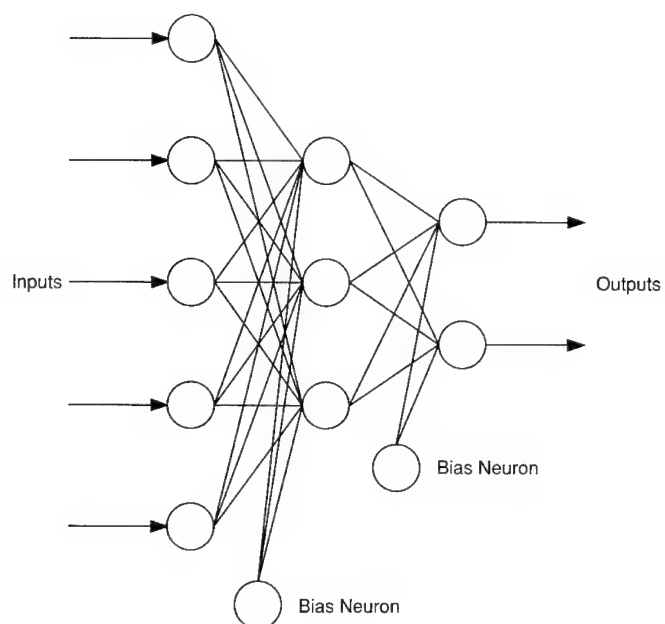


Figure 2. A typical three layer neural network with five inputs, a three neuron hidden layer, a two neuron output layer, and bias neurons.

A typical network is shown in Figure 2. Notice that a bias neuron is included in every layer except the input layer. The biases, like the interconnection weights, are learned during backpropagation. The bias neuron provides a constant threshold term in the weighted sum of the neurons in the succeeding layer, which translates their sigmoid activation functions to the left or right depending upon its sign. This bias term helps the network train faster by forcing the sigmoid function to operate at its midrange values where the error convergence is optimum.

Biases and weight adjustments in the various layers are calculated using the generalized delta rule (ANSim, 1988). This is a steepest descent method of computing the interconnection weights that minimizes the total squared output error over a set of training vectors (pairs). After each pass through the training set (cycle), the total normalized root mean square (RMS) error is calculated for the output. This is

used to calculate the weight matrix changes, which are then backpropagated through each layer within the network.

Backpropagation

Backward error propagation or backpropagation is a method used to train multilayer networks. It compares the actual output of the network with the expected or target output, then backpropagates adjustments in the weights proportional to the calculated error. Network training is a two step procedure -- forward and backward -- propagating the inputs and their concomitant activations forward to the output layer, then propagating the error adjustments backward through the middle or hidden layers to upgrade the interconnection weights.

This means that inputting the amplitude distribution data for specimen 01-5 (Figure 1) should yield its ultimate strength of 51.5 ksi as the output. The known input (amplitude distribution) and target output (ultimate strength) constitute a training pair in this supervised learning scenario. Typically, several training pairs (specimens) and numerous cycles are needed to train the network to arrive at the appropriate weight components.

Once trained, a set of test data is used to verify the prediction accuracy of the neural network. The test data set, like the training set, consists of known inputs with known outputs. Thus, a prediction error can be calculated.

EXPERIMENTAL PROCEDURE

Eleven 5/16x1x12 inch tensile test specimens were cut from butt welded sheets. Both sheets were made of 2195 aluminum-lithium with a 2319 filler. In each case the weld was in the center of the specimen and transverse to the direction of pull.

A 10 kip/min linear load ramp was generated by a computer controlled Tinius Olsen tensile test machine. The load cell output ranged from 0.00 to 1.00 V (0.00 to 36.3 kips). A Physical Acoustics Corporation (PAC) 3000/3004 acoustic emission analyzer and R15I piezoelectric sensor (with integral preamplifier) were used to collect the AE data. The AE sensor was taped to the specimen next to the weld and acoustically coupled using Sonotrace 40 ultrasonic couplant. The PAC 3000/3004 threshold was set at 0.3 V with a total system gain of 81 dB. In order to develop the technique, all eleven specimens were taken to failure with the AE sensor attached. Otherwise, the sensor would have been removed after the application of the proof load.

DATA INPUT AND NETWORK ARCHITECTURE

Prior to training the network, the interconnection weights were initialized to small random numbers within the - 0.5 and + 0.5 range of the sigmoid activation function (ANSim, 1988), and the amplitude and ultimate strength data were normalized to fit into the same range. This was done to facilitate training.

As was mentioned previously, several training pairs (specimens) are needed to train the network. It is also necessary to have sufficient variety in the training inputs such that the network will be able to make valid correlations for unfamiliar cases -- a good distribution of possible inputs and outputs, both good and bad results, plus any border cases.

Specimens 01-5, 01-6, 01-7, 01-9, and 01-15 were chosen as a representative training set.

Some general rules apply when developing the network architecture for optimum performance. To improve accuracy on the training set, increase the size of the hidden layer(s). Alternately, to improve generalization capabilities and thus improve performance on new cases, reduce the size of the hidden layer(s). The optimal size for the hidden layer(s) is a balance between the objectives of accuracy and generalization for each application.

The network architecture was developed through trial and error using the above stated general rules. This resulted in an input layer of 50 neurons for the AE amplitude data, two hidden layers of 12 neurons each, and an output layer consisting of a single neuron for ultimate strength, all fully interconnected.

RESULTS

A summary of the neural network training is provided in Table 1. Altogether six networks were trained using the normalized amplitude data and the normalized ultimate strengths from the five specimen training set. In each case, the learning rate was set at $\eta = 0.4$ and the momentum at $\alpha = 0.9$. Two networks were trained using 100% of the AE amplitude data from load inception to specimen failure, one to a 3% maximum training error and the other to a 1% maximum training error. This procedure was then repeated for two networks using the AE data up to 50% of the expected failure load and for two using the data up to 25% of the expected failure load. (The value for the expected failure load was obtained by taking the average of the ultimate loads over the training set.)

Table 1. Summary of neural network training.

Network Name	Percentage Load Data	Training Cycles Req'd	Training Time Req'd*	Network Training
ASNT_01.NET	100%	1211 Cycles	1 Min., 43 Sec.	3%
ASNT_02.NET	100%	1625 Cycles	2 Min., 35 Sec.	1%
ASNT_03.NET	50%	1333 Cycles	1 Min., 55 Sec.	3%
ASNT_04.NET	50%	2077 Cycles	3 Min., 1 Sec.	1%
ASNT_05.NET	25%	2157 Cycles	3 Min., 18 Sec.	3%
ASNT_06.NET	25%	2807 Cycles	3 Min., 58 Sec.	1%

*486DX2-50 Computer

Because the ultimate strength data were normalized prior to input, the output prediction values from the neural network were also in a normalized format. As such, they had to be denormalized before any comparisons could be made. Table 2 presents a summary of the actual versus predicted ultimate strengths and the associated errors. These results were given by the three networks that were trained to a 1% maximum training error. The AE data from all eleven specimens were applied to these three networks. (This included the five training set specimens plus the six test set specimens.)

Table 2. Summary of the actual versus predicted errors for the three neural networks trained to a 1% maximum training error.

Specimen	Actual Ult Str [ksi]	100% Load Data		50% Load Data		25% Load Data	
		Predicted Ult Str [ksi]	% Error	Predicted Ult Str [ksi]	% Error	Predicted Ult Str [ksi]	% Error
01-5*	51.5	51.3	-0.39	51.3	-0.39	51.3	-0.39
01-6*	51.4	51.3	-0.20	51.4	0.00	51.4	0.00
01-7*	51.2	51.4	0.39	51.4	0.39	51.3	0.20
01-8	51.0	52.3	2.55	53.5	4.90	53.2	4.31
01-9*	50.8	50.7	-0.20	50.8	0.00	50.8	0.00
01-10	50.8	50.4	-0.79	50.4	-0.79	50.5	-0.59
01-11	50.6	50.5	-0.20	50.5	-0.20	50.5	-0.20
01-12	49.9	51.7	3.61	50.9	2.00	51.8	3.80
01-13	49.1	51.1	4.07	51.2	4.27	51.1	4.07
01-14	50.4	51.9	2.98	52.2	3.57	52.4	3.97
01-15*	49.5	49.7	0.40	49.6	0.20	49.6	0.20

*Training set

Note that the prediction errors on the five training set specimens were very small, as expected, while the prediction errors on the six test set specimens were an order of magnitude larger. Overall, the percent errors for the networks trained to a 1% maximum training error were only slightly less on average than those obtained from the networks trained to a 3% maximum training error. The 1% network had a worst case error of 4.3% for specimen 01-8.

Because the 25% load data contained the least amount of AE data, they were expected to yield the largest error, with the 50% data having the next largest error, and the 100% data having little or no error. This, however, was not found to be the case. Instead, the resulting errors were approximately the same for the 100%, 50%, and 25% load data, with the 50% data having the largest errors.

Acoustic emission due to gripping noise was experienced for the first few hundred pounds of load before each specimen became seated in the test machine grips. The amount of AE activity associated with grip slip varied from test to test. While it was anticipated that this might prevent accurate predictions, the neural networks were able to account for this effect and accurately predict ultimate strengths.

CONCLUSIONS

Ultimate strengths can be predicted in aluminum-lithium welds using acoustic emission amplitude data taken at loads up to 25% of the expected ultimate. This prediction is accomplished through the use of a backpropagation neural network with two hidden layers. The network automatically accounted for the AE activity associated with grip slip (through the interconnection weights) without having to remove this extraneous data *a priori* from the data set. It also adjusted for the overlap in the failure mechanism amplitudes. All of this was accomplished with a relatively small training set of only five specimens.

The fact that the prediction errors were essentially equal for the three AE data sets (taken to 25%, 50%, and 100% of ultimate load) suggested two things. First, the source of the error was the same in each case, that being the limited accuracy ($\pm 1.7\%$) of the load data, and second, that the same basic ultimate strength information was inherent in all three data sets. This suggests the possibility of obtaining accurate ultimate strength predictions from the AE data at proof loads even lower than 25% of the expected ultimate.

Finally, the prediction errors being an order of magnitude larger than the training errors meant that the network had memorized the training set because it was trained to closely. It should have been trained to a maximum error of 3% to 5% rather than the 1% value that was used. Also, the architecture could probably have been optimized further. The previously mentioned optimization rules indicate that in order to increase the prediction or generalization capability of the network, there should be a reduction in the number of neurons in the hidden layers. Better predictions might also have been obtained by increasing the number of training sets, but probably the greatest need was to increase the accuracy of the load data (parametric input voltage).

Acknowledgements

This research was performed while on sabbatical leave at the NASA Marshall Space Flight Center under the auspices of the NASA/JOVE program, a jointly funded venture between Embry-Riddle Aeronautical University and NASA.

REFERENCES

- "ANSim User Manual," 1988, Scientific Applications International Corporation, San Diego, CA, 4-13 to 4-17.
- Hill, E.v.K., 1992, Predicting burst pressures in filament-wound composite pressure vessels by using acoustic emission data, *Materials Evaluation*. 50:1439.
- Hill, E.v.K., and Knotts, G.L., 1993, Predicting ultimate strengths of aluminum-lithium (Al-Li) welds using acoustic emission, in: "ASNT 1993 Spring Conference," American Society for Nondestructive Testing, Columbus, OH.
- Kaloo, F.R., 1988, "Predicting Burst Pressures in Filament Wound Composite Pressure Vessels Using Acoustic Emission Data," MS Thesis, Embry-Riddle Aeronautical University, Daytona Beach, FL.
- Pollock, A.A., 1981, Acoustic emission amplitude distributions, *International Advances in Nondestructive Testing*. 7:215.
- Tennant-Smith, J., 1985, "BASIC Statistics," Butterworth & Co. Ltd., London, UK. 106.
- Walker, J.L., 1992, Ultimate strength prediction of ASTM D-3039 tensile specimens from acoustic emission amplitude data, Paper No. 92-0258, American Institute of Aeronautics and Astronautics, New York, NY.

ACOUSTIC EMISSION MONITORING OF THICK COMPOSITE LAMINATES UNDER COMPRESSIVE LOADS

Chris Byrne and Robert E. Green, Jr.

Center for Nondestructive Evaluation
The Johns Hopkins University
Baltimore, MD 21218

INTRODUCTION

Fiber reinforced polymer composites have become quite popular in recent years and have been used for a wide variety of applications ranging from sports equipment to advanced aircraft components. There has recently been considerable interest in the behavior of thick composite laminates under compressive loads¹. This interest stems from the development of novel materials for applications in submersed vessels. A submersible vessel hull is one of the few structures in which the material would experience nearly pure compressive loads. For a structure which is designed to be brought to the depths normally encountered by submarines, a skin of material several inches thick is required. In order to utilize composites for this purpose research into the compressive strength and fatigue life of these materials is needed. In addition, in service inspection techniques must be developed to assess the integrity of such a structure.

The work described in this paper was part of a research effort undertaken which was aimed at determining the strength and fatigue life of thick graphite-epoxy composites subjected to compressive loads. Goals were to characterize the material mechanical response and to apply nondestructive techniques for the characterization of those materials. Towards those ends several NDE methods were applied. Contact and fluid coupled ultrasound, laser speckle decorrelation, infrared thermography penetrant enhanced radiography and optical microscopy were used to locate and identify specific damage modes in the composite specimens tested. Results from these techniques can be found in references 2, 3 and 4.

Mechanical characteristics of composite laminates are known to undergo changes as a result of cyclic tensile loading. Stiffness and strength have been shown to diminish as damage in the material accumulates^{5,6}. In cross ply laminates, as was studied in this work, damage takes the form of matrix microcracks which extend parallel to the reinforcement fibers. Transverse matrix cracks (TMCs) occur in off-load axis plies at stresses well below the ultimate strength of the laminate. These TMCs accumulate rapidly during the first 20% of fatigue life and tend to reach a saturation spacing, referred to as the characteristic

damage state. Longitudinal matrix cracks (LMCs) occur in plies aligned with the load axis and often result from the different Poisson ratio of adjacent plies. Other damage modes consist of ply delaminations and fiber breaking. These damage modes have been shown to occur in a certain causative sequence as fatigue life progresses^{5,6}. Along with this degradation there is a reduction in the measured stiffness. Stiffness drop in the early stages of tensile fatigue is associated with the accumulation of TMCs while an additional drop near the end of life is commonly associated with the failure of individual lamina or fiber bundles.

Acoustic emission (AE) monitoring of composite laminates has been utilized to detect both the presence of damage and the occurrence of damage progression⁷. It has been shown that AE occurs from the strain relief mechanisms resulting from the damage modes mentioned above. It has also been shown that the presence of damage in a composite can lead to rubbing internal surfaces which generate acoustic waves. Though specific AE fingerprints have yet to be recognized for the different modes of damage there is common agreement among researchers as to some of the characteristics of each of the damage mechanisms. High amplitude, short duration events are thought to originate from fiber breaks. Delamination progression, depending on the length of the crack front, generally gives longer duration events of lower amplitudes. Often long duration events are associated with all forms of matrix damage including crazing and cracking.

The load rate at which the composite is subjected as well as the load history of the specimen has been shown to influence the rate at which AE is generated. Awerbuck *et al.* present the results from the monitoring of graphite-epoxy composites during tensile fatigue^{8,9,10}. They found that the initial stages of fatigue resulted in relatively intense AE at the higher loads in the fatigue cycle. These events were attributed to LMCs originating from stress concentration notches in the specimen. Later in the fatigue life a great many events were detected during the low load portions of the cycle. These were attributed to rubbing crack faces. A methodology for distinguishing between this internal friction and damage progression was implemented which took into account the applied load and the intensity of the acoustic event. Using this method to separate AE sources the researchers were able to track the matrix crack front using a location algorithm. It was also apparent that the presence of AE at low loads in the fatigue cycle indicated the presence of a specific form of matrix cracks in the laminate. This phenomena could clearly be used as a tool for the inspection of the structural integrity of a composite structure, while continuous monitoring would be useful in the detection of damage progression and possibly as a means to predict impending failure.

Experimental results from acoustic emission monitoring and mechanical characterization are presented in this paper. Mechanical tests were performed both in a quasi-static manner and by cyclic fatigue. Correlations were found between measured mechanical changes and detected acoustic activity. Damage accumulation early and late in specimen life was detected by acoustic emission monitoring. Composite failure was preceded by a high rate of high amplitude, high energy events at the high load portion of the fatigue cycle. Similar AE results were obtained from quasi-static loading.

EXPERIMENTAL

Composite panels of AS4/3501-6 prepreg were made with a (0₂,90)_{32,5} stacking sequence giving a thickness of approximately one inch. Specimens 3 inches high by 1 inch wide were cut from these panels. Stress concentration notches of 1/8 in radius were cut in the through thickness direction at mid height of the specimens to localize fatigue induced damage. Specimens were epoxied into recessed steel endcaps to prohibit brooming and end splitting while allowing

the load to be applied through the specimen ends. A 110 kip capacity MTS servo hydraulic load frame equipped with flat parallel platens and interfaced with a PC was used for mechanical testing and data acquisition. A one inch gauge length extensometer was mounted symmetrically about the stress concentration notch to measure axial strain. Specimens were then set in the load frame and a 200 lb compressive preload was applied. Fatigue cycles were load controlled using a 1 Hz haversine fatigue cycle. Quasi-static tests were performed by ramp loading to a predetermined load, holding for twenty seconds and then unloading to the preloaded state (considered no load). Additional load sequences were performed, after another hold period, to higher load values until the specimen failed. For example, load to 5 kip, unload to preload, load to 10 kip, unload to preload, then repeat until failure. Typical failure loads were 78 kip. A 10 kip/min load rate was used.

Acoustic emissions were monitored by a Physical Acoustic Corporation acoustic emission resonant transducer having a nominal center frequency of 125 kHz. Sensor preamplification was 40 dB with a signal band pass of 100 kHz to 300 kHz. A PAC 3000/3104 acoustic emission analyzer was used for data storage and manipulation and was set to provide a threshold of 58 dB (1 microvolt base) to omit background noise. Emissions were monitored continuously during fatigue and quasi-static testing. A schematic of the test specimen and equipment is shown in Fig. 1.

RESULTS AND DISCUSSION

In previous work⁴ damage accumulation was found to go through three stages during compressive fatigue cycling. The first stage consisted of the development of LMCs above and below the stress concentration notches along with some localized TMCs. Stage two, lasting for some 80% of fatigue life, consisted of the maturation of the LMCs and TMCs found in stage one. The final stage in damage accumulation of the thick composite lasted for a relatively short time and was characterized by the development and progression of an interlaminar crack which started at the root of the stress concentration notches. This crack would propagate rapidly through the laminate breaking fibers and

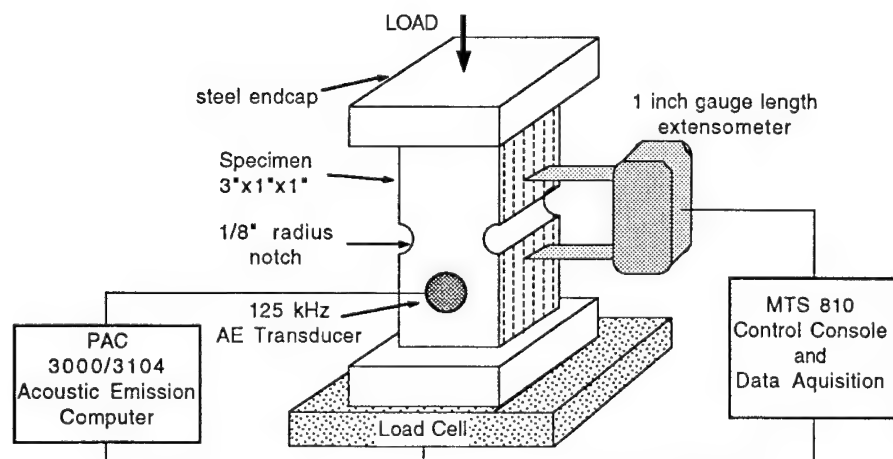


Figure 1. Specimen and equipment schematic.

matrix along the way. This crack often had delaminations associated with it and would lead to complete failure of the load bearing capabilities of the specimen. A schematic of the evolution of damage is shown in Fig. 2.

The results from monitoring specimen mechanical response indicated three stages of change occurred in the three parameters of secant stiffness, permanent deformation and hysteresis. Considering the type of damage found in the specimens the measured strain readings were not indicative of the response of the entire thickness of the specimen but were a superposition of the deformation of the central portion and the relative degree of detachment of the material above and below the stress concentration notches. Figure 3 is a plot of the measured mechanical response of a specimen fatigued to failure. Clearly a great deal of permanent deformation occurred with the first few cycles which is consistent with the development of LMCs above and below the notches. Concurrently, significant

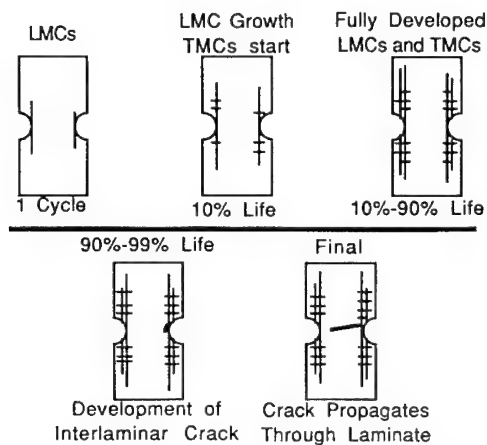


Figure 2. Compression-compression fatigue damage development (from ref. 4).

mechanical losses occurred as indicated by the development of hysteresis in the load cycle. Both of these parameters demonstrated dramatic changes early in the fatigue test after which a gradual change was recorded until just prior to failure when the mechanical loss increased at a renewed rate. Specimen stiffness was also observed to change in a three stage manner, but to a lesser degree.

The measured changes in specimen mechanical response suggested that different damage modes were active during each of the three stages of fatigue. It was shown⁴ that during the first few cycles LMCs were created which would have the effect of creating a plane of strain discontinuity defined by the notch root and the load axis. Then prior to failure an interlaminar crack would develop, often in concert with a delamination, which would rapidly cause failure of the specimen. This type of damage progression could have been responsible for both the measured mechanical response and the acoustic emission results which are presented next.

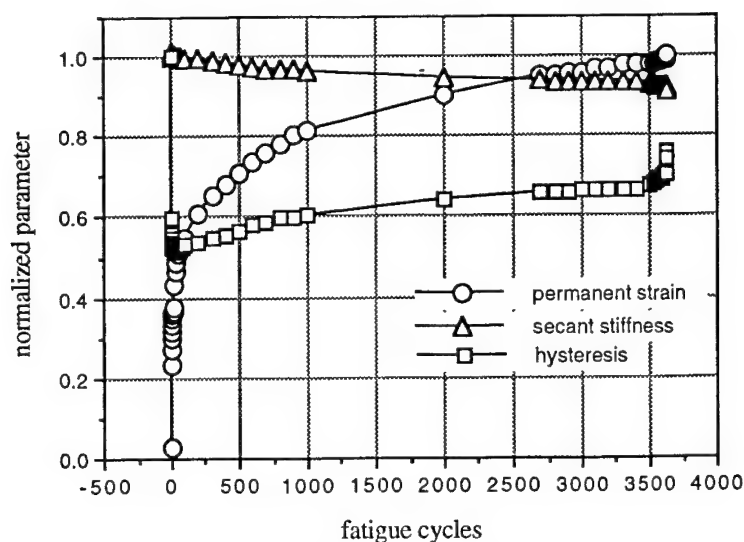


Figure 3. Mechanical characteristics during compressive fatigue.

Previously we have shown that when all detected acoustic events are considered no trends during fatigue are apparent³. However, filtering out events which occurred at the low load portion of the fatigue cycle indicated that the highest amplitude events occurred at the greatest loads. In addition, a pattern was detected in the rate of events occurring at the higher loads in the fatigue cycle. Both the beginning and end of fatigue life were marked by the highest rate of events. Little change in the rate of acoustic events at the higher loads was found during the majority of fatigue life. This three stage trend is also demonstrated when looking at just the higher amplitude events in the fatigue test.

Figure 4 shows the AE monitoring results from the specimen for which mechanical data has been presented. Both Hits and Energy of detected high amplitude events (greater than 64 dB) are plotted on a cumulative sum basis versus fatigue cycles. It can be seen that the first few cycles were marked by a high rate of high amplitude events which contained a considerable amount of energy. The majority of fatigue life was marked by little appreciable high amplitude or high energy acoustic activity. Just prior to failure an increase in the rate of high amplitude, high energy events occurred.

The results from the AE monitoring were consistent with the three stages of damage development and corresponding mechanical characteristics. The initial high energy events were associated with the rapid development of LMCs above and below the notches. This damage was also largely responsible for the measured permanent deformation and associated mechanical losses found during the first few fatigue cycles. Later on, less damage occurred with each cycle and the measured mechanical parameters showed little change. The monitoring of AE during this second stage gave few high amplitude events but many low amplitude events at the lower loads in the fatigue cycle. These low amplitude events often occurred at the same load in each cycle and repeated for many subsequent cycles indicating that the same source was responsible for them. Rubbing of crack faces associated with LMCs are proposed as the source of these events and therefore indicate the presence of damage and not the progression of damage. The final stage in the fatigue test was characterized by the development and propagation of an interlaminar crack in the notch region which caused a reduction in measured

stiffness and increased mechanical hysteresis. This damage was responsible for the high rate of high amplitude and high energy acoustic events detected just prior to failure.

Several tests were performed with a ramp load, unload sequence to progressively higher loads while mechanical response and AE were monitored. These were done to identify whether the Kaiser effect would be found in the composite from compressive loading. Figure 5 is a graph of the measured permanent strain after unloading versus the stress level prior to unloading. Also shown is the number of detected AE during the loading portion of the load, unload sequence. It was found that little permanent deformation occurred from stresses less than 35 ksi and no acoustic events were detected. Above that stress level both the number of detected acoustic events and the amount of permanent deformation increased dramatically. The data showed that events were often detected during loading before surpassing the prior maximum load level. Thus,

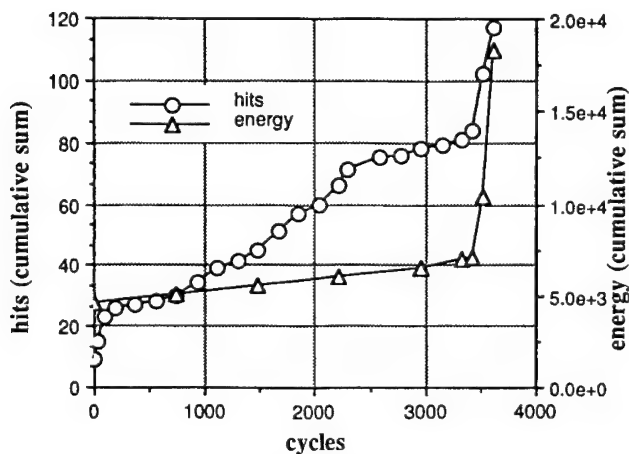


Figure 4. High amplitude (>64 dB) events during compressive fatigue.

the Kaiser effect was not observed to occur with any repeatability. Calculation of a Felicity ratio showed no apparent trend. When detected events were separated based upon their intensity (as with fatigue testing) different observations were made. The lower energy events occurred before surpassing the previous maximum load level. A higher rate of events were detected at higher loads and these tended to be of greater intensity. This behavior is attributed to the creation and presence of LMCs which generate AE by the rubbing of crack faces. The data in Fig. 5 also demonstrates that some mechanical recovery occurred when permanent deformation was high. Though not presented in the figure, AE was detected when the recovery was recorded. It was also found that the unloading portion of the test generated AE. These observations are all consistent with the concept of internal rubbing surfaces generating acoustic events at low loads from a cyclic loading condition.

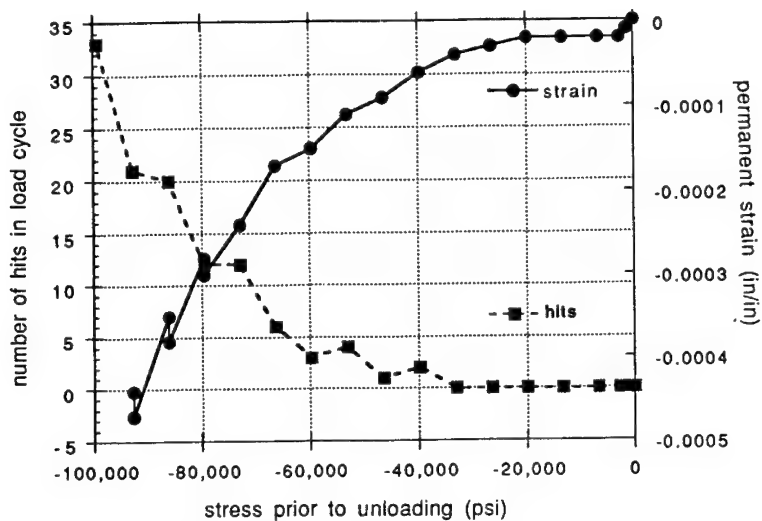


Figure 5. Acoustic emission and permanent deformation from a ramp load-unload sequence.

CONCLUSION

Acoustic emission monitoring of thick composites subjected to compressive loads was performed while specimen mechanical characteristics were recorded. It was found that the three stages in damage state were characterized by changes in both mechanical response and AE parameters. Stage one was identified by substantial permanent deformation and development of hysteresis losses. Specimen stiffness was also observed to drop early in the fatigue test. Damage in stage one was previously found to consist of a rapid development of localized LMCs and TMCs. Acoustic activity during this stage was typically of high amplitude and high energy. As fatigue continued into stage two the detected AE was of lower intensity with considerable activity during the low load portion of the load cycle. Since the load cycle did not pass through a null point it is suggested that the low amplitude events came from rubbing crack faces and not the load frame as has been seen in other test configurations. Indeed, separate monitoring of the machine noise verified this. Specimen mechanical response went through little change during this second stage of fatigue and no new damage mechanisms were found. The third stage was characterized by rising mechanical hysteresis, stiffness reduction, increasing permanent deformation, and an increasing rate of high amplitude and high energy AE. Damage during this stage consisted of development and propagation of an interlaminar crack originating at the stress concentration notch with delaminations emanating from it.

Acoustic emission monitoring of quasi-static tests indicated no trends in Felicity ratio. The Kaiser effect was not observed except when low intensity events were filtered out. The generation of AE while unloading and with no applied load suggested the mechanism of internal friction at crack faces as a source.

ACKNOWLEDGMENTS

This research was funded by the Defense Advanced Research Projects Agency, program manager Mr. James J. Kelly, through the Office of Naval Research, Mechanics Division, Dr. Yapa D.S. Rajapakse, DARPA agent. Additional support was provided by The Johns Hopkins Center for Nondestructive Evaluation. Recognition is given to Joseph W. Krynicki for his participation in the acoustic emission testing. The authors would also like to thank the many faculty and students at the Johns Hopkins University who have made numerous contributions to this research.

REFERENCES

1. G.M. Wood, Proceedings of the Fourth Annual Thick Composites in Compression Workshop, iii, 1990.
2. N.J. Gianaris and R.E. Green, Jr., Proceedings of the Symposium on Nondestructive Evaluation and Material Properties of Advanced Materials, TMS Annual Meeting, New Orleans (1991).
3. C. Byrne, J.W. Krynicki and R.E. Green, Jr., in Review of Progress in Quantitative Nondestructive Evaluation, Vol. 12B, edited by D.O. Thompson and D.E. Chimenti (Plenum Press, New York, 1992).
4. C. Byrne, Masters Essay, The Johns Hopkins University, 1993.
5. K.L. Reifsnider, Fatigue of Composite Materials, Edited by K.L. Reifsnider, (Elsevier Science, New York, 1991).
6. R. Talreja, Fatigue of Composite Materials, edited by R. Talreja, (Technomic Publishing, Pennsylvania, 1987).
7. M. Arrington in Non-Destructive Testing of Fiber Reinforced Plastics Composites, Vol. 1, edited by J. Summerscales, (Elsevier Science, New York, 1987).
8. J. Awerbuck and S. Ghaffari, Monitoring Progression of Matrix Splitting During Fatigue Loading Through Acoustic Emission in Notched Unidirectional Graphite/Epoxy Composite, J. Reinforced Plastics and Composites, Vol 7, pp. 245-264, 1988.
9. W. Eckles and J. Awerbuck, Monitoring Acoustic Emission in Cross-Ply Graphite/Epoxy Laminates During Fatigue Loading, in J. Reinforced Plastics and Composites, Vol 7, pp. 265-283, 1988.
10. S. Ghaffari and J. Awerbuck, On the Correlation Between Acoustic Emission and Progression of Matrix Splitting in a Unidirectional Graphite/Epoxy Composite, in Acoustic Emission: Current Practice and Future Directions, ASTM STP 1077, W. Sachse, J. Roget, and K. Yamaguchi, Eds., ASTM 1991.

ULTRASONIC EVALUATION OF COMPOSITE FATIGUE DAMAGE

Andrew J. Gavens and Robert E. Green, Jr.

Center for Nondestructive Evaluation
The Johns Hopkins University
Baltimore, Maryland 21209

INTRODUCTION

Damage in composite materials has been detected using ultrasonic nondestructive techniques.¹⁻⁵ These studies were all performed on thin composite samples subjected to either a quasi-static tensile force or a constant amplitude tensile fatigue load. Changes in basic ultrasonic parameters, attenuation or velocity, were used as an indicator of damage. Damage was detected once a sufficient amount was present. Attenuation was observed to be dependent on the frequency of the ultrasonic transducers that provides an indication of the dispersive nature of these materials.

The ability to detect damage ultrasonically becomes more difficult on thick composite materials. Being a highly attenuative material makes it hard to obtain multiple echoes for the accurate calculation of attenuation and velocity. The ultrasonic signal evaluates the material through the thickness of the specimen. Any damage must be sufficient to alter the ultrasonic parameters when compiled with the remaining undamaged material. For thick composites the amount of damage may need to be extensive to alter the ultrasound.

In the present study an investigation was initiated to evaluate the ability of standard contact ultrasonic techniques to determine fatigue damage in a thick composite sample subjected to compression-compression fatigue loading. Different pulse wave forms, transducer frequencies and ultrasonic methods were evaluated.

The stages of damage progression occurring in thick composites subjected to compressive-compressive fatigue loads were determined by Byrne.⁶ The materials and specimen geometry were the same as those in the present study. Using double edge notched specimens it was observed that longitudinal matrix cracks occur in the first few load cycles, blunting the notches. Growth of localized regions of longitudinal and transverse matrix cracks then occurs which progresses away from the notch until close to failure. Just before failure, a transverse matrix crack initiates from the root of the notch. This crack then grows quickly and interlaminar cracking reduces the stability of the specimen leading to failure.

EXPERIMENTAL PROCEDURE

Double edge notched compression fatigue specimens were machined from autoclave fabricated plates of AS4/3501-6 prepreg to the dimensions shown in Figure 1. The composite plates had a stacking sequence of [90₂/0]_s and were 196 plies thick (25 mm nominal thickness). The specimens were mounted in steel endcaps with a titanium filled epoxy to eliminate brooming of the specimen ends during testing. By using double edge

notched specimens, damage was anticipated to initiate in the region of the notches allowing damage detection to be performed on a localized region of the specimen.

Compression-compression fatigue tests were performed on a MTS servo-hydraulic test machine. A sinusoidal load was applied to the specimens at a rate of 1 Hz. The specimens were loaded from -45 N to -8,990 N (~82 percent of the quasi-static failure strength) between two flat parallel platens. These loads were chosen based on earlier test results to obtain fatigue failures around 100,000 cycles.⁶

The fatigue tests were periodically stopped to inspect the specimen for damage. At each inspection the specimen was radiographed and ultrasonically evaluated. The notched region of the specimen was coated with zinc iodide penetrant before x-raying with a Hewlett Packard 43855A Faxitron. Radiographs were obtained with the x-ray beam directed normal and parallel to the lamina.

Both pulse-echo and through-transmission ultrasonic techniques were used to evaluate damage in the specimens. Two ultrasonic pulse systems were used. A Panametrics Pulser

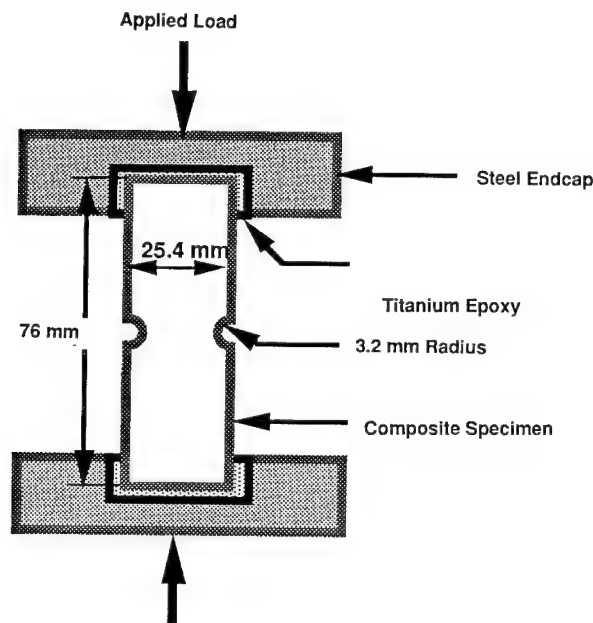


Figure 1. Double edge notched compression fatigue specimen.

Receiver (Model 5055PR) that produced a 10 nsec spike pulse having an amplitude of 200 to 380 V, depending on the equipment settings. The other pulse system was a Matec Pulse Modulator and Receiver (Model 6600) with a RF Plug-in (Model 950B) used in conjunction with a Ritec Broadband Receiver (Model BR-640). This system produces a tone burst pulse having a constant 800 V amplitude. The frequency and duration of the tone burst were adjusted to match the transducers and materials being used.

The equipment settings on both ultrasonic systems were adjusted to provide the largest amplitude received signal without an obvious distortion of the waveform. These settings were determined on each specimen prior to fatigue testing and were used for the duration of the fatigue test.

Ultrasonics Laboratories Standard Miniature Contact Transducers (12.7 mm diameter) having nominal center frequencies of 0.5, 1.0, and 2.0 MHz were used. The 0.5 MHz transducers were only used with the Panametrics pulse system. Transducers designed with a narrow bandwidth (KC models) were used as the pulsing transducers to introduce more ultrasonic energy to the specimen. Wider bandwidth transducers (WC models) were used for receiving the through-transmission signals.

The transducers were mounted on the specimen between the notches with the ultrasound directed normal to the lamina. A fixture was designed to consistently position the transducers on the specimen each time it was evaluated. Sonotech Soundsafe Industrial Couplant was used to couple the transducers to the specimen. Elastic bands were placed around the fixture to keep the transducers in place.

The received ultrasonic signal was analyzed on a Data Precision digital oscilloscope (Model 6000A) with a 620 Plug-in unit. The signal was sampled at a rate of 100 MHz and averaged over 10 pulses to improve the signal to noise ratio. The averaged signal was rectified and the peak amplitude, RMS voltage, area under the curve, and the time of flight to the peak amplitude of each echo were recorded. The transducers were then recoupled to the specimen and the measurements were replicated a total of 5 times. The measurements were averaged and attenuation and velocities were calculated. A coefficient of variation of 5 to 10 percent was typical for these measurements.

RESULTS AND DISCUSSION

Longitudinal cracks at the root of the notch were observed radiographically after the first cycle. As the fatigue test progressed the number and length of longitudinal cracks increased. Away from the notch, the longitudinal cracks were often connected by fine transverse cracks. After approximately 75 percent of the fatigue life, transverse cracks developed near the root of the notch. Radiographs obtained within a few percent of failure showed that there was a significant increase in the number of longitudinal cracks and an increase in the length of the transverse cracks, as shown in Figure 2. The transverse cracks often extended to the surface of the specimen, although they initiated several plies deep. In the notch, a shear crack coupled several of the longitudinal cracks from which it is believed final failure resulted.

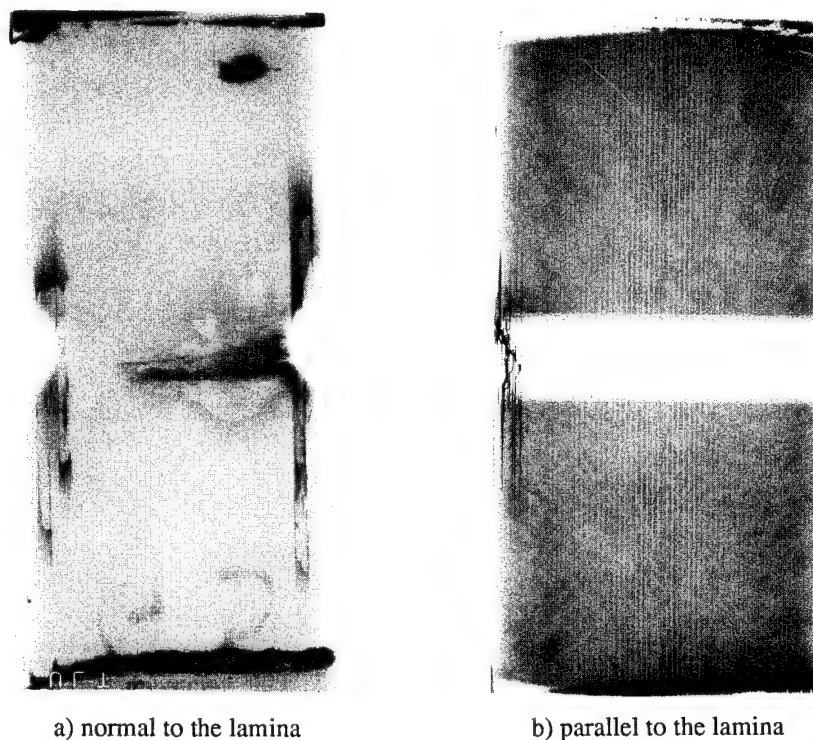


Figure 2. Radiographs of a specimen at 98 percent of the fatigue life
a) normal and b) parallel to the lamina.

Only two echoes were obtained using any of the ultrasonic methods and transducers, even prior to fatigue testing. The basic shape of the curve of attenuation versus fatigue cycles was the same regardless of whether attenuation was calculated using the peak amplitude, RMS voltage or the area under the curve. No significant change in attenuation was observed until just before failure, as shown in Figure 3. Typically there was a decrease in attenuation followed by an increase before failure. The decrease occurred when the transverse crack was first observed radiographically. Higher frequency transducers tended to yield higher attenuations which agrees with previous studies.^{1, 5} Through-transmission produced greater attenuation than obtained using a pulse-echo method.

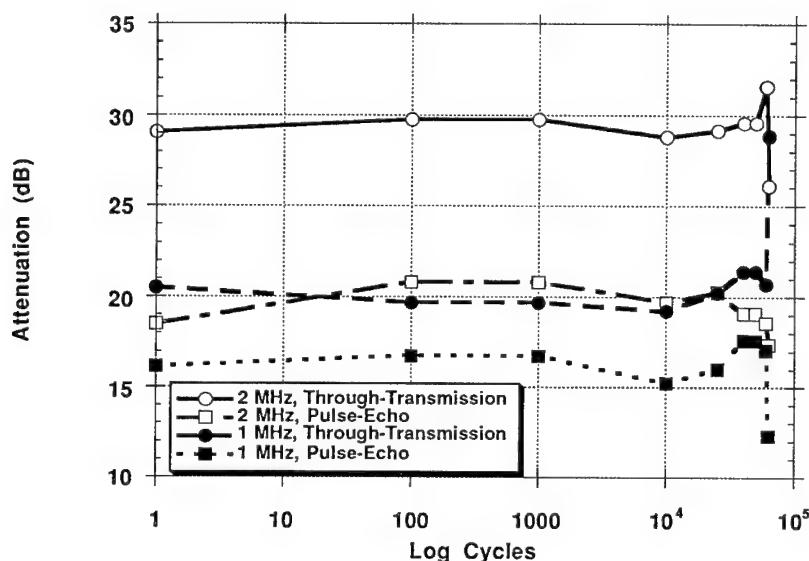


Figure 3. Attenuation measured using the Matec ultrasonic system.

The velocity was dependent on the method by which it was calculated. Velocities were calculated using three different values for the time of flight (tof), as shown in Figure 4. The first method used the tof from the excitation pulse to the maximum amplitude of the first echo (tof1), the second method used the tof to the second echo (tof2), and the third method used the difference in time between these two methods (tof1-2). Methods tof1 and tof2 were significantly more dependent on the ultrasonic method and transducer frequency than method tof1-2. Although the values were different, similar indications of fatigue damage were obtained with any of the velocity measurement methods, as shown in Figure 5. Method tof1-2 was still dependent on transducer frequency (Figure 6) but not on either through-transmission or pulse-echo ultrasonic methods. Similar to the attenuation there was no significant change in ultrasonic velocity until just before failure, as shown in Figures 5 and 6.

Some of the differences observed with the different frequency transducers, pulse systems, and ultrasonic methods could be due to differences in the spread of the ultrasonic beam. The transducers could have different beam profiles that may be dependent on the type of excitation pulse. This would result in different regions of the composite being evaluated.

In this study there was only 3.1 mm between the edge of the specimen and the transducer. Due to the thickness of the specimens the ultrasonic beam could have interacted with the edge of the specimen. To determine the effect of this on the ultrasonic parameters, a plate of the same material and thickness as the fatigue specimens was evaluated. The plate had a surface area significantly greater than the test specimens such

that it could be considered as an infinite plate. The plate was ultrasonically tested in the same manner as the fatigue specimens. Figures 7 and 8 show the results obtained from these tests. Attenuation remains dependent on the frequency of the transducer. When the Matec system was used the attenuation decreased with an increase in the transducer frequency. The opposite occurred when the Panametrics pulser was used. Attenuation values for the plate were similar to the initial values measured on the fatigue specimens. The ultrasonic velocity of the plate decreases with decreasing transducer frequency for both the Matec and Panametrics pulsers. The velocities measured on the unfatigued specimens were slightly less than those measured on the plate. These results indicate that either the ultrasonic beam did not interact with the edge of the specimen or the interaction had minimal effect. The type of excitation pulse and ultrasonic method still had an affect on the measurements.

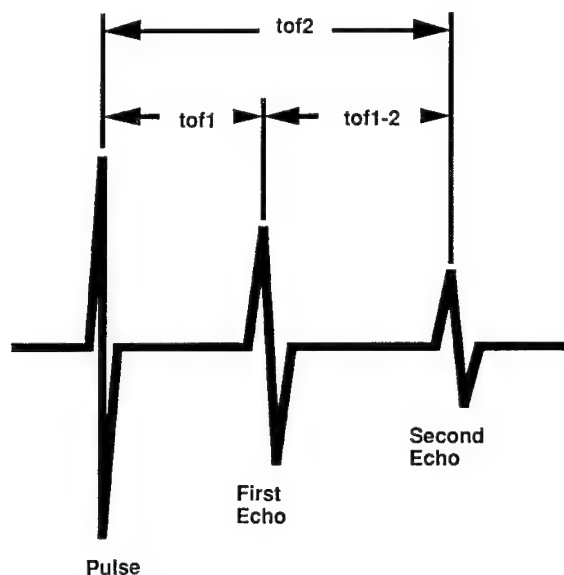


Figure 4. Different measurements of time of flight for calculating velocity.

Fatigue damage in the composite was not detected until just before failure for a variety of reasons. At every inspection interval, the transducers had to be recoupled to the specimen resulting in there being a change in the exact placement and coupling of the transducers to the specimen. This increases the variation in the data making it difficult to distinguish changes that are due to fatigue damage. In addition to this variation, the effect of any damage that is present is averaged with the undamaged material. This occurs both through the thickness of the specimen and across the area that the ultrasonic beam investigates. Until damage extends into the region of the ultrasonic beam and is sufficient to significantly alter the ultrasonic parameters there will not be any change in the detected attenuation or velocity. The attenuation measured in this study did begin to change when transverse cracks emanating from the root of the notch were observed radiographically to extend into the region under the transducers. Prior to this, although there was damage present in the specimen, there was not any damage in the direct path of the ultrasonic beam.

CONCLUSIONS

Ultrasonic measurements on a composite specimen subjected to compressive fatigue loading did not detect the presence of fatigue damage until very close to failure. Attenuation and velocity were both observed to be dependent on the frequency of the transducer, the type of excitation pulse and the ultrasonic method. Further work to reduce experimental error and utilize more advanced ultrasonic techniques should improve the damage detection capabilities.

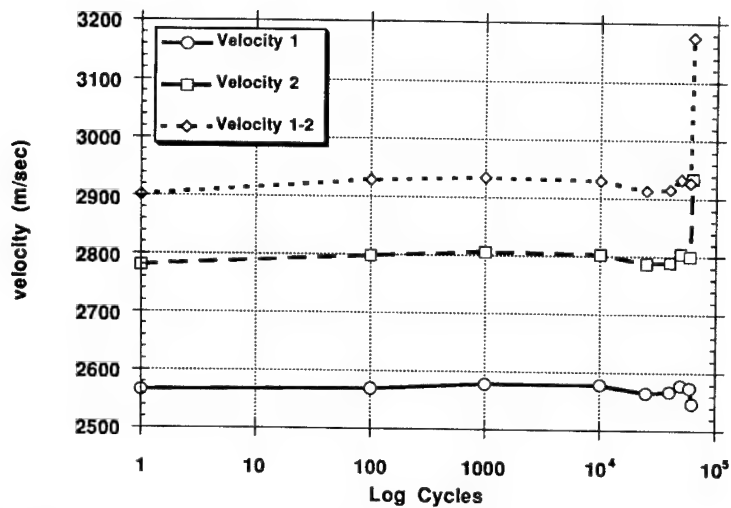


Figure 5. Ultrasonic velocity calculated using three different methods to determine the time of flight from results with the Panametrics ultrasonic system.

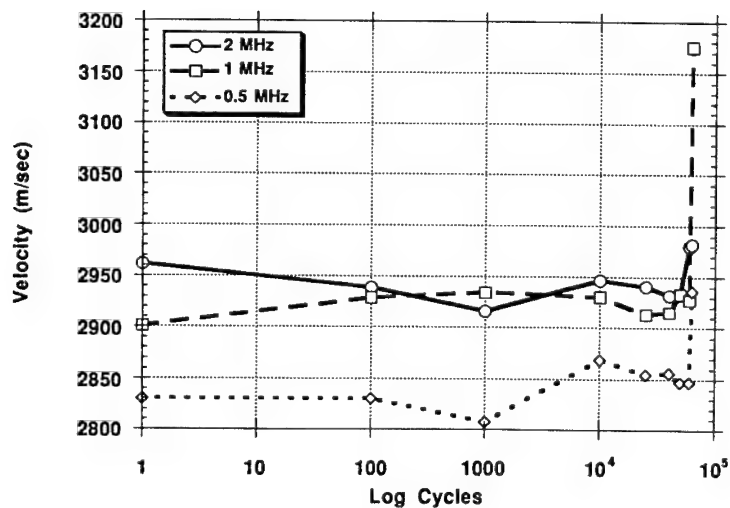


Figure 6. Ultrasonic velocity measured with different frequency transducers, tof1-2, and the Panametrics ultrasonic system.

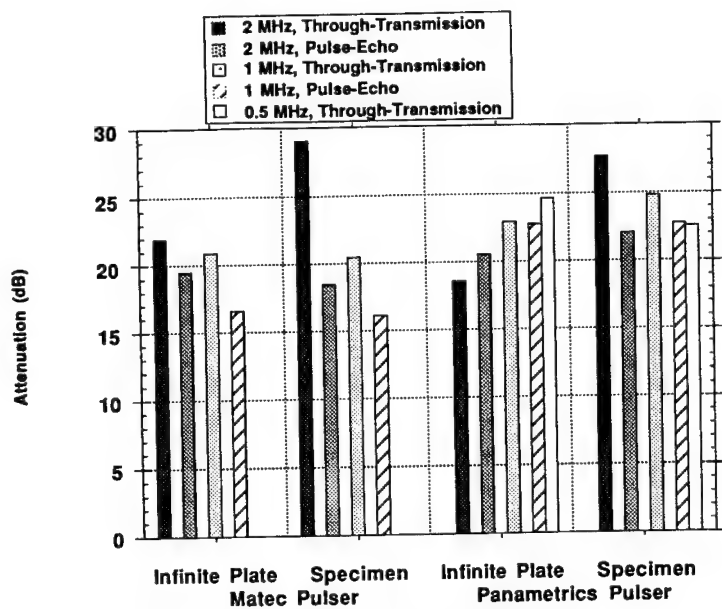


Figure 7. Effect of specimen size on attenuation.

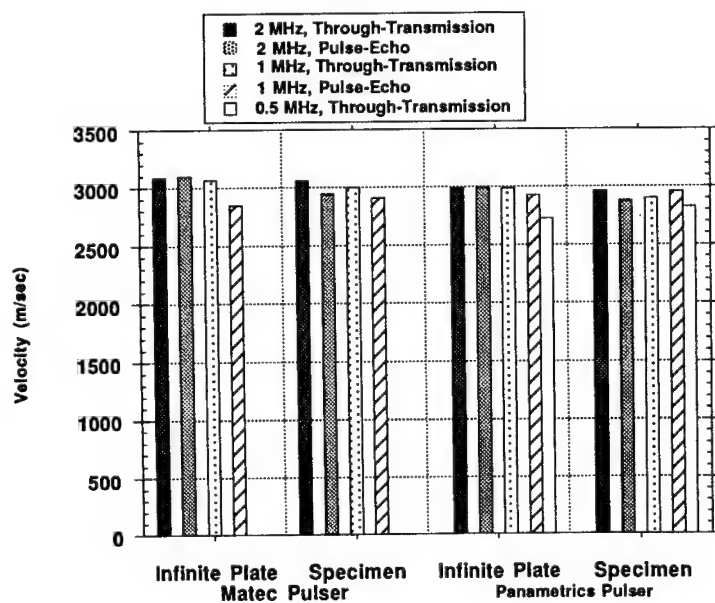


Figure 8. Effect of specimen size on ultrasonic velocity.

ACKNOWLEDGMENTS

This research was funded by the Defense Advanced Research Projects Agency, program manager Mr. James J. Kelly, through the Office of Naval Research, Mechanics Division, Dr. Yapa D.S. Rajapakse, DARPA agent. Additional support was provided by The Johns Hopkins Center for Nondestructive Evaluation.

REFERENCES

1. J. H. Cantrell Jr., W. P. Winfree, and J. S. Heyman, Profiles of fatigue damage in graphite/epoxy composites from ultrasonic transmission power spectra, *in*: "Recent Advances in Composites in the United States and Japan, ASTM STP 864," J. R. Vinson and M. Taya, Eds., American Society for Testing and Materials, Philadelphia, (1985).
2. V. Dayal, V. Iyer, and V. K. Kinra, Advances in Fracture Research, Proceedings of the 7th International Conference on Fracture (ICF7), 5, 3291 (1989).
3. D. T. Hayford, and E. G. Henneke II, A model for correlating damage and attenuation in composites, *in*: "Composite Materials: Testing and Design (Fifth Conference), ASTM STP 674," S. W. Tsai, Eds., American Society for Testing and Materials, Philadelphia, Pennsylvania, (1979).
4. B. Hosten, and S. Baste, Ultrasonics measurements of anisotropic damage in polymeric matrix/glass fibers composite laminates subjected to tensile stresses, to be published in Review of Progress in Quantitative Nondestructive Evaluation, 12, (1993).
5. J. H. Williams, and B. Doll, Ultrasonic attenuation as an indicator of fatigue life of graphite fiber epoxy composite, *Materials Evaluation*, 38:33, (1980).
6. C. Byrne, "Damage accumulation in thick graphite-epoxy composites during compressive fatigue," Master of Science, The Johns Hopkins University (1993).

A STUDY ON THE ACOUSTIC EMISSION CHARACTERISTICS OF THE CARBON FIBER REINFORCED PLASTICS

Y.K. Ji¹ and J.W. Ong²

¹Korea Atomic Energy Research Institute, Daeduk Science Town

²Mechanical Eng. Department, Chungnam National Univ.
Daejeon, 305, Republic of Korea

INTRODUCTION

Carbon fiber reinforced plastics(CFRP) have good characteristics; high specific strength and stiffness, corrosion-resistance, and excellent insulation. In addition, they can be designed and fabricated to get adequate strength and stiffness by changing the angle and sequence of their laminations. Therefore, the composite materials are increasingly used in industries of aerospace, automobile, ship, leisure and sports. Many investigations on their performance improvement and material evaluation have been studied, but the failure mechanism is difficult to clarify because the composite materials have complex failure process caused by their non-homogeneous and anisotropic characteristics.^{1,2}

To evaluate their performance and analyze their failure mechanism, Acoustic Emission (AE), one of the non-destructive testing methods has been performed. AE is used for detection of initial defects, clarification of failure mechanism, estimation of final fracture stress, back data to integrity evaluation. AE parameters are count, event, amplitude distribution, frequency spectrum, etc. Primary sources for AE of the composite materials are plastic deformation of matrix, matrix cracking, debonding of matrix and fiber, fiber pull-out, delamination, fracture of fiber, and secondary sources are friction of fiber, disclosure of cracks, etc. Extensive studies on various NDT as well as the relation of AE parameters and AE sources are needed to synthetically evaluate and clarify failure characteristics and damage region of the composite materials, but they are restricted by experimental equipments, materials, etc.

In this report, we are trying to compare fracture behaviour and AE characteristics generated during tensile test using a laminate of carbon/epoxy prepreg and hence clarify availability of AE method and failure characteristics of the CFRP.

EXPERIMENTAL METHOD

Material of specimens used in this experiment is 8 layer-laminated carbon/epoxy prepreg according to the designated sequence and angle of lamination, which is fabricated

in dry oven to a fiber volumetric fraction of 0.6. In accordance with ASTM D 3039-76,³ laminates are fabricated to total 14 kinds of specimen in shape and dimension shown in Figure 1 and free edges of the specimen are ground in order to prevent their damage region from occurring on cutting. To protect the specimen from tensile grip, epoxy tab in thickness of 3 mm is glued at both ends.

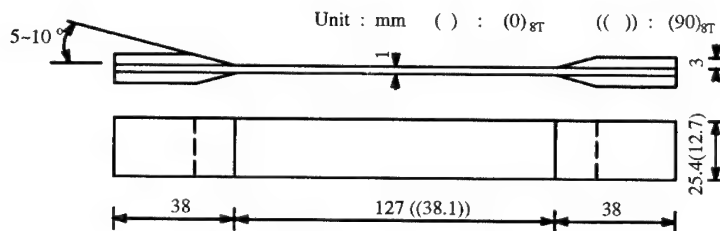


Figure 1. Configuration of test specimen

As shown in Figure 2, experimental equipments are composed of universal testing machine (Tensilon/UTM1-10000C) containing 5 ton-load cell and AE equipment (AET 5000) for detection of failure process in the test specimen. Also, dynamic strainmeter, X-Y recorder, PC/AT, and strain gauge are used. Cross head speed of UTM is 0.5 – 1.0 mm /min and variation of micro resistance detected by strain gauge is amplified in dynamic strainmeter and then load-displacement curve is plotted in X-Y recorder.

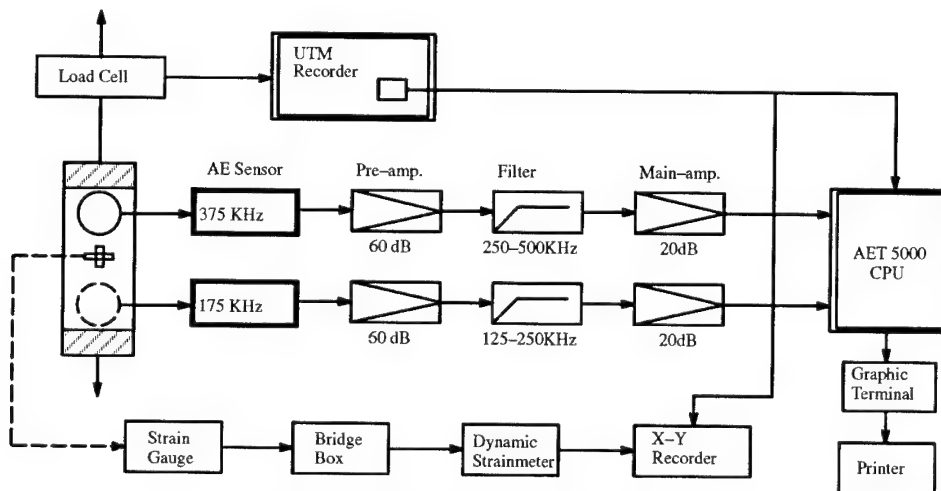


Figure 2. Block diagram of AE measuring system

Resonance type transducers, 175 kHz and 375 kHz transducers are provided as a AE sensor. For adhesion of transducers, specimen and transducer are greased and pressed using ring spring to collect generating AE signals sensitively. Signals detected from transducers

are amplified to 60 dB through pre-amplifier and then to 20 dB through main amplifier to get required data in CPU of AET 5000. Since environmental noise levels are 50 μ V for 375 kHz transducer and 80 μ V for 175 kHz transducer, the threshold voltages are 1.0 V (fixed) and 1.5 V (fixed) respectively. Experiment for measurement of variation of Felicity ratio is performed with increase of load ratio step by step until fracture of specimen i. e., loading-unloading-reloading cycle. Felicity ratio is calculated on the basis of the generating load of AE signals.

EXPERIMENTAL RESULTS AND DISCUSSION

Activity of Ringdown Counts (RC) and Total Ringdown Counts (TRC)

Figures 3(a) and 3(b) are plots of $(0)_{8T}$ specimen using 375KHz and 175KHz transducer. Comparing to the two figures, AE signals are significantly detected from 175KHz transducer. Therefore we tried to analyze failure mechanism with AE signals of 175KHz transducer which is mainly used in the composite materials.

Relations between RC(TRC) and load-displacement of typical one-directional CFRP are shown in Figures 3(a)–(e). In the case of $(0)_{8T}$ specimen, AE signals are initiated around 10 percent of maximum load.⁴ RC increases continuously from the initiation of AE signals and then decreases after it peaks about 60 percent of maximum load. As load increases, TRC increases almost linearly, but transition occurs near 60 percent of maximum load. It is considered that AE signals at 10 percent of maximum load are caused by matrix cracking or deformation and those at 50 percent of maximum load, initiating point of transition, are due to intra-delamination. Many researchers have reported^{5–9} that CFRP failure processes have matrix cracking, delamination, fiber fracture as load increases and, especially, delamination takes place at the point of rapid increase of RC and TRC. Since the matrix cracking which could occur in the region of extremely low load is not propagated before fiber fracture in other region and remains stable isolated, it is known to have no effects on the final fracture.

However a few fibers may fail in the region of extremely low load due to statistical characteristics of fiber strength, these phenomena do not nearly affect tensile strength while they have influence on the final fracture.⁵ Therefore, it is considered that, as load increases continuously, many matrix cracks are generated and developed along vertical fiber direction and final fracture results from gradual increase of fiber-matrix debonding, delamination, and fiber pull-out. $(90)_{8T}$ specimen fails just after the AE generation at the 75 percent region of maximum load. It represents aspect of brittle fracture compared to AE generation of the 20 to 30 percent region of maximum load, which could be caused by weakness of matrix itself. Behaviour of $(45)_{8T}$ specimen is similar to that of $(90)_{8T}$ specimen. Most of the AE signals are generated when final fracture occurs and are caused by matrix cracking. As angle of unidirectional specimen increases, RC, TRC and maximum load decrease.

Figures 3(f)–3(j) show relations between typical load-displacement and RC for $(\pm\theta)_{2S}$, where maximum load, RC, and TRC are reduced as angle of stacking sequence for $(\pm\theta)$ increases. As shown in figures 3(f)–3(j), $(\pm15)_{2S}$, $(\pm30)_{2S}$, $(\pm45)_{2S}$ specimens failed not due to fiber fracture, but due to transverse crack and delamination. $(\pm15)_{2S}$ specimen led to fail at 90 percent of maximum load accompanying many signals, after AE signals appear at around 30 percent of maximum load and increase more or less in spite of increase of comparatively high load. It is indicated that RC increases rapidly by delamination near 90 percent of maximum load after generation of transverse crack along fiber direction and matrix cracking and specimen fail suddenly without fiber damage. For $(\pm45)_{2S}$ specimen, AE

signals are generated at about 14 percent of maximum load and increase gradually up to 40 percent and exponentially after that. Matrix cracking is initiated at about 14 percent of maximum load and delamination is generated and superimposed during long time compared to other specimens, with propagated in the transverse direction. It is considered that $(\pm 60)_{2S}$ specimen and $(\pm 75)_{2S}$ specimen are observed to have matrix cracking under the very small load less than 100 kg, and failed by fiber pull-out after propagation of transverse crack along the fiber direction, not by delamination.

Figures 3(k)–3(o) represent phenomena of three-directional specimens. For $(90/0/\pm 45)_S$, $(90/\pm 45/0)_S$ specimens, outer stacking laminate of 90 degree is observed to fail as first step during tensile test. That is, TRC is very small due to that. After that, aspect of AE signal is similar to $(0)_{8T}$ specimen. Rapid increase in TRC curve is due to 0 degree laminate fiber fracture. Effect of ± 45 degree laminate debonding is insignificant compared to fiber fracture. For $(\pm 45/0/90)_S$ specimen, also we expect initial failure of 90 degree laminate and then complicated failure mechanism is affected. Especially, delamination occurs between 45 degree–0 degree and 0 degree–0 degree laminates caused by failure of 90 degree laminate and hence twisting appears considerably. Final fracture load is similar, but TRC is very different according to arrangement of stacking sequence in the three directional CFRP. Also, three steps can be classified by the slope of TRC curve. The first step with slow slope of TRC is considered causing generation and propagation of matrix cracking. Delamination is initiated with audible sound at the second step which shows the steep slope of TRC. Fiber pull-out and final specimen breakage take place at the last step.

Felicity Effect

Felicity effect is defined as the opposite concept of Kaiser effect.^{10–12} During the cycle of loading–unloading–reloading, AE signals generated by Felicity effect are generated at reloading less than maximum load at the previous loading step while AE signals generated by Kaiser effect are initiated over that. Especially CFRP has the stringent characteristics of Felicity effect because the material has anisotropic property and an effect on inter-relation of complicated fiber fracture. Felicity ratio is introduced to explain Felicity effect as follows:

$$\text{Felicity Ratio (R)} = P_i / P_o$$

where: P_i = load initiating AE signals at reloading, and

P_o = maximum load at loading.

Figure 4 shows variations of representative R value for each direction as a function of load ratio. For $(0)_{8T}$ specimen, R remains 1.0 up to a load ratio of 0.15 as shown in Figure 4 (a). For load ratios of 0.15–0.75, R value decreases slowly while over a load ratio of 0.75 it decreases sharply. For $(45)_{8T}$, $(90)_{8T}$ specimens, R remains 1.0 up to a load ratio of 0.9 and then decreases sharply. Compared to AE activity, matrix cracking occurs as R get to a value of 1.0 and more failure occurs because R value decreases rapidly with increase of angle of stacking sequence.

Figure 4(b) shows the characteristics of $(\pm \theta)_{2S}$ specimen, which indicates that R value does not change and the detection of AE signals decreases with increase of angle.

For three directional CFRP of figure 4(c), R value remains 1.0 up to a load ratio of 0.3. They show different values depending on stacking sequences and, especially, R value decreases clearly with ± 45 lamina arranged outside.

Matrix cracking occurs when R value is around 1.0, that is, Kaiser effect is dominant. Then, more failure occurs with decrease of R value which is changed due to the effect of complicated failure mechanism. As discussed above, relation between R value and failure mechanism is difficult to define clearly. It is considered that 1.0 to 0.85 of R is caused by

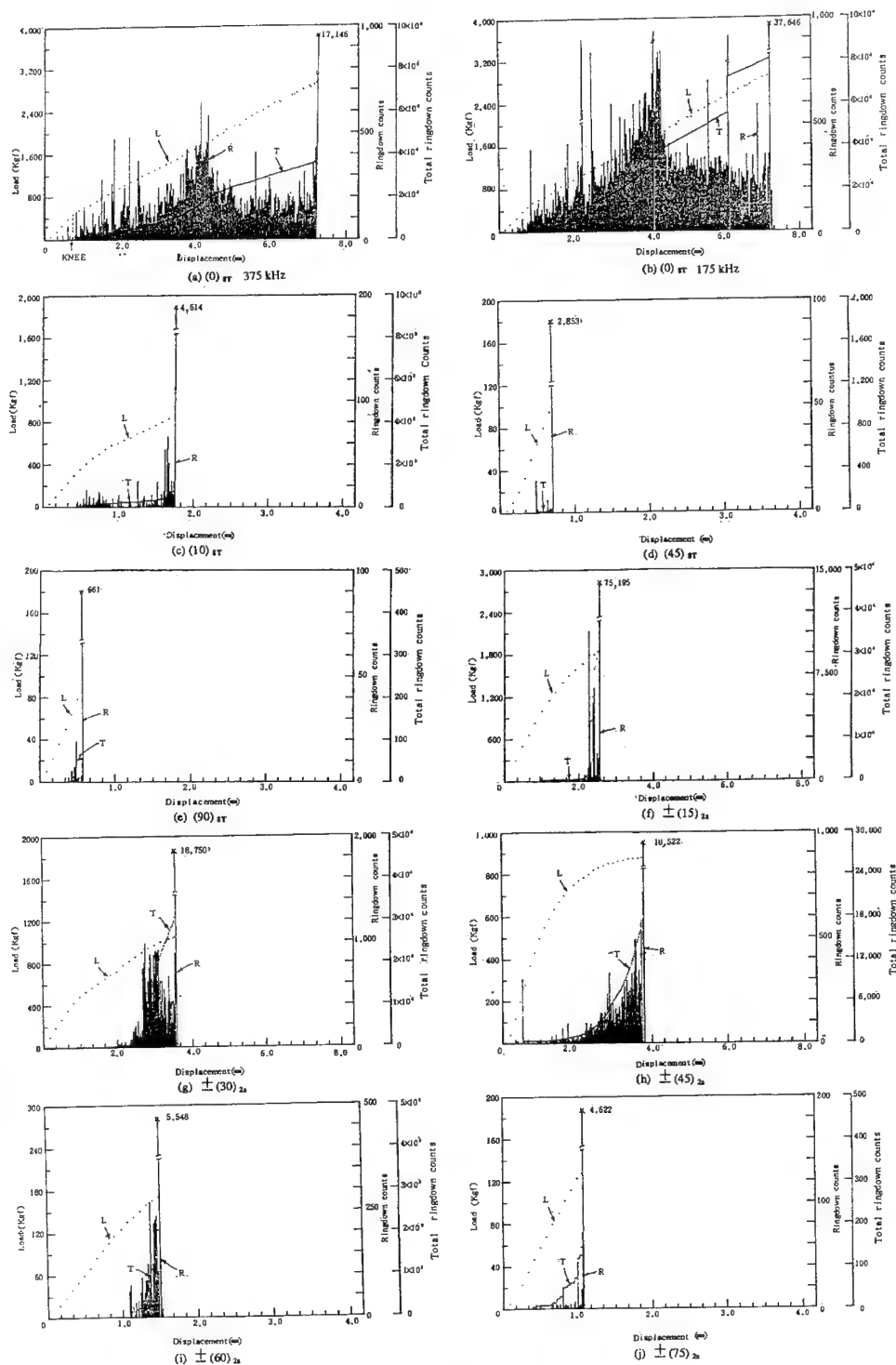


Figure 3. Plot of displacement vs. load , counts, total counts

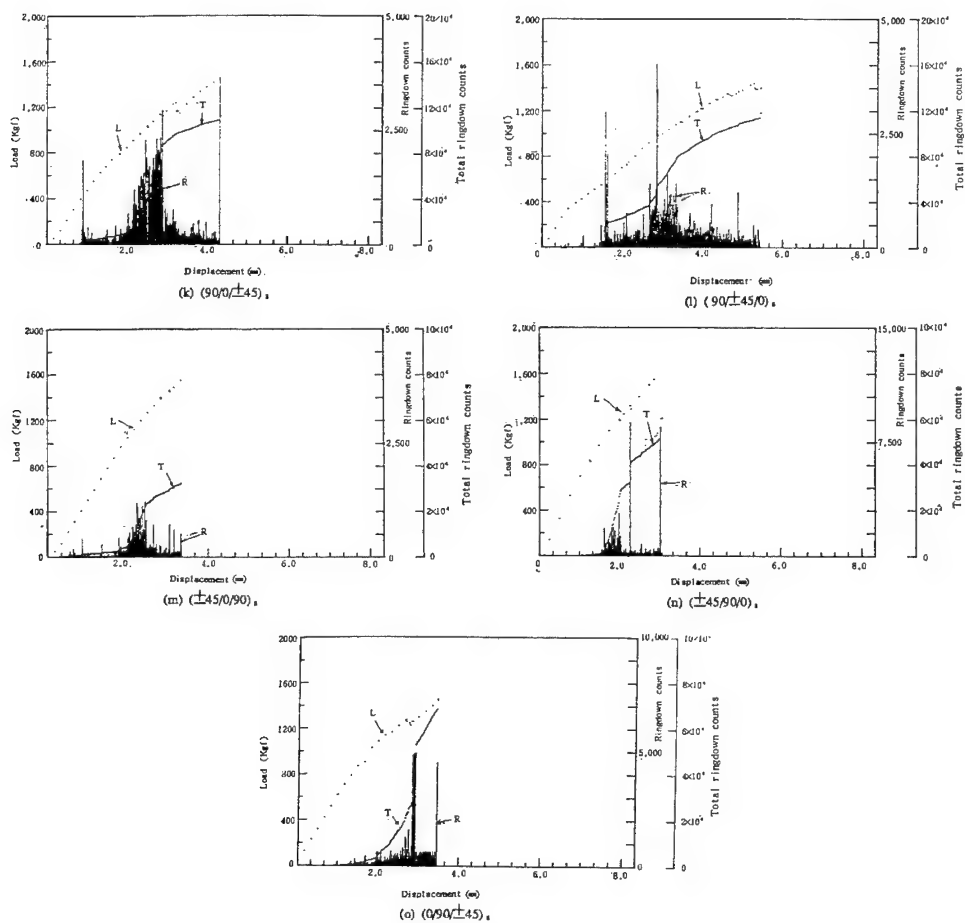


Figure 3. (continued)

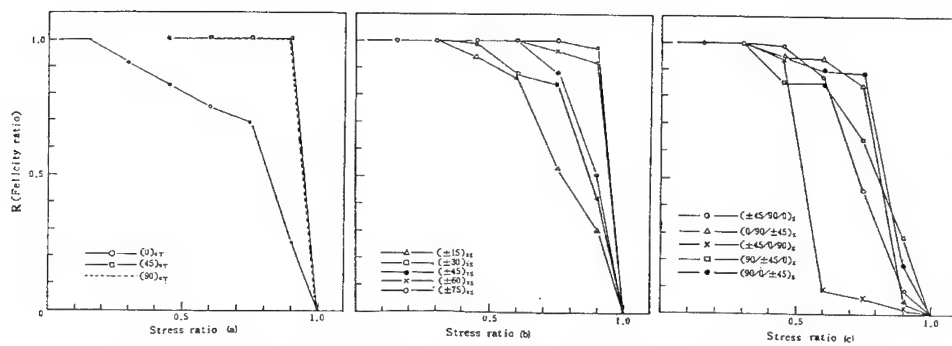


Figure 4. Plot of R vs. stress ratio : (a) one-direction (b) two-direction (c) three-direction

matrix cracking, 0.85 to 0.40 by generation and propagation of the delamination, and below 0.4 by fiber fracture, but failure mechanism is acted on complicated process.

Peak Amplitude Distribution

It is known that brittle materials, containing defects, of high strength, anisotropy and non-homogeneous have high amplitude and amplitude distribution is related to failure mechanism. Figure 5 shows typical experimental results obtained from relation between peak amplitude distribution and events.

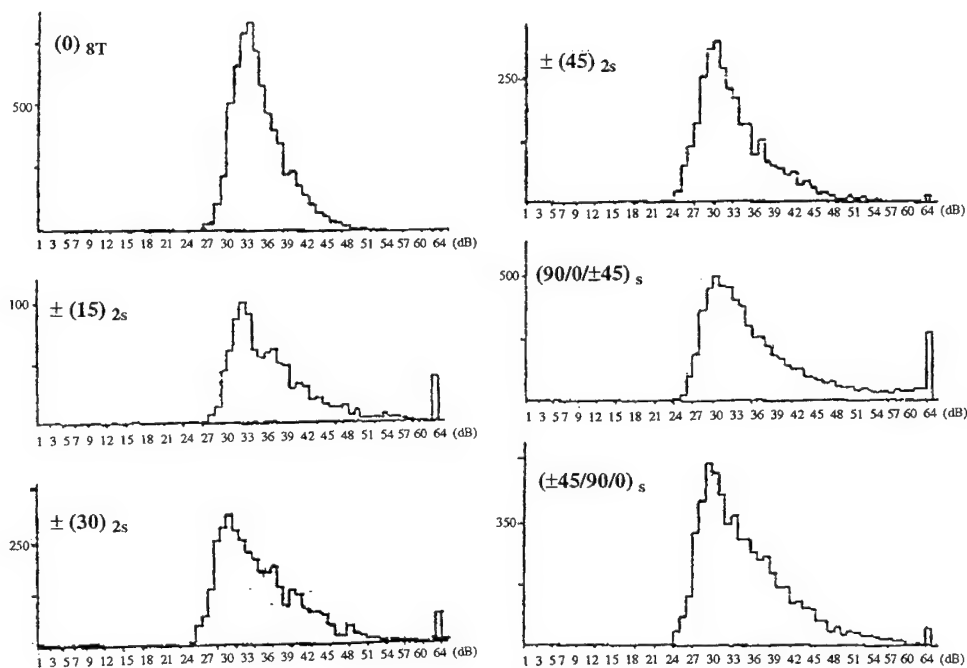


Figure 5. Plot of AE peak amplitude distribution and events

For (0)_{8T} specimen, minimum amplitude appears at 26 dB and most of amplitude distribution is detected at range of 30 to 39 dB. AE signals, events peak at 34 dB and then tend to decrease exponentially. For (90)_{8T} specimen, a few events, if any, are initiated at 25 dB since this specimen fails at once. Results of (±60)_{2S}, (±75)_{2S} are similar to that of (90)_{8T}, they are not shown in Figure 5.

For (±θ)_{2S} specimens, (±15)_{2S} shows relatively high amplitude distribution and (±30)_{2S}, (±45)_{2S} show similar tendency, that is, peak event occurs near 30 dB. According to total events, (±45)_{2S}, (±30)_{2S}, (±15)_{2S}, (±60)_{2S}, (±75)_{2S} are shown in turn.

Three directional specimens are inclined to give peak event at 30 dB regardless of stacking sequence; for 24 dB – 30 dB, rapid increase and for 30 dB – 60 dB, exponential decrease.

Also, previous researchers have reported AE events caused by delamination below peak amplitude of 30 dB, by matrix cracking 30 to 40 dB, and by fiber fracture 40 to 80 dB through compression testing and tensile testing of matrix and fiber only. However, they show disagreement with results in this study. With increase of load, events showing peak amplitude are increasingly accumulated in a wide range of amplitude distribution.

CONCLUSIONS

According to angle and sequence of stacking, relations between AE signals and failure mechanism of CFRP during tensile testing are as follows:

(1) For $(0)_8T$ specimen, matrix deformation and cracking are initiated around 10 percent of maximum load and delamination takes place at 50 percent of maximum load. AE signals caused by fiber fracture are dominant. For $(90)_8T$ specimen, AE signals caused mainly by matrix cracking are detected.

(2) For $(\pm\theta)_{2S}$ specimens, TRC decreases with increase of θ (angle) and debonding of fiber and matrix occurs by the effect of shear force parallel to fiber direction.

(3) For three directional specimens, different failure mechanisms appear depending on stacking sequence of the weakest 90 degree laminate. They have stringent differences of TRC associated with stacking sequence while having similar fracture strength, about 1600 kgf.

(4) Failure mechanisms are considered having a relation with Felicity ratio (R); matrix cracking for 1.0–0.85, generation and propagation of delamination for 0.80–0.40, and fiber fracture below 0.40.

REFERENCES

1. Robert M.Jones, "Mechanics of Composite Materials", McGraw-Hill Book company, (1975).
2. Stephen W.Tasi, "Composite Design", 3rd Ed., Think Composites, Dayton, Ohio, (1987).
3. ASTM D 3039-76, "Standard Test Method for Tensile Properties of Fiber-Resin Composites", Annual Book of ASTM Standards, (1982).
4. E.G. Henneke, C.T. Harakovich, G.L.Jones and M.P. Renieri, "Acoustic mission from Composite-reinforced Metals", VPI-E-73-27, NASA Report, (1975).
5. A. Rotem, "The Discrimination of Microfracture mode of Fibrous Composite Material by Acoustic Emission Technique", Fiber Science and Technology, Vol. 10, pp. 101-121, (1977).
6. R.L. Mehan and J.V. Mullin, "Analysis of Composites Failure Mechanisms using Acoustic Emission", Journal of composite Material 5, pp. 256-269, (1971).
7. Pedro Feres Filbo, "Results Evaluation of Acoustic Emission Tests Applied in Industrial Equipment", Journal of Composite Materials, pp. 489-491, (1985).
8. M. Shiwa and T. Kishi, "Acoustic Emission during Load-Holding and Unload-Reload in Fiberglass-Epoxy Composites", The second International Conference on Acoustic Emission, pp. 195-198, (1985).
9. Yuan Zhenming, "Acoustic Emission Characterization of internal Damage for GFRP", The First International Conference on Acoustic Emission, pp. 458-463, (1985).
10. Jin Zhou Geng, Song Guo Gui and Zhu Cheng, "Acoustic Emission Characteristics of Carbon Epoxy Laminates Beams during Bending Failure", Progress in Acoustic Emission II, pp. 472-479, (1984).
11. H.C.Kim, A.P.Ripper Neto and R.W.B. Stephens, "Some Observations on Acoustic Emission during Continuous Tensile Cycling of a Carbon Fiber/Epoxy Composite", Nature Physical Science, 237, pp78-80, (1972).
12. D.E.W.Stone and P.F.Dingwall, "The Kaiser Effect in Stress Wave Emission Testing of Carbon Fiber Composites", Nature Physical Science, 241, pp63-69, (1973).

TOOL WEAR MONITORING AT TURNING AND DRILLING

Eckhard Waschkies, Christoph Sklarczyk, and Eckhardt Schneider

Fraunhofer-Institute for Nondestructive Testing (IzfP)
University, Building 37
D-66123 Saarbrücken, Germany

ABSTRACT

To improve economy and as a contribution in quality assurance in the domain of machining metallic materials a method for automatic tool wear monitoring at turning and drilling has been developed based on the analysis of the acoustic emission (AE) generated on the tool at machining procedure (machining noise). Different wear types (tool flank face and tool chipping) result in changes of the different characteristic values of the continuous part of AE. In case of a uniform abrasion of the insert, e.g. flank face or crater wear, an increased mean signal level is observed, whereas for microbreakage at tool edge, an increase of the crest factor with nearly constant mean signal level is found. The burst-like signals from collision between chip and tool and from chip breakage have to be eliminated from analysis to avoid the distortion of the signal parameters of continuous AE. This method should be well suited especially for monitoring of finishing processes (with small depth of cut).

1. INTRODUCTION

There is an industrial need on a method for automatic untended monitoring of tool wear during machining of metallic materials especially in the domain of finishing with small depth of cut. The method described below shall meet this requirement. It is based on the analysis of the acoustic emission (AE) generated during cutting process and consisting of continuous AE and transient (burst) AE. This monitoring method has been developed in the frame of a research project supported by the European Community in cooperation between the Fraunhofer-Institute for Nondestructive Testing (IzfP), Robert Bosch GmbH, Germany, and Danfoss A/S, Denmark [1].

2. THEORETICAL CONSIDERATIONS

2.1 Definition of the measuring quantities

The characterization of continuous AE can be performed by the following signal parameters

$$\text{Average Signal Level} \quad \text{ASL} = 1/T \cdot \int_0^T |A(t)| dt \quad (1)$$

$$\text{Root Mean Square} \quad \text{RMS} = \left\{ 1/T \cdot \int_0^T A^2(t) dt \right\}^{1/2} \quad (2)$$

$$\text{Crest factor} \quad C = A_{\max}/\text{ASL} \quad (3)$$

with $A(t)$: deflection of AE-signal as function of time, A_{\max} : maximum amplitude of AE-signal within integration time T .

2.2. Sources of the AE during machining

Fig. 1 shows schematically the cutting procedure on a tool edge, especially for turning. The possible sources of the AE are [2]:

continuous AE (machining noise):

- friction contact between the tool flank face and the work piece resulting in flank wear
- friction contact between the tool rake face and the chip resulting in wear, e.g. crater wear
- plastic deformation during cutting process in the work piece
- plastic deformation in the chip

transient (burst) AE:

- collisions between chip and tool or tool holder
- crack formation in the chip (chip breakage)
- tool edge chipping

According to some researchers plastic deformation and friction have comparable importance with regard to the generation of the continuous AE [2]. However, Uehara has found that under turning conditions the sound amplitude of the signals from workpiece is reduced decisively during sound transfer from workpiece to tool possibly by reflection of the sound at the interface [3]. That means that the friction between workpiece and tool has to be regarded as the most important source of continuous AE. In the present investigation corresponding measurements have yielded the same results: the signal amplitude loss at the interface was about 35 dB (factor of 50 - 60). These findings are supported by more indirect experiments by Heiple et al. [4]. Therefore the authors of this paper support the view that the friction between workpiece and tool is the essential source of the continuous AE.

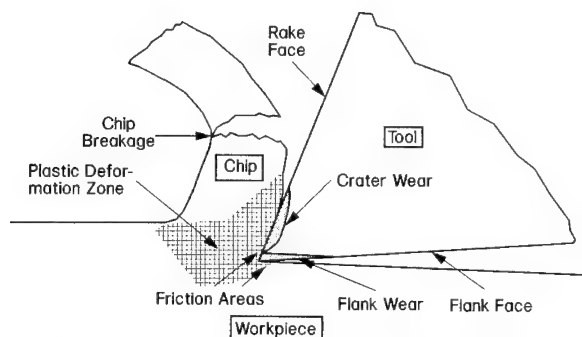


Fig. 1. Acoustic emission sources at cutting process

2.3. Continuous AE and tool wear

Starting from the experimentally well established view that the continuous AE is generated essentially by the friction between work piece and tool (see 2.2), the dependence of the signal parameters of continuous AE on abrasive tool wear can be described by a simple model. In microscopic scale the surface contact between work piece and tool can be regarded as a big number of point contacts [1]. During relative movement of the contact areas local stresses σ_i arise at the contact points which spontaneously release elastic waves and hence AE bursts. The signal amplitudes A_i are approximately proportional to σ_i . Since the rate of the AE bursts is very high, these bursts interfere and their superposition results in a continuous or quasi-continuous AE signal with undistinguishable individual bursts. The ASL-level and the crest-factor of this continuous AE can be calculated from the machining and tool wear parameters [1]:

$$ASL = n_0^{1/2} \cdot a_p \cdot VB \cdot v_c \quad (4)$$

$$C = 1/(n_0^{3/2} \cdot a_p \cdot VB \cdot v_c) \quad (5)$$

where a_p is the depth of cut, v_c the velocity of cut, VB the wear land and n_0 the area density of contact points. A similar relationship like (4) holds for RMS, too.

The density of the contact points n_0 can be locally different and depends on the structure (roughness) of the surface [5]. In the equations (4) and (5) only the flank face area ($F = a_p \cdot VB$) is considered, since predominantly flank wear was found at the experiments reported below. In case of additional wear types (crater wear, notch on the rake face produced by the chip) the equations have to be modified by additional terms.

From the equations given above in principle two cases can be distinguished:

Case 1: n_0 remains nearly constant with increasing wear. This is true for uniform flank wear if only VB increases, but the structure of the wear contact area is unchanged. According to equation (4) an increase of the ASL-value proportional to VB is to be expected.

Case 2: n_0 changes to lower value, e.g. by chipping of the cutting edge. According to equation (4) and (5) ASL decreases and C increases.

3. EXPERIMENTAL CONDITIONS

The experiments have been performed with computer based AE equipment designed, developed and built by IztP. The signals have been digitized with 10 MHz/12 bit, processed with regard to the signal parameters like peak amplitude or duration and stored on mass storage for evaluation. Furthermore the ASL- and RMS-values have also been determined. Commercial broadband piezoelectric ultrasound transducers have been used as sensors. The frequency domain was chosen between 0.1 and 1 MHz to avoid the influence of structure born noise which mainly occurs in the lower frequency range. The sensor with a diameter of about 5 mm was integrated in the tool holder directly underneath the insert.

One part of the experiments has been performed by using a cooling lubricant. Here no sensor cooling was necessary. Another part was performed without cooling lubricant. For these experiments a special cooling device has been constructed, and the sensor was cooled by flowing water. In both cases sensor temperature was held constant during the whole test.

The experiments described below have been carried out during NC-turning of a big variety of work materials (roller-bearing-steel 100 Cr 6, case-hardened-steel 16 MnCr 5, machining steel 9 SMn 28, cast iron (Meehanite)), inserts (coated carbide metal tools with and without chip breaking flute like CNMM, ceramics CBN) and cutting parameters ($v_c = 80$ to 600 m/min., $a_p = 0.1$ to 2.5 mm, feed $f = 0.04$ to 0.4 mm/rev.).

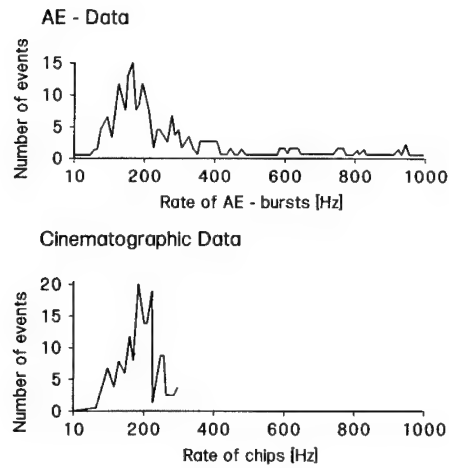


Fig. 2. Comparison of AE and cinematographic data for the occurrence of chips

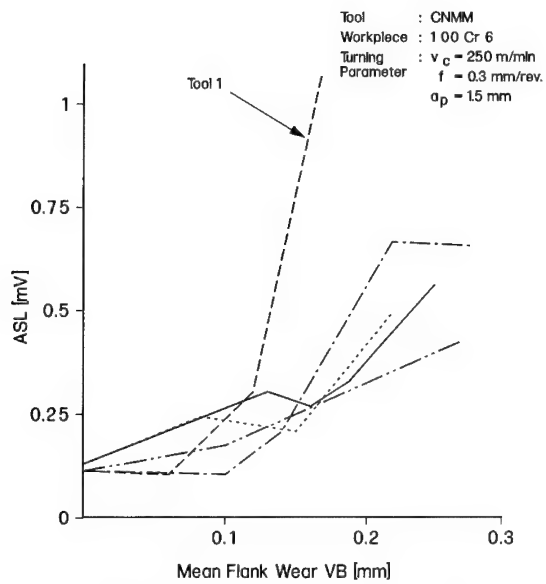


Fig. 3. Mean noise level versus mean flank wear for different tools

4. EXPERIMENTAL RESULTS

4.1. Chip collisions

From section 2.3 it can be expected that the friction between work piece and tool generates a continuous or quasi-continuous AE which can be characterized by ASL- or RMS-value. However, the experimental results show that sometimes burst-signals with high peak amplitudes interfere with the continuous AE. To clarify the origin of these bursts, simultaneously both AE has been recorded and the machining process has been filmed with high speed. The comparison of the AE and cinematographic data - by analysing chip behaviour slide by slide - has shown that the bursts were generated by collisions of the chips with the tool or tool holder and by chip breakage. This is shown in Fig. 2: both maxima of the rates of AE-bursts and chips, determined from the reciprocal values of time intervals between two AE-bursts resp. chips, are found at about 200 Hz indicating the coincidence of both processes.

It has been found that the AE related to the chips - especially the frequency of occurrence of the chips - provides some information on the chip behaviour but not on tool wear. However these AE bursts distort the signal parameter ASL and C described above. Therefore for a reliable tool wear monitoring these bursts have to be filtered out from the continuous AE before further analysis is performed. Ref. [7] describes this procedure in detail.

4.2. Continuous AE and cutting parameters

In agreement to the theoretical relations in equations (4) and (5) the experiments have given following dependences of the continuous AE on cutting parameters [1]:

- ASL is independent of feed.
- ASL is proportional to v_c .
- ASL is proportional to a_p only, if wear occurs uniformly over the whole depth of cut and if it is not concentrated on certain areas of the flank face.

4.3. Dependence of continuous AE on wear

Fig. 3 shows an experimental example for the dependence of ASL on wear, characterized here by the width of flank wear VB. For predominant flank wear (= all curves except for tool 1) the level of continuous AE is approximately proportional to VB. The results displayed in Fig. 3 show that a flank wear of VB = 0.2 mm, which is often regarded as no more acceptable, is detectable by an increase of ASL by a factor of about 2-3. This result is in accordance with the theory given above (case 1 in 2.3.).

Additionally to flank wear, tool 1 exhibited a deep notch generated by chip edge sliding along the rake face (Fig. 3). The stronger increase of ASL compared to the other curves can be explained by the coincidence of both types of wear which resulted in a bigger contact area between workpiece and tool. The insert has become unusable at VB = 0.17 mm.

Similar results as shown in Fig. 3 have been obtained by a variety of other tools and workpieces. Fig. 3 shows that continuous AE gives an integral information on tool wear condition and not only on one single wear type like flank wear.

If microscopic fracture of tool (tool edge chipping) occurs, the proportion of signals with high amplitudes in continuous AE increases. This results in a distinct increase of C. In Fig. 4 (bottom) C, which is normalized on the starting value (new tool) is shown as a function of the number of turning parts machined with one tool. At about 100 parts an abrupt increase of C can be seen which coincides with the rise of chipping of the cutting edge found by microscopic examination. Fig. 4 (top) shows that the mean level of continuous AE (noise) is

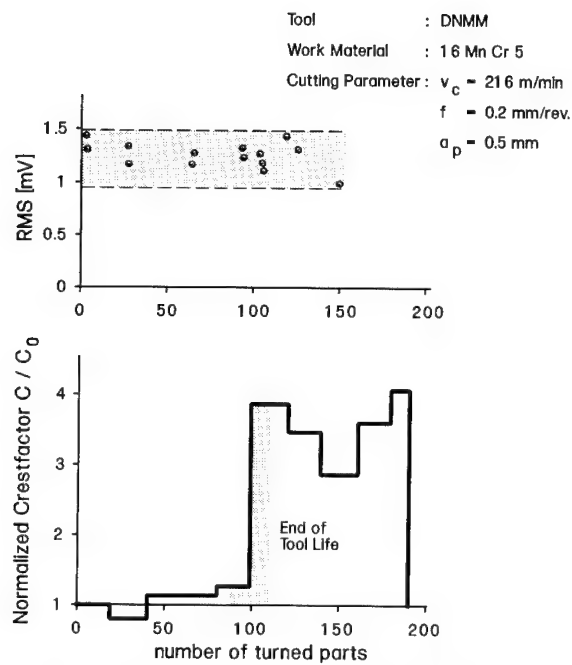


Fig. 4: AE-noise parameters versus number of turned parts
 top: mean noise level
 bottom: normalized crest factor

approximately constant or decreases slightly as wear increases. This result is in accordance with case 2 in 2.3. From these facts it is evident that the tool wear monitoring solely on the basis of increase of ASL is not sufficient, since it does not detect all types of wear.

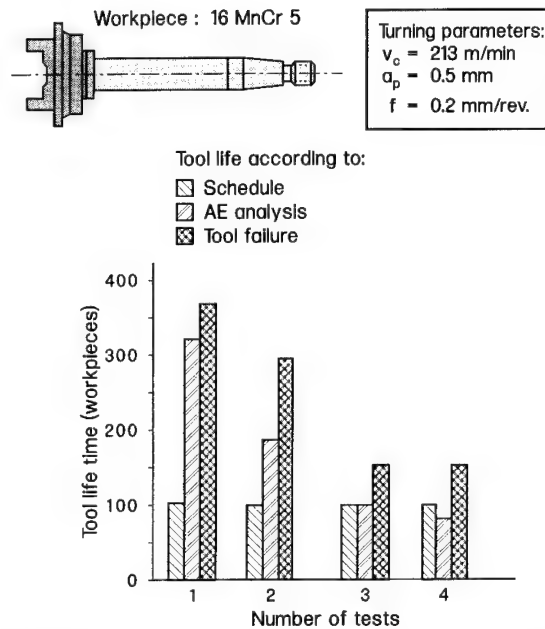


Fig. 5. Production parts with and without tool wear monitoring

4.4 An example for tool wear monitoring under industrial conditions

To verify the conception of AE-monitoring of tool wear given above, a big number of workpieces (driving shafts of a fuel pump) has been turned under industrial conditions using cooling lubricant. An increase of C by a factor of 2 has been regarded as clear indication for beginning tool wear. Without tool wear monitoring the tool would have been changed by schedule after 60 workpieces to prevent premature failure. However, in this test the tools have been used far beyond this limit. For tool no. 1 (Fig. 5) a clear increase of C has been observed after about 320 workpieces. This tool failed after ≥ 370 workpieces. That means that with the help of AE-monitoring this tool could be exploited much more better ($> 500 \%$) than without it. This holds partly for the other tools in test (no. 2 - 4 in Fig. 5), too.

4.5 Tool wear monitoring at drilling

During drilling experiments a clear increase of ASL has been found as wear of the drilling tool increased (Fig. 6). The drill exhibited a uniform flank wear. In this test the continuous AE has been captured by a sensor fixed on the workpiece.

5. CONCLUSIONS WITH REGARD TO PROCESS MONITORING

The theoretical considerations concerning the change of the continuous AE due to tool wear are in good accordance with the experimental results. For a reliable determination of tool wear both ASL and C have to be measured and evaluated from the continuous AE. Bursts from chip collisions and breakage have to be filtered out if they exhibit high amplitudes (see 4.). The relations between ASL and C and the characteristic values of wear, e.g. VB, depend on the details of the machining process and have to be determined by a teach-in process taking place before or at the beginning of tool monitoring. As already mentioned in section 3 the sensor should be placed as near as possible to the insert in the tool holder. This may restrict the application area of the method. However, the detection sensitivity and the reliability of tool wear detection is increased distinctively compared to the monitoring systems presently available where the sensor is placed on the machine housing or spindle (e.g. at cutting force measurement). This is particularly true for the machining process with small cutting forces which cannot be monitored up to now in satisfactory way [6].

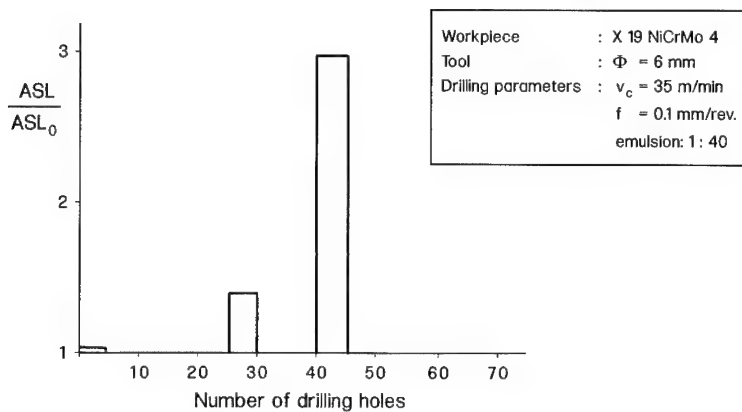


Fig. 6: ASL versus number of drilling holes at drilling

6. REFERENCES

- [1] E. Waschkies, K. Hepp, J. Fisker, H. Pitsch: "Acoustic emission for process monitoring during turning and drilling", *Final report of the BRITE-project 1300-4-85*, 1991
- [2] D.A. Dornfeld: "Tool wear sensing via acoustic emission analysis", *Proc. 8th NSF Grantee's Conf. on Production, Research and Technology*, Stanford Univ., 1981, A1-A8
- [3] K. Uehara: "Identification of chip formation mechanism through acoustic emission measurement", *Annals of the CIRP*, Vol. 33 (1), 71-74
- [4] C.R. Heiple, S.H. Carpenter, D.L. Armentrout: "Changes with material properties of acoustic emission produced during single point machining", *Progress in Acoustic Emission V*, The Japanese Society for NDI, 1990, 44-50
- [5] I. Kragelski, M.N. Dobycyn, V.S. Komalov: "Grundlagen der Berechnung von Reibung und Verschleiß", Carl Hanser Verlag, München, Wien, 1983
- [6] K.-D. Vöhringer: "Zerspanprozeß-Überwachung in der Großserie sinnvoll einsetzen", *Werkstatt und Betrieb*, Vol. 123 (1990), 763-766
- [7] E. Waschkies, K. Hepp: "Process and device for monitoring the chip-removing treatment of a workpiece", *United States Patent 5,159,836*, Nov. 3, 1992

NONDESTRUCTIVE EVALUATION OF MICROMECHANISM OF DEFORMATION PROCESS DURING FATIGUE TESTING ON POLYMER BY ETFuM (ELASTIC-WAVE TRANSFER FUNCTION METHOD)

Y. Higo¹, H. Kawabe², Y. Natsume² and S. Nunomura¹

¹Precision and Intelligence Laboratory,
Tokyo Institute of Technology
4259 Nagatsuta Midori-ku Yokohama 227, Japan

²NIPPONDENSO Co., Ltd.
1-1 Showa-cho Kariya 448, Japan

INTRODUCTION

According to comparison between fatigue phenomena on metals and on polymer, intrusion or extrusion were generated in slip bands at early stage of fatigue life on metals¹. On the other hand, it is considered that fracture of molecular chains is equivalent to these phenomena on polymer. But micromechanism of deformation process during fatigue is not clear². One of the reasons is that the micromechanism of nucleation and growth of microdefects is not clear. If polymer has perfect elastic property, fatigue does not generate during cyclic deformation. Therefore, the accumulation of microdefects is needed for fatigue. But micromechanism of stress concentration equivalent to conversion on metals is not clear.

Most investigations concerning the micromechanism of deformation process are studied under no-load. It is hard to find the researches concerning "dynamic evaluation of micromechanism of deformation process during fatigue". As for micromechanism of a deformation process which ends up fracture, it is considered that elastic heterogeneous area will be nucleated like as density, acoustic impedance and elastic modulus. Therefore, if elastic heterogeneous area can be evaluated dynamically and quantitatively on real time, we can investigate the dynamic microanalysis during fatigue process on polymer.

We have been investigated that new nondestructive evaluation method of ETFuM (Elas-

tic-wave Transfer Function Method) in order to make clear the micromechanism of deformation process on polymer quantitatively^{3,4}. This method has advantage of monitoring the specimen nondestructively, furthermore evaluating it under operating condition without removing the structural components. The change of the transfer function is caused by the existence of crazes and microcracks in the materials^{5,6}. Furthermore, quantitative analysis of the damaged area on the tensile or fatigue specimen by scanning acoustic microscope was performed^{7,8}.

In this study, ETFuM is applied to make clear the micromechanism of a deformation process during fatigue testing dynamically in amorphous polymer (ABS; acrylonitrile butadiene styrene) and crystalline polymer (POM; acetal homopolymer), and discussed.

EXPERIMENTAL PROCEDURE

MATERIALS

Rods of commercially available ABS (ET-70 of Mitsui Touatsu Chemicals Inc.) and POM (M-25 of Polyplastics Co. Ltd.) were used in this study. Both materials are thermoplasticity polymer. But ABS is amorphous and POM is crystalline polymer. Crystallinity of POM was 63% by measuring the density at amorphous or crystalline domain. Mechanical properties of the materials in this study used are given in Table 1. Specimens were machined from extruded rods of ABS and POM which have 40mm diameter. Figure1 shows the dimension of test specimen used. The residual stress of the machined specimens was removed by annealing them at the condition of 80° in ABS and 140° in POM for 3hours, and then cooled in the furnace^{9,10}. Specimens are prepared by buffing to obtain smooth surface enough for SAM observation. After that, Specimens are exposed in thermo-hygrostat at 25° and relative humidity of 5, 42, 97% for over 2000 hours and then used on fatigue test⁷.

FATIGUE TEST

Fatigue tests were performed by closed loop servohydraulic fatigue test machine (Shimadzu Co.,Ltd.) at 1Hz in load control. The R ratio (minimum load/maximum load) was maintained at $R = -1$ for all of the test. Environmental conditions are shown in Table 2, which are the same as exposure conditions of specimens.

Table 1. Mechanical properties of polymer tested

		ABS	POM
Specific gravity		1.05	1.41
Tensile strength	MPa	45.0	62.0
Modulus of elasticity	GPa	2.0	2.8
Deflection temperature	°C	93	158

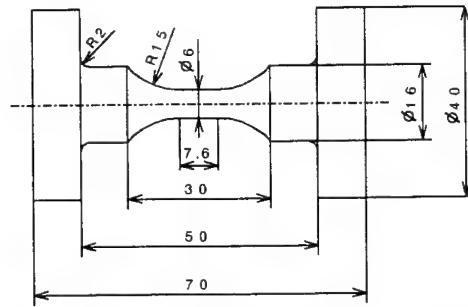


Figure 1. Shapes and dimensions of test specimen

Table 2. Fatigue testing conditions

No.	ABS		POM	
	Temperature (°C)	Humidity (%)	Temperature (°C)	Humidity (%)
1	25	5	25	5
2	25	42	25	42
3	25	97	25	97

EXPLANATION OF ETFuM

The respective functions in time domain are defined as follow⁵.

$$g(t) = \int_{-\infty}^{+\infty} h(t-\tau)f(\tau)d\tau = h(t) \otimes f(t) \quad (1)$$

Then, they are transformed to frequency domain by performing a Fourier transform operation on the integral equation.

$$G(\omega) = H(\omega) \cdot F(\omega) \quad (2)$$

Where, $G(\omega)$, $H(\omega)$ and $F(\omega)$ are the respective Fourier transform of $g(t)$, $h(t)$ and $f(t)$. The input signal path is expected and defined as follow.

$$G_A(\omega) = M \cdot \beta_2 \cdot h_A \cdot \beta_1 \cdot S \cdot F(\omega) \quad (3)$$

Where, M and S are the received and transmitted transducer sensitivity, and β_1 and β_2 is transfer function of coupling condition between transducer and specimen. The transfer function of elastic signal through the specimen is expressed as follows.

$$H_A(\omega) = G_A(\omega)/F(\omega) = S \cdot \beta_1 \cdot h_A \cdot \beta_2 \cdot M \quad (4)$$

The transfer function, H_A is found by multiplying the transfer functions of the system components in frequency domain as indicated in this equation. We only want to obtain information on the polymer specimen h_A . So we need to separate that information from the characteris-

tics of the transducers, and the coupling condition between the transducers and specimen expressed as β_1 or β_2 . We will use the same transducers shown here as S and M. In addition, we have developed a method of coupling the transducer to the specimen so as to obtain good acoustic reproducibility. The transfer function of H_{AN} including other specimen is defined in the same way as H_{A0} including standard specimen. In this experiment, we used the transfer function on virgin specimen as H_{A0} . Then all components of the transfer function that reflect the characteristics of the transducers S and M, and coupling conditions β_1 and β_2 are canceled out, leaving only the information on the specimen as follows.

$$\begin{aligned} H_{AN}/H_{A0} &= (G_{AN}/F_N)/(G_{A0}/F_0) \\ &= (S_N/S_0) \cdot (\beta_{1N}/\beta_{10}) \cdot (h_{AN}/h_{A0}) \cdot (\beta_{2N}/\beta_{20}) \cdot (M_N/M_0) \\ &= (h_{AN}/h_{A0}) \end{aligned} \quad (5)$$

Also, the signal source F provides good reproducibility. The ratio of the output signal G_{AN} to G_{A0} directly explains the difference corresponding to dynamic property of specimen.

$$G(\omega) = G_{AN}/G_{A0} = h_{AN}/h_{A0} \quad (6)$$

Therefore, the effects of specimen shape, transducer sensitivity and so on were eliminated on equation (6). Then, the evaluation function $\Delta h_{A\Omega 2}$ was defined as follows.

$$\Delta h_{A\Omega 2} = \int_{f_2}^{f_1} |G(\omega)| d\omega \quad (7)$$

Here, $\Delta h_{A\Omega 2}$ is integrated value in a frequency range from f_1 to f_2 on equation (7).

METHOD OF MEASUREMENT

The block diagram of ETFuM measurement system is shown in Fig.2. Two piezoelectric transducers were used as transmitter and receiver, respectively. They put in direct contact with the specimen with couplant grease. Signal F is generated by a function generator, input to the transmitting transducer S, passes through the polymer specimen and is picked up by the receiving transducer M and amplifier during fatigue test. It is then fed into a FFT analyzer along with the input signal. The signal are compared and only information on the specimen is extracted by previous equation (5) or (6). Also, cyclic stress-strain curve was measured in same specimens. During fatigue test, load was measured by load cell and displacement was measured by clip gauge.

A flat type PZT transducers (0.01–5.0MHz) were employed and the contact agent between the transducers and the specimen was W-400 (Nippon Steel Co., Ltd.). It provides good reproducibility of the mounting condition, for both the amplitude and phase components¹¹. The measured data obtained with these transducers were sufficiently reliable for comparison without performing any special sensitivity calibration. In this study, f_1 and f_2 were selected from 0.01 to 5.0 MHz on equation (7).

In order to measure the transfer function at anytime during fatigue test, special measuring system was constructed using the trigger generator. In this study, the transfer function was measured at four points in 1 fatigue cycle as shown in Fig.3; (1) maximum tensile stress, (2) ap-

plied stress=0 (under no-load from tension to compression), (3) maximum compression stress, (4) applied stress=0 (under no-load from compression to tension). In this system, measurement time of the transfer function for each point was $640\mu\text{s}$. The change of applied stress during measurement is biggest at points of (2) and (4). But the applied stress changes within 0.4% of stress amplitude. Therefore, it is considered that the change of applied stress is negligible small during measurement.

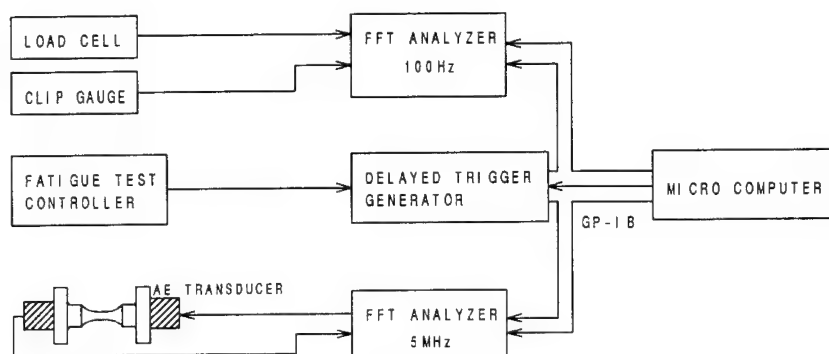


Figure 2. Block diagram of ETFuM measuring system

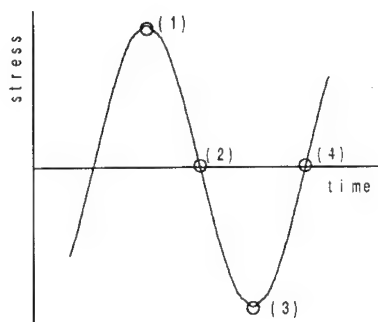


Figure 3. Measurement points of the transfer function

EXPERIMENTAL RESULTS AND DISCUSSION

In order to evaluate the transfer function quantitatively, difference of attenuation Δh_{Af12} was analyzed from equation (7). Figures 4(a)–(d) show the relation between the number of cycles and Δh_{Af12} of 0.5–1.0 MHz in frequency domain in ABS. Because we analyzed the transfer function from 0.5 to 5 MHz at every 0.5 MHz from equation (7), and the change of the transfer function was clearest in 0.5–1.0 MHz. In Figs. 6(a)(b), Δh_{Af12} decreased at the end of fatigue life.

But it began to change from $n=1 \times 10^4$, which was approximately half of the fatigue life $n=2 \times 10^4$. The sense of the results were the same in both ABS and POM.

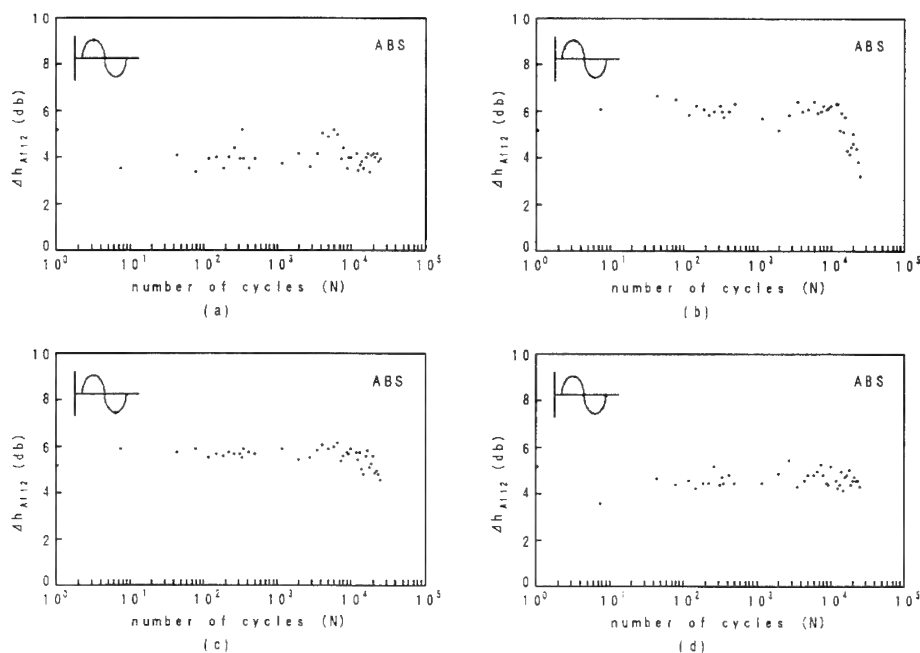


Figure 4. The relation between the number of cycles and Δh_{Af12} of 0.5–1.0MHz in frequency domain in ABS

During fatigue test, cyclic stress–strain curve was measured at the same time on same specimen measured the transfer function. Relation between the number of cycles and strain amplitude, elastic modulus analyzed from hysteresis loop are shown in Fig.5. Strain amplitude began to increase after $n=1 \times 10^4$ and elastic modulus began to decrease in ABS. These trend are correspond to the results of the transfer function in Fig.4(b). In POM, the sense of the results was same.

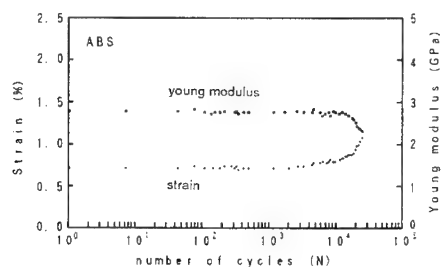


Figure 5. The variation of strain amplitude and elastic modulus during fatigue testing in ABS

We discuss the relation between the transfer function and the micromechanism of deformation process during fatigue on polymer. We had reported the micromechanism of a deforma-

tion process before crazing as follows¹². Molecular chains locally were oriented in a very small area with increasing stress. It is considered that a fibril structure is constructed in the local oriented area, which are thought to be embryo crazing. The embryo crazing was produced from the early stage of plastic deformation, and developed with increasing plastic strain. And in the precursor stage of degradation process in tensile test, the variation of the transfer function indicated the dependence of molecular chain and initiation and growth of craze^{5,6}. From scanning acoustic microscopy, it was found that the damaged area of the specimen was widely dispersed in tensile testing. On the other hand, in fatigue testing, the damaged area was concentrated near the fracture surface^{7,8}. One of the reasons was explained by the nucleation and coalescence of crazes and microcracks. Crazes will be nucleated easily because of temperature rise in a very small area during fatigue testing.

Micromechanism of a deformation process under monotonic applied stress is discussed. At first, texture and stress under each measuring point in Fig.3 were considered as follows. (1) Maximum tensile stress; Crazes or microcracks open due to tensile stress, and texture becomes heterogeneous and anisotropic. (2) Applied stress=0 (under no-load from tension to compression); Crazes and microcracks are transition from open to close. Though stress is not applied, texture becomes anisotropic a little. (3) Maximum compression stress; Crazes and microcracks close. Texture becomes homogeneous due to compression stress. (4) Applied stress=0 (under no-load from tension to compression); Crazes or microcracks are transition from close to open, and texture becomes homogeneous because compression stress is released.

Finally, the transfer function was influenced by applied stress, loading hysteresis and micromechanism of deformation process during fatigue testing. In spite of stress was not applied at points of (2) and (4), micromechanism of deformation process was different due to stress hysteresis. It is considered that the fatigue on polymer depends on the accumulation of microdefects nucleated from the beginning of fatigue life. The transfer function is correspond to the micromechanism of deformation process on polymer dynamically.

CONCLUSIONS

New nondestructive evaluation method of ETFuM (Elastic-wave Transfer Function Method) has been applied to make clear the micromechanism of deformation process during fatigue testing dynamically in ABS and POM.

(1) The transfer function measured under no-load was very sensitive for the micromechanism of deformation process during fatigue testing in both ABS and POM. Because the oriented fibril was nucleated in crazes, and the influence of crazes or microcracks was negligible small, because the transfer function was measured under no-load.

(2) In spite of the transfer function was measured under no-load, the results of two measuring points (under no-load from tension to compression, and from compression to tension) were different. It suggested that the micromechanism of deformation process depended on loading hysteresis.

(3) ETFuM was good correspond to the micromechanism like as local orientation of molecular, nucleation of crazes and microcracks during fatigue process. It has been observed that ETFuM may be appropriate in evaluating the micromechanism of cyclic deformation on polymer dynamically and nondestructively.

REFERENCES

1. T.Yokobori, "Materials strength (in Japanese)", Gihodo press:153(1958) Tokyo
2. I.Narisawa, "Materials strength in plastics (in Japanese)", Ohm press:301(1982) Tokyo
3. Y.Higo, S.Nunomura, "Nondestructive evaluation of adhesive strength by ETFuM", Proceedings of 2nd symposium of nondestructive evaluation in new material and products:131(1988)
4. Y.Hushimi, A.Wada, "Time domain measurement of dielectric dispersion as a response to pseudorandom noise", Review of Scientific Instruments, vol.47, No.2:213(1976)
5. H.Kawabe, Y.Higo, "Nondestructive evaluation of craze and microcrack on polymer by ETFuM", Journal of Materials Science, in press
6. H.Kawabe, Y.Higo, "Nondestructive evaluation of precursory stage of fracture on polymer by ETFuM", Nondestructive Testing Evaluation, vol.8-9:745, Gordon and Breach S.A.(1992)
7. H.Kawabe, Y.Higo, "The influence of environmental conditions on the fatigue strength of plastics", Japan Society of Mechanical Engineers International Journal, in press
8. H.Kawabe, Y.Higo, "Micromechanism of deformation process in polymer during fatigue test (in Japanese)", Japan Society of Mechanical Engineers, vol.58, No.554:1759(1992)
9. "Technical paper of Santac (in Japanese)", Mitsui Touatsu Chemicals Inc.(1986)
10. "Design data of Duracon (in Japanese)", Polyplastics Co.Ltd.(1987)
11. Y.Higo and M.Ono, "On a real time calibration of AE transfer function", Progress in A.E., vol.3, Japan Society of N.D.I.:685(1986)
12. H.Kawabe and Y.Higo, "Micromechanism of a deformation process before crazing in a polymer during tensile testing", Journal of Materials Science, vol.27:5547(1992)

APPLICATION OF ULTRASONIC IMAGING TO WRAP ANALYSIS THROUGH FLOW PATTERN OBSERVATION OF INJECTION MOLDED F RTP PRODUCT

Toshihiko Abe¹, Isao Hanada², Takashi Kuriyama³
and Ikuo Narisawa³

¹Government Indst. Res. Inst., Tohoku,
Nigatake 4-2-1, Sendai

²Hitachi Kasei Mold, Higtashitaga 1-1-1, Hitachi

³Yamagata University, Jounan 4-3-16, Yonezawa, Japan

INTRODUCTION

Fiber reinforced thermoplastics, F RTP, are widely used in many fields of industry because the strength of thermoplastics can be very much increased by fiber addition. Although most of the F RTP products are produced by the injection mold method, there are several problems which relate to the shape or size accuracy such as warp, fin and misrun. All of these problems relate to the flow path of the molten F RTP in a metal mold and also relate to the fiber density and orientation in the product. For this reason many inspection methods, destructive and nondestructive, were applied to observe the flow path and the fiber distribution. Conventional nondestructive methods, including X-ray and optical images proved to be insufficient for this purpose. Scanning acoustic microscopy using high frequency ultrasound is not applicable to internal observation of the polymer composites. However, relatively low frequency, 5 to 25MHz, ultrasound can reach to positions deeper than 1mm from the surface of polymers and polymer composites.

At the present time we are trying to observe the internal structure of many kinds of materials by ultrasonic imaging with this frequency range and found that the flow path of injection molded neat thermoplastics and the fiber distribution in F RTP or CFRP can be clearly shown. We therefore applied this ultrasonic imaging technique to warp analysis to produce high quality F RTP products.

INSTRUMENTATION

Ultrasonic images were obtained using an immersion type point focusing pulse wave probe possessing frequencies of either 5, 10 or 25MHz. After a specimen was immersed in water, the probe was scanned mechanically keeping at a constant distance from the surface so as to maintain focus at

the measuring depth. All the images shown in this paper were measured using longitudinal waves, without image processing by sharpening or edge enhancement.

Fig. 1 shows the positional relation between a reflected ultrasonic pulse and the electrical gate which selects a received signal. In this figure, T is the trigger delay time to eliminate noise signals arriving before the main signal. A and D are surface and back echoes which were reflected at the specimen surface and the back surface. B and C are gate position and width, that is, measuring depth and thickness, respectively.

During measurements, the first pulse which appeared after T was regarded as the surface echo, i.e. A to be the surface. Therefore the reflected signal from a constant depth could be measured even if the specimen surface curved a little. A signal selected by the gate was converted to digitized to a 256 bit level, stored in memory, and used for intensity modulation of the image at the measuring point. The ultrasonic internal image, maximum 750 x 500 bits, was formed by repeating this process while the probe was scanned mechanically to X-Y direction up to 140mm.

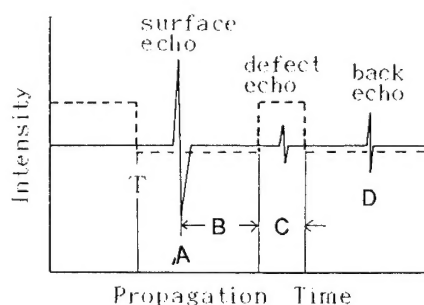


Fig. 1 Relation between echoes and gate position

SPECIMENS

To investigate the depth resolution of the ultrasonic image, laminate type carbon fiber reinforced plastics, CFRP, were prepared. The specimen was 32 ply with $(+45/0/-45/90)_{4s}$ of 4.5 mm in thickness. For the purpose of flow pattern observation, the following two types of neat thermoplastics were injection molded into a bar or a tensile test piece of thickness from 2 to 4 mm. (1) Crystalline type: polyethylene, PE, polypropylene, PP, liquid crystal polymer, LCP. (2) Amorphous type: polymethyl methacrylate, PMMA, polyvinyl chloride, PVC, polycarbonate, PC.

Injection molded FRTP product made by polybutyrene terephthalate, PBT, with 30% glass fiber, and also no fiber, were prepared for warp analysis.

ULTRASONIC IMAGING OF CFRP

Figs. 2a and 2b show the fiber orientation and delamination area in a buckling tested 32 ply CFRP (laminate composite) measured at 25MHz. Fig. 2a shows 1-2 ply in which a delaminated area appeared as a white part due to a strongly reflected echo at the delaminated interface. The fiber orientation $(+45^\circ)$ was recognized in a non-delaminated area.